



UNIVERSITÀ  
DI PAVIA

**COMPMECH**  
Computational Mechanics & Advanced Materials

**University of Pavia**

---

DEPARTMENT OF CIVIL ENGINEERING AND ARCHITECTURE

Doctoral program in Design, Modeling and Simulation in Engineering  
XXXV cycle

DOCTORAL THESIS

**Development of Advanced IsoGeometric Methods  
with Applications in Active Tissue Modeling**

Candidate:  
**Michele Torre**

Advisors:  
**Prof. Alessandro Reali**  
**Prof. Simone Morganti**  
**Prof. Francesco S. Pasqualini**

---

Academic Year 2021/2022



*What do you care what other people think?*

---

Roses are Red, Violets are Blue, there is an error on line 32.



# Acknowledgments

Firstly, I would express my gratitude to my advisors Professors Alessandro Reali, Simone Morganti, and Francesco S. Pasqualini for their continuous mentoring activities and for sharing their deep knowledge in many different fields during these years. Further, I want to thank them for having created a friendly environment, that made everything easier.

I want to thank Dr. Sofia Botti and Prof. Luca F. Pavarino for their collaboration on stem-cell and in-vitro tissue modeling.

I would like to thank Prof. Alexander Düster, who hosted me at the Hamburg University of Technology and dedicated a huge amount of time to discussions. It was a real pleasure to learn about immersed with your help. Further, I want to thank my labmates and friends in Hamburg, you made my stay happier!

My gratitude goes to Prof. Marco de Tullio and Dr. Alessandro Nitti who shared their deep experience in electromechanics and fluid dynamics, giving me the opportunity of collaborating on the simulation of the jellyfish in Bari. Moreover, my period there would have not been that funny if Il Maestro Ale Nitti and the group had not included me. It was a very great time!

At the very beginning of this Ph.D., many colleagues helped me Gaetano, Mauro, Gian F., Karim, Alex, Lorenzo, and others shared a longer part of this journey Ale C., Marco, Sajad, Riccardo, Gian A., Stefania, and all the guys of the ProtoLab. During these years, I had the opportunity of learning a lot from all of you, especially Lau, Annina, Sai, Vale, Madda, Lucia, Fra R., Donato, Ahmed, and Ariel.

Sometimes I need craziness, thank you Marti, Cla, Simo, and Gian for the “discussions” before 8:00.

Sometimes I need to share ideas, also related to science, thank you Max, Guille, and Lars.

Sometimes I need small talks on beer and phase-field modeling, thank you, Gigi!

Sometimes I need “only” a Lot Of Laughs and a bit of support, isn't it Ale P., Ali, and Fra D.?

Very often my mood depends on how bad my code fails, thank you Alfre, Giulia, Giada, and Franca for sharing the office for a long time without kicking me out. Thanks also to Chri, he shares, somehow, the office popping in :)

No result would have been achieved without the continuous support of my Mom, my Dad, and my brother Iac. You are an example for me.

Many longtime friends helped me, directly or indirectly, to grow over these years: I want to thank you all, especially Toni, Dinho, Ire, Chiara, Dadone, Ito, Tolla, Ceci, Pol, Ale T., and Seba.

Finally, a very big hug goes to *Meri*!



# Abstract

The ability to manufacture biologically active tissues has generated increasing interest over the last years in various fields, ranging from personalized and regenerative medicine to soft robotics.

To provide a systematic design framework, many authors have used Finite Element Methods to perform numerical simulations of the electro-mechanical response of contractile tissues. Instead, in this Thesis, I used Isogeometric Analysis to improve the solution of the partial differential equations underlying the tissue models.

Specifically, I investigated the extent to which the Isogeometric-Galerkin method enhances the solution of the coupled electro-mechanical problem and proposed innovative approaches based on the Isogeometric-Collocation method. Further, I demonstrated the performance of traditional and novel approaches using classical multi-dimensional geometries (e.g., 1D cables, 2D manifolds) and real-world applications (e.g., tissue-engineered heart ventricles and jellyfish shaped swimmers).

Part I of this Thesis collects contributions focused on modeling active tissues in various context using traditional isogeometric discretization approaches. Part II, instead, focuses on the new numerical methodologies based on IgA-Collocation that I developed and validated in this field. Finally, we summarize the potential of Isogeometric Analysis in modeling biologically active tissues in the future.

Part of the outcomes of this Thesis are the results of collaborations with other research groups of the University of Pavia, the Polytechnic University of Bari, and the Hamburg University of Technology, as acknowledged in the manuscript.



# Contents

<b>Abstract</b>	<b>vii</b>
<b>1 State-of-the-art of Isogeometric modeling for cardiac biophysics</b>	<b>1</b>
1.1 Fundamentals of Isogeometric Analysis . . . . .	1
1.1.1 Geometry . . . . .	2
1.1.2 Analysis . . . . .	3
1.1.3 Implementation and software . . . . .	5
1.2 Hemodynamic simulations . . . . .	6
1.2.1 Vessel and heart geometry . . . . .	6
1.2.2 Isogeometric methods for blood flow dynamics . . . . .	6
1.2.3 Simulation of the left ventricle and aortic arch . . . . .	7
1.3 Valve modeling . . . . .	8
1.3.1 Heart valve geometry . . . . .	8
1.3.2 Valve mechanics . . . . .	8
1.3.3 Contact between the leaflets . . . . .	9
1.3.4 Interaction with the blood . . . . .	10
1.4 Myocardium modeling . . . . .	10
1.4.1 Modeling of the passive response . . . . .	11
1.4.2 Tissue electromechanical activation . . . . .	11
1.5 Devices and treatments . . . . .	12
1.6 Conclusions . . . . .	13
<b>2 Motivation and structure of the Thesis</b>	<b>15</b>
<b>I Classical Galerkin-based numerical methods for simulation of complex active tissue systems</b>	<b>19</b>
<b>3 Electrophysiological simulations of engineered ventricles</b>	<b>21</b>
3.1 Biophysical model for engineered ventricles . . . . .	22
3.1.1 hiPSC-CMs ventricle model . . . . .	22
3.1.2 The ionic model for cells at the microscale . . . . .	22
3.1.3 The <i>Monodomain</i> formulation for tissues at the macroscale . . . . .	23
3.1.4 Strang operator splitting . . . . .	25
3.1.5 Canonical semi-discrete formulation for the reaction term . . . . .	25
3.2 Isogeometric framework and discrete problem . . . . .	27
3.2.1 B-spline functions for approximations . . . . .	27
3.2.2 Computation of the geometrical mapping . . . . .	28
3.2.3 Spatial discretization . . . . .	29
3.2.4 Time discretization . . . . .	31
3.3 Numerical simulations . . . . .	31
3.3.1 Accuracy investigation . . . . .	32
3.3.2 Electrophysiological simulation of the engineered ventricle . . . . .	34
3.4 Summary . . . . .	35

<b>4</b>	<b>Electromechanical formulations for active tissues</b>	<b>39</b>
4.1	Coupled formulations for electromechanics . . . . .	39
4.1.1	<i>Monodomain</i> formulation for deformable domains . . . . .	40
4.1.2	Active stress formulation . . . . .	41
4.1.3	Active strain formulation . . . . .	41
4.1.4	Tissue mechanics . . . . .	42
4.2	Solution algorithm for active stress . . . . .	42
4.2.1	Spatial discretization . . . . .	42
4.2.2	Staggered time marching algorithm . . . . .	44
4.2.3	Electromechanical simulation of the muscle contraction . . . . .	44
4.3	Summary . . . . .	45
<b>5</b>	<b>Fluid-structural-electrophysiological simulations of swimmers</b>	<b>47</b>
5.1	Mathematical model for the Aurelia Aurita . . . . .	47
5.1.1	Axisymmetric kinematics . . . . .	49
5.1.2	Constitutive model of the solid phase . . . . .	49
5.1.3	Weak formulation for elastodynamics . . . . .	50
5.1.4	Muscle activation via active strain approach . . . . .	51
5.1.5	Electrophysiology and its corresponding weak formulation . . . . .	52
5.1.6	Fluid-Dynamics model . . . . .	54
5.2	Numerical discretization of the multiphysics framework . . . . .	55
5.2.1	Isogeometric discretization for axisymmetric structural dynamics . . . . .	55
5.2.2	Isogeometric discretization for axisymmetric monodomain . . . . .	57
5.2.3	Electro-mechanical coupling . . . . .	58
5.2.4	Finite difference scheme for the fluid problem . . . . .	59
5.2.5	Solid-fluid coupling . . . . .	60
5.2.6	Multiphysics solution algorithm . . . . .	61
5.3	Coupled simulation of the jellyfish swimming . . . . .	61
5.3.1	Mesh and time step calibration . . . . .	61
5.3.2	Conductivity coefficient calibration . . . . .	62
5.3.3	Simulation results . . . . .	63
5.4	Summary . . . . .	64

## II Novel Collocation-based numerical methods for efficient simulation of active tissue systems 67

<b>6</b>	<b>Isogeometric Collocation approach to cardiac electrophysiology</b>	<b>69</b>
6.1	Godunov splitting scheme . . . . .	70
6.2	Spatial discretization via Isogeometric Collocation . . . . .	71
6.2.1	Methodological approach for space discretization . . . . .	71
6.2.2	Semi-discrete Collocation scheme for the reaction step . . . . .	72
6.2.3	Semi-discrete Collocation scheme for the diffusion step . . . . .	74
6.2.4	Summary of the Collocation schemes in matrix form . . . . .	74
6.3	Time discretization . . . . .	75
6.3.1	Discrete <i>Monodomain</i> approximation employing the SVI-C approach . . . . .	75
6.3.2	Discrete <i>Monodomain</i> approximation employing the ICI-C approach . . . . .	76
6.4	State variables recovery in the post-processing phase for the SVI-C approach . . . . .	76
6.5	Numerical experiments . . . . .	76
6.5.1	Cable model . . . . .	77
6.5.2	Action potential propagation in layered tissue . . . . .	79
6.5.3	Curved activation patterns . . . . .	81
6.6	Summary . . . . .	83

<b>7</b>	<b>Immersed Isogeometric Analysis based on a Hybrid Collocation/Finite Cell Method for electrophysiology</b>	<b>85</b>
7.1	Hybrid formulation for space discretization	86
7.1.1	Notation for shell-like manifolds and remarks on the Isogeometric Collocation method	86
7.1.2	Basis of the Finite Cell Method	87
7.1.3	Hybrid Isogeometric Collocation/Finite Cell Method approach for spatial discretization	89
7.2	Extension to dynamics	92
7.2.1	Transient Poisson's-like problem	92
7.3	Numerical tests	93
7.3.1	Poisson's-like problem in 1D	93
7.3.2	Diffusion on a square with a hole	94
7.3.3	Transient diffusion on a curved manifold	95
7.4	Extension to electrophysiology	96
7.4.1	Numerical discretization	97
7.4.2	Simplified example of scar modeling	97
7.5	Summary	98
<b>8</b>	<b>Isogeometric Collocation scheme for coupled electromechanics</b>	<b>101</b>
8.1	Mixed u-p formulation for nearly-incompressible materials in finite deformations	102
8.1.1	Nearly-incompressible hyperelasticity	102
8.1.2	Mixed u-p formulation for Isogeometric Collocation method	103
8.1.3	Numerical tests and discussion	104
8.1.4	Considerations on the applicability to cardiac electromechanics	105
8.2	Isogeometric Collocation scheme for cardiac electromechanics	106
8.2.1	Isogeometric Collocation scheme for cardiac electromechanics	106
8.2.2	Coupled simulations employing separate meshes	110
8.2.3	Considerations on the coupled electromechanical simulator towards future developments	112
8.3	Summary	113
<b>9</b>	<b>Conclusions and outlook</b>	<b>115</b>
<b>A</b>	<b>Details on the engineered ventricle simulations</b>	<b>117</b>
A.1	Mapping procedure for unstructured surfaces	117
A.2	Alternative organization of the convergence plots	118
<b>B</b>	<b>Details on the jellyfish modeling</b>	<b>121</b>
B.1	Summary of physical parameter for the jellyfish model	121
B.2	Validation of the structural solver	121
B.2.1	Linear analysis	121
B.2.2	Nonlinear analysis	123
B.3	Validation of the electrophysiological solver	124
B.4	Validation of the flow solver	125
B.4.1	Laminar vortex ring formation	125
B.4.2	Sphere settling under gravity	126
<b>C</b>	<b>Details on the Isogeometric collocation method for electrophysiology</b>	<b>127</b>
C.1	Stiffness matrix for the case of non-constant conductivity tensor	127
C.2	Computation of the derivatives of the basis functions with respect to the physical coordinates	127
C.3	Implicit-Explicit Euler time discretization scheme without splitting operator	128
C.4	Conduction velocity convergence in semi-logarithmic scale	128
C.5	Ionic current approximations for different knot span sizes	129

<b>D</b>	<b>Details on the Hybrid Collocation/Finite Cell Method</b>	<b>131</b>
D.1	Equations in curvilinear coordinates . . . . .	131
D.2	Convergence test for odd degrees . . . . .	133
D.3	Solution of the Poisson's-like problem on a hollow 2D space . . . . .	133
D.4	Transient problem on a curved manifold . . . . .	135
<b>E</b>	<b>Details on the Isogeometric Collocation method for coupled electromechanics</b>	<b>137</b>
E.1	Simulation setup for the nearly-incompressible cube . . . . .	137
E.2	Simulation setup of the curved body in finite deformation regime . . . . .	138
E.3	Additional convergence test . . . . .	138
E.4	Convergence analysis of the passive component of the pressure field . . . . .	139
E.5	Alternative selections of meshes . . . . .	140
	<b>Bibliography</b>	<b>143</b>

# Chapter 1

## State-of-the-art of Isogeometric modeling for cardiac biophysics

I start this work reviewing Isogeometric Analysis applied to the biophysical modeling of the heart, providing the scientific background to develop this Thesis. I focus on hemodynamics, valve modeling, cardiac tissue mechanics, and on the simulation of medical devices and treatments. For every topic, I provide an overview of the methods employed to solve the specific numerical issue entailed by the simulation. I try to cover the complete process, starting from the creation of the geometrical model up to the analysis and post-processing, highlighting advantages and disadvantages of the methodology. Such a literature review identifies the topics that are subsequently addressed, as described in Chapter 2.

Recent advancements in medicine and diagnostic techniques have increased our understanding of the functionality of the heart in physio-pathological conditions, providing a great amount of patient-specific data. In the perspective of precision medicine [3], these data can be used to construct computational models [1, 4], as shown in Fig. 1.1, so that therapies and surgeries can be calibrated in advance on the patient-specific conditions increasing their success rate.

Numerical simulations naturally represent a suitable framework for preliminary investigations since they allow for testing of alternative strategies in a safe and controlled environment. However, two main source of difficulties arise: the correct modeling of the complex biophysics, and the appropriate selection of the numerical methods to perform the simulation.

Many efforts focused on providing realistic mathematical models and the reader is referred to recent reviews [5, 6, 7, 8, 9] for thorough discussions. In most of the computational frameworks, the Finite Element Method (FEM) is the base technology, achieving impressive results [10]. Nevertheless, those simulations are computationally intense, calling for high performance computing facilities, that limit their use in the clinical routine.

Herein, we review the numerical aspects of the simulations and how Isogeometric Analysis (IgA) can enhance the process reducing the computational effort. I highlight the pros and cons of IgA applied to cardiac modeling, using FEM as a reference for comparisons since they share some common features and providing some tips for implementation.

This chapter is organized as follows: In Sec. 1.1 I briefly review the basic concepts of Isogeometric Analysis for geometrical modeling, analysis, and software implementation. In Sec. 1.2, I address hemodynamic simulations analyzing the techniques adopted in this field. Sec. 1.3 is completely devoted to the modeling of the heart valves, since they involve peculiar computational challenges. In Sec. 1.4, I present the developments in the simulation of cardiac tissues, while, in Sec. 1.5, I review some applications oriented to clinical scenarios. Finally, Sec. 1.6 draws some conclusions and future prospective.

### 1.1 Fundamentals of Isogeometric Analysis

Isogeometric Analysis is a numerical technique to discretize in space Partial Differential Equations (PDEs) using spline functions – typical of Computer Aided Design (CAD) technologies – for the representation of both the geometry, as schematically shown

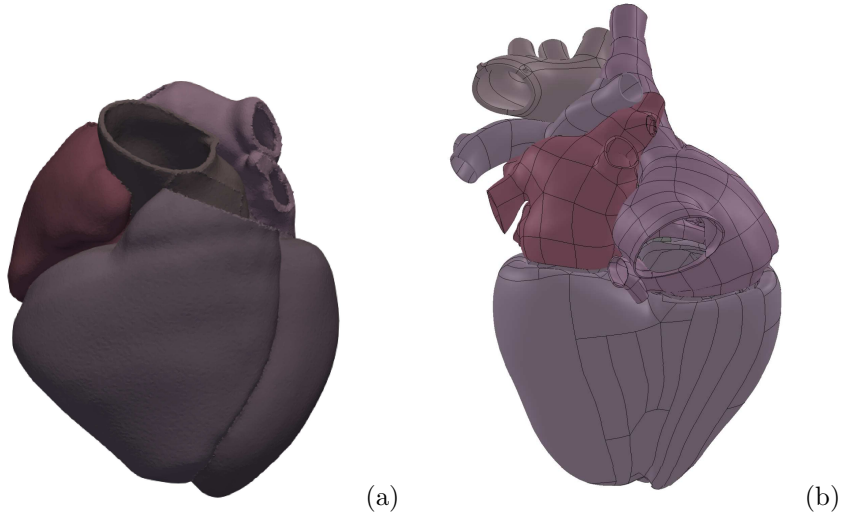


Figure 1.1: Finite element mesh adapted from [1] (a) and CAD representation adapted from [2] (b) of patient-specific models of the human heart.

in Fig. 1.2, and the solution of the equations, in Fig. 1.3. Following this definition, I initially review the geometrical aspects and then the simulation step, which in the IgA literature is also called the analysis step. Later I introduce some software for IgA.

### 1.1.1 Geometry

In the IgA framework, the geometry of a generic body is represented using spline functions, that are defined in a portion of an abstract parametric space, namely the patch [11, 12]. Different types of splines have been investigated, but the most widely used in cardiac applications are B-splines, Non Uniform Rational B-splines (NURBS), and T-splines. They are sets of polynomial functions constructed using the knot vectors – collections of non-decreasing parametric coordinates (i.e., the knots) – specified for a given polynomial degree. When combined with a network of control points, defined in the physical space and herein referred to as control net, the patch is mapped into the physical manifold reconstructing the actual geometry. I refer to this function as the geometrical mapping.

In the case of B-splines in Fig. 1.2, the representation of curves, surfaces, and solids starts from the definition of uni-variate B-splines, that are highly continuous, scalar functions defined using the Cox-de Boor recursion formula [11]. It takes as an input the polynomial degree  $p$  and the knot vector, that governs the continuity of the splines at the element interfaces (i.e., the interface between two knot spans) varying in the range  $C^0 \leq C^{p-m} \leq C^{p-1}$ , where  $m$  is the multiplicity of the knot. Usually, the maximum continuity is enforced to attain a great accuracy in the solution of the PDEs [13]. By taking the tensor product of uni-variate splines, a two- or three-dimensional parametric space is built and successively mapped onto a physical manifold of the same dimension exploiting the linear combination of splines and control point coordinates that act as coefficients for the splines.

NURBS are constructed taking the ratio of B-splines functions enabling the exact representation of conic sections (e.g., a circle). The denominator is called weighting function and is given by the linear combination of B-splines and weights, one per control point. If the weight function is constant and equal to one, B-splines and NURBS coincide [12].

Both multi-dimensional B-splines and NURBS are based on a tensor product structure, therefore their meshes are composed by quadrilateral (or hexahedral in 3D) elements organized in a regular grid. T-splines [14, 15], instead, differ from the previous functions for the possibility to create T-junctions at the element interfaces and, consequently, the control points does not create a regular net. This simplifies the creation of a mesh but it must be noted that T-splines are not linearly independent in their original version (i.e., they are not a suitable for the numerical discretization) and a proper selection of the blending functions must be done to perform the simulation [16].

A refinement of the geometry localized near to a specific feature cannot be carried out acting only on the knot vectors because the tensor product structure of NURBS and B-splines propagates the refinement

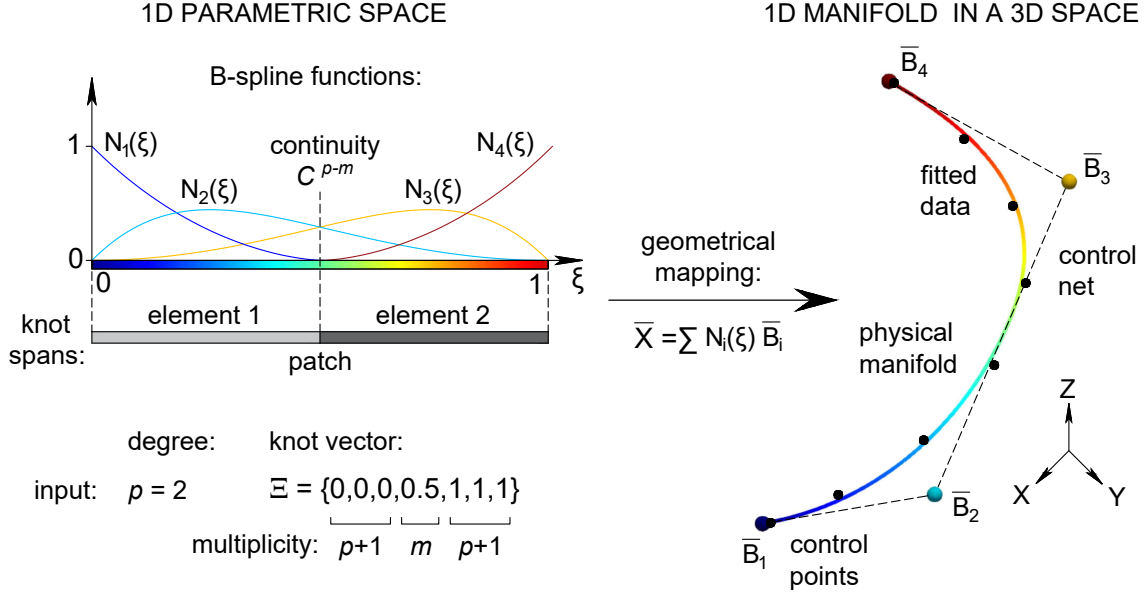


Figure 1.2: Schematic of the geometrical representation based on splines. The splines (here:  $N_1(\xi)$ ,  $N_2(\xi)$ ,  $N_3(\xi)$ , and  $N_4(\xi)$ ) are defined using the knot vector  $\Xi$ , the degree  $p$ , and the multiplicity of each knot  $m$ . When the multiplicity of the first and the last entries of the knot vector is  $p + 1$ , the knot vector is called open knot vector. Using these information the patch is subdivided in elements ruling the continuity at the element interfaces. The physical geometry  $\bar{X}$  is then constructed using a net of points, that in general is composed by non-interpolatory points denominated control points (here:  $\bar{B}_1$ ,  $\bar{B}_2$ ,  $\bar{B}_3$ , and  $\bar{B}_4$ ). The linear combination of splines and the control point coordinates maps the parametric space into the physical one. Adapting the control point coordinates, the geometry of the manifold can be modified to fit a set of data.

in the whole patch. To keep the refinement localized, the hierarchical (truncated) splines were introduced [17].

I remark that T-splines, NURBS, and B-splines belong to the same family of functions. Indeed, B-splines are special cases of NURBS, that in turn are special cases of T-splines retrieved regularizing the control net. Consequently, some features are preserved: since all the splines are continuous functions, the parametric space and the physical body share the same topology in a boundary-fitted framework. To create complex topologies [18], several patches can be combined using specialized algorithm to define the interactions at the interfaces during the simulation [19, 20].

In practical applications, the coordinates of the control points are unknown, for example because the geometrical data are provided in the form of diagnostic images and not CAD models. In these cases, special algorithms can be used to approximate [11] complex geometries, entailing advanced meshing operations. This is one of the reason IgA has not been widely adopted in cardiac modeling so far. However, if the meshing process is excessively demanding, it can be avoided using ad-hoc algorithms, namely, the Immersed Method, during the analysis, as shown in the following.

### 1.1.2 Analysis

Once the geometrical mapping is defined, the same spline functions are usually adopted to represent the finite-dimensional functional space used to approximate the solution of the PDEs, following the isoparametric paradigm [12] schematically represented in Fig. 1.3. Splines exhibit many valuable properties, useful to improve the accuracy and the robustness of the simulation [12]. Herein, I will focus mainly on the regularity. Indeed, highly continuous splines provide a straight forward approach to the approx-

# SIMULATION FRAMEWORK

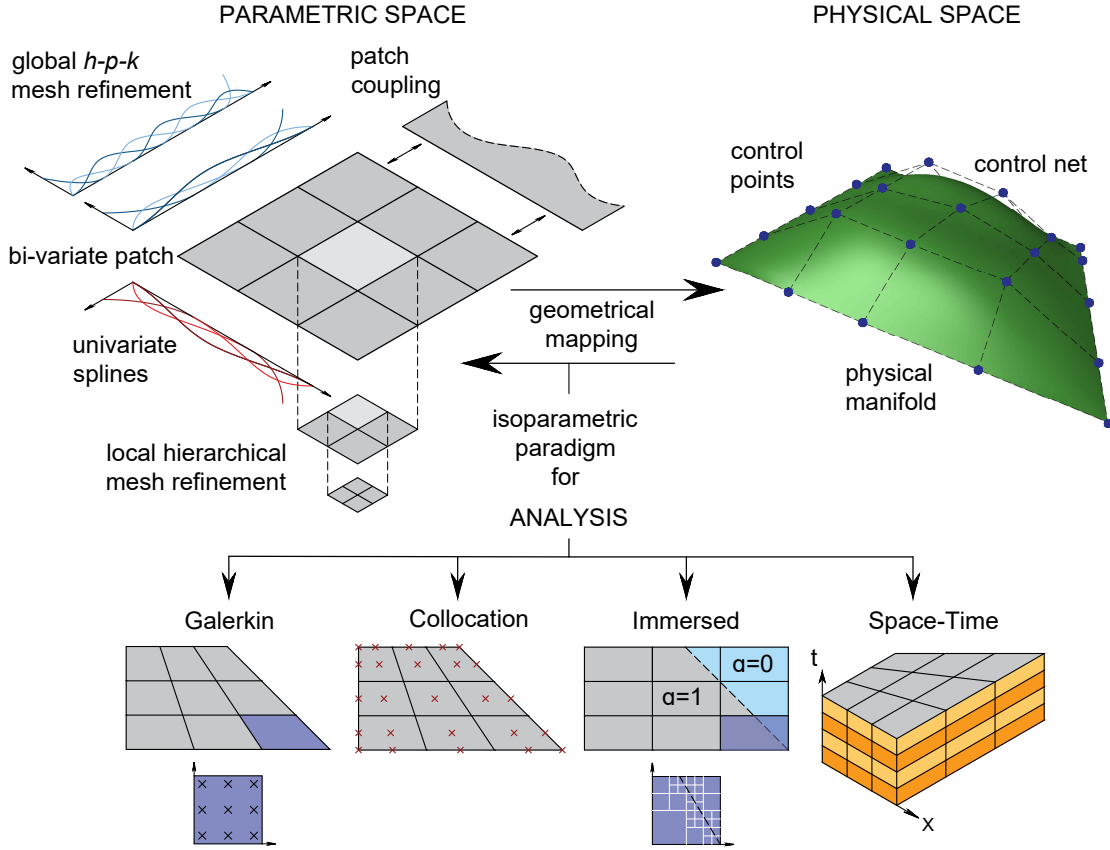


Figure 1.3: Schematic of the Isogeometric Analysis framework. The geometrical mapping connects the parametric and physical spaces, possibly combining several patches to create complex topologies. In the analysis, the same spline functions are used to discretize the equations according to the adopted approach, for instance: Isogeometric-Galerkin, Isogeometric-Collocation, Immersed, and Space-Time methods. Since the geometrical representation is often too coarse for the analysis, the mesh is refined either at the global level modifying the uni-variate splines or with a local hierarchical scheme.

imation of high order PDEs, that might define structural models [21, 22], and better approximate the frequency spectrum in vibration analysis [23, 24], entailing major implications in dynamic simulations.

The most popular strategy for analysis is the Isogeometric-Galerkin method [13], which is similar to the classical FEM. Indeed, bilinear (trilinear) quadrilateral (hexahedral) finite elements and first order splines are equivalent in this approach. The continuity, in combination with the polynomial degree, results in an enhanced accuracy at the cost of a greater effort for integral computation. To limit this burden, improved quadrature rule were developed [25, 26, 27, 28, 29].

The Isogeometric-Collocation method [30] differs from the Galerkin approach since it is based on the strong (differential) form of the PDEs instead of the weak (integral) one. It aims to reduce the computational burden [31] avoiding quadrature, so limiting the number of function evaluations, at the cost of a reduced accuracy.

Additionally, a variety of Immersed methods are available [32, 33, 34, 35], they aims at simplifying the meshing operation for complex shapes by immersing the analyzed body in a regular mesh. The aspect ratio and volume of the elements are easily controlled in a regular rectangular (hexahedral) grid, avoiding the presence of distorted elements. However, an advanced quadrature rule for cut elements is needed to reconstruct the actual geometry during the analysis. Chapter 7 introduces a combination of Collocation and Immersed methods [36], that may be employed in cardiac applications exploiting the potential of both approaches.

Software	Language/user interface	Short description
GeoPDEs [50, 51]	Octave MATLAB	Open-source package featuring Div-conforming splines and hierarchical adaptivity
Nutils [52]	Python	Open-source library with native implementation of IgA and FCM
tIGAr [53]	Python	Open-source library to perform IgA using the FE code FEniCS [54]
CouDALFISh [55]	Python	Open-source library that implements IMGA for FSI using tIGAr
PSYDAC [56]	Python	Open-source library with native implementation of IgA
igafem [41]	MATLAB	Open-source package oriented to structural mechanics
ISOGAT [57]	MATLAB	Tutorial code for 2D examples
PetIGA [58]	C	Open-source extension of PETSc to IgA leveraging parallel computing
Igatools [59]	C++	Open-source library with native implementation of IgA
AdHoC++ [60, 61]	C++	Academic high-performance code for FCM and IgA
G+Smo [62]	C++	Open-source library for IgA featuring hierarchical splines and multi-patch technology
FEAP [63]	Fortran	Extension of the academic FE code to IgA
Geomiso DNL [64]	—	stand-alone code oriented to mechanics
LS-DYNA [65]	—	commercial code for explicit dynamics using IgA
Coreform [66]	—	commercial code with native implementation of IgA
kiwi!3D [67]	—	plugin to perform IgA in Rhino

Table 1.1: Summary of the software available for IgA.

Finally, splines are effectively used also in the time discretization for dynamic problems as an alternative to classical time marching schemes. It leads to the so called Space-Time methods [37], that are effectively used in fluid dynamics.

The discretization methods entail different requirements for the splines to be analysis-suitable from a mathematical point of view. In general, the functional space spanned by the splines must be complete and the spline functions must be continuous and linearly independent. For more details on these definitions, the reader is referred to the classical book on FEM [38]. Herein, I simply note that the linear independence of T-splines is not always guaranteed [16], while the tensor product structure of B-splines and NURBS always fulfills such a requirement. Moreover, the numerical discretization of a PDE requires a higher basis function continuity when the order of the involved derivatives is increased. In this regard, IgA outperforms classical finite elements since the continuity is easily modified, allowing for a direct discretization of high order PDEs and enabling the development of the Isogeometric-Collocation method, which requires a higher continuity than the Galerkin approach.

Depending on the simulation requirements and the accuracy of the method, the functional space spanned by the splines involved in the geometrical mapping may be too coarse to achieve precise results. In this case, the mesh can be refined – preserving the geometry and the parametrization – exploiting the knot insertion and degree elevation algorithms for uni-variate splines. These algorithms are the equivalent of the  $h$ -refinement (split the elements) and  $p$ -refinement (increase the element order) for the FEM [38, 39]. However, in IgA, they can be combined in the  $k$ -refinement to refine the mesh maintaining the spline continuity. Furthermore, the mesh can be refined at local (element) level using a hierarchical scheme [17]. Such an approach is often employed during the analysis, to adaptively refine the mesh where the solution is more complex [40], limiting the computational effort.

### 1.1.3 Implementation and software

I conclude this brief introduction presenting software that can be used to perform IgA simulations. For more details on the implementation aspects of IgA, the reader is referred to the classical book on

IgA [12] or to a comprehensive review [41]. In the finite element framework, several software tailored for biomedical applications were developed, for instances the Living Heart Project [10] based on the commercial code Abaqus and stand-alone implementations like Chaste [42] or `lifex` [43, 44, 45], but an equivalent for IgA is still missing. Nevertheless, I highlight that an Isogeometric-Galerkin formulation can be recast in a Finite Element software, for instance Abaqus [46], using the Bézier extraction operator [47, 48, 49]. Such a machinery can be used to perform IgA reusing the structures developed for FEM.

In Tab. 1.1, I report a (non exhaustive) list of available codes and plugins for general-purpose implementations to help the interested readers.

## 1.2 Hemodynamic simulations

Computational fluid dynamics (CFD) is a methodology, recognized even by regulatory authorities [68], suitable for biomedical investigations thanks to its noninvasive nature [69] and the possibility of designing and optimizing cardiovascular devices [70, 71, 72]. Moreover, CFD and Fluid-Structure Interaction (FSI) simulations are attractive for their ability to predict the clinical outcomes [73] and in personalizing the clinical treatments [74] to improve their success rate. In this regard, simulations allows for a straightforward quantification of hemodynamic parameter information [75], such as the Wall Shear Stress, or the pumping efficiency during systole in ventricle simulations, that are not captured by alternative techniques, such as the 4D MRI [5].

In this framework efficient solvers have to fulfill several requirements. Patient specific anatomies, reconstructed starting from diagnostic images, must be correctly represented since small imperfections in the mesh may lead to significant errors in the computation of the flow field [76]. The numerical solution of complex 3D flows entails a great computational effort, challenging even for high-performance computers. Therefore, the maximum computational efficiency of the algorithm is needed. This is achieved by focusing on relevant aspects only and improving the efficiency of the scheme, such that the required accuracy can be achieved using a minimal number of degrees-of-freedom. A classical example of simplified assumption is the Newtonian fluid for the blood modeling [77, 78], while the computational efficiency strongly depends on the algorithm. I will review how IgA addresses such questions on a number of relevant CFD problems in cardiac modeling.

### 1.2.1 Vessel and heart geometry

The first step in the simulation is the definition of the geometrical mapping, i.e., the computation of the control point coordinates starting from the result of the medical image segmentation.

Most of the meshing tools for patient-specific analysis of the vasculature were developed within the finite element framework [79], mainly relying on unstructured tetrahedral discretizations, that are not suitable for IgA since it uses hexahedral elements. To define an isogeometric representation of interconnected blood vessels, a common procedure is to extract the vessel center-line and to adapt a template to the patient anatomy, as shown in several papers [80, 72, 74] and recently improved [79].

In meshing the heart, different strategies may be employed for the atria and the ventricles [81]. Indeed, the former are often considered as 2D manifolds [82, 83] since the thickness is limited, while the latter are considered as trivariate solids. In both cases, the geometry is subdivided in patches to simplify the fitting procedure and then assembled. Similar techniques were applied in the representation of complete organs [84, 40] but for more complex, general-purpose, meshing tools the reader is referred to relevant recent publications [18, 85, 86].

If a direct computation of the geometrical mapping is too complex, an Immersed approach, based on the Finite Cell Method [87, 88, 32, 89, 90], was successfully employed in the analysis of the artery stenosis [91, 92], leveraging a direct integration of the Computer Tomography (CT) scan in the computational framework.

### 1.2.2 Isogeometric methods for blood flow dynamics

In simulations of incompressible flows, one of the main issues to be addressed is the stability of the numerical solution of the Navier-Stokes equations discretized by means of the Galerkin approach. Therefore, suitable functional spaces for the representation of the pressure and velocity unknowns [93, 94, 95, 96, 97]

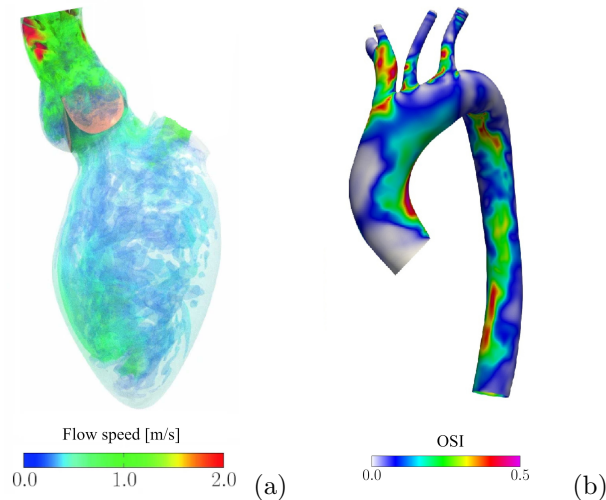


Figure 1.4: Results of hemodynamic simulations. (a) Simulation of the flow velocity in the left ventricle at the beginning of systolic phase [37]. (b) Computation of the Oscillatory Shear Index (OSI) in the aortic arch [111].

and ad-hoc techniques [98, 99, 100, 101, 102, 103, 104, 105] to stabilize the numerical algorithm are employed.

The Reynolds number typical for hemodynamics takes on values ranging from few thousands in the ventricle and aortic arch to many thousands in arteries and in the aortic valve [106, 78, 107]. To simulate this kind of flows, most of the isogeometric solvers [108, 109, 110, 111] split the velocity and the pressure fields into coarse and fine scales. They resolve the macroscopic scale only according to the Variational Multiscale (VMS) approach [112, 103] and stabilize the fine scale. Notably, the stabilization term can be derived in a fully-consistent way from the Navier-Stokes equations [103]. The accuracy of the spline-based approximation in space for Reynolds numbers in the range of interest was proven and favorably compared with linear FEM [103, 113, 114].

In accurate computations of the Wall Shear Stress, or other indexes like the Oscillatory Shear Index, a detailed reconstruction of boundary layers is needed, requiring a finer mesh in those regions [111]. In this regard, conforming mesh performs better than non-conforming methods. Consequently, when the vessel deformability must be considered [115, 116, 117, 118, 119], the Arbitrary Lagrangian Eulerian approach is typically used to properly track the interface between the solid and the fluid [120, 121, 122].

To integrate the Navier-Stokes equations in time, two approaches are viable: classical time marching schemes and Space-Time (ST) methods. In the former case, the second-order accurate generalized- $\alpha$  method is often employed thanks to its ability in dissipating high-frequency modes, that are poorly represented in the numerical algorithms. In Space-Time methods, a spline-based discretization is adopted also in time [110, 111, 37, 123]. The techniques developed for space discretization are further improved by the continuity of the shape functions in time [110], at the cost of a more complex code implementation.

In fluid dynamics simulations, boundary conditions are usually prescribed either in terms of fluid velocity, or traction, or resistance, according to physiological data [124, 121, 111]. However, in the Galerkin framework, the strong imposition of Dirichlet boundary conditions, for instance the no-slip boundary conditions, can lead to inaccurate results and a weak enforcement seems more appropriate [125, 126, 120, 127]. Moreover, spurious numerical back-flow at an outlet may lead to the divergence of the analysis, requiring stabilization. Such an instability, may arise when Neumann boundary conditions are enforced or when a 3D domain is coupled to lumped parameter models [128]. In the IgA context, the back-flow stabilization can be addressed using the techniques applied in several investigations [72, 128, 35] or adding a special-purpose element at the boundary [37].

### 1.2.3 Simulation of the left ventricle and aortic arch

Combination of the techniques presented in Sec. 1.2.2 have been successfully employed to simulate 2D and 3D flows in simplified ventricle geometries [109, 108] as well as in patient specific anatomies [37],

as shown in Fig. 1.4(a). The deformation of the ventricle wall can be imposed a priori according to simplified laws or using data from CT-scans [37]. In a recent work [129], a similar approach, integrating structural simulations [130, 131], was used to define the boundary conditions of a mixed finite element-isogeometric analysis. Simulations of the cardiac tissue by means of IgA are possible, I address this topic in Sec. 1.4.

In CFD and FSI simulations, the velocity and pressure fields are computed and are available for post-processing to derive the quantities of interest. I remark that the high regularity of splines is beneficial also in this step, since, differently from standard FEM, it provides a continuous representation of the derivatives of the fields (e.g., the stresses) without any additional step. Indeed, indexes related to the shear stress are of great interest in investigations on the blood dynamics, as shown in Fig. 1.4(b). Similar considerations are applicable also to all the other types of simulations presented in this chapter.

Examples of simulations using time marching schemes [120, 72, 80] or ST methods [111, 37] to compute hemodynamic parameters can be found in the literature. Moreover, analyses of the ventricle [108] and of the aortic arch [111] can be combined to obtain more realistic simulations [37], including the aortic valve, which entails several difficulties, that are addressed in Sec. 1.3.

## 1.3 Valve modeling

Heart valves play a major role in the definition of the blood stream imposing a unidirectional flow through the chambers. However, impairments in the response of the valves may lead to blood regurgitation and in a redistribution of the stresses, possibly entailing tissue remodeling, lipid deposition and calcification [132, 133]. To quantify the risk of occurrence of such phenomena, the coaptation length or the coaptation area are often used [134, 135, 136] as a quantitative metric, since they represent the extension of the contact between the leaflets [132]. If the valve functionality is not sufficient, a prosthetic surrogate may be implanted to restore healthy conditions. However, in this kind of surgery, an optimized design of the valve geometry [135] and a proper selection of the materials [137, 138] are primary factors for a successful transplant. In this regard, the impact of different intervention strategies on postoperative outcomes, for instance the assessment of regurgitation or the orifice area, can be investigated in a controlled framework by means of numerical simulations [135].

To be a suitable framework in the context of heart valves, numerical simulations must handle patient-specific anatomies [136, 139] and efficiently solve three main numerical issues: (i) The leaflet modeling by means of shell elements is challenging because thin-structure are either not directly discretizable in primal formulation using FEM [140] or prone to the shear-locking instability [141, 142, 143, 21]; (ii) An efficient contact algorithm is required to properly model the interaction between the leaflets and, possibly, with the chordae tendinaea [134, 144]; (iii) These kind of FSI simulations require an algorithm capable of addressing topological changes in the fluid domain occurring during the cardiac cycle [35, 145, 146] (i.e., the atrium and the ventricle are interconnected only when the valve is opened). IgA has the ability of fulfill all these requirements, as I will demonstrate in the following.

### 1.3.1 Heart valve geometry

Several patient-specific models, as shown in Fig. 1.5(a), were reconstructed starting from diagnostic images [134, 144, 136, 139, 135, 37]. The procedure [134, 35] relies on the subdivision of the valve in patches and on a spline fitting procedure to reconstruct the parametrization of the geometry. In such a process, the aim is to minimize by means of a least-square method the distance between the spline geometry and the collection of points derived from the clinical data. More details are available for the tricuspid valve in [136] and the chordae tendinaea modeling, while details on the aortic valve and the aortic root are provided in [134]. Moreover, also a correct modeling of the arterial wall may have a great impact on the simulation result, as highlighted in a dedicated work [121]. In simulating prosthetic valves, the mapping step may be avoided since it is already encoded in the CAD model [121, 122], proving that the spline representation is analysis-suitable.

### 1.3.2 Valve mechanics

Isogeometric Analysis exhibits convenient numerical properties to simulate the valve motion: the high regularity [13] of the basis functions at the element interfaces enables the discretization of Kirchhoff-Love

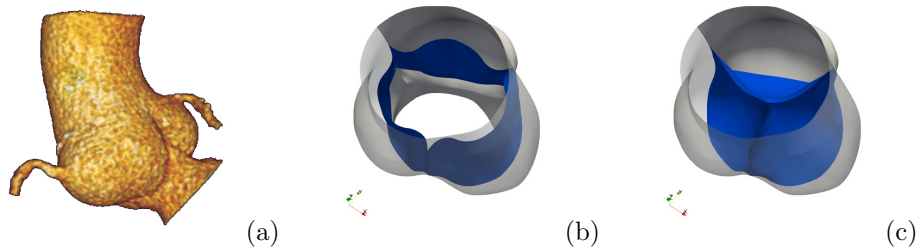


Figure 1.5: Patient specific model of the aortic valve. (a) Segmentation result of a Computer Tomography Angiography integrated with ultrasound measurements [134]. Snapshots of a numerical simulation representing the opened (b) and closed (c) phases of the valve. For visibility, the leaflets are highlighted in blue and part of the aortic root, in grey, is rendered translucent.

shells in primal form (i.e., a pure displacement-based formulation) [140, 21], that nicely approximate the leaflet mechanics [134], as shown in Fig. 1.5(b). This approach – that cannot be applied in the standard finite element framework [140] – uses only three degrees of freedom per control point to describe the complete motion in terms of mid-surface displacements, avoiding the shear-locking instability inherited by Reissner-Mindlin-based theory. The high accuracy per-degree-of-freedom strongly reduces the computational time required to complete dynamic simulations for two consequential motivations: a limited number of elements is needed to achieve a predefined accuracy, and, at the same time, it guarantees a larger stable time step size in explicit time-marching schemes. Indeed, the constraint on the time step imposed by the Courant-Friedrichs-Lewy condition is relaxed if the characteristic element size is increased. Proof of this concept is provided in a comparison between IgA and FEM [134].

Beside the efficient discretization, a displacement-based formulation offers the opportunity of using a broad list of material models developed for 3D continua [21]. Several material laws, calibrated for valve modeling, are available in the literature [139], ranging from simplified Kirchhoff-Saint Venant and Neo-Hookean models calibrated to partially represent more complex behaviors [147, 35, 121], to Mooney-Rivlin and Fung-type laws [134, 144], and more refined anisotropic formulations [137, 138]. Different portions of tissues rely on distinct kinematic hypothesis. For instance, the aortic root in healthy conditions is thicker than the leaflets and a shear-deformable shell [143] may be more representative of the actual mechanics [140, 134]. Several formulations for the Reissner-Mindlin shells are available for both the IgA-Galerkin [143, 148, 149] and IgA-Collocation [150] methods. However, in several cases, the artery wall is modeled using solid elements [121, 137]. The isogeometric framework offers the possibility of coupling manifolds of different dimensions [151] (e.g., 2D and 3D sub-domains) or kinematics [152] (i.e., K-L and R-M shells) to recreate complex anatomies, combining different approaches.

### 1.3.3 Contact between the leaflets

The coaptation length is measured during the fully-closed phase of the valve, shown in Fig. 1.5(c), when a uni-directional constraint to the displacements of the leaflets holds. In simulations focusing on the solid structure solely [134, 144], the implementation of the contact is mandatory, while it is not strictly necessary in FSI simulations since the compatibility of the fluid flow should fulfill the constraint. However, the contact algorithm is usually included also in FSI to improve the quality of the simulation [35]. The adopted formulation must be robust, to guarantee the convergence of the analysis, and accurate, to correctly capture the actual interaction. In this kind of simulations, the representation of the geometry is a sensible factor: the faceted representation of a surface, typical of linear finite elements, could make the convergence more complex and produce inaccurate results [153]. Consequently, several finite element algorithms implement a surface-smoothing algorithms [154, 155] to improve the stability and the accuracy of the simulation. The IgA framework does not require any additional step thanks to the native smooth representation of the geometry provided by the splines [156]. Several contact formulations are available for IgA [157], ranging from the classical penalty method for IgA-G [134, 35] and IgA-C [158, 159], to the mortar method [156] and potential-based [144] approach. Depending on the valve under consideration, multiple contacts should be considered. For instance, in the aortic valve only the contact between the leaflets is considered, while in the right atrioventricular (tricuspid) valve also the interaction with

the chordae tendineae should be included [144]. In the latter case, the contact algorithm must handle interactions between manifolds of equal (i.e., shell-to-shell and cable-to-cable) and different (i.e., cable-to-shell) dimensions.

### 1.3.4 Interaction with the blood

In simulating the blood flow through the valve, many of the core components of the solvers presented in Sec. 1.2, such as the VMS method, are employed to solve the Navier-Stokes equations. However, in valve simulations, the fluid domain rapidly changes in topology during the cardiac cycle, thus immersed methods [35, 160] are often employed to avoid complex re-meshing operations needed to redefine the shape of the domain. The leaflets can be modeled [161] as an implicit surface and the sharp variation in the pressure across the valve is enforced using the level-set-based approach [162], while in a different approach [107, 163] the FSI problem is tackled combining a Finite Difference scheme and the Immersed Boundary (IB) method. In such an approach, a direct numerical simulation for fluid-dynamics and a representation of the leaflets by means of the Fedosov’s interaction potential was accomplished. However, a recent work has demonstrated that the same methodology can be improved by modeling the leaflets using isogeometric Kirchhoff-Love shells [164]. Moreover, the IB was successfully integrated in the Isogeometric-Collocation approach [165], that may be further improved using a recent divergence-conforming approach [166]. Regarding the Isogeometric-Galerkin framework, the Divergence-Conforming Immersed Boundary method [167, 168] was successfully employed, for instance, in the simulation of red blood cell motion. Therefore, it may be employed to investigate the effect of blood stream on the deposition of cells and particles in stagnation areas.

A modification of the IB method, actually consisting of a reinterpretation of the Finite Cell Method, gave rise to one of the most used approach for heart valve simulations, called Immersogeometric Analysis [35](IMGA). A macroscopic difference with previous methods relies in the computation of the flow in the part of the domain superimposed to the solid body: such a part of the fluid domain is removed during the integration of the weak form using an indicator function according to the Finite Cell Method. However, in simulating interactions between fluids and shells, a special treatment of the FSI problem is needed since shells are manifolds with no thickness and both sides of the leaflets are represented by the same surface. To this end, the Dynamic Augmented Lagrangian was introduced [35], further improved by means of stabilization algorithms [169, 170, 171, 172], and combined with divergence-free basis functions [173]. Combinations of these algorithms were successfully employed in many valve simulations [137, 35, 173, 171, 122, 169, 172]. In most of the cited isogeometric methods, the incompressibility constraint – and the inherited stability issues – is conveniently addressed constructing a suitable functional spaces for the analysis, improving the accuracy in the fulfillment of the mass conservation. As a limitation of this methodology – inherited by the immersed approach – I report the reduced accuracy, with respect to boundary-fitted approaches, in the local approximation of the flow field close to leaflets.

An evolution of the IMGA is the Sequentially-Coupled FSI method [37]. It combines the IMGA and high-fidelity fluid simulations, based on ST methods, to improve the reconstruction of the flow field. A peculiarity is the possibility of handling different levels of mesh refinement and time step sizes for the sub-problems. Moreover, the variation in the domain topology is exploited degenerating elements and constraining the degrees of freedom according to the ST Topology Change method [145]. Adopting such a methodology, the boundary layer near to the leaflets was successfully captured enabling a precise computation of the Wall Shear Stress [174].

## 1.4 Myocardium modeling

Simulations of the myocardium involve many delicate aspects of solid mechanics, ranging from finite deformations to material non-linearities, as well as the incompressibility constraint. Moreover, cardiomyocytes contract when stimulated, thus investigations on the cardiac tissue can involve coupled electrophysiological-mechanical problems. Also in this kind of simulations, the complexity of the problem is even increased by the reconstruction of the patient-specific geometry, as already discussed in Sec. 1.2.1.

IgA has been largely exploited in mechanics with application ranging from the analysis of mechanical components [175, 89], to fracture mechanics [176, 177], and additive manufacturing process [178].

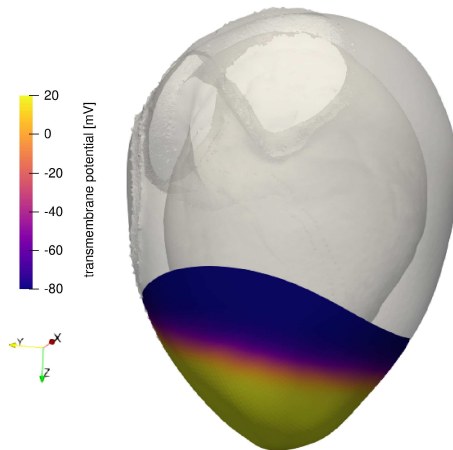


Figure 1.6: Isogeometric simulations of active tissues. Propagation of the action potential in a portion of the human left ventricle, partially rendered translucent.

However, despite the appealing premises, a limited literature is available for the cardiac muscle modeling.

#### 1.4.1 Modeling of the passive response

The response of the cardiac tissue subject to an external load (e.g., the blood pressure) has been modeled enforcing many different hyperelastic laws, ranging from the simple Neo-Hookean [179, 180] to more physiological models [181, 182]. In most of the cases, biological tissues exhibit a nearly-incompressible response, introducing a major difficulty in the simulations. Indeed, similarly to the CFD case, numerical instability due to the incompressibility constraint, often referred to as volumetric locking, may affect the numerical solution. To tackle this issue a high-order approximation, or mixed formulations, or projection-based methods are often adopted.

High order approximations – i.e., discretizations based on basis functions of high degree – are a straight forward approach for IgA since degree elevation is a well-known algorithm [11], and in many cases it is sufficient to significantly alleviate locking, as proven for IgA [183] and high-order FEM [184, 185, 186]. If high order approximations are not a viable strategy, the  $\bar{B}$  and  $\bar{F}$  methods [187] – developed for linear and finite elasticity, respectively – can be adopted. Furthermore, mixed formulations can be derived. In the Isogeometric-Collocation context [188, 189], they retrieve a high accuracy even for low order basis functions.

Although the literature for IgA applied to cardiac muscle simulations is limited, the applicability in mechanobiology was demonstrated through the modeling of blood vessels [121], biological tissue and membranes [179, 190, 191, 192, 193, 194], cell migration [195], tumor growth [84], and the coupling of tumor growth with mechanics [196].

#### 1.4.2 Tissue electromechanical activation

The mechanical contraction of the cardiac muscle activated by the calcium dynamics inside the cell entails the simulation of a coupled electromechanical problem, that is a multiscale problem since the phenomena involved differ in the time and space scales [197, 9].

To simulate the electrophysiology of the cardiac tissue, as show in Fig. 1.6, two main mathematical formulations are available in the literature, namely the monodomain and bidomain models [198, 199, 200], that integrate complex cellular models [201, 202, 203] in the simulation of the tissue. Both theories were successfully applied in simulation of the propagation of the action potential in the human atria [82, 83], in bi-ventricular models [81], and on generic manifolds [179] using an Isogeometric-Galerkin discretization. Chapter 6 presents an Isogeometric-Collocation method for electrophysiological simulations [204] exploiting Nutils [52] to reduce the computational effort. It aims at combining the accuracy of spline-based discretizations with the cost effectiveness of collocation schemes [31]. Indeed, an accurate and fast

simulator for electrophysiology may be helpful in assessing the effects of diseases on the overall heart functionality [205].

In electromechanical simulations the electrophysiology is coupled to the mechanics according to either the active stress [206, 207], or the active strain [208], or combined formulations [209]. Coupled electromechanical simulations were carried out in the IgA framework [179] also simulating the contraction of a Kirchhoff-Love shell governed by an electrophysiological stimulation. This is clearly a proof of the potential of IgA, but more investigation is needed.

IgA electrophysiological solvers can be further improved including some fundamental features, like the Purkinje fiber network, to enhance the realism of the simulation [210]. With a complete framework, that models the whole heart using the bidomain approximation, studies on the cardiac arrhythmia could be conducted to assess, for example, the dynamics of the spiral waves and the consequent variation in the trace of the electrocardiogram. Indeed, the simulation of the action potential propagation in the heart can be coupled with a model of the torso to simulate the wave signal on the skin surface [199], enabling a direct comparison with standard clinical data. The complete framework may be employed to calibrate pharmacological therapies, assessing the interaction between drugs and/or with previous clinical conditions. Furthermore, the simulator may be used to help clinicians in the planning of the surgery. For instance, in the case of arrhythmia, the minimal area to ablate during the surgery could be assessed *in-silico* [211].

The multi-scale nature of the coupled electromechanics can be addressed using nested meshes to reduce the computational effort. However, in an effective scheme, the information exchange between the meshes must be efficient to keep the computational gain provided by the mesh tailoring as high as possible [212]. IgA could take advantage of the exact preservation of the geometry and parametrization [12] during mesh refinement to simplify such a process. These concepts, for instance, were addressed in Chapter 8 and in [213]. These kind of structural simulations may be, in turn, coupled with a fluid dynamic solver, as mentioned in Sec. 1.2.3, to simulate the heart pumping activity [9], providing relevant data to the clinicians, such as the effect of a drug on the volume of blood pumped in a cycle. The possibility of coupling an isogeometric discretization of the electromechanical problem with a fluid dynamic solver was recently investigated [214], as explained in Chapter 5.

Pathological conditions are clearly of great interest but underlie an even greater complexity. For example, in the case of post-infarction scars, part of the cardiac tissue may vary its properties becoming unresponsive to an electrophysiological stimulation [205], while its stiffness still affects the deformation. Therefore, such a simulation involves the solution of a coupled problem defined on two different geometries – one for electrophysiology and one for mechanics – which is not trivial. In this context, an Immersed method may be used to deactivate part of the computational domain of the electrical sub-problem without modifying the geometry, that is shared by both sub-problems [215]. Furthermore, Immersed methods are well-suited to integrate diagnostic images into the analysis. Therefore, leveraging such a feature, they may greatly improve the realism of the simulation.

## 1.5 Devices and treatments

The numerical approaches presented herein aims at providing a framework to analyze the functionality of the cardiovascular system to improve the calibration and personalization of medical treatments. However, the lack of a software tailored for the isogeometric discretization of biomedical problems limits the spreading of the technique in the daily practice. Nevertheless, many examples of applications exist.

IgA was applied in the design of drug delivery systems deployed in coronary arteries [74] and to simulate injections [216, 217] addressing the interaction between the tissue permeability and the pressure.

Focusing on the hemodynamics of the heart, the effect of a left ventricular assist device was analyzed [72] providing a better understanding in the modification of the flow due to the implantation.

The main field investigated using IgA is the design of prosthetic heart valves, represented in Fig. 1.7. Several surrogates were developed, ranging from models fixed on a rigid frame [122] to self-expandable devices [218]. To validate the IgA framework, the approach has been employed to model an experimental setup simulating the flow through the valve [173]. In the design of the prosthetic valve [122], particular care is posed in the choice of the leaflet thickness, to avoid flutter instability [219], and of the materials, to optimize the response of the leaflet [137, 135, 138], even under cyclic loading [220] avoiding long-term failures.

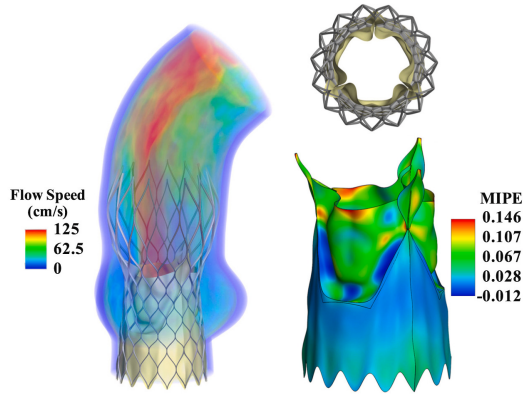


Figure 1.7: Simulation of the aortic valve replacement employing a self-expandable valve [218]. Representation of the flow speed through the valve and of the maximum in-plane principal Green–Lagrange strain (MIPE) on the deformed configuration.

Vascular stents are lattice structures effectively modeled using beam elements [221, 222]. The deployment of a such a structure in the vessels is a complex simulation involving the modeling of the lattice, the contact with the vessel, and the interaction with the blood. IgA efficiently embeds such problems within a single framework [218], providing a substantial reduction in the computational effort for structural analysis with respect to the FEM [223].

Switching to a different context, IgA could be used to reproduce *in-vitro* experiments on the cardiac tissue, like Organ-On-Chips [224, 207], since the numerical modeling is similar to the pure cardiac case and their geometry may derive from CAD systems. An initial study [225] in this sense is conducted in Chapter 3. Investigations can assess if the parametric description of the domain, typical of IgA, is beneficial in defining the best spatial distribution of the tissue. For instance, a specialized algorithm may be developed to optimize the design of the assay such that several requirements (e.g., a target displacement) are fulfilled with a minimal amount of cultured tissue, reducing the manufacturing cost. Indeed, in IgA the geometry of the analyzed body can be view as a standard field, like the displacements, the pressure, or the potential.

## 1.6 Conclusions

In this chapter, I have discussed the applicability of Isogeometric Analysis to the modeling of the heart in cardiac simulations.

The main difficulties are related to the complex mesh generation, however many strategies are currently available to simulate patient-specific models, ranging from advanced meshing tools to Immersed approaches.

Regarding analysis, IgA offers a broad class of methods, that can be employed and combined to accurately simulate the heart biophysics and the effect of clinical treatments. In particular, I focused on hemodynamic simulations, showing the performance of the VMS approach further combined with ST methods. The simulations of heart valves highlight the power of IgA, especially in the modeling of the leaflets by means of thin-shell structures.

Investigations on the myocardium modeling are more limited, with respect to the other fields. However, the technologies developed for FEM can be recast in the IgA framework and further improved by advanced discretization techniques. Particularly challenging is the simulation of the tissue activation in physiological and pathological conditions because they involve complex coupled problems, possibly defined on different meshes, characterized by different spatial and temporal scales. Nevertheless, IgA offers many possibilities to efficiently address these problems.

I have concluded the overview reporting several examples of biomedical applications powered by the IgA, which confirm the effectiveness of the approach in this research field. Nevertheless, IgA is not only limited to the design of devices: it can also be used to reproduce models of the cardiac tissue, potentially opening a framework for the *in-silico* optimization of the assay design.



## Chapter 2

# Motivation and structure of the Thesis

In the previous chapter, using the work presented in [226], I have introduced the Isogeometric framework applied to the simulation of the heart, showing the main challenges of such a complex problem. The literature on the simulation of the blood flow and valves is more developed than that for the simulation of the active tissue, as highlighted in Section 1.4, which represents the topic I further investigate.

Active tissue simulations originate from cardiovascular applications, but the recent advancements in the tissue-engineering techniques have extended the interest to the modeling of a new set of biomedical scenarios, namely the simulations of engineered cell culture platforms for precision medicine (e.g., Organs-On-Chips) [224], introduced in Section 1.5. Furthermore, looking at the simulations from a purely mathematical point of view, completely different biological systems, like the jellyfishes, are modeled using the same approach. This latter problem has major implications in a broad class of applications ranging from studies of jellyfish biology to the design and optimization of bio-inspired swimmers [227].

In this Thesis, I focus on numerical algorithms targeted to simulate active tissues since their applications are of great interest. I investigate the effectiveness of IgA for the spatial discretization of this particular biological problem, since it is not completely proved. Afterwards, several improvements, based on the observed critical aspects in the initial studies, are proposed. I focus on the following three types of applications: *in-vitro* models, swimmers, and human cardiac tissues. However, simulations of the whole human heart are not considered in this Thesis because they involve a strong code parallelization to keep the problem computationally tractable. In this work, I do not address this computational topic, but the herein proposed algorithms may be applied to this kind of simulations successively.

The Thesis addresses the simulation of active tissues focusing in cascade on three main subjects, namely the electrophysiology, the electromechanics, and the fluid-structure-electrophysiological interactions. The cell and tissue models are initially discretized within a Galerkin framework. However, I propose several improvements of the numerical formulation using the Isogeometric Collocation method, as summarized in Table 2.1. Consequently, the Thesis may be presented using two alternative structures, governed either by the modeled physics or by the adopted numerical methods. To better highlight the innovations proposed, I follow the subdivision based on the numerical methods organizing the manuscript in two main parts: one related to the canonical Galerkin-based simulations of the active tissues, and one to the novel Collocation-based methods.

Three chapters investigate the effectiveness of standard Isogeometric-Galerkin methods in the active tissues modeling. Based on the work presented in [225], the electrophysiological simulation of an engineered ventricle is discussed in Chapter 3. Successively, in Chapter 4, the coupled formulation for electromechanics is investigated. Finally, fluid-structure-electrophysiological simulations, based on the work presented in [214], describe the jellyfish swimming, as presented in Chapter 5.

In presenting these topics, potential weak points in the standard numerical formulations are observed. Therefore, the second part of the Thesis is devoted to present an innovative framework, based on the Isogeometric-Collocation method, to address these issues. In Part II, I focus on exemplificative problems to better describe the peculiarities of the methodology, while biophysically applications are left to future investigation since they require an optimization of the numerical implementations.

	Canonical methods				Novel approaches		
	Part I	Investigated topics	Achieved results		Numerical criticisms observed	Solution methods proposed	Part II
Electrophysiology	Chapter 3	Modeling of the electrophysiological response of an engineered tissue made of stem-cells	Calibrated <i>in-silico</i> model for parametric investigations of the response of the construct	→	The sharp wavefront must be discretized using several elements regardless of the basis function degree	The IgA-C discretization for electrophysiology limits the computational burden under <i>h</i> -refinement	Chapter 6
				Functional holes in the tissue require complex meshing operations	The Hybrid IgA-C/FCM approach limits the mesh complexity incorporating IgA-C in an immersed framework	Chapter 7	
Electromechanics	Chapter 4	Formulations for coupled electromechanics to simulate the tissue contraction	Coupled solver to simulate the mechanical activation of a contractile tissue	→	An efficient coupling strategy is needed when different discretizations for the sub-problems are used	The method for nested mesh selection avoids history variable interpolations in the IgA-C context	Chapter 8
Complex coupled problems	Chapter 5	Definition of a coupled solver for fluid-structure-electrophysiological interactions to study the efficiency of the jellyfish swimming	Detailed simulator used to investigate the biological parameters regulating the efficiency of the jellyfish swimming	→	Non-standard cellular models cannot be coupled to the tissue formulation using state variable interpolations	The IgA-C based discretization computes the state variable evolution at the collocation points avoiding the interpolations	Chapter 6
				The incompressibility constraint of biological tissues may restrict the choice of the eligible basis functions	The two-field formulation based on IgA-C models nearly-incompressible solids in finite deformation regime	Chapter 8	

Table 2.1: Summary of the topics illustrated in this Thesis.

In particular, Chapter 6, that is based on the work presented in [204], exploits the cost-effectiveness of the Collocation scheme in electrophysiological simulations, enabling the use of a wider class of cell models. This is the core idea, further elaborated in the subsequent chapters. Part of the simulation of the engineered ventricle discusses the geometrical modeling, highlighting the complexity of the generation of a structured mesh for irregular biological tissues. Therefore, in Chapter 7, that is based on the work presented in [36], I enhance the formulation proposing an immersed version of the Isogeometric-Collocation method to simplify the meshing procedure. The last investigated subject is a coupling scheme for electromechanical simulations. In Chapter 8, based on the work presented in [213], I present a coupled Collocation scheme extending the mixed  $\mathbf{u}$ - $p$  formulation, developed for linear elasticity, to the finite deformation regime.

Eventually, the main results of my work are summarized in Chapter 9 along with several future

perspectives.

Part of the results presented in this Thesis were achieved in collaboration with other research groups: Prof. Pavarino and Dr. Botti from the Department of Mathematics of the University of Pavia participated to the engineered ventricle simulations; Prof. de Tullio and Dr. Nitti from the Department of Mechanics Mathematics and Management of the Polytechnic University of Bari contributed in the fluid-structure-electrophysiology-interaction simulations; and Prof. Düster from the Institute for Ship Structural Design and Analysis of the Hamburg University of Technology collaborated to the development of the hybrid immersed-collocation method. Coherently, I respectfully adopt the first-person plural-form hereinafter in the manuscript.



## Part I

# Classical Galerkin-based numerical methods for simulation of complex active tissue systems



## Chapter 3

# Electrophysiological simulations of engineered ventricles

Regenerative cardiology recently advanced in patient-specific medicine by employing somatic cells to derive pluripotent stem cells and differentiate them into cardiomyocytes. To be useful, these cells have been used with increasingly complicated *in-vitro* platforms, ranging from traditional cell culture dishes, to engineered simplified platforms such as organs-on-chips, to miniaturized 3D ventricles. The design of these platforms has so far been mostly by trial-and-error. However, a rich framework for biophysically-detailed computational modeling of cardiac electromechanics exists, and we reasoned that it could be brought to bear on the problem of designing *in-vitro* platforms for precision medicine.

In this chapter, developed in collaboration with Department of Mathematics of the University of Pavia, the cardiac *Monodomain* model is coupled with stem cell ionic models to simulate the action potential propagation in the engineered ventricle. The cardiac model is then discretized by means of Isogeometric Analysis, carrying out numerical experiments to assess the accuracy of the approach. Finally, the presented framework is used to investigate the propagation of an action potential on the calibrated model of the engineered ventricle. Our results demonstrate the increasing accuracy of the virtual representation of innovative stem cells ventricle, suggesting an *in-silico* low-cost approach to stem cells tissue investigations.

Human Induced Pluripotent Stem Cells-Derived Cardiomyocytes (hiPSC-CMs) are spontaneously beating cardiomyocytes derived from somatic cells. This field was pioneered in 2006 by S. Yamanaka [228], who was awarded the Nobel Prize in Medicine in 2012 for the discovery of mature cells reprogrammed to become pluripotent. Further, hiPSC can be driven towards the cardiac lineage through differentiation protocols [229]. hiPSC-CMs express the major cardiac markers and ion channels, they are functionally like adult human cardiomyocytes, and exhibit expected responses to cardiac stimuli. Although several studies have shown that iPSC-CMs have molecular, structural, and functional properties resembling those of adult cardiomyocytes, they have proved to be less mature than adult cells, as they do not display the sub-cellular, cellular and tissue-level adult myocyte morphology and sarcomeric protein content and organization [230]. Even though such cells are molecularly and functionally immature, in the cardiovascular field, hiPSC-CMs provide a powerful tool to develop reliable *in-vitro* models for drug toxicity screening.

The possibility to engineer hiPSC-derived cardiac cell cultures being as similar as possible to undiseased and diseased regions of the human heart is the first step to improving the translation of hiPSC-CMs to humans. 2D cultures of hiPSC-CMs are often used as a platform for investigating new therapies, even if intrinsic limitations arise in terms of spatial architecture. Re-creating *in-vitro* a reliable 3D tissue is undoubtedly more complex than using standard cell cultures, and several new aspects have to be considered simultaneously. Besides these efforts, researchers have bioengineered a three-dimensional model of a human left heart ventricle, used to measure time-dependent pressure and volume, as described in [224, 231].

Since modern cardiac models have transformed and increased the understanding of cardiac function in health and disease and the clinical practice of cardiology [9], a virtual rendering of the engineered ventricle can provide a robust environment to conduct preliminary investigations, otherwise entailing expensive

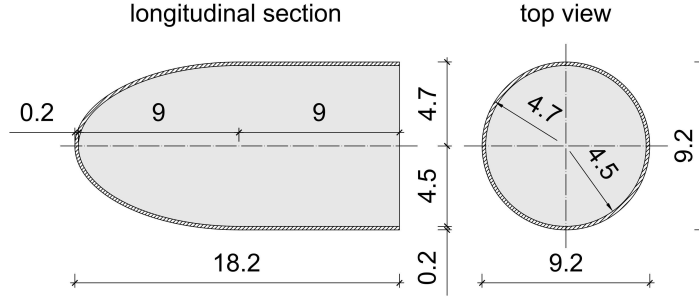


Figure 3.1: Schematic representation of the ellipsoidal scaffold. Dimensions are expressed in millimeters.

trial-and-error tests. In this direction, this work aims to develop a comprehensive framework, based on Isogeometric Analysis, for electrophysiological simulations representing the response of engineered tissues. The mathematical modeling of the heart involves systems of PDEs and ordinary differential equations (ODEs) coupled to model cardiac electrophysiology.

To describe the proposed model, we start, in Section 3.1, with the description of the ventricle architecture and we review the micro and macroscopic models of cardiac electrophysiology at the continuous level. In Section 3.2, we introduce the numerical methods to discretize the space, by means of Isogeometric Analysis, and time. Section 3.3 provides an extensive analysis of the method accuracy varying the spatial discretization, that aims to select the scheme for an effective simulation. Afterward, we calibrate the model and reproduce the propagation of the action potential in the engineered ventricle. Finally, Section 3.4 recapitulates the main findings and derives possible future perspectives.

## 3.1 Biophysical model for engineered ventricles

In the following Section, we briefly present the tissue-engineered scale model of the ventricle, which we model using an Isogeometric approach. Firstly, we describe the geometry of the *in-vitro* model and the formulation adopted for the modeling of hiPSC-CMs. Afterward, we describe the *Monodomain* formulation, entailing a reaction-diffusion PDE coupled with a suitable ionic model, employed to model the tissue. Finally, we present the splitting of the reactive and diffusive terms of the PDE by means of continuous Strang operator, posing the base for the numerical discretization.

### 3.1.1 hiPSC-CMs ventricle model

By *Engineered heart tissue* we mean three-dimensional muscle strips, or muscular thin films, that can be generated from isolated heart cells or hiPSC-CMs [232, 233, 234]. Herein, we are taking into account the tissue-engineered scale model built at Harvard University [224, 231], where the scaffold was designed taking inspiration from the human myocardial tissue architecture and recreated using a nanofiber production system. The strategy developed for the production of a nanofiber ventricle is based on pull-spinning fibers on a rotating ellipsoidal collector. The resulted fabricated thin-wall chambers were then sutured to tubing or bioreactor components. Catheter sensors were then introduced and stable contraction of hiPSC-CM ventricles permitted time-dependent pressure and volume measurements. Thus, this kind of scaffold can promote the assembly of cardiomyocytes into functional 3D tissue-engineered ventricle chambers.

In order to model this engineered ventricular chamber, we use the ellipsoidal geometry of the scaffold presented in [224] and depicted in Fig. 3.1. Indeed, the engineered ventricle manufacturing process consists of seeding and growing hiPSC-CMs on a scaffold previously formed on a collector. We schematize such a shape using a constant-thickness extrusion of the molding surface, even though it becomes irregular during cell maturation.

### 3.1.2 The ionic model for cells at the microscale

Cardiomyocytes' cultures include spontaneously beating cells, but also express a mixture of different adult profiles, such as atrial, ventricular and nodal markers [235]. Because of these significant differences

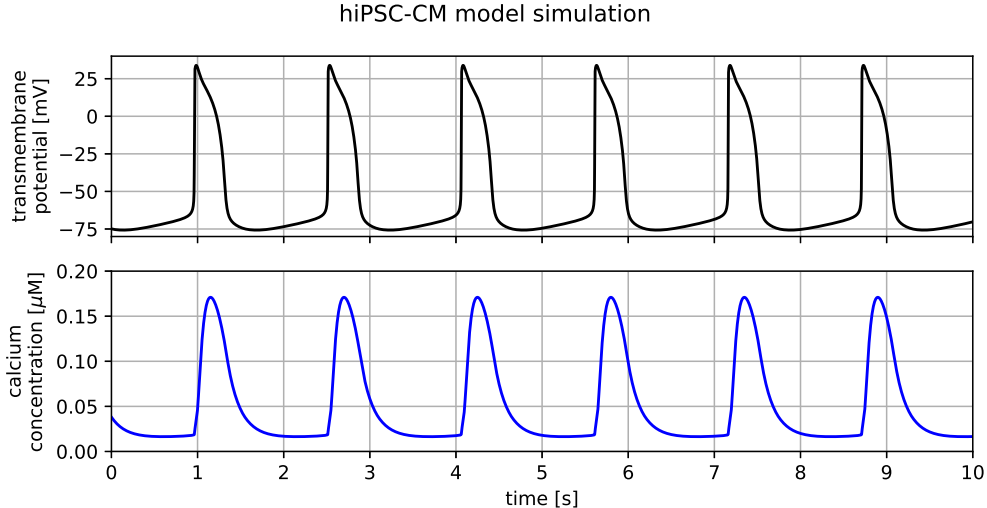


Figure 3.2: The adopted ionic model. Ten second of simulations show the spontaneous firing activity of the transmembrane potential  $v$  (top), and  $Ca^{2+}$  concentration in the sarcoplasmic reticulum (bottom).

with respect to adult myocytes, models of adult cardiac action potential inadequate describe the hiPSC-CM electrophysiology. To fill this gap, some specific computational methods have been developed in the last decade. A primal formulation was published in 2013 [236], then updated in 2018 with a more flexible Calcium ( $Ca^{2+}$ ) handling formulation, [237]. This model focused on the ventricular-like phenotype, the predominant phenotype emerging during the differentiation process. A deep analysis of different ionic models for hiPSC-CMs has been conducted in [238].

The latter ionic model is perfectly suitable to model an engineered tissue, since it recapitulates several relevant features of hiPSC-CMs, such as the  $Ca^{2+}$  concentration and the spontaneous firing activity, shown in Figure 3.2. Consequently, we adopt such a model [237] to simulate the electrophysiological activity of the tissue.

The ionic model describes the evolution in time of the transmembrane potential and several ionic currents following the classical Hodgkin-Huxley formulation. For a detailed presentation of the equations underlying the model, the reader is referred to [237]. Herein, we sum up some relevant features. The system of ODEs consists in a set of 22 variables, differentiated into (i) the transmembrane potential  $v$ ; (ii) 3 ionic concentrations  $c^s$  ( $Na_i$ ,  $Ca_i$ ,  $Ca_{SR}$ ); (iii) 15 gating variables  $w^r$ , involved in 7 different membrane currents; (iv) 3 gating variables  $w^r$  ( $RyR_o$ ,  $RyR_c$ ,  $RyR_a$ ), standing for the Ryanodine Receptors' probabilities of activation, inactivation and adaptation, needed for the novel characterization of  $Ca^{2+}$  dynamic, [239]. Such an ionic model is integrated in the tissue formulation through equations (3.2c), (3.2d), and (3.2e).

### 3.1.3 The *Monodomain* formulation for tissues at the macroscale

The canonical description of cardiac electrophysiology models the behaviour of the tissue in space ( $\mathbf{x} \in \Omega$ ) and time ( $t \in (0, T)$ ) by means of two superimposed continua, representing the intra-cellular and the extra-cellular spaces. These compartments exchange the charge via the ionic current  $I^{ion}$  across the cellular membrane, whose intensity depends in a point-wise manner (i) on the difference between the intra-cellular potential  $u_i$  and the extra-cellular potential  $u_e$

$$v(\mathbf{x}, t) = u_i(\mathbf{x}, t) - u_e(\mathbf{x}, t), \quad (3.1)$$

and (ii) on the cellular state by means of the  $s$  ion concentrations  $c^s$  and the  $r$  gating variables  $w^r$ . Inside a single compartment, the charge redistributes according to the linear diffusion law governed by the conductivity tensors  $\mathbf{D}$ ,  $\mathbf{D}_e$ , for the intra-cellular and extra-cellular spaces respectively, linking the local cellular state to the one of the neighboring cells.

Moreover, the charge flux through the cellular membrane depends on the capacitance  $C_m$  and ratio  $\chi$  – between the membrane surface area and the volume enclosed by this surface – regulating the time delay,

while intra-cellular  $I_i^{app}$  and extra-cellular  $I_e^{app}$  currents can be applied to simulate external stimuli. The charge conservation law finally leads to the *Bidomain* formulation [199, 200, 240].

It embeds the single cell model, described by a system of ODEs (equations (3.2c), (3.2d), and (3.2e)), into the tissue model (PDEs (3.2a) and (3.2b)):

$$\begin{cases} \chi C_m \frac{\partial v}{\partial t} - \nabla \cdot (\mathbf{D} \nabla v) - \nabla \cdot (\mathbf{D} \nabla u_e) + \chi I^{ion} = I_i^{app} & \text{in } \Omega \setminus \partial\Omega \times (0, T) & (3.2a) \\ -\nabla \cdot (\mathbf{D} \nabla v) - \nabla \cdot ((\mathbf{D} + \mathbf{D}_e) \nabla u_e) = I_e^{app} + I_i^{app} & \text{in } \Omega \setminus \partial\Omega \times (0, T) & (3.2b) \\ I^{ion} = I^{ion}(v, w^1, \dots, w^k, c^1, \dots, c^q) & \text{in } \Omega \times (0, T) & (3.2c) \\ \frac{\partial w^r(\mathbf{x}, t)}{\partial t} = m_w^r(v, w^1, \dots, w^k) \quad \forall r = 1, \dots, 18 & \text{in } \Omega \times (0, T) & (3.2d) \\ \frac{\partial c^s(\mathbf{x}, t)}{\partial t} = m_c^s(v, w^1, \dots, w^k, c^1, \dots, c^q) \quad \forall s = 1, \dots, 3 & \text{in } \Omega \times (0, T). & (3.2e) \end{cases}$$

The system is then coupled with appropriate initial conditions for both transmembrane potential and ionic model variables

$$\begin{cases} v(\mathbf{x}, 0) = v_0 & (3.3a) \\ w^r(\mathbf{x}, 0) = w_0^r \quad \forall r = 1, \dots, 18 & (3.3b) \\ c^s(\mathbf{x}, 0) = c_0^s \quad \forall s = 1, \dots, 3. & (3.3c) \end{cases}$$

and homogeneous Neumann boundary conditions for the no flux assumption through the external surface  $\partial\Omega$  (i.e., we suppose an electrically isolated domain):

$$\begin{cases} \mathbf{n} \cdot \mathbf{D} \nabla (v + u_e) = 0 & \text{on } \partial\Omega \times (0, T) & (3.4a) \\ \mathbf{n} \cdot (\mathbf{D} + \mathbf{D}_e) \nabla u_e + \mathbf{n} \cdot \mathbf{D} \nabla v = 0 & \text{on } \partial\Omega \times (0, T) & (3.4b) \end{cases}$$

where  $\mathbf{n}$  is the outward pointing normal. Finally, since the charge has to be conserved, the applied currents have to obey to the compatibility condition:

$$\int_{\Omega} (I_i^{app} + I_e^{app}) d\mathbf{x} = 0. \quad (3.5)$$

The conductivity of an engineered tissue built on a scaffold depends on (i) the spatial organization and geometrical orientation of the cells [241], and (ii) on the gap junctions expression and other biological factors related to the cell maturation [224, 231]. The engineered ventricle manufacturing process guarantees a high cell alignment, quantified by the Oriental Order Parameter, in the circumferential direction. Coherently, we assume an anisotropic, transversally isotropic, intercellular conductivity tensor with a greater eigenvalue in the fiber direction. The cell maturation affects the conductivity in an involved manner, resulting in a complex experimental quantification of the parameters. We simplify the mathematical formulation by assuming that the extracellular and intercellular conductivity are proportional:

$$\mathbf{D}_e = \lambda \mathbf{D}, \quad (3.6)$$

as already done in various studies regarding the human heart [242, 82]. Consequently, we reduce the number of unknown parameters to two: the intra-cellular conductivity in the direction of the fibers and in the orthogonal direction, which we can calibrate using the available experimental results.

The equal anisotropy hypothesis (equation (3.6)) greatly simplifies the Bidomain formulation (equations (3.2a), (3.2b), and (3.4)). Indeed, after some algebraic manipulations, presented in [199], we recover the *Monodomain* formulation:

$$\begin{cases} \frac{\partial v}{\partial t} = -\frac{1}{C_m} I^{ion} + \frac{1}{\chi C_m (\lambda + 1)} [\lambda \nabla \cdot (\mathbf{D} \nabla v) + (\lambda I_i^{app} - I_e^{app})] & \text{in } \Omega \setminus \partial\Omega \times (0, T) & (3.7) \\ \mathbf{n} \cdot \mathbf{D} \nabla v = 0 & \text{on } \partial\Omega \times (0, T), \end{cases}$$

that describes the electrophysiology of the tissue with a single PDE coupled to (3.2c), (3.2d), and (3.2e). Clearly, the *Monodomain* formulation is less demanding from the computational point of view, leading to better conditioned matrices in the discrete approximation.

### 3.1.4 Strang operator splitting

To solve the *Monodomain* formulation in equation (3.7), we adopt the Strang's symmetrical splitting scheme [199], which is a second order accurate operator. This fractional step method separates the integration in time of the diffusive and reactive terms [82, 212] subdividing the solution process in an arbitrary time interval ( $t \in [t_n, t_{n+1}]$ ) in three steps as schematized in Figure 3.3.

#### Step 1

Given the initial conditions  $v(t_n)$ ,  $w^r(t_n)$ , and  $c^s(t_n)$  we integrate the reactive term (i.e., the ionic model) to find  $v$ ,  $w^r$ , and  $c^s$  at time  $t_{\theta/2}$ , being  $\theta/2$  the midpoint of the time interval. The integration of the system:

$$\begin{cases} \frac{\partial v}{\partial t} = -\frac{1}{C_m} I^{ion} & \forall t \in [t_n, t_{\theta/2}] & (3.8a) \\ \frac{\partial w^r}{\partial t} = m_w^r(v, w^1, \dots, w^k) \quad \forall r = 1, \dots, 18 & \forall t \in [t_n, t_{\theta/2}] & (3.8b) \\ \frac{\partial c^s}{\partial t} = m_c^s(v, w^1, \dots, w^k, c^1, \dots, c^g) \quad \forall s = 1, \dots, 3 & \forall t \in [t_n, t_{\theta/2}] & (3.8c) \end{cases}$$

returns  $v_{\theta/2}, w_{\theta/2}^r, c_{\theta/2}^s$ .

#### Step 2

Given the initial condition  $v_{\theta/2}$ , we integrate the diffusive term by solving the PDE:

$$\begin{cases} \frac{\partial v}{\partial t} = \frac{1}{\chi C_m (\lambda + 1)} [\lambda \nabla \cdot (\mathbf{D} \nabla v) + (\lambda I_i^{app} - I_e^{app})] & \text{in } \Omega, \forall t \in [t_n, t_{n+1}] & (3.9a) \\ \mathbf{n} \cdot \mathbf{D} \nabla v = 0 & \text{on } \partial\Omega, \forall t \in [t_n, t_{n+1}] & (3.9b) \end{cases}$$

to compute  $v_{\theta}$ .

#### Step 3

Given as initial conditions  $v_{\theta}, w_{\theta}^r, c_{\theta}^s$ , we integrate the reactive term for  $t \in [t_{\theta/2}, t_{n+1}]$  and the system

$$\begin{cases} \frac{\partial v}{\partial t} = -\frac{1}{C_m} I^{ion} & \forall t \in [t_{\theta/2}, t_{n+1}] & (3.10a) \\ \frac{\partial w^r}{\partial t} = m_w^r(v, w^1, \dots, w^k) \quad \forall r = 1, \dots, 18 & \forall t \in [t_{\theta/2}, t_{n+1}] & (3.10b) \\ \frac{\partial c^s}{\partial t} = m_c^s(v, w^1, \dots, w^k, c^1, \dots, c^g) \quad \forall s = 1, \dots, 3 & \forall t \in [t_{\theta/2}, t_{n+1}] & (3.10c) \end{cases}$$

gives as a result  $v(t_{n+1}), w^r(t_{n+1}), c^s(t_{n+1})$ .

We remark that the operator does not discretize in time the equations, as highlighted in [199]. Indeed, the time integration schemes will be introduced in the following.

### 3.1.5 Canonical semi-discrete formulation for the reaction term

In the framework of a standard Bubnov-Galerkin method, Eq.(3.8a), for instance, is discretized multiplying it by a test function  $\delta v$  and taking the integral over the domain. Subsequently, the unknown and the test functions are then projected on to the same, at least  $C^0$ -continuous, finite dimensional functional space. The approximations:

$$v(\mathbf{x}, t) = \mathbf{N}(\mathbf{x}) \hat{\mathbf{v}}(t) \quad (3.11)$$

and

$$\delta v(\mathbf{x}, t) = \mathbf{N}(\mathbf{x}) \delta \hat{\mathbf{v}}(t) \quad (3.12)$$

lead to the classical formulation:

$$\int_{\Omega} \mathbf{N}^T \mathbf{N} d\mathbf{x} \dot{\hat{\mathbf{v}}} = - \int_{\Omega} \frac{1}{C_m} \mathbf{N}^T I^{ion} d\mathbf{x}. \quad (3.13)$$

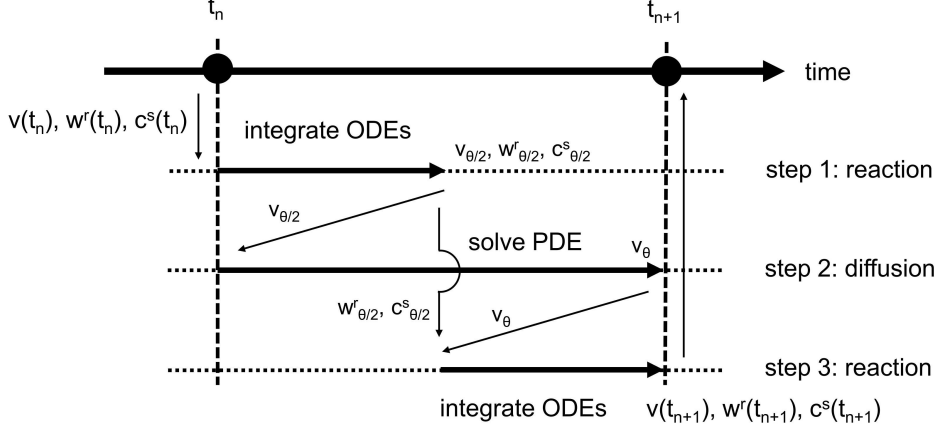


Figure 3.3: Schematic representation of the Strang splitting operator.

The numerical computation of the integral on the right hand side of Eq. (3.13) requires the evaluation of the ionic current defined in Eq. (3.2e), which involves the solution of the ODE system. To compute this integral, one of the following three different strategies is usually employed:

- The ionic current values are computed at the integration points  $\mathbf{x}_{gp}$ , interpolating the nodal values of the transmembrane potential  $\hat{v}$  and integrating Eqs.(3.2d) and (3.2e) at the same locations:

$$I_{GI}^{ion}(\mathbf{x}_{gp}, t) = I^{ion}(\mathbf{x}_{gp}, \mathbf{N}(\mathbf{x}_{gp}) \hat{v}(t), w^r(\mathbf{x}_{gp}, t), c^s(\mathbf{x}_{gp}, t)) \quad (3.14)$$

$$\forall r = 1, \dots, k, \quad \forall s = 1, \dots, q,$$

leading to the so-called Gaussian Integration (GI) approach.

- The gating variables and the ionic concentrations are approximated using the basis functions:

$$w^r(\mathbf{x}, t) = \mathbf{N}(\mathbf{x}) \hat{w}^r(t) \quad \forall r = 1, \dots, k, \quad (3.15)$$

$$c^s(\mathbf{x}, t) = \mathbf{N}(\mathbf{x}) \hat{c}^s(t) \quad \forall s = 1, \dots, q. \quad (3.16)$$

The state variable evolution is calculated at the nodes and then the result is interpolated at the quadrature points:

$$I_{SVI}^{ion}(\mathbf{x}_{gp}, t) = I^{ion}(\mathbf{x}_{gp}, \mathbf{N}(\mathbf{x}_{gp}) \hat{v}(t), \mathbf{N}(\mathbf{x}_{gp}) \hat{w}^r(t), \mathbf{N}(\mathbf{x}_{gp}) \hat{c}^s(t)) \quad (3.17)$$

$$\forall r = 1, \dots, k, \quad \forall s = 1, \dots, q.$$

This method is referred to as State Variable Interpolation (SVI) method.

- The computational effort can be reduced assuming that the membrane capacitance  $C_m$  is constant and interpolating the ionic current distribution in space using the basis functions:

$$I_{ICI}^{ion}(\mathbf{x}_{gp}, t) = \mathbf{N}(\mathbf{x}_{gp}) \hat{\mathbf{I}}^{ion}(t). \quad (3.18)$$

where the components of the vector  $\hat{\mathbf{I}}^{ion}$  are given by:

$$\hat{I}_b^{ion}(t) = I^{ion}(\hat{\mathbf{x}}_b, \hat{v}_b(t), \hat{w}_b^r(t), \hat{c}_b^s(t)) \quad (3.19)$$

$$\forall r = 1, \dots, k, \quad \forall s = 1, \dots, q.$$

Indeed, Eq. (3.13) reduces to a relation between nodal quantities:

$$\dot{\hat{v}} = -\frac{1}{C_m} \hat{\mathbf{I}}^{ion}. \quad (3.20)$$

Since we need the ionic current values at the nodes, Eqs.(3.2d) and (3.2e) are also integrated at the same points. This method is called Ionic Current Interpolation (ICI) approach.

The standard Galerkin formulation requires the time integration of the cellular model multiple times for each time step. In biologically detailed cellular models, this process is computationally demanding because the number of state variables can be large [243]. For this reason, the ICI approach is often preferred. Indeed, it requires less computations and the ionic current integral can be assembled in a matrix-vector product fashion if the splitting operator is not applied [244]. Unfortunately, the ICI approach is less accurate than other methods, especially near the wave front. To achieve a better precision with a reduced computational cost, a mixed ICI-SVI method was proposed in [244]. This method detects the wave front and employs the SVI method in its proximity, while the ICI approach is used for the rest of the domain.

## 3.2 Isogeometric framework and discrete problem

Isogeometric Analysis is the framework for the spatial approximation of PDEs herein adopted, which uses spline functions for the geometrical representation of the computational domain and the approximation of the unknown fields. Thus, the geometrical mapping described in Section 3.2.2 defines the basis functions used in the computation of the transmembrane potential and its derivatives.

### 3.2.1 B-spline functions for approximations

In the present chapter, we test several shape functions to assess the effect of the polynomial degree and continuity at the element interfaces on the numerical approximation of potential. We focus on multi-variate B-splines basis functions, defined through the tensor product of uni-variate B-splines, as they easily control these features. Indeed, the degree  $p$  and the open knot vector  $\Xi = \{\xi_1, \xi_2, \dots, \xi_{m_\xi+p+1}\}$  define the  $m_\xi$  splines  $H_a(\xi)$  in the parametric direction  $\xi$  through the Cox-de Boor recursive formula:

$$\begin{aligned} \text{for } p = 0 \quad H_{a;0}(\xi) &= \begin{cases} 1 & \text{if } \xi_a \leq \xi < \xi_{a+1} \\ 0 & \text{otherwise} \end{cases} \\ \text{for } p = 1, 2, 3, \dots \quad H_{a;p}(\xi) &= \frac{\xi - \xi_a}{\xi_{a+p} - \xi_a} H_{a;p-1}(\xi) + \frac{\xi_{a+p+1} - \xi}{\xi_{a+p+1} - \xi_{a+1}} H_{a+1;p-1}(\xi). \end{aligned} \quad (3.21)$$

By increasing the multiplicity of a knot of the vector  $\Xi$ , we reduce the spline continuity at that element interface.

To define functions in a 3D space, we take the tensor product of uni-variate B-splines  $H$ ,  $L$ , and  $K$  in three different parametric directions  $\xi$ ,  $\eta$ ,  $\zeta$ , for which similar definitions hold. Moreover, assuming a lexicographical order, we recast such functions in the vector  $\mathbf{N}$  as follows:

$$\mathbf{N}_a = H_b(\xi) L_c(\eta) K_d(\zeta). \quad (3.22)$$

Following the standard Isogeometric approach, we define the geometry of the body as a linear combination of basis functions and control points – also referred as nodes – coordinates  $\mathbf{B}_a$  as follows:

$$\mathbf{x}(\xi, \eta, \zeta) = \sum_{a=1}^m N_a(\xi, \eta, \zeta) \mathbf{B}_a, \quad (3.23)$$

where  $m$  is the number of three-variate splines:  $m = m_\xi \times m_\eta \times m_\zeta$ .

In this chapter, we test three sets of splines to approximate  $v$ :

- degree  $p = 1$  and continuity  $C^0$ , equivalent to linear hexahedral finite elements.
- high order splines with  $C^0$  continuity, also known as Bernstein polynomials, obtained repeating the internal knots  $p$  times.
- high order splines with maximum continuity  $C^{p-1}$ , obtained using internal knots with multiplicity equal to one.

The accuracy of the basis functions is investigated in Section 3.3.1.

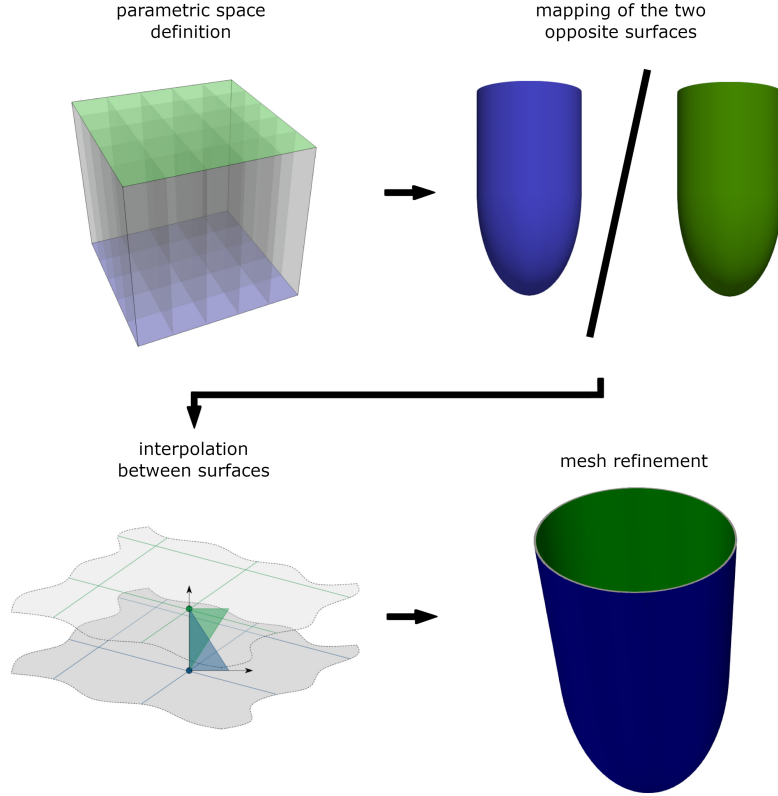


Figure 3.4: Schematic representation of the workflow to define the geometrical mapping.

### 3.2.2 Computation of the geometrical mapping

In this chapter, we represent the ventricle as an extrusion between two opposite target surfaces mapped through the strategy herein presented and depicted in Figure 3.4.

The pipeline to define a structured mesh composed of hexahedral elements is similar to the one presented in [81], and it is articulated in four steps as follows:

#### Step 1

Initially, we set up the parametric space (i.e., we define the degree and knot vectors) to be mapped into the ventricle. Since the engineered ventricle is topologically equivalent to a cube, we use a single three-variate patch to represent the ventricle selecting two opposite faces of the cube – for instance, the planes spanned by  $\xi$  and  $\eta$  at  $\zeta = 0$  and  $\zeta = 1$  – as the parent surfaces mapped into internal and external surfaces, in Figure 3.4 represented in green and blue, respectively. Coherently, the third parametric direction  $\zeta$  refers to the transmural direction of the ventricle. We initially use a single linear element in such a direction to mimic the extrusion.

#### Step 2

The second step consists in mapping the two parametric surfaces (indexes  $\bar{\zeta} \in 0, 1$ ) into the two main physical surfaces (indexes  $j \in \{int, ext\}$ ) one at a time. Each surface is represented as:

$$\mathbf{x}^{*,j}(\xi, \eta, \bar{\zeta}) = \sum_{s=1}^{m_\xi \times m_\eta} N_s(\xi, \eta, \bar{\zeta}) \mathbf{B}_s^{*,j} \quad (3.24)$$

where  $\mathbf{B}_s^{*,j}$  are the coordinates of the control points related to the splines with support on the parametric surface (i.e., half of the set of splines). We optimize the control point coordinates such that the distance

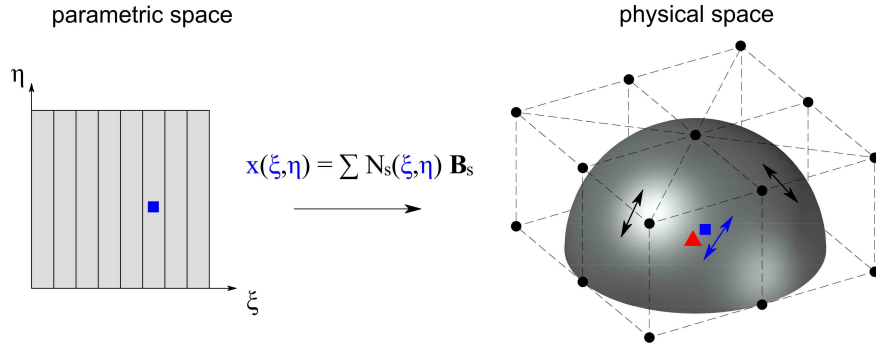


Figure 3.5: Schematic representation of the mapping procedure for a surface. A point defined in the parametric space (blue square) is mapped in the physical space by a linear combination of splines and control point coordinates (the black dots). The position of those points in the physical space is optimized such that the images of a set of points (blue square) match their target positions (red triangle).

between the analytical surface  $\mathbf{x}^{a,j}$  and its B-spline approximation  $\mathbf{x}^{*,j}$  is minimized, as schematically depicted in Figure 3.5.

Such a problem is formalized as follows:

$$\mathbf{B}^{*,j} = \arg \min_{\mathbf{B}^{*,j}} \{ \|\mathbf{x}^{a,j} - \mathbf{x}^{*,j}(\mathbf{B}^{*,j})\|^2 \}, \quad (3.25)$$

where we consider the standard  $L^2$  norm as the metric for the computation of the distance between the surfaces sampled in a discrete set of points. Since the system is overdetermined, we solve equation (3.25) by means of least square method.

In this application, the center of the selected face of the parametric space is mapped into the ventricle apex, whereas the edges correspond to the circular base. This strategy enables the mapping of the 3D engineered ventricle avoiding mapping singularities near the ventricle apex, which is the region of interest in the simulation. However, it comes at a cost of eight singularities – corresponding to the vertex of the parametric cube – located at the ventricle base. Nevertheless, according to [245], they do not affect significantly the accuracy of the analysis because no Gauss point lies in those positions. If the original surface is not analytical, as in most of the biomedical applications, an alternative procedure is provided in A.1.

### Step 3

Once the surfaces are mapped, we extrude the volume in direction  $\zeta$  interpolating the two sets of coordinates  $\mathbf{B}^{*,j}$ ,  $j \in \{int, ext\}$  with a single linear element. Indeed, a one-to-one relation holds between the control points on opposite surfaces thanks to the tensor product structure of the parametric space.

### Step 4

In the last step, the mesh is refined employing the order elevation and knot insertion algorithms to achieve a suitable discretization for accurate simulations. For more details on the refinement scheme the reader is referred to [12]. We remark that in this chapter we adopt the same polynomial degree in all the parametric directions, even in the transmural direction.

## 3.2.3 Spatial discretization

To discretize the *Monodomain* formulation, we consider the weak formulation of the PDE (3.7) and define the trial and test spaces for the transmembrane potential

$$\mathcal{V} = \{v | v \in H^1(\Omega, [0, T]) \wedge v = v_D \text{ on } \partial\Omega_D\}, \quad (3.26)$$

$$\delta\mathcal{V} = \{\delta v | \delta v \in H^1(\Omega, [0, T]) \wedge \delta v = 0 \text{ on } \partial\Omega_D\}, \quad (3.27)$$

respectively. In these definitions,  $H^1(\Omega, [0, T])$  is the Sobolev space of functions with square integrable first derivatives in  $\Omega$ , while  $\partial\Omega_D$  and  $\partial\Omega_N$  are the partitions of the boundary ( $\partial\Omega_N \cup \partial\Omega_D = \partial\Omega$  and  $\partial\Omega_N \cap \partial\Omega_D = \emptyset$ ) where Dirichlet and Neumann boundary conditions, respectively, are applied. Moreover, we assume the gating variable  $w^r$  and the ionic concentration  $c^s$  in

$$\mathcal{WC} = \{f | f \in L^2(\Omega, [0, T])\}, \quad (3.28)$$

where  $L^2(\Omega, [0, T])$  is the space of square integrable functions in  $\Omega$ . In the spirit of a Bubnov-Galerkin discretization, we use the same space as test space  $\delta\mathcal{WC}$

Then, the weak form of the *Monodomain* formulation combined with the Strang splitting scheme reads as follows [200]:  $\forall t \in [0, T]$ , find  $v(t) \in \mathcal{V}$ ,  $w^r(t), c^s(t) \in \mathcal{WC}$  such that the following relations hold for the first and the third steps of the splitting:

$$\begin{cases} \int_{\Omega} \delta v \frac{\partial v}{\partial t} d\mathbf{x} = -\frac{1}{C_m} \int_{\Omega} \delta v I^{ion} d\mathbf{x} & \forall \delta v \in \delta\mathcal{V} & (3.29a) \\ \int_{\Omega} \delta w \frac{\partial w^r}{\partial t} d\mathbf{x} = \int_{\Omega} \delta w m_w^r d\mathbf{x} & \forall \delta w \in \delta\mathcal{WC}, r = 1, \dots, 18 & (3.29b) \\ \int_{\Omega} \delta c \frac{\partial c^s}{\partial t} d\mathbf{x} = \int_{\Omega} \delta c m_c^s d\mathbf{x} & \forall \delta c \in \delta\mathcal{WC}, s = 1, \dots, 3 & (3.29c) \end{cases}$$

and the following equation holds for the second step (3.9a):  $\forall \delta v \in \delta\mathcal{V}$

$$\int_{\Omega} \delta v \frac{\partial v}{\partial t} d\mathbf{x} = -\frac{1}{\chi C_m (\lambda + 1)} \left( \int_{\Omega} \lambda \nabla \delta v \cdot \mathbf{D} \nabla v d\mathbf{x} + \int_{\Omega} \delta v (\lambda I_i^{app} - I_e^{app}) d\mathbf{x} \right). \quad (3.30)$$

Replacing the functional spaces with a finite dimensional approximation, the transmembrane potential  $v$  and the test function  $\delta v$  are written as a linear combination of shape functions  $\mathbf{N}$  – derived from the geometrical representation following the isoparametric paradigm – and nodal variables  $\hat{\mathbf{v}}$  and  $\delta\hat{\mathbf{v}}$  as

$$v(\mathbf{x}, t) = \mathbf{N}(\mathbf{x}) \hat{\mathbf{v}}(t) \quad (3.31)$$

$$\delta v(\mathbf{x}, t) = \mathbf{N}(\mathbf{x}) \delta\hat{\mathbf{v}}(t). \quad (3.32)$$

In the present chapter, we test several shape functions to assess the accuracy of the discretizations. Therefore, the symbol  $\mathbf{N}(\mathbf{x})$  refers to one of the generic set of adopted basis functions.

By replacing equations (3.31) and (3.32) in (3.30), we obtain the semi-discrete formulation of the PDE:

$$\mathbf{M} \dot{\hat{\mathbf{v}}} = -\mathbf{K} \hat{\mathbf{v}} + \hat{\mathbf{I}}^{app}, \quad (3.33)$$

where the entries of the mass  $\mathbf{M}$  and stiffness  $\mathbf{K}$  matrices are given by:

$$M_{ab} = \int_{\Omega} N_a N_b d\mathbf{x}, \quad (3.34)$$

$$K_{ab} = \frac{\lambda}{\chi C_m (\lambda + 1)} \int_{\Omega} \frac{\partial N_a}{\partial x_i} d_{ij} \frac{\partial N_b}{\partial x_j} d\mathbf{x}, \quad (3.35)$$

and the entries of the vector  $\hat{\mathbf{I}}^{app}$  read as:

$$\hat{I}_a^{app} = \frac{1}{\chi C_m (\lambda + 1)} \int_{\Omega} N_a (\lambda I_i^{app} - I_e^{app}) d\mathbf{x}. \quad (3.36)$$

In the numerical computation of these integrals, we employ the standard Gauss quadrature rule with  $p + 1$  Gauss points in each direction per element, where  $p$  is the basis functions degree, although it is not the optimal choice for highly continuous B-splines [26].

Electrophysiological simulations with detailed cellular models may be computationally demanding [199]. To reduce this effort, we adopt the Ionic Current Interpolation (ICI) approach, based on interpolation of the ionic current at the quadrature nodes, see [82], requiring the integration of the ionic model at the nodes only. In this chapter, we investigate the effect of the basis function degree and continuity on the accuracy of such an approach. The ICI method interpolates the ionic current as shown in Eq.(3.18).

Substituting equation (3.18) in equation (3.29) and introducing the same approximation for the state variables and their tests:

$$\begin{cases} w^r(\mathbf{x}, t) = \mathbf{N}(\mathbf{x}) \hat{\mathbf{w}}(t)^r & \forall r = 1, \dots, 18 \\ c^s(\mathbf{x}, t) = \mathbf{N}(\mathbf{x}) \hat{\mathbf{c}}(t)^s & \forall s = 1, \dots, 3 \end{cases} \quad (3.37a)$$

$$(3.37b)$$

$$\begin{cases} \delta w(\mathbf{x}, t) = \mathbf{N}(\mathbf{x}) \delta \hat{\mathbf{w}}(t) \\ \delta c(\mathbf{x}, t) = \mathbf{N}(\mathbf{x}) \delta \hat{\mathbf{c}}(t), \end{cases} \quad (3.38a)$$

$$(3.38b)$$

we obtain a set of nodal relations for the steps one and three of the Strang scheme. Indeed, every entry corresponds to the integration of the ionic model at a node:

$$\begin{cases} \dot{\hat{\mathbf{v}}} = -\frac{1}{C_m} \hat{\mathbf{I}}^{ion} \\ \dot{\hat{\mathbf{w}}}^r = \hat{\mathbf{m}}_w^r & \forall r = 1, \dots, 18 \\ \dot{\hat{\mathbf{c}}}^s = \hat{\mathbf{m}}_c^s & \forall s = 1, \dots, 3. \end{cases} \quad (3.39a)$$

$$(3.39b)$$

$$(3.39c)$$

### 3.2.4 Time discretization

To discretize in time the *Monodomain* formulation, we subdivide the time into equal intervals of size  $\Delta t$ . In every time step, we solve the splitted form of the problem (equations (3.39) and (3.33)) using different schemes. Indeed, Implicit-Explicit schemes are often employed since they guarantee a compromise between numerical stability and computational efficiency.

The non-linear system of ODEs (3.39) is integrated using the Explicit Euler method, with a reduced step size to guarantee a sufficient accuracy. Therefore, when considering the sub-step  $[t_k, t_{k+1}]$ , we adopt the step size  $\Delta \tilde{t} = \Delta t / (2k)$ :

$$\begin{cases} \hat{\mathbf{v}}_{k+1} = \hat{\mathbf{v}}_k - \frac{\Delta \tilde{t}}{C_m} \hat{\mathbf{I}}^{ion}(t_k) \\ \hat{\mathbf{w}}_{k+1}^r = \hat{\mathbf{w}}_k^r + \Delta \tilde{t} \hat{\mathbf{k}}_w^r(t_k) & \forall r = 1, \dots, 18 \\ \hat{\mathbf{c}}_{k+1}^s = \hat{\mathbf{c}}_k^s + \Delta \tilde{t} \hat{\mathbf{k}}_c^s(t_k) & \forall s = 1, \dots, 3. \end{cases} \quad (3.40a)$$

$$(3.40b)$$

$$(3.40c)$$

In this chapter, we perform 100 sub-steps (i.e.,  $k = 100$ ) during the integration of every reactive step.

In the diffusion step, we use a single increment  $\Delta t$  adopting the implicit, second order accurate, Crank-Nicolson method to increase the stability of the scheme. The resulting discrete formulation reads as:

$$\left( \mathbf{M} + \frac{\Delta t}{2} \mathbf{K} \right) \hat{\mathbf{v}}_{n+1} = \mathbf{M} \hat{\mathbf{v}}_\theta + \frac{\Delta t}{2} \left( -\mathbf{K} \hat{\mathbf{v}}_\theta + \hat{\mathbf{I}}_n^{app} + \hat{\mathbf{I}}_{n+1}^{app} \right). \quad (3.41)$$

## 3.3 Numerical simulations

In this section, we present the results of the electrophysiological simulations, which aims to assess the proficiency of the presented approach. Indeed, most of the studies in the literature focus on native tissues, not on engineered replicas.

The conductivity coefficient  $d$  of the engineered ventricle is reduced with respect to the native cardiac tissue, entailing major implications in the accuracy of the simulation. Indeed, a reduction in the tissue conductivity, for a fixed discretization, results in an increased error in the numerical approximation [246]. Therefore, we first focus on the accuracy in a simple 1D problem: we investigate such a feature limiting the discussion to hiPSC-CMs and varying the normalized conductivity  $d^*$

$$d^* = \frac{\lambda}{\chi C_m (\lambda + 1)} d \left[ \frac{\text{m}^2}{\text{s}} \right]. \quad (3.42)$$

The Thiele modulus was used to distinguish between reaction-dominated and diffusion-dominated electrophysiological simulations [246] involving several values of conductivity and ionic models. Since we focus on a single-cell model, the Thiele modulus and the normalized conductivity are equivalent definitions.

Based on these results, the 3D model is calibrated and a complete simulation of the action potential propagation in the ventricle is presented. Parameters adopted to perform the simulation are either provided in the text or available in [237].

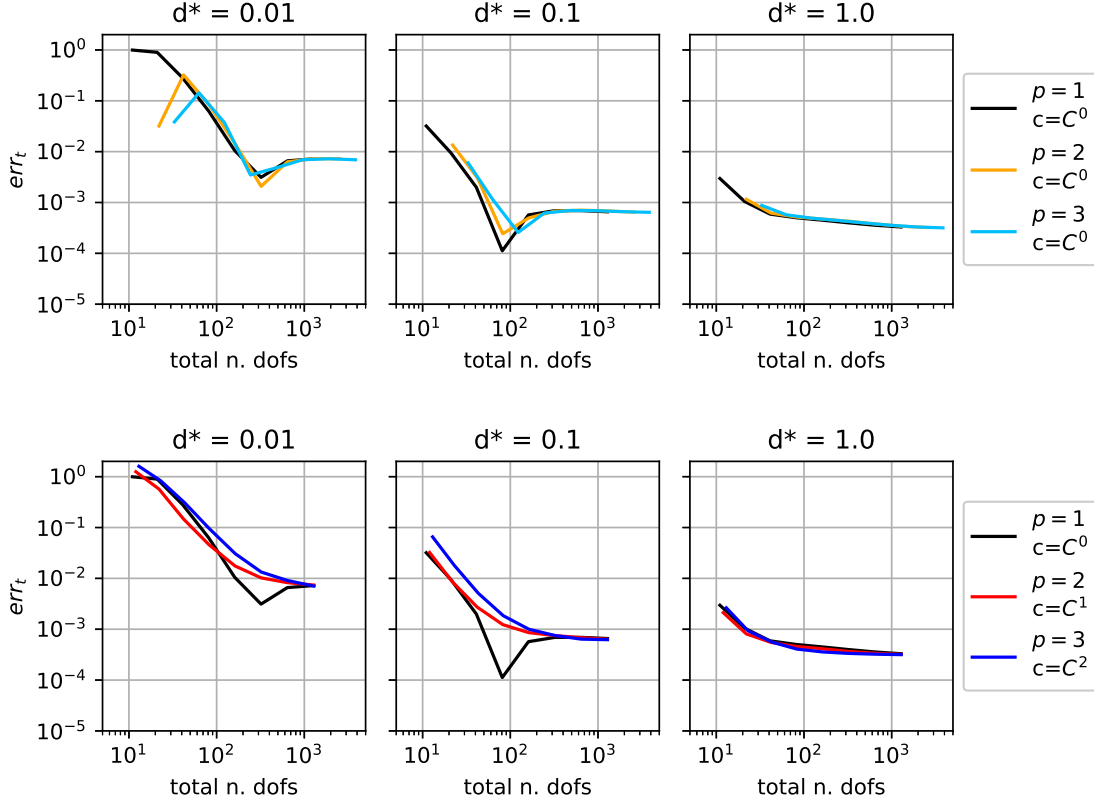


Figure 3.6: Relative errors in the time trace for basis  $C^0$  (top) and  $C^{p-1}$  (bottom) basis functions. The black curve, representing linear functions, is repeated in both plot for better comparison. Furthermore, the same results are subdivided by degree in A.2.

### 3.3.1 Accuracy investigation

We investigate the response of a straight fiber (length  $L = 3.2$  mm) to assess the effect of different basis function degrees and continuity on the accuracy of the numerical discretization for different values of tissue conductivity. Specifically, we test the basis functions of orders  $p = 1, 2, 3$  and continuity  $C = 0, p-1$  presented in Section 3.2.1 for three different values of conductivity  $d^* \in \{1.0, 0.1, 0.01\}$   $\text{mm}^2/\text{ms}$ .

We conduct the convergence analysis under  $h$ -refinement simulating a single action potential propagation ( $T = 1250$  ms) – triggered by 10 ms of stimulation at the left end ( $\mathbf{x}^* = 0$  mm) – using a time step size  $\Delta t = 10^{-2}$  ms and an element sizes  $h \in \{0.32/(2^k), k = 0, 1, \dots, 7\}$  mm. Since no analytical solution is available, we adopt as a reference  $v^{ref}$  an overkill simulation performed using linear finite elements on a four times finer mesh ( $h = 0.32/(2^9)$  mm), and  $\Delta t = 10^{-4}$  ms. The results are compared using different metrics.

#### Error in the time trace

We analyze the convergence of the potential in a fixed point of the fiber ( $\mathbf{x}^* = 2.7933$  mm, such that the point is never a node) defined as:

$$err_t = \sqrt{\frac{\int_0^T (v(\mathbf{x}^*, t) - v^{ref}(\mathbf{x}^*, t))^2 dt}{\int_0^T (v^{ref}(\mathbf{x}^*, t))^2 dt}}. \quad (3.43)$$

The results of the analyses are presented in Figure 3.6 and discussed as follows.

When the mesh is refined, the error decreases reaching a plateau due to the residual time discretization error, as in [204]. Indeed, a finer time step is adopted in the computation of  $v^{ref}$ . Therefore, after a

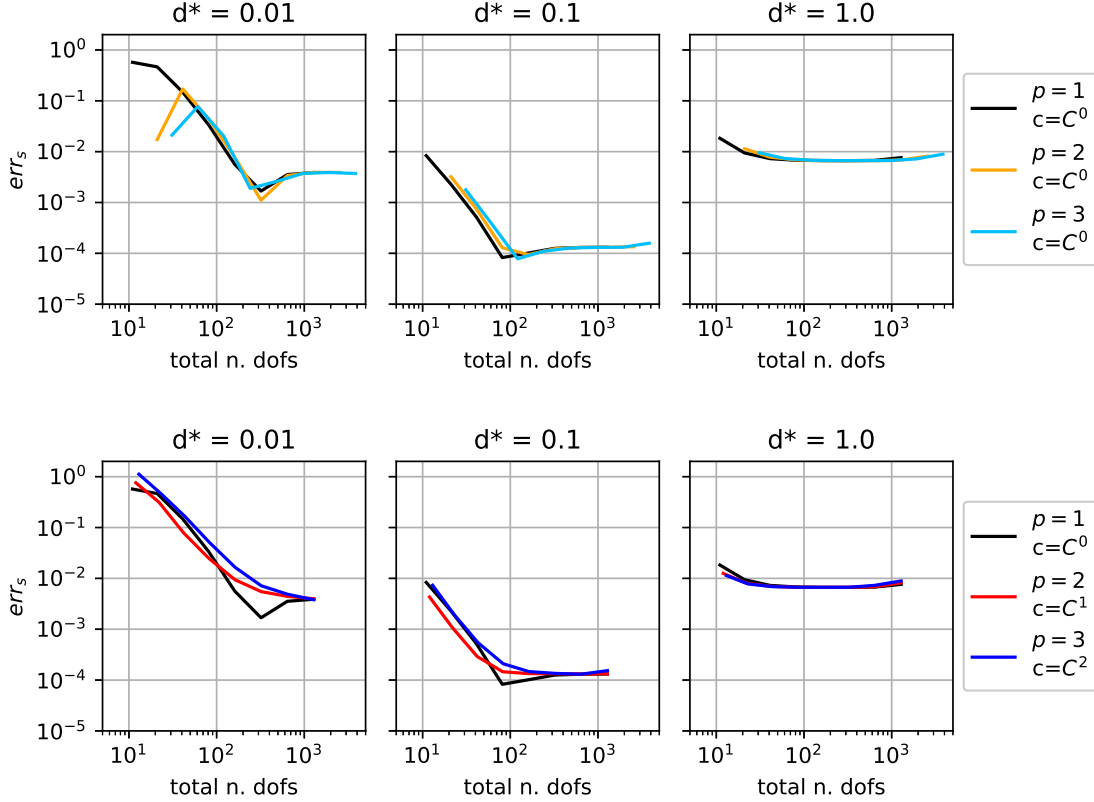


Figure 3.7: Relative errors in spatial representation of the wave for  $C^0$  (top) and  $C^{p-1}$  (bottom) basis functions. The black curve, representing linear basis functions, is repeated in both plot for better comparison. Furthermore, the same results are subdivided by degree in A.2.

threshold value, both the element size  $h$  and the time step size  $\Delta t$  must be refined to improve the accuracy of the solution. Results also highlight that the convergence path depends on the conductivity, confirming that for reaction-dominated simulations the mesh must be finer to retrieve a predefined level of accuracy [246]. The basis function degree and continuity do not affect significantly the accuracy of the solution. Indeed, the error stabilizes approximately for the same number of degrees of freedom (dofs). However, a high continuity (i.e.,  $C = 1, 2$ ) provides a monotone convergence path, avoiding the error oscillation before the plateau.

### Error in the spatial representation of the wave

We analyzed the convergence in a fixed instant  $t^*$ , defined as:

$$err_s = \sqrt{\frac{\int_0^L (v(\mathbf{x}, t^*) - v^{ref}(\mathbf{x}, t^*))^2 dx}{\int_0^L (v^{ref}(\mathbf{x}, t^*))^2 dx}}. \quad (3.44)$$

In this case, we select different instants for different values of conductivity ( $t^* = 11$  ms for  $d^* = 1, 0.1$  mm<sup>2</sup>/ms, and  $t^* = 95$  ms for  $d^* = 0.01$  mm<sup>2</sup>/ms) to avoid the analysis of completely depolarized domains.

Results are presented in Figure 3.7 and herein discussed.

Differently from the previous analysis, a direct comparison between values of conductivity is no more applicable. Indeed, the temporal shape of an action potential is not affected by the conductivity values up to a temporal shift, while this is not true for the spatial distribution, since the entire impulse is not included in the physical domain. Nevertheless, they confirm the previous findings, suggesting a qualitative independence of the accuracy on the basis function continuity and degree.

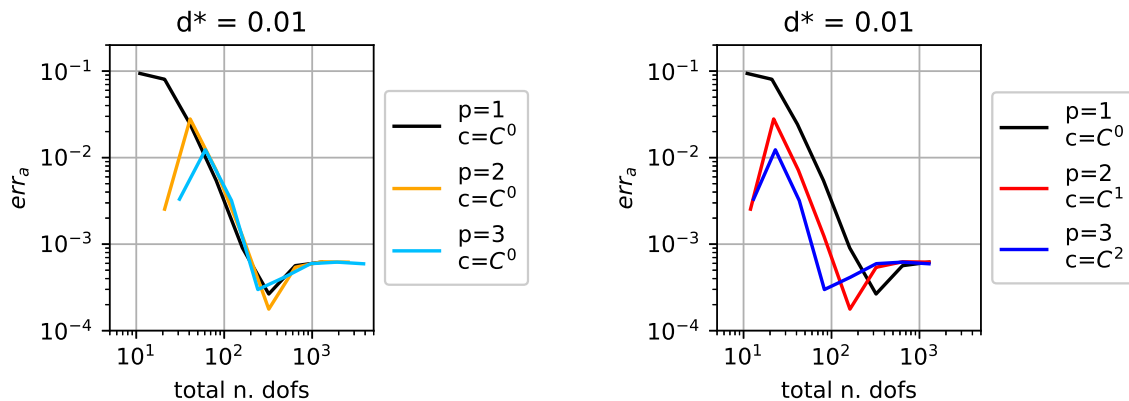


Figure 3.8: Relative errors on arrival time, for  $C^0$  (left) and  $C^{p-1}$  (right) basis functions. The black curve, representing linear basis functions, is repeated in both plot for better comparison.

### Error in the wave arrival time

Having assessed the effect of the conductivity on the accuracy, we specialize our study on the engineered tissue. We further investigate the approximation of wave arrival time, defined as:

$$err_a = \left| \frac{\bar{t} - \bar{t}^{ref}}{\bar{t}^{ref}} \right|, \quad \text{where } \bar{t} = \arg \max_{t \in [0, T]} \frac{dv(\mathbf{x}^*, t)}{dt} \quad (3.45)$$

since it is fundamental in the reconstruction of the time activation maps. In such a definition  $\bar{t}^{ref}$  represents the arrival time, computed with the same approach, of the reference solution.

As depicted in Figure 3.8, we focus only on the conductivity value qualitatively representative of our problem, which we anticipate to be  $d^* = 0.01 \text{ mm}^2/\text{ms}$ .

In this case, results highlight that the curves related to the high continuity of splines  $C = 1, 2$  reach the plateau for a coarser mesh. The highly continuous cubic splines further improve the accuracy with respect to quadratic splines of the same type. However, the gain in accuracy comes at a cost of a denser matrix structure and, therefore, a greater computational effort. Consequently, we adopt quadratic  $C^1$  B-splines for the analysis of the ventricle as they represent a good compromise between accuracy and computational efficiency, producing a stable convergence path in the previous analysis.

We conclude this section by explaining the differences between the results of the error norms. The wave arrival is mainly influenced by the conduction velocity, which in turn is related to the diffusion term, not to the shape of the action potential. Since the spatial derivatives of the basis functions are only involved in the diffusive term, the wave arrival time may be more sensitive to the continuity of the basis functions than other error metrics. Moreover, the dependence of the solution on the ratio between reactive and diffusive terms has already been observed in [246]. Eventually, we note that the relatively low the error predicted by the coarsest meshes is an unstable behavior of the pre-asymptotic branch of the error convergence. From an application point of view, the accuracy provided by a relatively coarse mesh could be sufficient. However, particular care is needed in simulating complex activation patterns (e.g. spiral waves) since the involved phenomena are sensitive to a correct representation of the state variables and to the depolarization time.

### 3.3.2 Electrophysiological simulation of the engineered ventricle

In the ventricle, hiPSC-CMs are arranged in fibers conferring an anisotropic microstructure to the tissue [224]. It results in a speed propagation of the  $Ca^{2+}$  wave in the fiber direction  $\mathbf{a}_0$  higher than in the orthogonal directions. The speed of propagation of the  $Ca^{2+}$  signal measured in the engineered ventricle using an imaging technique is  $5.2 \text{ [cm/s]}$  in the direction from the apex to the base, while, to compute the velocity in the fiber direction, we refer to an additional investigation on *in-vitro* cultured tissues [241]. Indeed, they report the ratio of the velocities for the value of interest of the Orientation Order

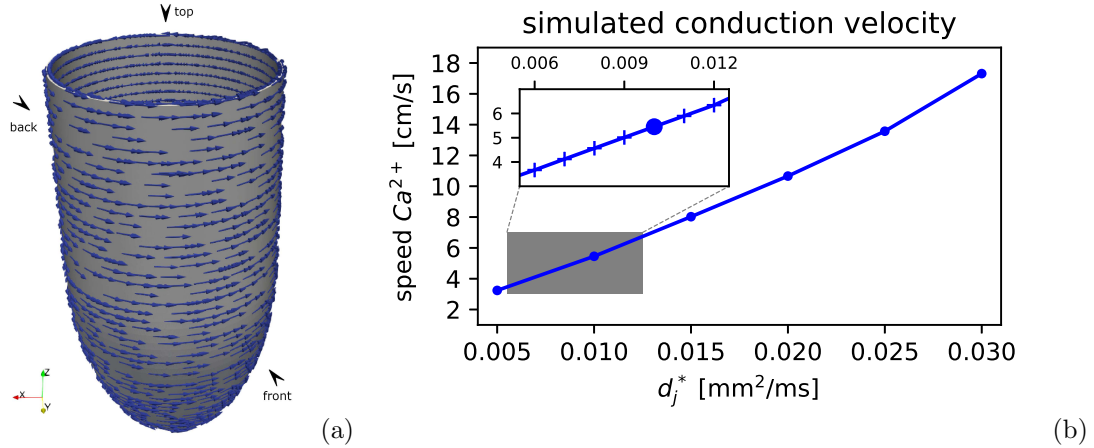


Figure 3.9: Calibration of the ventricle model. (a) Fibers direction is represented on the B-spline volume. (b) The conductivity-velocity response curve of calcium waves.

Parameter [237], that recapitulates the fiber organization in the ventricle. The estimated velocity is equal to 14 [cm/s].

To represent this feature, we defined an anisotropic, transversely isotropic, conductivity tensor  $\mathbf{D}$ , characterized by two different eigenvalues:  $d_{\parallel}$  (multiplicity  $m(d_{\parallel}) = 1$ ) associated to  $\mathbf{a}_0$ , and  $d_{\perp}$  (multiplicity  $m(d_{\perp}) = 2$ ) that spans the space in the orthogonal directions. We assume that fibers are oriented in the pull-spinning direction used to build the scaffold, approximately  $5^\circ$  with respect to the XY plane, as shown in Figure 3.9.

Since the conductivity values are unknown, a calibration to fit the experimental wave velocity is needed: we compute the conductivity for every principal direction  $d_j^*$  by constructing a response curve, shown in Figure 3.9. We simulate 50 [s] of isotropic action potential propagation in a flat slab computing the average  $Ca^{2+}$  speed for different conductivity values. The conductivities in the two orthogonal directions are then obtained by interpolation of the discrete response curve substituting  $d^*$  with  $d_j = d_{\parallel} \vee d_{\perp}$  in equation (3.42).

The results of the conductivity calibration are  $d_{\parallel}^* = 0.0094$  and  $d_{\perp}^* = 0.0256$  [mm<sup>2</sup>/ms]. Clearly, more sophisticated procedures are available in the literature [247, 248, 249, 250]. However, they require complete sets of imaging data in space and time to solve the inverse problem, which is out of the scope of this work.

Once the computational framework to simulate the electrophysiological activity of the engineered ventricle is completed, we perform the simulation of an action potential propagation ( $T = 1250$  ms,  $\Delta t = 0.01$ ms) on the ellipsoidal geometry using a mesh composed by 756012 quadratic  $C^1$  B-splines.

The tissue is stimulated using an applied current (20 pA) for 100 ms spatially distributed near  $\mathbf{x} = (0, 4.5, 2)$ mm to mimic the electrode used in the experimental protocol. The initially repolarized membrane ( $v = -74.9$  mV) undergoes an action potential that propagates from the stimulation site toward the rest of the tissue before the spontaneous firing activity of the cells.

The elongated shape of the wave (for instance:  $v$  at time  $t = 0.2$  s, plot (a)) confirms the faster propagation in the fiber direction. Moreover, the simulation reveals a smooth wave front, for both the transmembrane potential and the intercellular  $Ca^{2+}$ , as shown in Figure 3.10. Finally, the opposite wave fronts correctly merge on the posterior side of the ventricle, confirming the reliability of the proposed approach and the possibility of conducting trial-and-error investigations on the *in-silico* replica of the ventricle.

### 3.4 Summary

In this chapter, we have developed a computational framework useful to investigate the electrophysiological response of the engineered ventricle [224]. To model the tissue, we have included an advanced ionic model [237], tailored for hiPSC-CMs, into the *Monodomain* formulation. Furthermore, we have

reproduced the fibrous structure of the construct using an anisotropic conductivity tensor with principal directions variable over the ellipsoidal geometry.

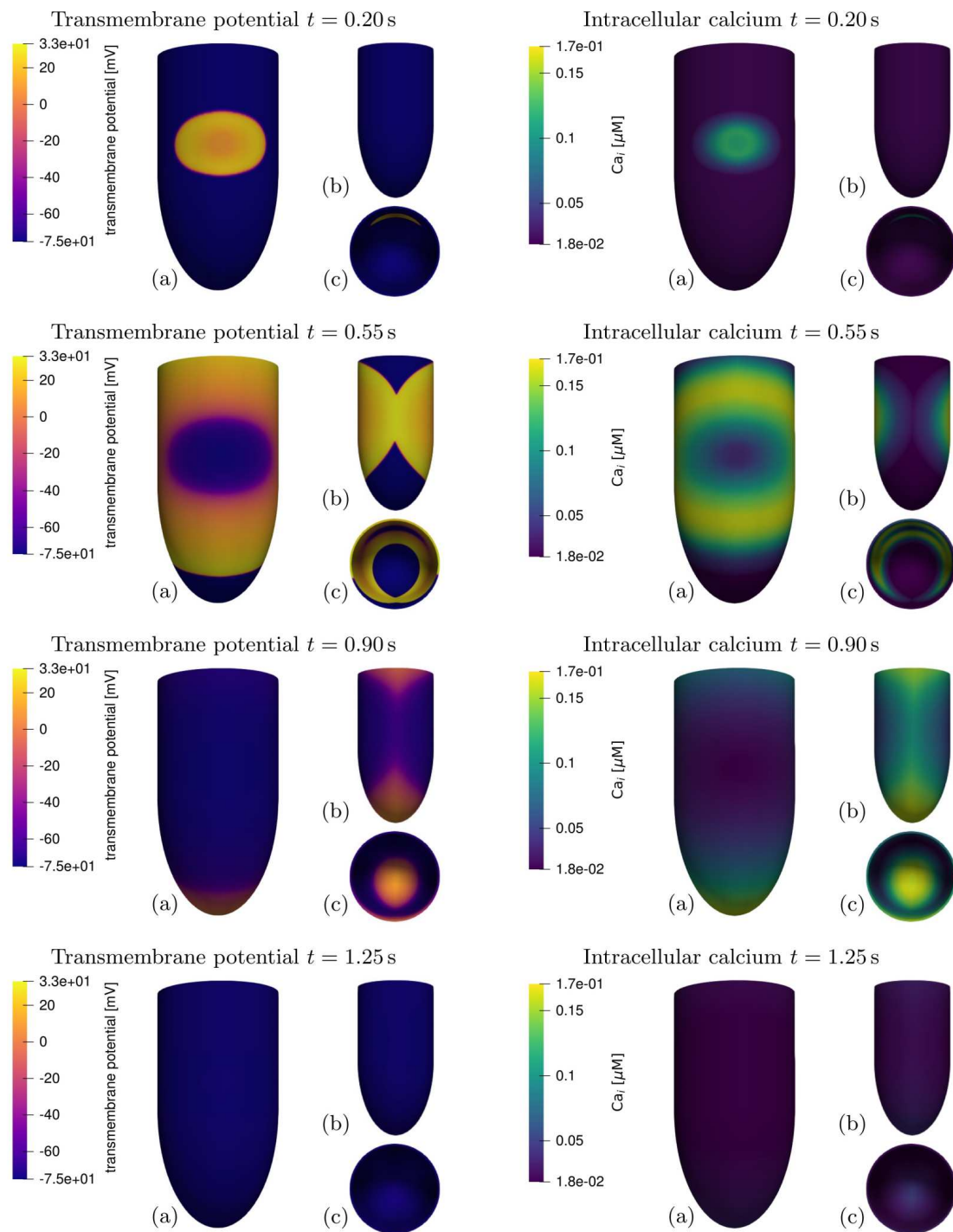


Figure 3.10: Simulation of the engineering ventricle. Representation of the transmembrane potential and intracellular  $Ca^{2+}$  concentration on the front (a), back (b), and top (c) views (cf. Fig. 3.9) for representative time steps.

The mathematical formulation is discretized, in the spirit of a Galerkin method, using several sets of B-splines. Differently from previous investigations [82, 81], we are not approaching the human adult tissue, but we focused on a novel regenerative medicine frontier based on hiPSC-CMs technology, which

entails different numerical issues. We have assessed the dependence of the discretization accuracy on the basis function degree and continuity, using several metrics to define the error. Based on our findings, quadratic  $C^1$  B-splines are a good compromise between accuracy and computational effort. Such an Isogeometric framework was then employed in the calibration of the numerical model and in the simulation of the propagation of an action potential in the engineered ventricle.

We remark that the accuracy of a reaction-dominated simulation is, substantially, insensitive to the basis function degree and continuity. However, different Isogeometric methods may be more effective, independently of the reactive/diffusive nature of the problem; since they exploit different possibilities offered by the B-splines, as discussed in Chapter 6.

In summary, our results suggest a good virtual representation of innovative stem cells tissues and organoids, with implications for regenerative medicine research. Since hiPSC-CMs have the same genetic heritage of the donor, this may extend patient-specific assays from individual cells to complete organ models. Specifically, our computational framework enables fast parametric investigation when considering different scenarios depending on the patient specific conditions. Conversely, laboratory tests require a higher number of ventricle replications to guarantee a significant statistical sample entailing a great economic effort.

Once more, maturation studies provide innovative pools of hiPSC-CMs in the direction of a more adult phenotype. Since the *in-silico* framework reveals the possibility of disentangling the ionic model from tissue properties, we offer a tool to simulate the variation of the physiological response due to the maturation process, considering several ionic models for different maturation states.

Furthermore, investigations could aim to model more complex experimental setup, such as a hole in the virtual geometry using an immersed technology [36], as discussed in Chapter 7. Investigations on injured tissue, considering a single-hole injury or a hole pair, may provide a better understanding in complex pathological phenomena, for instance the formation of spiral waves. In such a context, the non-homogeneous distribution of the tissue properties should be considered in the future to assess their effect in pathological conditions.

This work only considers cardiac electrophysiological simulations, neglecting tissue contraction. Mechanics could also be included, as shown in [179], further improving the realism of the simulation. Indeed, the *in-vitro* setup also investigates the intraventricular pressure-volume loops using catheter-based systems to assess the effect of compounds on tissue contractility.



## Chapter 4

# Electromechanical formulations for active tissues

The electrical activity of the heart regulates the organ functionality synchronizing the muscle contraction to achieve an efficient blood pumping. In this chapter, we analyze the coupled electromechanical formulations available in the literature to model such a phenomenon and the corresponding discretization approach.

In the heart, a subtype of dedicated nodal cardiomyocytes spontaneously generate periodic variations of their membrane potential via current and calcium clock mechanisms [251] that result in periodic action potential (AP) firings and heart-beats. The AP then diffuses to neighboring atrial and ventricular cardiomyocytes via dedicated membrane proteins (connexins) where it triggers ion fluxes needed to regenerate the action potential. As the intracellular calcium concentration changes, acto-myosin cross-bridges are activated generating the cell contraction and tissue deformation. For more details on the tissue physiology, the reader is referred to [252, 253]; herein we focus on the computational aspects related to the simulation of the electromechanical (EM) process of the heart. Indeed, multiscale modeling of the heart physiology has a rich literature and important practical implications for the understanding of pathologies and the management of patients [7, 254].

To better focus on the numerical issues of such complex simulations, in this chapter, we analyze simple geometries recalling that *in-vitro* scaled version of the heart, recapitulating only few features, are of great interest. Indeed, models can be used to calibrate the parameters of the constitutive laws [207] increasing the fidelity of the investigations. Examples range from uni-dimensional constructs [255] to bi-dimensional cantilevers [207] and scaled 3D organs [224].

In this chapter, we present the canonical formulations for cardiac electromechanics used in the following chapters. The contraction of the cardiac muscle induced by the electrical signaling can be model using two alternative methodologies: the *active stress* and *active strain* approaches. In Section 4.1 we briefly review the two formulations, while Section 4.2 is devoted to discretize the *active stress* approach, leaving the description of the *active strain* method to successive investigations in Chapter 5. Finally, Section 4.3 drafts several conclusions.

### 4.1 Coupled formulations for electromechanics

Three different sub-problems compose the coupled cardiac electromechanical problem: Essentially, the electrophysiology (EP) governs the mechanics (ME) through the tissue activation (ACT). Therefore, the effect of the cellular activity on the tissue activation and, in turn, its effect on the mechanics must be considered, while several further feedback can also be considered to enrich the fidelity of the model, as schematically depicted in Fig. 4.1.

The coupled electromechanics naturally adopts the finite elasticity theory to model the tissue deformation since the displacements are significant. Consequently, herein, we introduce the deformed and undeformed configurations used to describe the position of a body.

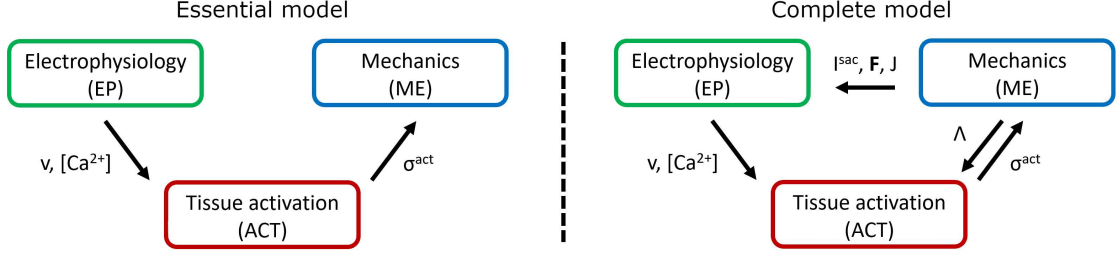


Figure 4.1: Schematic representation of the essential part of the electromechanical problem, on the left, and the fully coupled formulation, on the right.

In large deformations, a point located at coordinates  $\mathbf{X}$  in the initial – or undeformed – configuration  $\Omega_0$  is mapped into the current – or deformed – coordinates  $\mathbf{x}$  by the deformation map  $\phi : \Omega_0 \rightarrow \Omega$ :

$$\mathbf{x} = \phi(\mathbf{X}) \quad (4.1)$$

and the displacement vector  $\mathbf{u}$  is defined as the difference of these coordinates:

$$\mathbf{u} = \mathbf{x} - \mathbf{X}. \quad (4.2)$$

Consequently, the gradient of the deformation map,  $\mathbf{F}$ , reads as:

$$\mathbf{F} = \frac{\partial \phi}{\partial \mathbf{X}} = \mathbf{I} + \nabla_{\mathbf{X}} \mathbf{u}, \quad (4.3)$$

where we use a subscript to specify the set of coordinates involved in the differentiation:

$$\nabla_{\mathbf{X}}(\bullet) = \frac{\partial(\bullet)}{\partial \mathbf{X}}. \quad (4.4)$$

and we denote with  $J$  the determinant of  $\mathbf{F}$ :  $J = \det(\mathbf{F})$ .

According to the Nanson's relation [256], the deformation gradient is involved in the transformation of infinitesimal element of area:

$$dA \bar{\mathbf{N}} = \frac{1}{J} \mathbf{F}^T da \mathbf{n} \quad (4.5)$$

and volume:

$$JdV = dv, \quad (4.6)$$

where the unit-vectors  $\bar{\mathbf{N}}$  and  $\mathbf{n}$  represent the outward-pointing normal in the reference and current configurations, respectively, while  $dA$  and  $da$  are the corresponding area elements. Please, note the difference between the symbols  $\bar{\mathbf{N}}$  and  $\mathbf{N}$ , that is used to represent the matrix collecting the basis functions. Such kinematic relations affects the definition of the *Monodomain* formulation, that was presented earlier for the case of a rigid domain and herein reformulated for a deformable body.

#### 4.1.1 *Monodomain* formulation for deformable domains

According to [257, 43], the formulation for EP in a deformable domain is obtained posing the *Monodomain* equation on the deformed configuration. The evolution of the transmembrane potential  $v(\mathbf{X}, t)$ , the gating variables  $w^r(\mathbf{X}, t)$ , and the ion concentrations  $c^s(\mathbf{X}, t)$  depends on the position  $\mathbf{X}$  and one several sources of coupling. We neglect the effect of the stretch activated channels [258], as done in [180, 259], including only the effects of the displacements on the conductivity tensor  $\mathbf{D}$ , defined in the deformed

configuration. After a pull-back operation, the strong form in the reference configuration reads as follows:

$$\left\{ \begin{array}{ll} \chi C_m \frac{\partial v}{\partial t} - \frac{1}{J} \frac{\lambda}{\lambda + 1} \nabla_{\mathbf{X}} \cdot (J \mathbf{F}^{-1} \mathbf{D} \mathbf{F}^{-T} \nabla_{\mathbf{X}} v) + \chi I^{ion} = I^{app} & \text{in } \Omega_0 \setminus \partial\Omega_0 \times (0, T) \quad (4.7a) \\ \bar{\mathbf{N}} \cdot (J \mathbf{F}^{-1} \mathbf{D} \mathbf{F}^{-T}) \nabla_{\mathbf{X}} v = 0 & \text{on } \partial\Omega_0 \times (0, T) \quad (4.7b) \\ I^{ion} = I^{ion}(\mathbf{X}, v, w^1, \dots, w^k, c^1, \dots, c^q) & \text{in } \Omega_0 \times (0, T) \quad (4.7c) \\ \frac{\partial w^r(\mathbf{X}, t)}{\partial t} = m_w^r(\mathbf{X}, v, w^1, \dots, w^k) \quad \forall r = 1, \dots, k & \text{in } \Omega_0 \times (0, T) \quad (4.7d) \\ \frac{\partial c^s(\mathbf{X}, t)}{\partial t} = m_c^s(\mathbf{X}, v, w^1, \dots, w^k, c^1, \dots, c^q) \quad \forall s = 1, \dots, q & \text{in } \Omega_0 \times (0, T) . \quad (4.7e) \end{array} \right.$$

The mechanical activation of the tissue can be modeled using two alternative approaches relying on the definition either of the stress tensor or the deformation gradient. Herein, we review both approaches that, along with the response of the tissue electrically-at-rest, constitute the mathematical model for the tissue mechanics.

### 4.1.2 Active stress formulation

The *active stress* approach modifies the definition of the first Piola-Kirchhoff stress tensor, that for a standard hyperelastic material is given by the gradient of the strain energy function  $\psi$

$$\mathbf{P}(\mathbf{F}) = \frac{\partial \psi}{\partial \mathbf{F}}, \quad (4.8)$$

adding an active component  $\mathbf{P}^{act}$  to the standard passive term  $\mathbf{P}^{pas}$  [208]:

$$\mathbf{P} = \mathbf{P}^{pas} + \mathbf{P}^{act} = \frac{\partial \psi}{\partial \mathbf{F}} + \mathbf{P}^{act}. \quad (4.9)$$

The active term depends on the electrical activity of the cell, encoded in the variables  $v$  and  $c^s$ , through the activation model. Indeed, it describes the stress generated by the cardiomyocytes in the direction of the cardiac fibers according to one of the several formulation available in the literature. The general ACT system [257] reads as follows:

$$\left\{ \begin{array}{ll} \mathbf{P}^{act} = \sigma^{act} \mathbf{F} \frac{\mathbf{a}_0 \otimes \mathbf{a}_0}{\mathbf{a}_0^T \mathbf{F}^T \mathbf{F} \mathbf{a}_0} & \text{in } \Omega_0 \setminus \partial\Omega_0 \times (0, T) \quad (4.10a) \\ \sigma^{act} = \sigma^{act}(\mathbf{X}, v, c^s, \Lambda, z^1, \dots, z^l) & \text{in } \Omega_0 \times (0, T) \quad (4.10b) \\ \frac{\partial z^r(\mathbf{X}, t)}{\partial t} = m_z^r(\mathbf{X}, v, c^s, \Lambda, z^1, \dots, z^l) \quad \forall r = 1, \dots, l & \text{in } \Omega_0 \times (0, T) . \quad (4.10c) \end{array} \right.$$

In Eq. (4.10),  $\sigma^{act}$  is the so-called active stress,  $\mathbf{a}_0$  is the fiber orientation in the reference configuration,  $\Lambda(\mathbf{u})$  is the tissue stretch in the fiber direction, and  $z^r$  are the "l" variables regulating the activation, whose evolution is described by the functions  $m_z^r$ .

We highlight that the *active stress* formulation [209, 206] is of great interest, especially in modeling *in-vitro* assays [207, 260], since it provides an accurate quantification of the activation phenomenon.

### 4.1.3 Active strain formulation

The *active strain* approach, as described in [261, 208], relies on the definition of the deformation gradient, that is multiplicatively decomposed in the passive  $\mathbf{F}^{pas}$  and active  $\mathbf{F}^{act}$  parts:

$$\mathbf{F} = \mathbf{F}^{pas} \mathbf{F}^{act} \quad (4.11)$$

with the active component depending on the cellular activity through an ACT model:

$$\left\{ \begin{array}{ll} \mathbf{F}^{act} = \mathbf{I} + \gamma^{act}(\mathbf{a}_0 \otimes \mathbf{a}_0) & \text{in } \Omega_0 \setminus \partial\Omega_0 \times (0, T) \quad (4.12a) \\ \gamma^{act} = \gamma^{act}(\mathbf{X}, v, c^s, \Lambda, z^1, \dots, z^l) & \text{in } \Omega_0 \times (0, T) \quad (4.12b) \\ \frac{\partial z^r(\mathbf{X}, t)}{\partial t} = m_z^r(\mathbf{X}, v, c^s, \Lambda, z^1, \dots, z^l) \quad \forall r = 1, \dots, l & \text{in } \Omega_0 \times (0, T) . \quad (4.12c) \end{array} \right.$$

In this second approach, we assume that the strain energy function depends only on the passive part of the deformation gradient [179, 208]:

$$\psi = \psi(\mathbf{F}^{pas}) = \psi\left(\mathbf{F}(\mathbf{F}^{act})^{-1}\right), \quad (4.13)$$

and the first Piola-Kirchhoff stress tensor is computed, by definition of *active strain*, applying a pull-back operation to the derivative of the strain energy as follows:

$$\mathbf{P} = J^{act} \frac{\partial \psi}{\partial \mathbf{F}^{pas}} (\mathbf{F}^{act})^{-T}. \quad (4.14)$$

Herein, we have presented unidirectional activation model for the two formulations for active tissues. However, more general models with independent activation functions in the three spatial directions can be enforced. For instance isotropic or fully anisotropic distributions, can be modeled acting on the structures of the active tensors.

Both activation models describe the part of the mechanical response of the tissue due to the electrical stimulation, that is completed by the model for the response at rest (passive response), as shown in the following.

#### 4.1.4 Tissue mechanics

The passive response of the tissue is modeled adopting one of the hyperelastic constitutive model classically used in mechanics. Depending on the fidelity needed in the simulation, several laws are available in the literature, for instance the simple isotropic Neo-Hookean law [180] or two more complex orthotropic models [182, 181].

The tissue mechanics differs from the modeling of standard materials only in the definition of the active tensor. Indeed, the equilibrium equations reads:

$$\begin{cases} \nabla_{\mathbf{x}} \cdot \mathbf{P} + \mathbf{b}_0 = \rho \frac{\partial^2 \mathbf{u}}{\partial t^2} & \text{in } \Omega_0 \setminus \partial\Omega_0 \times (0, T) & (4.15a) \\ \mathbf{P}\bar{\mathbf{N}} - \mathbf{t}_N = \mathbf{0} & \text{on } \partial\Omega_{0N} \times (0, T) & (4.15b) \\ \mathbf{u} - \mathbf{u}^* = \mathbf{0} & \text{on } \partial\Omega_{0D} \times (0, T) & (4.15c) \end{cases}$$

where  $\rho$  is the tissue density,  $\mathbf{b}_0$  represents the distributed body load,  $\mathbf{t}_N$  the traction applied to the boundary  $\partial\Omega_{0N}$ ,  $\bar{\mathbf{N}}$  is the outward-pointing normal, and  $\mathbf{u}^*$  are appropriate essential boundary conditions applied on the boundary  $\Omega_{0D}$ .

The three sub-problems presented define an initial-value problem, that is solved by means of appropriate numerical method. In discretizing the equations, we account for the insights provided by the physics. Indeed, the muscle contraction occurs at a greater spatial scale than the depolarization wave front, enabling the use of a coarser mesh for the mechanical part of the simulation [259], as described in the next Section.

## 4.2 Solution algorithm for active stress

We present the discretization of the coupled electromechanical problem by means of Galerkin-based IgA with a focus on the *active stress* formulation.

We start the presentation with the discretization of the space using a total lagrangian formulation. Afterwards, we introduce the discretization in time based on a staggered solution algorithm, that is successively enforced in the simulation of a bar using different meshes in the electrical and mechanical sub-problems.

### 4.2.1 Spatial discretization

The semi-discrete formulation for the *Monodomain* Equation (4.7) discretize the weak form of the problem introducing the finite dimensional approximation of the transmembrane potential

$$v = \mathbf{N}\hat{v} \quad (4.16)$$

and test functions

$$\delta v = \mathbf{N} \delta \hat{\mathbf{v}}. \quad (4.17)$$

Consequently, the PDE (4.7a, 4.7b) reads:

$$\mathbf{M}^E \dot{\hat{\mathbf{v}}}(t) = -\mathbf{K}^E(\mathbf{u}) \hat{\mathbf{v}}(t) - \mathbf{I}^{ion}(t) + \mathbf{I}^{app}(t) \quad (4.18)$$

where the mass matrix of the electrical sub-problem  $\mathbf{M}^E$  is given by:

$$\mathbf{M}^E = \int_{\Omega_0} \chi C_m \mathbf{N}^T \mathbf{N} dV, \quad (4.19)$$

the stiffness matrix  $\mathbf{K}^E$  reads:

$$\mathbf{K}^E = \frac{\lambda}{\lambda + 1} \int_{\Omega_0} (\nabla_{\mathbf{x}} \mathbf{N})^T \mathbf{F}^{-1} \mathbf{D} \mathbf{F}^{-T} (\nabla_{\mathbf{x}} \mathbf{N}) dV, \quad (4.20)$$

and the applied current vector is computed as follows:

$$\mathbf{I}^{app} = \int_{\Omega_0} \mathbf{N}^T I^{app} dV \quad (4.21)$$

To compute the ionic current vector  $\mathbf{I}^{ion}$ :

$$\mathbf{I}^{ion} = \int_{\Omega_0} \chi \mathbf{N}^T I^{ion} dV, \quad (4.22)$$

one of the three canonical method presented for the conduction in the rigid domain can be adopted. In the example that follows, we adopt the ICI method, while the SVI approach is investigated successively. It is worth noting that the stiffness matrix in the case of a deformable domain is no more constant since it depends on the displacement field through the deformation gradient  $\mathbf{F}$ .

The solution of the mechanical sub-problem, in turn, is coupled to electrophysiological activity of the cell. Indeed, the total lagrangian weak form

$$\int_{\Omega_0} \delta \mathbf{E} : \mathbf{S}^{pas} dV + \int_{\Omega_0} \delta \mathbf{E} : \mathbf{S}^{act} dV - \int_{\Omega_0} \delta \mathbf{u} \cdot \mathbf{b}_0 dV - \int_{\partial \Omega_{0N}} \delta \mathbf{u} \cdot \mathbf{t}_N dA = 0, \quad (4.23)$$

derived from Eq. (4.15) neglecting the inertia of the system [43], depends on the active stress tensor  $\mathbf{S}^{act} = \mathbf{F}^{-1} \mathbf{P}^{act}$ . In such a equation, we introduce the approximated displacement field:

$$\mathbf{u} = \mathbf{N} \hat{\mathbf{u}} \quad (4.24)$$

and the virtual variation:

$$\delta \mathbf{u} = \mathbf{N} \delta \hat{\mathbf{u}} \quad (4.25)$$

from which the variation of the Green-Lagrange strain tensor  $\delta \mathbf{E}$  is derived. Please, note that the B-spline basis functions  $\mathbf{N}^u$  are potentially different from the set of functions  $\mathbf{N}$  used for the electrophysiology but both are derived from the refinement of the same geometry, guaranteeing that the same parametrization of the geometry holds. Consequently, the evaluation of a field – for instance the displacements – at a point selected in the opposite mesh, – i.e., the mesh used for the *Monodomain* – is trivial as the two meshes share the same parametrization.

To solve the discrete version of the residual form (4.23) of the mechanical sub-problem  $\mathbf{R}^M(\hat{\mathbf{u}}) = \mathbf{0}$ , where

$$\mathbf{R}_a^M(\hat{\mathbf{u}}) = \int_{\Omega_0} \delta \hat{\mathbf{E}}_{IJ a} S_{IJ}^{pas} dV + \int_{\Omega_0} \delta \hat{\mathbf{E}}_{IJ a} S_{IJ}^{act} dV - \int_{\Omega_0} N_{I a}^u b_{0I} dV - \int_{\partial \Omega_{0N}} N_{I a}^u t_{NI} dA \quad (4.26)$$

and

$$\delta \hat{\mathbf{E}}_{IJ a} = \frac{1}{2} (u_{K,I} N_{K a, I}^u + N_{S a, I}^u u_{S, J} + N_{J a, I}^u + N_{I a, J}^u), \quad (4.27)$$

we use the standard Newton's method, that requires the linearization of the residual  $D_{[\hat{\mathbf{u}}]}\mathbf{R}^M$  with respect to the argument  $\hat{\mathbf{u}}$ :

$$D_{[\hat{\mathbf{u}}]}\mathbf{R}^M = \int_{\Omega_0} D_{[\hat{\mathbf{u}}]}\delta\hat{\mathbf{E}} : \mathbf{S}^{pas} dV + \int_{\Omega_0} \delta\hat{\mathbf{E}} : D_{[\hat{\mathbf{u}}]}\mathbf{S}^{pas} dV + \int_{\Omega_0} D_{[\hat{\mathbf{u}}]}\delta\hat{\mathbf{E}} : \mathbf{S}^{act} dV + \int_{\Omega_0} \delta\hat{\mathbf{E}} : D_{[\hat{\mathbf{u}}]}\mathbf{S}^{act} dV \quad (4.28)$$

Given the semi-discrete forms of Eqs. (3.7, 4.15), a time marching scheme must be introduced since Eq. (4.18) and  $\mathbf{S}^{act}$  in Eq. (4.26) depend on time.

#### 4.2.2 Staggered time marching algorithm

In the discretization of the coupled equations in time, we adopt a staggered solution algorithm, based on implicit and explicit schemes, to split the two sub-problems reducing the complexity, as done in [257, 262].

The main idea behind the staggered scheme is to integrate explicitly the activation model (4.10) such that the mechanics is independent of electrophysiological sub-problem. Subsequently, the *monodomain* formulation is solved and the control variables of the potential, gating variables and ionic concentrations ( $\hat{\mathbf{v}}$ ,  $\hat{\mathbf{w}}$ ,  $\hat{\mathbf{c}}$ ) are updated, providing the data needed to integrate again the active-stress control variables  $\hat{\sigma}^{act}$ . More details about the scheme are provided in Algorithm 1.

---

#### Algorithm 1 Staggered solution scheme for electromechanics

---

**data:** initial conditions  $\hat{\mathbf{u}}(0), \hat{\mathbf{v}}(0), \hat{\mathbf{c}}(0), \hat{\mathbf{w}}(0), \hat{\sigma}^{act}(0)$   
**loop** over time steps:  $t_n = n\Delta t \quad n = 0, 1, 2, \dots$

- integrate explicitly the activation model  $\rightarrow \hat{\sigma}^{act}(t_{n+1})$  ▷ Explicit Euler  
     project at the Gauss points used in mechanics  $\sigma^{act}(\mathbf{X}_{gp}^M, t_{n+1})$
- solve finite elasticity  $\rightarrow \hat{\mathbf{u}}(t_{n+1})$   
     project at the Gauss points used in electrophysiology  $\mathbf{u}(\mathbf{X}_{gp}^E, t_{n+1})$
- update the stiffness matrix  $\mathbf{K}^E(t_{n+1})$
- solve *-monodomain* formulation  $\rightarrow \hat{\mathbf{v}}(t_{n+1}), \hat{\mathbf{c}}(t_{n+1}), \hat{\mathbf{w}}(t_{n+1})$  ▷ Strang splitting

**end**

---

#### 4.2.3 Electromechanical simulation of the muscle contraction

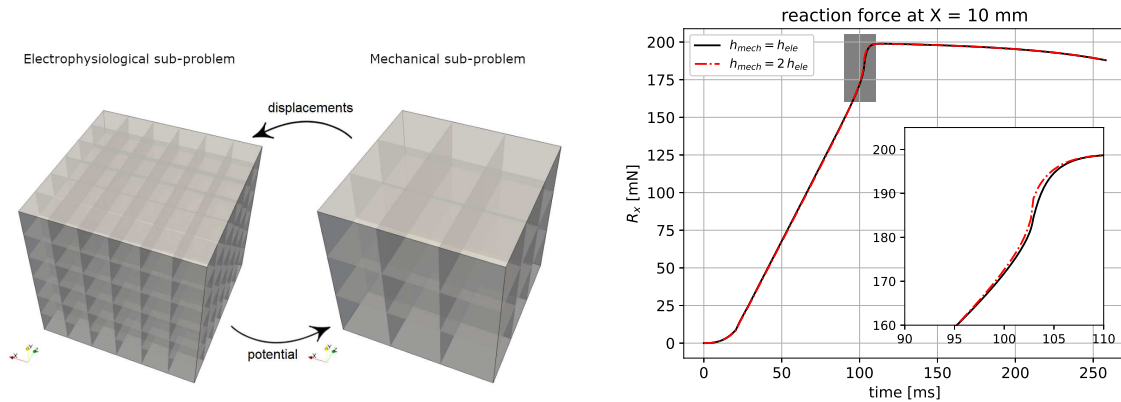


Figure 4.2: Schematic representation of the solution algorithm employing two meshes, on the left, and comparison of the axial reaction force at the right end (in Fig. 4.3) computed using equal and different meshes, on the right.

We verify the proposed formulation simulating the deformation of an active bar induced by the electrical stimulation triggered on one side. To model the electropysiological and mechanical behavior of the tissue, shown in Fig. 4.3, we adopt the models and parameters proposed in [263] discretizing them with quadratic B-splines. To assess the possibility of using different meshes for the two sub-problems, we preform two simulations: Initially, we use an equal discretization ( $h^E = h^M = 0.0625$  mm) and, afterwards, a coarser discretization for the mechanical sub-problem ( $h^E = 0.0625$  mm and  $h^M = 0.125$  mm), as shown in Fig. 4.2.

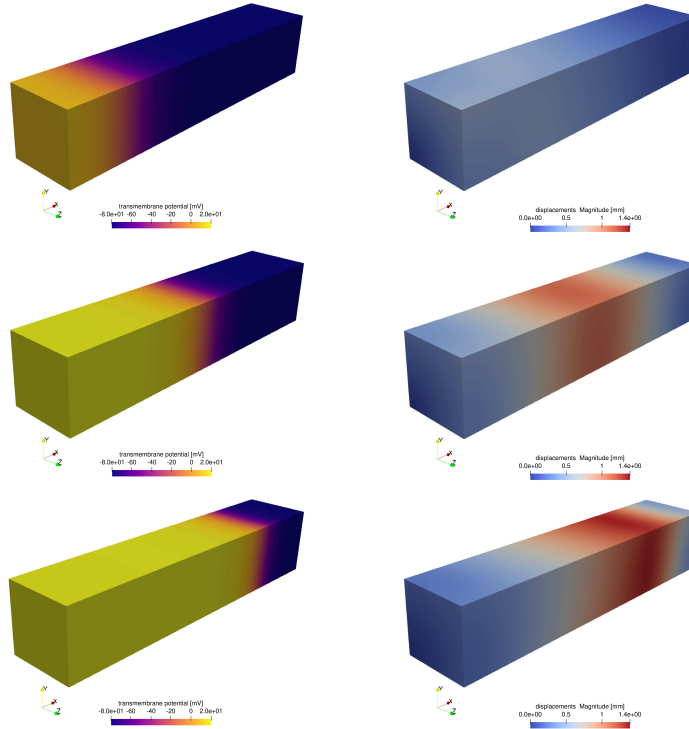


Figure 4.3: Coupled electromechanical simulation. The propagation of the action potential (on the left) governs the muscle contraction (on the right), as shown for time  $t = 25$  (top),  $50$  (center), and  $75$  ms (bottom).

### 4.3 Summary

In this chapter, we have analyzed the two formulations, namely the *active stress* and the *active strain*, available in the literature to model the mechanical activation of excitable tissues. Using such a model, we have simulated the mechanical contraction of a muscle fiber governed by the electrophysiological activity of the cells, as shown in Fig. 4.3.

In particular, we have focused on the *active stress* formulation, discretizing the problem by means of a Galerkin method. To improve the computational efficiency of the solver, we adopts two different meshes for the mechanical and electrophysiological sub-problems. Indeed, a refined mesh is need to correctly predict the sharp front of the action potential only, as shown in Fig. 4.2. This idea is further developed in Chapter 8.

In time, we have adopted a staggered solution scheme to reduce the computational burden. Indeed, the time scales of the electrophysiological activation and the muscle contraction are well-separated.

The concepts presented in this chapter serve as a preliminary investigation for a more complex studies, for instance, the electromechanical activation of a biological tissue immersed in a fluid, presented in Chapter 5.



## Chapter 5

# Fluid-structural-electrophysiological simulations of swimmers

Soft robots [227] are gaining more and more interest in the scientific community thanks to the possibility of undergoing large deformations without complex joints between rigid parts. In this setting, bio-inspired swimmers, made of polymers and layers of active tissue, are exemplary applications where the numerical simulations are used to optimize the robot functionality [264]. In this chapter, – developed within a more extended collaboration with the Department of Mechanics Mathematics and Management of Polytechnic University of Bari – we establish a coupled solver to simulate the swimming governed by the electrophysiological activation of the muscles proposing a combination of different discretization schemes. Further, investigations on the efficiency of the swimming can be found in [214].

The efficiency of the swimming of jellyfish-type swimmers depends on complex interactions between vortexes originating under the bell. This kind of phenomena are effectively investigated *in-silico*. Therefore, we develop a numerical solver focusing on the simulation of an Aurelia Aurita specimen, a type of jellyfish, since a broad literature for model calibration is available. Once such a model is set, it can be successively used to investigate the jellyfish biology or, with minimal modifications, adapted to the design of bio-inspired swimmers.

To this end we combine constitutive models derived from experimental results to define a complete mathematical framework for the electrophysiological, structural, and fluid sub-problems, that are later discretized using tailored numerical methods. Specifically, for the electromechanical problem we use IgA, while Finite Differences and the Immersed Boundary method are used for the Fluid-Structure interaction problem. Indeed, it allows for a direct numerical simulation of the fluid problem with an immersed body undergoing large displacements.

Using the mentioned techniques, we define a calibrated coupled solver, that can be used, for instance, to study the efficiency of the swimming. To limit the computational effort in future parametric investigations, we focus on the straight swimming only. Therefore, the model is developed under the assumption of axial-symmetry.

This chapter is organized as follows: Section 5.1 provides a description of the mathematical model and the simplifications with respect to the actual biological scenario. Section 5.2 brings a description of the numerical techniques used to solve the partial differential equations drafted in the previous section. Section 5.3.1 presents a detailed simulation of the fully-coupled calibrated jellyfish model, whereas conclusions are drawn in Section 5.4.

### 5.1 Mathematical model for the Aurelia Aurita

Two reference frames are used in the formulation of the differential equations occurring in the present model: a Cartesian frame, defined by the base vectors  $\{\mathbf{e}_1, \mathbf{e}_2, \mathbf{e}_3\}$ , and a convective curvilinear frame, locally identified by the covariant base vectors  $\{\mathbf{g}_1, \mathbf{g}_2, \mathbf{g}_3\}$ . The former refers to the directions  $\{x, y, z\}$ , whereas the latter to the convective coordinates  $\{\theta^1, \theta^2, \theta^3\}$ . The sketch in Fig. 5.1 shows both reference frames as well as the electrophysiological  $\Omega_e$ , elastic  $\Omega_s$ , and fluid  $\Omega_f$  domains.

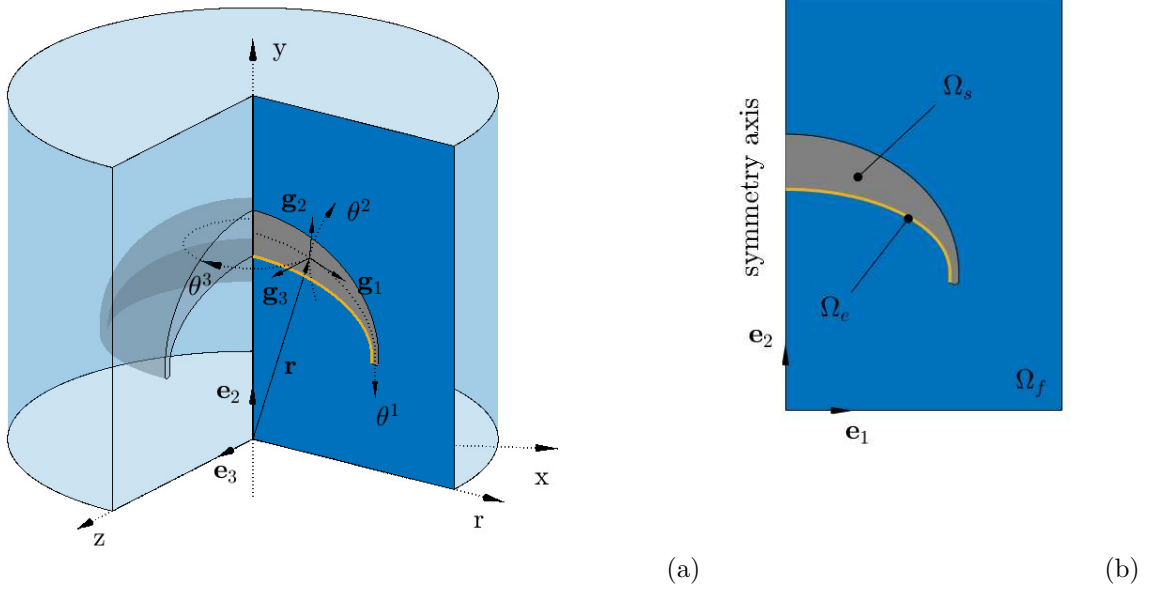


Figure 5.1: Sketch of the Cartesian  $\{x, y, z\}$  and the convective curvilinear  $\{\theta^1, \theta^2, \theta^3\}$  coordinate systems used for the mathematical formulation (a). Summary outline of each sub-domain topology (b): the blue region ( $\Omega_f$ ) covers the fluid domain, the gray area ( $\Omega_s$ ) is the solid domain, the yellow line ( $\Omega_e$ ) represents the electrophysiological domain.

Recent investigations have described the bell geometry as a solid made up from an extraumbrellar and a subumbrellar surface [265, 266, 267]. Following the parametrization introduced by [266], the axisymmetric profile of bell is delimited by the curves:

$$\frac{(r - r_c)^2}{a_{ex}^2} + \frac{(y - y_c)^2}{b_{ex}^2} = 1, \quad \frac{(r - r_c)^2}{a_{in}^2} + \frac{(y - y_c)^2}{b_{in}^2} = 1. \quad (5.1)$$

where the minor- and major semi-axis coefficients take the values:  $b_{ex} = 0.8 a_{ex}$ ,  $a_{in} = 0.948 a_{ex}$ ,  $b_{in} = 0.46 a_{ex}$ . The coordinate pair  $\{r_c, y_c\}$  represents the location of the center of the ellipses. The major axis of the ellipse,  $a_{ex}$ , corresponds to half the bell diameter. Such a geometry was originally proposed by [268], and subsequently used by [266] as a sample representative of oblate rowing jellyfish, such as the *Aurelia Aurita*. The rear part of the bell is rounded by a circular arc of radius  $r_d = 0.036 a_{ex}$ . The elliptical profiles have been elongated by a distance  $d = 0.14 a_{ex}$  to account for the flexible marginal flap encountered in many cnidarian species. Such a planar geometry  $\mathbf{X}_s$  is represented using a bivariate NURBS patch :

$$\mathbf{X}_s = \sum_{i=1}^{n_g} N_i(\theta^1, \theta^2) \mathbf{B}_i, \quad (5.2)$$

where  $N_i(\theta^1, \theta^2) = H_j(\theta^1)L_k(\theta^2)$  represents the tensor product structure and, consequently, the number of bivariate function is equal to the product of the number of univariate functions in the parametric directions  $\theta^1$  and  $\theta^2$ :  $n_g = n_{g1} \times n_{g2}$ . In our model, the two opposite edges of the parametric space,  $\theta^2 = 0$  and  $\theta^2 = 1$ , represent the subumbrellar surface and the external surface, while the remaining two sides represent the straight segment coincident with the axis of symmetry and bell margin. Adopting this parametrization, the electrophysiological domain  $\Omega_e$  – that is a subset of the mechanical domain  $\Omega_s$  – is simply identified by:

$$\mathbf{X}_e = \sum_{i=1}^{n_g} N_i(\theta^1, 0) \mathbf{B}_i = \sum_{j=1}^{n_{g1}} H_j(\theta^1) \mathbf{B}_j^e, \quad (5.3)$$

In the IgA context the knot-insertion and the degree-elevation algorithms can be directly used to obtain analysis-suitable functions preserving both the geometry and the parametrization.

### 5.1.1 Axisymmetric kinematics

Following the assumption of an axisymmetric deformation field, any radial section along the axis of symmetry is assumed to remain planar under axisymmetric loads. However, any radial displacement induces a tangential strain, therefore an out-of-plane component of strain and of the associated stress must be considered [38]. A point in the body continuum can be identified in the Cartesian frame by the position vector  $\mathbf{r}$ . Then, the covariant tangent base vectors are obtained by  $\mathbf{g}_i = \partial \mathbf{r} / \partial \theta^i$ . We emphasize that the bases of the curvilinear frame are neither orthonormal, nor unitary.

The assumption of axisymmetric displacement field lets the curvilinear coordinate  $\theta^3$  describes a circumference. Consequently, it yields:

$$\mathbf{r} = r \cos(\theta^3/r) \mathbf{e}_1 + r \sin(\theta^3/r) \mathbf{e}_3 + y \mathbf{e}_2, \quad (5.4)$$

$$\mathbf{g}_3 = -r \sin(\theta^3/r) \mathbf{e}_1 + r \cos(\theta^3/r) \mathbf{e}_3, \quad (5.5)$$

The metric tensor of an arbitrary point in the solid continuum is defined by the first fundamental form of surfaces:

$$G_{ij} = \mathbf{g}_i \cdot \mathbf{g}_j. \quad (5.6)$$

The axial symmetry yields the coefficients:

$$\begin{cases} G_{\alpha\beta} \neq 0 & \alpha, \beta = 1, 2 & \text{for the in-plane components,} & (5.7a) \\ G_{\alpha 3} = G_{3\alpha} = 0 & & \text{for the mixed components,} & (5.7b) \\ G_{33} = r^2 & & \text{for the out-of-plane component.} & (5.7c) \end{cases}$$

When expressing strain and stress variables as a function of the metric tensor coefficients, Eq.(5.7) allows to carry out a fully curvilinear formulation without the need for coordinate transformations. The tensor deformation gradient is consistently defined as:

$$\mathbf{F} = \mathbf{g}_i \otimes \mathring{\mathbf{g}}^i, \quad (5.8)$$

where the symbol  $(\mathring{\cdot})$  indicates a quantity in the reference configuration,  $\Omega_{s0}$ , and the superscript refers to contravariant vectors. A sketch of the reference configuration is illustrated in Fig. 5.3 (b). The Green–Lagrange strain tensor is assumed as finite strain measure:

$$\mathbf{E} = \frac{1}{2} (\mathbf{F}\mathbf{F}^T - \mathbf{I}) = E_{ij} \mathring{\mathbf{g}}^i \otimes \mathring{\mathbf{g}}^j, \quad (5.9)$$

which yields the non-zero strain components:

$$E_{\alpha\beta} = \frac{1}{2} (G_{\alpha\beta} - \mathring{G}_{\alpha\beta}), \quad (5.10)$$

$$E_{33} = \frac{1}{2} (r^2 - \mathring{r}^2). \quad (5.11)$$

Local deformations are expressed in terms of the right Cauchy–Green deformation tensor, defined on the contravariant base vectors:

$$\mathbf{C} = \mathbf{F}\mathbf{F}^T = G_{ij} \mathring{\mathbf{g}}^i \otimes \mathring{\mathbf{g}}^j. \quad (5.12)$$

### 5.1.2 Constitutive model of the solid phase

The elastic properties of the jellyfish bell, here discretized over the mechanical domain  $\Omega_s$  (Fig. 5.1b), play a crucial role in the determination of the FSI dynamics. Regardless of the genus, the Mesoglea, a gelatinous substance comprised of randomly oriented collagen fibers and proteins networks [269], makes up the majority of jellyfish volume [270]. It provides structural support and stores the strain energy released in the elastic recoil stage.

Many prior studies indicate that the modulus of Mesoglea varies over a wide range of magnitude [271, 272]. For instance, Demont and Gosline [273] found that intact jellyfish bell of the species *Polyorchis penicillatus* has a Young’s modulus between 400 and 1000 Pa. Megill et al. [271] found the stiffness of the Mesoglea of the same specimen to be 350 Pa in compression while the softer joint Mesoglea has

stiffness of 50 Pa. We model the solid phase within  $\Omega_s$  as an homogeneous isotropic medium which takes the elastic properties of the Mesoglea. The elastic parameters are tailored accordingly to the Mesoglea measurements on the Aurelia Aurita. The Aurelia Aurita was found to have a water content of 96.3% with a standard deviation of 0.57% [274]. Hence, a nearly-incompressible constitutive law is considered suitable for the scope of the work. Specifically, we adopt a Neo-Hookean strain energy density function [275]:

$$\Psi(\mathbf{C}) = c_{10} (I_1 I_3^{-1/3} - 3) + K(J - 1)^2, \quad (5.13)$$

where  $I_1 = \text{tr}(\mathbf{C})$  and  $I_3 = \det(\mathbf{C})$  denote the first and third invariants of the right Cauchy-Green deformation tensor  $\mathbf{C}$  and  $J = \det(\mathbf{F})$  is the Jacobian of the deformation gradient tensor. The parameters  $c_{10}$  and  $K$  represent the shear and the bulk moduli. Following the tension-compression tests carried out by [271], we assume  $c_{10} = 400$  Pa and  $K = 5.0 \times 10^4$  Pa. The bulk modulus  $K$  is chosen as an arbitrary high value to get minimal volume changes; this assumption will be numerically verified in sub-section B.2. In the range of physiological muscle contraction frequency (0.2 ÷ 0.5 Hz) macro-rheological measurements [276] show that the Mesoglea exhibits an elastic shear modulus ten times larger than the viscous shear modulus. The viscoelastic response of the Mesoglea is thus neglected.

We adopt a total Lagrangian description, which relies on the second Piola-Kirchhoff stress tensor  $\mathbf{S}$ , and on the fourth-order material tensor  $\mathbb{C}$ . They are defined on the covariant base vectors as:

$$\mathbf{S} = S^{ij} \hat{\mathbf{g}}_i \otimes \hat{\mathbf{g}}_j, \quad (5.14)$$

$$\mathbb{C} = C^{ijkl} \hat{\mathbf{g}}_i \otimes \hat{\mathbf{g}}_j \otimes \hat{\mathbf{g}}_k \otimes \hat{\mathbf{g}}_l. \quad (5.15)$$

The above contravariant coefficients can be obtained by derivation of the strain energy density with respect to the Cauchy-Green deformation tensor:

$$S^{ij} = 2 \frac{\partial \Psi}{\partial C_{ij}}, \quad (5.16)$$

$$\mathbb{C}^{ijkl} = 4 \frac{\partial^2 \Psi}{\partial C_{ij} \partial C_{kl}}. \quad (5.17)$$

### 5.1.3 Weak formulation for elastodynamics

We model the jellyfish bell as a hyperelastic continuum defining the total energy of the body, that is a function of the displacement field  $\mathbf{u}$ . For the sake of completeness, we recall here the principle of the virtual power [256], already mentioned in Chapter 4, in axisymmetric conditions (the displacement field is invariant with respect to the coordinate  $\theta^3$ ):

$$\delta \Pi(\mathbf{u}, \delta \mathbf{u}) = 2\pi \int_{\Omega_{s0}} \rho_s \frac{\partial^2 \mathbf{u}}{\partial t^2} \cdot \delta \mathbf{u} \hat{r} dS + 2\pi \int_{\Omega_{s0}} \mathbf{S} : \delta \dot{\mathbf{E}} \hat{r} dS - 2\pi \int_{\partial \Omega_{s0}} \mathbf{t}_0 \cdot \delta \mathbf{u} \hat{r} dL = 0 \quad \forall \delta \mathbf{u}, \quad (5.18)$$

where  $dS$  and  $dL$  represent the infinitesimal area and arc-length in the reference configuration  $\Omega_{s0}$ , respectively. In Eq. (5.18), we recognize three terms: the inertia of the system relying on the bell density  $\rho_s$  and on the acceleration, the stress expressed in terms of the second Piola-Kirchhoff stress tensor  $\mathbf{S}$  deriving from the elastic energy  $\Psi(\mathbf{C})$  (as shown in the previous section), and the tractions  $\mathbf{t}_0$  on the boundary of the solid body  $\partial \Omega_{s0}$  depending on the action of the flow field. Each of them is work-conjugate with the virtual velocity  $\delta \mathbf{u}$ , or the virtual strain rate tensor [256]:

$$\delta \dot{\mathbf{E}} = \frac{1}{2} \left( \delta \dot{\mathbf{F}}^T \mathbf{F} + \mathbf{F}^T \delta \dot{\mathbf{F}} \right) \quad \text{with} \quad \delta \dot{\mathbf{F}} = \frac{\partial \delta \mathbf{u}}{\partial \theta^i} \otimes \hat{\mathbf{g}}^i, \quad (5.19)$$

providing an equation for each axisymmetric velocity field compatible with the Dirichlet boundary conditions. We solve such set of nonlinear equations by means of the Galerkin method. We remark that, as in plane-strain conditions, the axisymmetric virtual velocity field has only two non-zero components. However, the normal out-of-plane components of the stress and strain rate tensors are non-null, actively contributing to the total virtual power.

### 5.1.4 Muscle activation via active strain approach

In both oblate and prolate jellyfish the muscle cells are mostly located in the marginal part of the endothelial area, and absent in the center, where the mouth is located. In most Scyphozoan and Hydrozoan, muscle fibers are oriented in radial and coronal bundles. During the contraction phase in forward swimming, the coronal muscles, innervated by the Motor Nerve Net (MNN), seem to provide predominant contraction with respect to the radial ones [277]. Radial muscles, innervated by the Diffuse Nerve Net (DNN), are thought to be mostly involved in maneuvering [278, 279] operations. As a simplifying assumption, we assume the radial and coronal muscle layers to be governed by the same nerve net, although different fiber stretching magnitudes are allowed. Thus, the muscle contraction waves are generated by the same electrophysiological pulse, but different contraction levels can be achieved. This can lead to a biologically-aware correlation between actuation pattern and locomotion performance.

We propose the implementation of such a muscular architecture by means of the active strain approach [280, 281]. This allows to retrieve a realistic balance between actively contracting and passive part of the body in terms of volume fraction, as well as to disentangle the contribution of radial and coronal muscles in forward swimming.

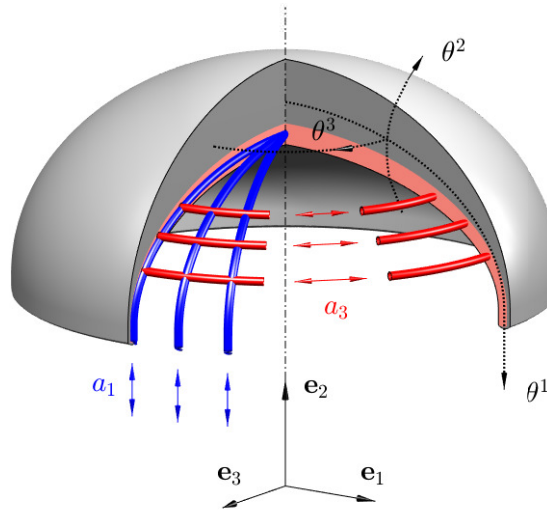


Figure 5.2: Sketch of the fiber orientation for coronal (red) and radial (blue) muscles within the body continuum. The pink area is the subset of the computational domain where the activation parameters take non-zero values, representing the subumbrellar muscle layer. Conversely, the rest of the domain provides a purely passive response. The proportion between these areas follows an illustrative purpose only.

The active strain approach is built on the multiplicative decomposition of the deformation gradient tensor into an elastic part  $\mathbf{F}_e$  and an active part  $\mathbf{F}_a$ :

$$\mathbf{F} = \mathbf{F}_e \mathbf{F}_a . \quad (5.20)$$

The active deformation  $\mathbf{F}_a$  mimics the macroscopic effects of the myofibril shortening driving the tissue contraction. In the present chapter, the instantaneous active gradient is prescribed by a phenomenological law which dictates the activation parameters embedded in  $\mathbf{F}_a$ . The explicit expression of  $\mathbf{F}_a$  is presented in the following of the present section. It is worth pointing out that  $\mathbf{F}_e$  and  $\mathbf{F}_a$  are not given by the gradient of a vector map. Kinematically, the active deformation leads to an intermediate non-compatible configuration which is subsequently relaxed towards the final configuration by the elastic response. Accordingly,  $\mathbf{F}_a$  is defined by the tensor product over base vectors in the reference configuration:

$$\mathbf{F}_a = F_a^{ij} \hat{\mathbf{g}}_i \otimes \hat{\mathbf{g}}_j . \quad (5.21)$$

In this chapter, the elastic strain energy  $\Psi_e$  is thought as a function of the elastic part of the right Cauchy-Green deformation tensor  $\mathbf{C}_e$ :

$$\Psi_e = \Psi_e(\mathbf{C}_e) , \quad (5.22)$$

which is defined following the deformation gradient split:

$$\mathbf{C} = \mathbf{F}_a^T \mathbf{C}_e \mathbf{F}_a . \quad (5.23)$$

The purely elastic quantities (denoted by the subscript “e”), as well as the elastic and active deformation gradient tensors, are all defined with respect to the reference configuration. We address the quantification of the determinant of the two parts of the tensor deformation gradient separately. Namely, for  $J = J_e J_a$ , we prescribe  $J_a = 1$  by properly building the active deformation gradient, whereas  $J_e$  follows up from the choice of the bulk modulus  $K$ . The second Piola-Kirchhoff stress tensor is expressed as a function of the active deformation tensor, as presented in Chapter 4.

Taking advantage of the reference frame depicted in Fig. 5.1 (a), the active part of the tensor deformation gradient is built such that the local fiber orientation matches the convective curvilinear frame: the natural orientation of radial and coronal muscle fibers follows the base vectors  $\mathbf{g}^1$  and  $\mathbf{g}^3$ , respectively. Thus,  $\mathbf{F}_a$  takes the form:

$$\mathbf{F}_a = \mathbf{I} - \gamma [a_1 (\mathring{\mathbf{g}}^1 \otimes \mathring{\mathbf{g}}^1) + a_3 (\mathring{\mathbf{g}}^3 \otimes \mathring{\mathbf{g}}^3)] + \gamma_2 (\mathring{\mathbf{g}}^2 \otimes \mathring{\mathbf{g}}^2) , \quad (5.24)$$

where  $\gamma$  is a smooth activation function of space and time (it takes values between 0 and 1), depending on the excitation state and  $a_2$  and  $a_3$  are space-dependent material parameters controlling the intensity of the active contraction for radial and coronal muscle fibers. The muscle fibers are sketched in Fig. 5.2, which highlights the consistency of the definition (5.24) with the local reference frame. Although the decomposition of the deformation gradient is carried out all over the solid domain, the activation parameters are null throughout most of the body, except that within a thin layer (pink region in Fig. 5.2), which plays the role of the subumbrellar muscles.  $\gamma_2$  controls the activation in the  $\theta^2$  direction, i.e. along the thickness. Despite no muscle fiber takes this orientation, this term is necessary to fulfill the incompressibility constraint of the active part. Bringing the terms of Eq. (5.24) on the same basis, the coefficient equation for  $\mathbf{F}_a$  yields:

$$F_a^{ij} = \mathring{G}^{ij} - \gamma (a_1 \mathring{G}^{1i} \mathring{G}^{1j} + a_3 \mathring{G}^{3i} \mathring{G}^{3j}) + \gamma_2 \mathring{G}^{2i} \mathring{G}^{2j} . \quad (5.25)$$

The volume-preserving assumption about the active deformation, i.e.,  $J_a = |F_a^{ij}| / |\mathring{G}^{ij}| = 1$ , allows to compute  $\gamma_2$  as:

$$\gamma_2 = \frac{-\gamma (a_1 \mathring{G}^{11} + a_3 \mathring{G}^{33} - \gamma a_1 a_3 \mathring{G}^{11} \mathring{G}^{33})}{(\gamma a_3 \mathring{G}^{33} - 1) (\gamma a_1 (\mathring{G}^{12})^2 + \mathring{G}^{22} - \gamma a_1 \mathring{G}^{11} \mathring{G}^{22})} . \quad (5.26)$$

The activation field is described in the parametric space associated to the NURBS geometry by an hyperbolic tangent function scaled by the maximal activation values  $\{\hat{a}_1, \hat{a}_3\}$ , namely:

$$a_1 (\theta^1, \theta^2) = \hat{a}_1 f_a , \quad (5.27)$$

$$a_3 (\theta^1, \theta^2) = \hat{a}_3 f_a , \quad (5.28)$$

$$f_a (\theta^1, \theta^2) = \frac{1}{4} [1 - \tanh (w_2 (\theta^2 - \delta_2))] [1 - \tanh (w_1 (\delta_1 - \theta^1))] , \quad (5.29)$$

with  $w_2 = 40.0$ ,  $w_1 = 10.0$ ,  $\delta_1 = 0.55$ , and  $\delta_2 = 0.2$ . We implicitly assume that the convective coordinates  $(\theta^1, \theta^2)$  in the parametric space take values within the interval  $[0, 1] \times [0, 1]$ . The extent of the active region is selected as a trade-off between zoological features and numerical robustness necessities. Along the  $\theta^1$  direction  $f_a$  goes to zero due to the presence of the mouth and the stomach, where no muscular tissue overlaps [282], whereas along the  $\theta^2$  direction we employ the minimal extension necessary for the convergence of the numerical method. The pattern function  $f_a$  on both the parametric space and the physical space are displayed in Fig. 5.3. The functional dependence of the activation function  $\gamma$  on the electrophysiological field variables is outlined in the following subsection.

### 5.1.5 Electrophysiology and its corresponding weak formulation

In most Scyphozoan, the neurons of the MNN have random orientation and they are electrically symmetric [283, 284], resulting in an electrically homogeneous network. According to this feature, the

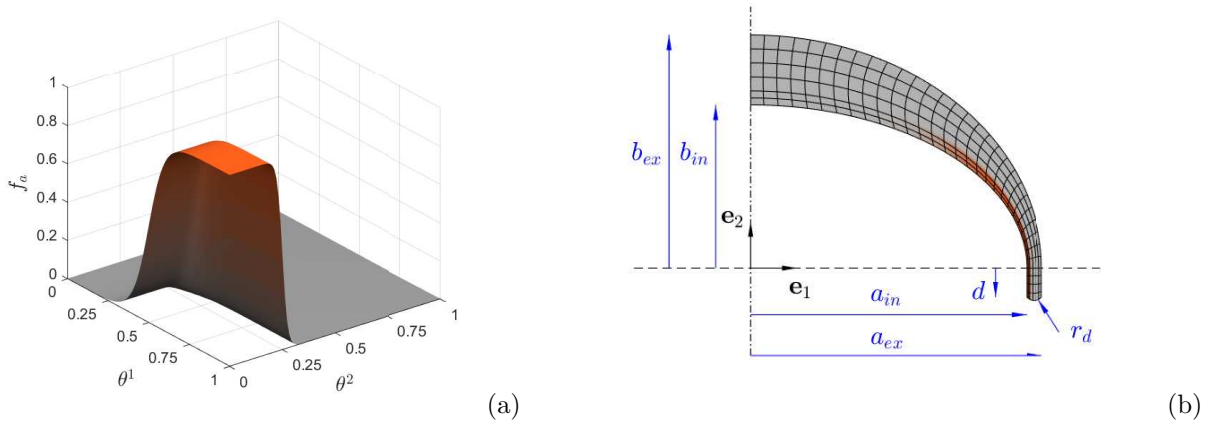


Figure 5.3: Spatial distribution of the activation pattern  $f_a$  used to build the active deformation gradient (5.24), visualized in the NURBS parametric space (a). NURBS patch used as computational domain of the structural problem with the relevant geometric dimensions (b). Black lines denote the element edges for IgA, whereas the orange region displays  $f_a$  in the physical space.

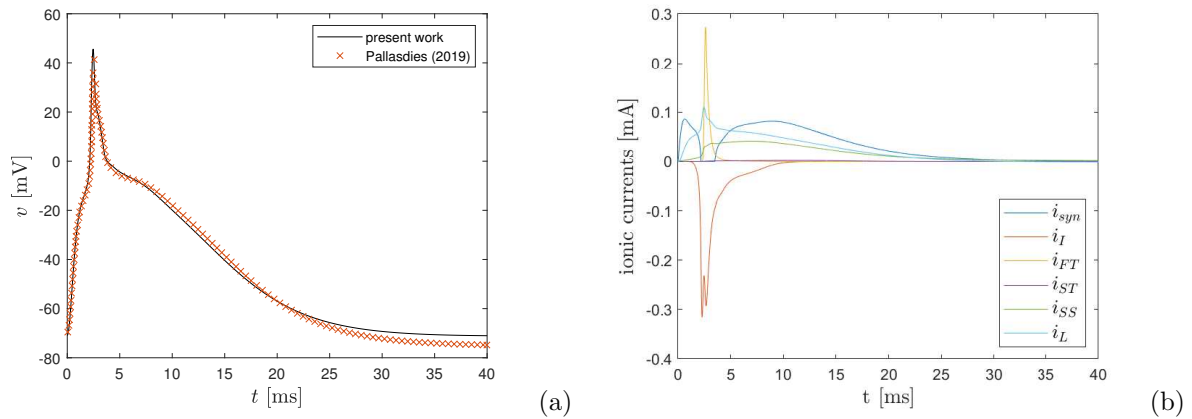


Figure 5.4: Time traces of the transmembrane potential (a). Disentangled ionic currents (b) involved in the neuron model.

electrophysiological activity of the body is modeled by means of the monodomain formulation [240]. The axial symmetry assumption entails a simultaneous firing of the pacemaker cells, which actually takes place in straight swimming. In view of the dimensionality reduction, a uniform instantaneous distribution of the action potential is assumed in the tangential direction. Simultaneous pacemaker discharges were found to produce independent excitation waves, that, when colliding, cancel out, owing to a state of mutual refractoriness in the area surrounding the collision [285]. Such a physiological feature allows to neglect the three-dimensional nature of the action potential pattern (i.e., the collision of spherical depolarization fronts) generated by the synchronous firing of multiple pacemakers. Thus, our axisymmetric model only describes the propagation of the action potential wave front in the radial direction, along a curvilinear abscissa on the subumbrellar profile (domain  $\Omega_e$ , displayed in Fig. 5.1). Neumann boundary conditions are enforced to let the electrophysiological wave exit the domain with minimal reflections. The monodomain problem, built out of a reaction-diffusion partial differential equation and  $k$  ordinary differential equations, is described in Chapter 3.

To obtain a weak formulation for a Galerkin-type discretization, one can multiply the PDE in by all the admissible test functions  $\delta v$  and integrating over the surface  $\Omega_{e0}$ , representing the endothelial surface in the reference configuration. In axisymmetric conditions, the unknown scalar fields  $v$  and  $G_k$ ,

representing the transmembrane potential and the gating variables of the neuron model, respectively, are computed solving the weak form:

$$2\pi \left( C_m \int_{\Omega_{e0}} \frac{\partial v}{\partial t} \delta v \hat{r} dl + \int_{\Omega_{e0}} \nabla \delta v \cdot (\mathbf{D} \nabla v) \hat{r} dl + \chi \int_{\Omega_{e0}} I^{\text{ion}}(v, G_k) \delta v \hat{r} dl \right) = 2\pi \chi \int_{\Omega_{e0}} I^{\text{app}} \delta v \hat{r} dl, \quad (5.30)$$

coupled to the system of ODE representing the neuron model [286]

The diffusion process takes place according to the axisymmetric hypothesis, therefore a consistent definition of the conductivity tensor must be adopted:

$$\mathbf{D} = D^{ij} \mathbf{g}_i \otimes \mathbf{g}_j, \quad (5.31)$$

with  $\mathbf{D}$  a diagonal matrix whose components are:  $D^{11} = D_0$   $D^{22} = 0$   $D^{33} = D_0 r^2$ .  $D_0$  represents the spatially uniform conduction coefficient. Following the previous equation,  $D^{22} = 0$  since the diffusion process is assumed to take place over the surface defined by the in-plane base vectors  $\mathbf{g}_1$ , and  $\mathbf{g}_3$ . The other in-plane coefficients  $D^{13} = D^{31}$  are set to zero too, for the problem to hold the axial symmetry. It is worth noting that the conductivity tensor depends on the local orientation of the base vectors to account for the mechano-electrical feedback arising from the body reconfiguration.

Pallasdies et al. [286] proposed a Hodgkin-Huxley neuron model to be integrated into the discrete representation of the MNN, made up of a set of randomly oriented neurons that propagate the action potential from a neuron to the surrounding ones after a time delay. In our monodomain formulation, the signal propagates in the continuum accordingly to the diffusion coefficients. To recast the discrete model in a continuous fashion, the synaptic current activates when the potential exceeds a predefined threshold. As the evolution of the potential upstroke is already included in the neuron model, we fix the threshold ( $-70.0$  mV) close to the resting potential ( $-70.85$  mV).

Quantitative observations about the space-time correlation between the electrical activity of the MNN and the muscle contraction pattern are still fairly limited. In Horridge et al. [287], experimental investigations on the Aurelia Aurita determined an approximate contraction duration of 1s and this value was recently employed in high-fidelity simulations of the jellyfish turning [279], providing a satisfactory agreement with the experimental observations. To limit the complexity of the model, we propose a direct relation between one of the gating variable and the activation function. We define the normalized muscle activation function  $\gamma$  by means of direct scaling of the dynamics of the gating variable  $G_a$ , associated to the transient inward current, as shown in Fig. 5.5. The scaling is performed such that the contraction holds for approximately 1s, and the contraction phase is more rapid than bell relaxation. As a result of the asymmetry in the timing of the two phases larger flow velocities are achieved during bell contraction than during bell relaxation [288]. Thus, the activation function takes the form:

$$\gamma(t) = \frac{1}{0.902} G_a (\eta t + \hat{t} (1 - \eta)), \quad (5.32)$$

where the scaling parameter  $\eta$  takes the value  $1/140$ , and  $\hat{t}$  represents the time for which  $G_a$  exceeds the threshold  $0.005$ . The parameters are chosen such that the duration of the muscle activity is in the range of a variety of jellyfish species (see Table 2 in [289]). A comparison of the time scale of the activation function and that of the transmembrane potential can be inferred from Fig. 5.5.

### 5.1.6 Fluid-Dynamics model

The incompressible Navier-Stokes equations are solved in a cylindrical reference frame (domain  $\Omega_f$  displayed in Fig. 5.1) under the assumption of axisymmetric flow. In view of this framework, the dimensionless continuity and momentum equations take the form:

$$\begin{cases} \frac{\partial q_1}{\partial r} + r \frac{\partial q_2}{\partial z} = 0, \\ \frac{\partial q_1}{\partial t} + \frac{\partial}{\partial r} \left( \frac{q_1^2}{r} \right) + \frac{\partial}{\partial y} (q_1 q_2) = -r \frac{\partial p}{\partial y} + \frac{1}{\text{Re}} \left[ r \frac{\partial}{\partial r} \left( \frac{1}{r} \frac{\partial q_1}{\partial r} \right) + \frac{\partial^2 q_1}{\partial y^2} \right] + f_r, \\ \frac{\partial q_2}{\partial t} + \frac{1}{r} \frac{\partial}{\partial r} (q_1 q_2) + \frac{\partial q_2^2}{\partial y} = -\frac{\partial p}{\partial y} + \frac{1}{\text{Re}} \left[ \frac{1}{r} \frac{\partial}{\partial r} \left( r \frac{\partial q_2}{\partial r} \right) + \frac{\partial^2 q_2}{\partial y^2} \right] + f_y, \end{cases} \quad (5.33)$$

where  $\text{Re}$  is the Reynolds number and the quantities  $q_1 = r v_1$  and  $q_2 = v_2$  denote the scaled radial and axial velocity components, respectively. With this expedient, the governing equations can be easily recast

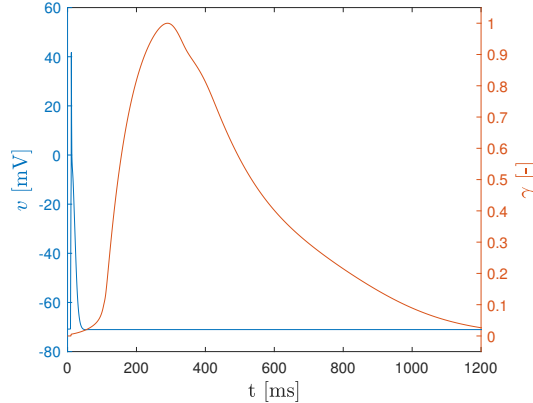


Figure 5.5: Time traces of the transmembrane potential and activation function

in a similar way to the Cartesian form [290]. When considering the bell diameter, hereafter referred as  $2a_{ex}$ , as characteristic length scale and the pacing frequency  $\phi$  as characteristic time scale, the Reynolds number yields:

$$\text{Re} = \frac{4 \rho_f \phi a_{ex}^2}{\mu}, \quad (5.34)$$

where the frequency driving the bell deformation is equal to the frequency of electrophysiological pulses. Here  $\rho_f$  and  $\mu$  represent the fluid density and dynamic viscosity, respectively. In our model we consider  $2a_{ex} = 3$  cm,  $\phi = 0.5$  Hz. In conjunction with the fluid properties summarized in table B.1, this yields  $\text{Re} = 450$ .

The propulsion features have been widely recognized to be correlated with bell streamlining (or bell fineness ratio) and velum-diameter ratio [291]. Prolate medusae generally possess a large velum/diameter ratio and perform fast contractions, resulting in a rapid ejection of the fluid from inside their bell while entraining minimal fluid from outside the bell into their wake. Consequently, a clearly defined jet structure is produced. Conversely, oblate species derive only a small portion of thrust from jet propulsion. They provide slower contractions which produce prominent vortices at the bell margins mostly observed in rowing propulsion. As their bells expand, after each contraction, water rushes in, and it refills the bell in the form of a large vortex ring that rotates in the opposite direction of the ring created when the bell is contracted. According to [277], this classification based on the propulsion mechanism mostly complies with the distinction between Hydrozoans and Scyphozoans, despite paddling/rowing propulsion is observed in oblate hydromedusae as well [292]. There exist species that evade the distinction between prolate and oblate jellyfish in terms of propulsion mechanism. For instance, the *Aurelia Aurita* [293] and the *Aequorea Victoria* [294] have been found to exploit both rowing and jet propulsion mechanisms together.

## 5.2 Numerical discretization of the multiphysics framework

The spatial discretization of the multiphysics problem follows a partitioned approach, by which different numerical techniques are employed for different sub-problems. We rely on a NURBS-based Isogeometric method for the solution of the electrophysiological and elastic sub-problems and a centered finite difference approach for the fluid sub-problem. The relevant details of the discretization techniques are reported in the present section.

### 5.2.1 Isogeometric discretization for axisymmetric structural dynamics

We discretize the finite elasticity problem by means of an isogeometric Galerkin method in space, and by the generalized- $\alpha$  method in time. The body displacement and the virtual velocity fields are approximated by:

$$\mathbf{u} = \mathbf{N}(\theta^1, \theta^2) \hat{\mathbf{u}} \quad (5.35)$$

$$\delta \mathbf{u} = \mathbf{N}(\theta^1, \theta^2) \delta \hat{\mathbf{u}} \quad (5.36)$$

Each of the  $2 \times n_m$  (with  $n_m$  being the number of control points of the structural mesh) resulting nonlinear equations corresponds to one variation of the finite-dimensional virtual velocity field:

$$\begin{aligned} \text{Res}_i = 2\pi \int_{\Omega_{s0}} N_{ki} \frac{\partial^2 u_k}{\partial t^2} \rho_s \dot{r} dS + 2\pi \int_{\Omega_{s0}} \overbrace{\frac{1}{2} \left( \frac{\partial N_{mi}}{\partial \theta^a} \dot{g}_k^a F_{ml} + \frac{\partial N_{mi}}{\partial \theta^b} \dot{g}_l^b F_{mk} \right)}^{F_i^{int}} S^{kl} \dot{r} dS + \\ - 2\pi \int_{\partial\Omega_{s0}} \overbrace{N_{ki} t_{0,k}}^{F_i^{ext}} \dot{r} dL = 0 \quad i = 1, \dots, 2 \times n_m, \quad (5.37) \end{aligned}$$

where the index  $i$  denotes the degree of freedom of the problem, while the indices  $k$ ,  $l$ , and  $m$  indicate the direction in space. In the latter equation we drop the functional dependence on the control variables and we adopt Einstein's notation on summations. Moreover, we recall that the deformation gradient depends on the active strain, coupling the displacement field to the monodomain problem.

The generalized- $\alpha$  method is a nonlinear predictor-corrector time integration scheme, that updates the displacement control variables solving the residual equations (5.37) by means of the Newton's method. Thus, the linearization of the first integral in (5.37) with respect to the acceleration control variables  $\hat{\mathbf{a}}_j = d^2 \hat{\mathbf{u}}_j / dt^2$ , with  $j = 1, \dots, 2 \times n_m$ , is needed, yielding:

$$\mathbf{M}_{ij} = 2\pi \int_{\Omega_{s0}} N_{ki} N_{kj} \rho_s \dot{r} dS \quad (5.38)$$

as well as the linearization of the second integral with respect to the displacement control variable  $\hat{\mathbf{u}}_j$ :

$$\begin{aligned} \mathbf{K}_{ij}(\hat{\mathbf{u}}) = 2\pi \int_{\Omega_{s0}} \overbrace{\frac{1}{2} \left( \frac{\partial N_{mi}}{\partial \theta^a} \dot{g}_k^a \frac{\partial N_{mj}}{\partial \theta^l} + \frac{\partial N_{mi}}{\partial \theta^b} \dot{g}_l^b \frac{\partial N_{mj}}{\partial \theta^k} \right)}^{D_{[\Delta \hat{\mathbf{u}}]} \delta \dot{\mathbf{E}} : \mathbf{S}} S^{kl} \dot{r} dS + \\ + 2\pi \int_{\Omega_{s0}} \overbrace{\frac{1}{2} \left( \frac{\partial N_{mi}}{\partial \theta^a} \dot{g}_k^a F_{ml} + \frac{\partial N_{mi}}{\partial \theta^b} \dot{g}_l^b F_{mk} \right) \mathbb{C}^{klwq} \frac{1}{2} \left( \frac{\partial N_{wi}}{\partial \theta^q} + \frac{\partial N_{qi}}{\partial \theta^w} + \frac{\partial u_w}{\partial \theta^b} \frac{\partial N_{ri}}{\partial \theta^b} + \frac{\partial N_{wi}}{\partial \theta^f} \frac{\partial u_q}{\partial \theta^f} \right)}^{\delta \dot{\mathbf{E}} : D_{[\Delta \hat{\mathbf{u}}]} \mathbf{S}} \dot{r} dS. \quad (5.39) \end{aligned}$$

Conversely, the hydrodynamic load depends only on time because of the adopted FSI scheme (see Section 5.2.6).

To integrate in time, we interpolate the displacements and accelerations between two successive time steps  $t_n$  and  $t_{n+1} = t_n + \Delta t$  as follows:

$$\hat{\mathbf{u}}^\alpha = \alpha_f \hat{\mathbf{u}}^{n+1} + (1 - \alpha_f) \hat{\mathbf{u}}^n, \quad (5.40)$$

$$\hat{\mathbf{a}}^\alpha = \alpha_m \hat{\mathbf{a}}^{n+1} + (1 - \alpha_m) \hat{\mathbf{a}}^n, \quad (5.41)$$

where the velocity and the displacements at time step  $t_{n+1}$  are computed by the Newmark update:

$$\hat{\mathbf{v}}^{n+1} = \hat{\mathbf{v}}^n + \Delta t ((1 - \gamma) \hat{\mathbf{a}}^n + \gamma \hat{\mathbf{a}}^{n+1}), \quad (5.42)$$

$$\hat{\mathbf{u}}^{n+1} = \hat{\mathbf{u}}^n + \Delta t \hat{\mathbf{v}}^n + \frac{\Delta t^2}{2} ((1 - 2\beta) \hat{\mathbf{a}}^n + 2\beta \hat{\mathbf{a}}^{n+1}). \quad (5.43)$$

The convergence of the generalized- $\alpha$  method is regulated by the set of adopted coefficients, that, furthermore, defines the amount of numerical damping for high-frequency modes. In the present chapter, we adopt the following set of coefficients [12], defined as a function of the spectral radius of the iteration matrix  $\rho_\infty$ :

$$\alpha_m = \frac{2 - \rho_\infty}{1 + \rho_\infty}, \quad \alpha_f = \frac{1}{1 + \rho_\infty}, \quad \beta = \frac{(1 - \alpha_f + \alpha_m)^2}{4}, \quad \gamma = \frac{1}{2} - \alpha_f + \alpha_m. \quad (5.44)$$

In this chapter, we follow the classical choice  $\rho_\infty = 0.5$  [12], which allows to damp out spurious high frequency modes while preserving most of the natural ones.

When updating the displacements, we solve Eq. (5.37), computed with the variables interpolated at the time fraction  $\alpha$ , in terms of acceleration by means of the Newton's method. The update formula can be obtained exploiting the chain rule to differentiate with respect to acceleration:

$$\frac{d\mathbf{Res}^\alpha}{d\hat{\mathbf{a}}^{n+1}} \Delta \hat{\mathbf{a}}^{n+1} = -\mathbf{Res}^\alpha, \quad (5.45)$$

which reads, in index notation:

$$(\alpha_m M_{ij} + \alpha_f \beta \Delta t^2 K_{ij}(\hat{\mathbf{u}}^\alpha)) \Delta \hat{a}_j^{n+1} = -M_{ij} \hat{a}_j^\alpha - F_i^{int,\alpha} + F_i^{ext,\alpha}, \quad (5.46)$$

where  $F_i^{int,\alpha}$  is the internal elastic power computed in term of displacements  $\hat{\mathbf{u}}^\alpha$  and  $F_i^{ext,\alpha}$  represents the hydrodynamic load extrapolated from the previous time step. As a starting guess for the Newton's method, we employ a constant velocity predictor. For more details on the method, the reader is referred to [12, 21]. In the present chapter, the classic Gauss-Legendre quadrature rule is employed to integrate the field variables over the elements. The linear system corresponding to Eq. (5.45) is solved via a standard LU decomposition with partial pivoting.

The validation of the implementation is presented in B.2.

## 5.2.2 Isogeometric discretization for axisymmetric monodomain

The weak form of the monodomain model (5.30) in this problem is approximated as:

$$v = \sum_{j=1}^{n_s} H_j(\theta^1) \hat{v}_j(t) \quad (5.47)$$

where the  $H_j$  basis function is obtained from the geometrical representation of the domain  $\Omega_{0e}$  after a suitable mesh refinement and  $\hat{v}_j$  is the corresponding control variable with  $j$  varying from 1 to the number of degrees of freedom  $n_s$ . Substituting Eq. (5.47) in the weak form (5.30) and using the same basis function  $H_i$  to approximate the test functions:

$$\delta v = \sum_{i=1}^{n_s} H_i(\theta^1) \delta \hat{v}_i, \quad (5.48)$$

we get the discrete isogeometric counterpart of the monodomain PDE. The following system of equations is obtained:

$$C_m M_{ij}^e \frac{d\hat{v}_j}{dt} + K_{ij}^e \hat{v}_j + \chi I_i^{ion} = \chi I_i^{app} \quad i = 1, \dots, n_s. \quad (5.49)$$

The matrices in the previous equation read:

$$M_{ij}^e = 2\pi \int_{\Omega_{e0}} H_i H_j \hat{r} dL, \quad (5.50)$$

$$K_{ij}^e = 2\pi \int_{\Omega_{e0}} \frac{\partial H_i}{\partial \theta^1} D^{11}(\theta^1) \frac{\partial H_j}{\partial \theta^1} \hat{r} dL, \quad (5.51)$$

$$I_i^{ion} = 2\pi \int_{\Omega_{e0}} H_i I^{ion}(v, G_k) \hat{r} dL, \quad (5.52)$$

$$I_i^{app} = 2\pi \int_{\Omega_{e0}} H_i I^{app}(\theta^1) \hat{r} dL. \quad (5.53)$$

System (5.49) is discretized in time by a semi-implicit scheme, where the diffusion term is treated implicitly and the reaction term explicitly, as this is believed to provide a satisfactory compromise between efficiency and stability [295, 179]. Indeed, the explicit treatment of the reaction term avoids the linearization of the ionic current at the cost of a restriction on the time step size due to the stability constraint.

In our implementation, the reaction term is discretized by means of an explicit second order Adams-Bashforth method, and the diffusion term is discretized by an implicit Crank-Nicholson method. The present scheme is outlined for the resolving time step  $m + 1$ , which refers to the discrete time  $t^{m+1} = (m + 1)\Delta t_e$ , with  $m$  being the discrete time counter and  $\Delta t_e = t^{m+1} - t^m$  the constant time step size chosen for the electrophysiological problem:

$$C_m M_{ij}^e \frac{\hat{v}_j^{m+1} - \hat{v}_j^m}{\Delta t_e} + \frac{1}{2} K_{ij}^e (\hat{v}_j^{m+1} + \hat{v}_j^m) + \frac{3}{2} \chi (I_i^{ion})^m - \frac{1}{2} \chi (I_i^{ion})^{m-1} = \chi (I_i^{app})^{m+1}, \quad (5.54)$$

which, rearranged for the time advancement, reads:

$$\left( C_m M_{ij}^e + \frac{\Delta t_e}{2} K_{ij}^e \right) \hat{v}_j^{m+1} = \left( C_m M_{ij}^e - \frac{\Delta t_e}{2} K_{ij}^e \right) \hat{v}_j^m - \frac{3\Delta t_e}{2} \chi (I_i^{ion})^m + \frac{\Delta t_e}{2} \chi (I_i^{ion})^{m-1} + \Delta t_e \chi (I_i^{app})^{m+1}. \quad (5.55)$$

In coupled electro-mechanical simulations the stiffness matrix  $K_{ij}^e$  must be recomputed at each time step to account for the changes in the conductivity (5.31) due to the deformation of the spatial reference frame. This feature represents a form of geometric mechano-electrical feedback [180, 179].

The integration of the ionic current by a Galerkin procedure (5.53) plays a fundamental role in the stability of the presented scheme, since the reaction term is treated explicitly and it represents the coupling term between the PDE and a set of stiff ODEs. The interpolation at the interior of the element is needed for the ionic current integration. Following the State Variable Interpolation (SVI) approach, we define the discrete values of gating variables at the control point location and, successively, they are interpolated at the generic quadrature points  $\theta_{gp}$  to get the integral (5.53):

$$\{I^{ion}(v, G_k)|_{\theta^1=\theta_{gp}}\} = I^{ion} \left( \sum_{j=1}^{n_s} H_j(\theta_{gp}) \hat{v}_j, \sum_{i=1}^{n_s} H_j(\theta_{gp}) \hat{G}_{k,j} \right). \quad (5.56)$$

Comparison of different ionic current interpolation strategies within an Isogeometric framework can be found in [179].

The system (5.55) is solved by a simple LU decomposition with partial pivoting. Afterwards, the computed value of transmembrane potential  $\hat{v}^{n+1}$  is used to solve the gating variable equations of the neuron model at each control point of the spatial discretization by means of an explicit fourth order Runge-Kutta method. Both reaction-diffusion equation and gating variable equations are advanced with the same time-step size.

In this chapter, several gating variables are modeled using discontinuous functions in time, for instance the neuron activation involves an Heaviside function of the potential, that depends on time. This reflects in a discontinuity in the spatial distribution of such variable, that can not be correctly captured using the SVI approach since the basis functions are continuous. Those variables are, therefore, treated using the so-called Gauss Integration approach (i.e., considering the variables as internal variables defined directly at the integration points). Mixing the approaches is affordable in uni-dimensional domains. However, an alternative approach to solve this issue at a reduced computational effort is investigated in Chapter 6.

The validation of the implementation is presented in B.3.

### 5.2.3 Electro-mechanical coupling

As often observed in cardiac simulations, the monodomain model requires a much finer grid than the mechanical sub-problem to handle the sharp front of the electrophysiological pulse. The optimal solution would be a gradient dependent refinement strategy for the electrophysiological discretization. However, this certainly requires a sophisticated computational framework. The NURBS discretization allows for an efficient implementation of two nested meshes. Indeed, the knot insertion algorithm preserves the geometry and the parametrization, enabling an information exchange by means of simple field evaluations at the Gauss point coordinates. For instance, the displacements are computed at the Gauss points of the electrophysiological mesh evaluating the basis functions  $N_i$  at the prescribed set of coordinates. In

fact, since the parametrization is preserved, a point is represented by the same parametric coordinates in both discretizations, avoiding complex projections between grids. Thanks to the linearity of Eqs. (5.47) and (5.35), such an operation comes at the cost of a matrix-vector multiplication, whose matrix can be computed just once in the pre-analysis stage.

The activation function is carried from the electrophysiological mesh to the mechanical discretization and vice-versa for the displacement field. However, in interpolating the field from a univariate to a bivariate domain an additional assumption on the spatial distribution is needed. Specifically, we assume a constant value of the activation function in the  $\theta^2$  direction, mimicking the actual muscle activation. In this regard, each problem is tackled with a suitably refined mesh, previously determined by uncoupled convergence analysis.

## 5.2.4 Finite difference scheme for the fluid problem

The flow field is solved via a centered difference discretization [296]. The moderate computational expense of finite differences allows to use a large number of nodes and to simulate multiple propulsive cycles. Moreover, the efficiency of the fluid solver coupled to an Isogeometric discretization for the solid was proven in [164].

The system of equation (5.33) is solved by means of a fractional step scheme, in the version proposed in [297]. First, a non-solenoidal intermediate velocity field is computed by advancing in time the momentum equation; then, a pressure-correction equation is solved to project the provisional field onto a solenoidal one. The momentum equation is integrated by means of a semi-implicit approach, where the implicit Crank–Nicholson scheme is employed for the viscous terms, and the three-step explicit Runge–Kutta scheme is used for the convective terms. The latter was found to guarantee a good accuracy at moderate CFL (Courant–Friedrichs–Lewy number) values for transitional flow simulations. This yields the discrete momentum equation of the  $i$ -th velocity component for the  $k$ -th Runge–Kutta substep to be:

$$\frac{\tilde{q}_i - q_i^k}{\Delta t} = -\alpha^k \frac{\partial p^k}{\partial x_i} + \beta^k \mathcal{H}_i^k + \gamma \mathcal{H}_i^{k-1} + \frac{\alpha^k}{2\text{Re}} \mathcal{L}_i (\tilde{q}_i + q_i^k) + f_i^k, \quad (5.57)$$

where the operators  $H_i$  and  $L_i$  contain the convective terms and the viscous terms, respectively. The time advancement coefficients for three substep levels are  $\alpha = [8/15, 2/15, 1/3]$ ,  $\beta = [8/15, 5/12, 3/4]$ ,  $\gamma = [0, -17/60, -5/12]$ . The computation of the IB forcing field  $f_i^k$  is addressed taking a preliminary fully explicit step for the purpose of interpolating the necessary field variables without further complications in the time scheme, as proposed in [298]. Subsequently, Eq (5.57) is solved for the increment  $\Delta q_i = \tilde{q}_i - q_i^k$ :

$$\left(1 - \frac{\Delta t \alpha^k}{2\text{Re}} \mathcal{L}_i\right) \Delta q_i = \left(-\alpha^k \frac{\partial p^k}{\partial x_i} + \beta^k \mathcal{H}_i^k + \gamma \mathcal{H}_i^{k-1} + \frac{\alpha^k}{2\text{Re}} \mathcal{L}_i q_i^k + f_i^k\right) \Delta t \quad (5.58)$$

The implicit treatment of term in Eq. (5.58) would the inversion of large sparse matrices. These are reduced to tridiagonal matrices by means of the approximate factorization [299] while introducing a factorization error  $\mathcal{O}((\Delta t)^3)$ , thus preserving the scheme accuracy in time.

Continuity is enforced by means of the auxiliary scalar field  $\phi$ , used to project the provisional velocity field  $\tilde{q}_i$  onto a divergence free-field. Thus, the final velocity and pressure fields at time  $n + 1$  can be evaluated as:

$$q_i^{k+1} = \tilde{q}_i - \alpha^k \Delta t \nabla \phi, \quad (5.59)$$

$$p^{k+1} = p^k + \phi - \frac{\Delta t \alpha^k}{2\text{Re}} \mathcal{L} \phi. \quad (5.60)$$

The scalar  $\phi$  is computed by taking the divergence of the previous equation and enforcing mass conservation. A Poisson equation is then obtained, reading:

$$\mathcal{L} \phi = \frac{1}{\alpha^k \Delta t} \frac{\partial q_i}{\partial x_i}. \quad (5.61)$$

A direct solution of the Poisson problem in (5.61) is preferred to fulfill the continuity equation without any numerical compromise. However, the computational efficiency of the resolution is enhanced by means of the eigen-decomposition of the discrete operator matrices. This technique, well suited in problems

where only the forcing term vary from step to step, allows to solve the system in (5.61) as a sequence of matrix multiplications and inversion of tridiagonal matrices [300].

The space discretization features follow the traces of the work by Verzicco and Orlandi [290], except that only the radial and the axial directions are resolved. The discrete analogues of the differential operators are obtained by straightforward second-order accurate centered finite differences. The field variables are located on staggered grids, whose beneficial effects in terms of accuracy are discussed in [290, 296].

### 5.2.5 Solid-fluid coupling

Following the approach proposed in [301], the forcing field is computed over a set of Lagrangian Markers (LM) located at the fluid-solid interface and then transferred back to the Eulerian nodes. The LM are distributed in the parametric space of the NURBS patch while requiring the distance between adjacent markers in the physical space to be comparable with that of the underlying Eulerian nodes. Numerical experiments in [164] suggested that a Lagrangian-to-Eulerian spacing ratio below 0.6 only provides a negligible reduction in flux error through the interface. Such an error is further reduced when considering the forcing iterations inherently obtained with the three steps Runge-Kutta scheme used to advance the fluid solution. As pointed out in [302], the repeated enforcement of the volume force  $f_i^k$  at each Lagrangian markers on a static contour leads to an improvement of the accuracy of the no-slip condition.

At the LM location the  $i$ -th forcing component  $F_i$  is evaluated as a body force, by the difference between the current LM velocity  $v_i$  and the interpolated velocity value  $Q_i$ :

$$F_i(\mathbf{r}_{LM}) = \frac{v_i - Q_i(\mathbf{r}_{LM})}{\Delta t}. \quad (5.62)$$

The interpolation procedure is performed with a Moving Least Squares approach which provides a smooth forcing field even with moving boundaries with minimal smoothing of the interface, especially when exponential weight functions are used [303, 304]. The interpolated  $i$ -th velocity at the marker location is thus computed by means of the transfer function  $\varphi$ :

$$Q_i(\mathbf{r}_{LM}) = \sum_{j=1}^{N_e} \varphi_j(\mathbf{r}_{LM}) (q_i)_j, \quad (5.63)$$

where  $N_e$  is the number of Eulerian nodes within a local support domain identified for the interpolation procedure. Time indices have been dropped for simplicity of notation. In two-dimensional axisymmetric simulations a 9 points support domain is employed. The same transfer function is used in the spreading of the volume forces (5.62), but including the scaling factor  $c_l$  that accounts for the discrete momentum conservation fulfillment. The volume force at the  $k$ -th Eulerian point location is thus evaluated as:

$$f_i^k = \sum_{l=1}^{N_l} c_l \varphi_l^k (F_i)_l, \quad (5.64)$$

where  $N_l$  indicates the number of Lagrangian points associated with the Eulerian point  $k$ . A detailed discussion about the properties of the transfer function  $\varphi_j$  and its application within IB methods for viscous flow simulations can be found in [305, 303]. It is worth pointing out that when considering  $q_1 = rv_1$  no differences occur in the MLS interpolation operators between plane 2D fields and 2D axisymmetric fields.

With the present IB treatment, the flow field across the surface presents a smooth transition layer whose thickness takes at most two Eulerian cells, as shown in [304] with 2D numerical experiments. Therefore, viscous and pressure loads contributing to the external body load  $F_i^{\text{ext}}$  in equation (5.37) are evaluated following the procedure thoroughly described in [303, 164]. The field variables are interpolated at a probe created along the outward-pointing normal from the surface and transported at the quadrature point laying on the surface by a simplified boundary layer equation. The probe length is selected as the averaged Eulerian cell size.

The validation of the implementation is presented in B.4.

### 5.2.6 Multiphysics solution algorithm

The computation of the action potential at the  $n$ -th time step requires the knowledge of the body configuration, whereas the solution of the elastic problem needs the action potential at the same time step. The prediction of the flow field and of the hydrodynamic loads at the  $n$ -th time step likewise requires the knowledge of the motion of the body and vice versa. The adopted time-advancement algorithm consists of a sequential approach, where each sub-problem is solved in a segregated fashion and data are progressively transferred. Once the monodomain model is solved, the resulting transmembrane potential field  $v(\mathbf{r}, t)$  is used to compute the active strain tensor  $\mathbf{F}_a$  at the quadrature points. The former, together with the hydrodynamic loads computed in the previous fluid step, are set as input field for the elastic analysis. Once obtained the deformed configuration, the immersed boundary procedure allows to enforce the no-slip condition at the fluid-solid interface, and thus to advance the flow field in time.

The comparison of the characteristic time scale of each sub-problem allows to build a computationally affordable time-advancement method. The action potential is expected to exhibit a conduction velocity of about 50 cm/s, whereas the characteristic velocity scale of the fluid-elastic problem is 1.5 cm/s. In this connection, the time-step size of the simulation is dictated by the electrophysiological sub-problem. Furthermore, the latter suffers from strict stability requirements since the action potential represented in Fig. 5.4 needs the solution of a 40 ms duration wave front. We therefore employ a sub-stepping technique where the mechanical and fluid-dynamic configurations are updated every  $M$  electrophysiological time steps.

We further simplify the fluid-structure problem by choosing the density of the solid body equal to  $\rho_s = 1200 \text{ kg/m}^3$ . This is a precaution needed for the sequential fluid-structure algorithm to handle a low solid-to-fluid density ratio without incurring in inaccurate results [306], although the high percentage of body water of real jellyfish entails that  $\rho_s = 1000 \text{ kg/m}^3$  would be a more realistic choice. However, the numerical experiments proposed in [307] suggest that such a variation does not significantly affect the swimming kinematics.

## 5.3 Coupled simulation of the jellyfish swimming

In this section we simulate the swimming of a  $a_{ex} = 3 \text{ cm}$  Aurelia Aurita [308]. To this end, we address two problems: first, we define a suitable mesh and time step size for the sub-problems. Afterwards, we set the conductivity coefficient such that the wave propagation fits the experimental observations.

### 5.3.1 Mesh and time step calibration

The minimal time and space scales of the coupled problem are those involved in the propagation of the electrophysiological pulses. Therefore, the sensitivity of the solution to the discretization features needs to be carefully addressed to find out the necessary refinement level. We tested several element and time step sizes against the electrophysiological stimulation of a static axisymmetric emi-ellipsoid corresponding to the subumbrellar surface of the bell. The action potential is triggered by an external current applied in the region within parametric coordinates  $0.96 \leq \theta^1 \leq 0.98$  for 1 ms, in order to mimic the activity of the Rhopalia.

The domain  $\Omega_e$  is discretized using quadratic elements, with element numbers  $n_e = \{200, 400, 800, 1600, 3200\}$  and time-step sizes  $\Delta t_e = \{0.02, 0.01, 0.005, 0.0025\}$  [ms]. We define the error directly using the Action Potential Duration time (APD). The APD is measured as the time interval  $T_d$  by which the depolarization front at  $v = 0.0 \text{ mV}$  moves from the parametric locations  $\theta^1 = 0.2$  to  $\theta^1 = 0.8$ . Two points aside from the boundaries are considered in order to minimize the influence of boundary conditions on the results. We thus compute the APD time error  $e_d$  as:

$$e_d = \frac{T_d - (T_d)_{\text{ref}}}{(T_d)_{\text{ref}}}, \quad (5.65)$$

assuming the solution from the most refined case  $(T_d)_{\text{ref}}$  as reference solution. The error convergence is shown by a combined space-time plot, whereas corresponding data are reported in table 5.1: Distinctly, the APD error converges with decreasing time step size and decreasing mesh size and justifies the choice of our reference solution. Different convergence trend are observed in time and space as a consequence

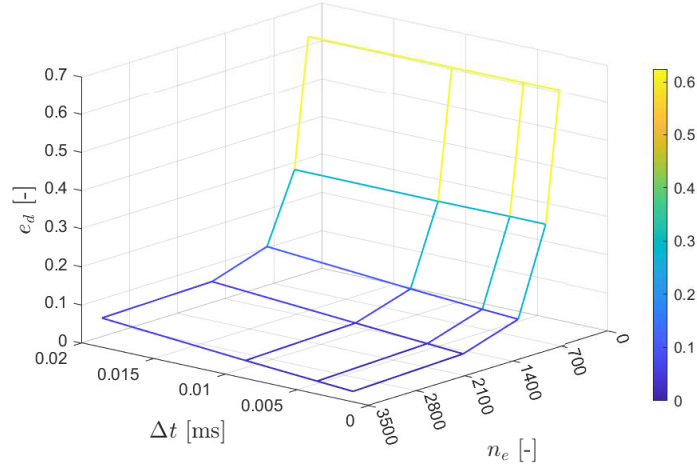


Figure 5.6: Convergence of the time-delay error depending on time step size  $\Delta t$  and mesh elements  $n_e$ . The colorbar refers to the magnitude of the time-delay error.

	$\Delta t_e = 0.02$ [ms]	$\Delta t_e = 0.01$ [ms]	$\Delta t_e = 0.005$ [ms]	$\Delta t_e = 0.0025$ [ms]
$n_e = 200$	0.6222	0.6232	0.6240	0.6246
$n_e = 400$	0.2820	0.2808	0.2821	0.2820
$n_e = 800$	0.1025	0.0735	0.0610	0.0554
$n_e = 1600$	0.0553	0.0286	0.0155	0.0092
$n_e = 3200$	0.0491	0.0196	0.0065	-

Table 5.1: Summary of the space-time convergence study of the electrophysiological stimulation of the static subumbrellar surface. The APD error is shown as a function of the time step size  $\Delta t_e$  and the element number  $n_e$ .

of the different theoretical accuracy provided by the discretizations. We observe that with  $n_e > 800$  and  $\Delta t_e < 0.01$  ms a converged solution can be obtained for the electrophysiological sub-problem.

In the jellyfish simulation, the elastic domain is discretized by  $35 \times 6$  cubic elements in the  $\theta^1$  and  $\theta^2$  directions, respectively (see Fig. 5.3 (b)), since such a mesh provide a sufficient accuracy when compared to reference solution, as shown in B.2.2. Conversely, 34 cubic elements are nested within each elastic element to fulfill the convergence requirement discussed for the electrophysiological solution. The monodomain model is advanced in time with the time step-size  $\Delta t_e \phi = 2.5 \times 10^{-6}$ , in order to achieve the time-convergence threshold (see Fig. 5.6). The structural and fluid solutions are updated every 100 electrophysiological time steps ( $M = 100$ ), namely by  $\Delta t \phi = 2.5 \times 10^{-4}$ , since the activation function is observed to exhibit less than 1% overall variation over this time window. For the fluid problem, we employ a rectangular domain of extension  $[0, 10a_{ex}]e_1 \otimes [0, 26a_{ex}]e_2$ . The Cartesian grid is uniformly refined only in the subset  $[0, 2.4a_{ex}]e_1 \otimes [5, 22a_{ex}]e_2$  with local grid size  $\Delta = a_{ex}/250$ , whereas a significant grid stretching is implemented in the far-field region. The Eulerian grid resolution was chosen to get 10 grid point within the marginal flaps of the bell, although less grid points are necessary to accurately capture the vortex dynamics.

### 5.3.2 Conductivity coefficient calibration

Most of the Scyphozoans present action potential waves traveling with a conduction velocity in between 45 cm/s and 1 m/s, depending on the species and the specimen maturity [309]. To the best of the author's knowledge, no conductivity value is available in the literature for the MNN of a Scyphozoan jellyfish. However, several researches report values of conduction velocity of approximately 50.0 cm/s [287, 289, 310, 279]. These data refer to the speed of propagation of the mechanical wave, that is assumed as a proxy for the speed of propagation of the electrical signal. The activation is triggered by the nervous system while the evolution is governed by the muscle properties, resulting in pulses of different duration [311].

In the present chapter, we seek for a conductivity value that matches a conduction velocity equal to  $CV = 47.4$  cm/s, as prescribed in the most recent investigation [279]. To this extent we apply a simple bisection algorithm to the  $CV-D_0$  function, similarly to what we have done in Chapter 3.

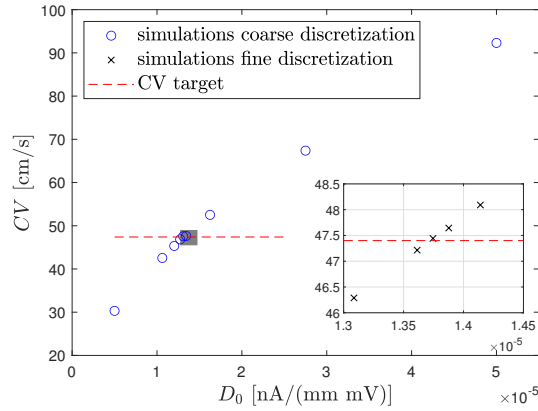


Figure 5.7: Tuning of the conductivity coefficient  $D_0$  by a bisection method.

In a generic axisymmetric surface, the wave front is curved, and the  $CV$  undergoes spatial variations. To overcome this issue, we conduct the simulations on a cylindrical domain (radius  $R = 15.0$  mm and length  $L = 20.0$  mm) activated by enforcing the action potential value  $v = -69.0$  mV at one end. The resulting wave front propagates in a planar fashion as the radius is constant through the entire domain, indeed. The conduction velocity is measured by the time delay of the wave arrival at two points 4.0 mm and 16.0 mm far from the stimulation site. Although the wave arrival is usually defined using half of the upstroke amplitude, we select time corresponding to  $v = +20$  mV to avoid the uncertainties due to the inflection in the depolarization time history (see Fig. 5.4).

The bisection method employs a fast analysis (600 elements,  $p = 2$ ,  $\Delta t = 0.01$  ms) to obtain a preliminary estimation of the conductivity, whereas a more refined discretization (2400 elements,  $p = 2$ ,  $\Delta t = 0.0025$  ms) computes an accurate result. The iteration-wise results are summarized in Fig. 5.7. According to our findings, the conductivity coefficient value corresponding to the target conduction velocity is  $D_0 = 1.375e - 05$  nA/(mm mV).

### 5.3.3 Simulation results

The swimming simulations is initialized by applying a  $0.1$  nA/mm<sup>3</sup> current for  $0.1$  ms on the still jellyfish body immersed in a quiet fluid with homogeneous no-slip boundary conditions except the symmetry axis. The stimulation is applied within a narrow  $0.4$  mm subset of the electrophysiological domain at the marginal flap hanging.

The jellyfish is placed in the initial position with the uppermost point of the bell at  $y = 10 a_{ex}$  and it is allowed to run 10 propulsive cycle, where a periodic advancement velocity is achieved within 6 to 8 strokes.

Instantaneous flow fields are displayed in Fig. 5.8 by vorticity contours. The contraction of the bell margin generates a counter-rotating vortex pair, already observed in oblate species [312], which takes a physiologically relevant role in the swimming process. In the contours of Fig. 5.8 the starting vortex ring takes negative vorticity values, whereas the stopping vortex ring has a positive vorticity. The former is generated by the roll up of the shear layer occurring with the reduction of the bell marginal section, whereas the latter takes shape from the flow squeezed in between the starting vortex and the bell margin in the recoil stage. The starting vortex travels away from the bell, while the stopping vortex is entrained inside the subumbrellar cavity. The interaction of such vortices with the background fluid motion induced by the bell translation generate a difference in the relative tangential velocity between the inner part and the outer part of the vortex ring.

The circulation analysis proposed in Fig. 5.9 confirms that the stopping vortex produces larger circulation values with a delayed peak [308, 266] in favor of the propulsion. According to experimental

and computational observations [308, 267] the clockwise flow rotation inside the bell cavity generates a localized pressure increment that provides the body with additional thrust in the passive motion stage.

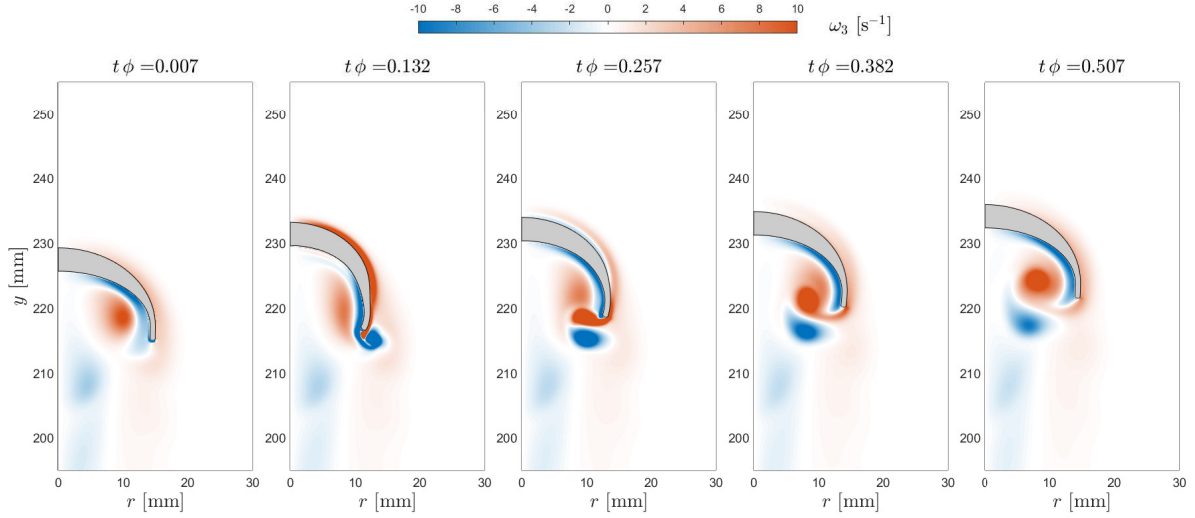


Figure 5.8: Instantaneous vorticity contour and body configuration at five subsequent instants of the rowing cycle in the periodic swimming regime. An electrophysiological pacing frequency of  $\phi = 0.5$  [Hz] was considered.

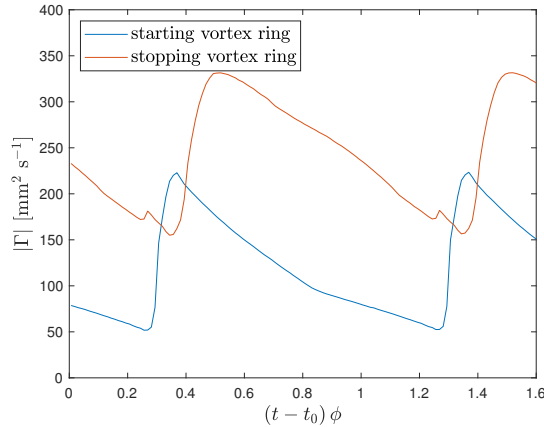


Figure 5.9: time-traces of circulation,  $\Gamma$ , of the starting and stopping vortex rings within the last propulsive cycle for the baseline case.

## 5.4 Summary

In this chapter, we have presented a complete framework to investigate the performance of the jellyfish swimming. Our calibrated model takes as an input the firing frequency of the pacemaker cells only, returning time histories for both the nerve activity, muscle contraction, bell displacement and fluid flow. Our solver offers the possibility of disentangle the effects of different features on the propulsion efficiency. For instance, the effect of the bell shape may be investigated leaving the force generated by a muscle and the stimulation frequency unchanged. This kind of investigations may provide useful insights in the jellyfish biophysics and in the design of bio-inspired swimmers.

In our solver, we enforce axisymmetric conditions to limit the computational burden improving the realism of the simulation with respect to pure 2D solvers. Furthermore, we have extended the neuron

model, developed for a discrete setting, to the continuous distribution adding the formulation for the force generation. Such a model is not standard requiring the definition of several internal variables at the quadrature points. In a mono-dimensional manifold the computational effort is limited, but in multi-dimensional domains more advanced techniques, presented in Chapter 6, may be adopted.

For the problem setup analyzed in this chapter, volumetric locking does not affect the accuracy of the simulation significantly. In case of severe effects, the techniques presented in Chapter 8 may be used combining different meshes for the electrophysiological and structural domains.

Eventually, we note that the framework herein presented may be used to simulate the interaction of active tissue with fluids in different contexts, for instance the contraction of the heart ventricle.



## Part II

# Novel Collocation-based numerical methods for efficient simulation of active tissue systems



## Chapter 6

# Isogeometric Collocation approach to cardiac electrophysiology

We propose an Isogeometric Collocation approach to an efficient solution of the *Monodomain* reaction-diffusion equation. The strong formulation, compared to standard Galerkin methods, easily models tissue composed of different cell types. Indeed, the state variables of the cells are treated as internal variables defined at the collocation points. Such a feature removes the hypotheses on their spatial distribution highlighted in Chapter 5. Moreover, the Collocation approach enables an effective discretization of the reactive term reducing the computational effort due to the integration of the cellular model.

We demonstrate the capabilities of the proposed approach with several numerical examples, ranging from the propagation of a planar wave front, to the simulation of complex tissue activation patterns and of the propagation of an action potential in a layered tissue.

Cardiomyocytes, namely, the cells composing the cardiac tissue, constantly experience a voltage difference across their membrane due to the unbalance of ion concentrations between the intracellular and extracellular spaces. A sufficiently strong electrical stimulation induces a variation in the potential and generates ionic fluxes through the cellular membrane, giving rise to a complex series of phenomena governing the tissue and the heart functionality.

Numerical simulations of such a complex electrical activity in physiological and pathological conditions are useful for a number of reasons, such as an improved understanding of pathological causes and conditions, drug discovery enhancement, and precision medicine development [3].

From the computational prospective, investigations of the cardiac tissue behavior, including the accurate description of ionic fluxes, require the solution of a complex system of equations with fine spatial and temporal discretizations. This makes organ-scale numerical simulations computationally demanding, even for high performance computing platforms.

Therefore, various strategies for the reduction of the computational expense have been introduced. Among them, the electrochemical response of the cell membrane [201] is often targeted to reduce the problem complexity, while efficient numerical schemes, both in space [244, 313] and time [295], are formulated to reduce the numerical burden. Space discretization is typically performed by means of finite element (or similar) approaches [242, 314, 82], based on the weak form of the considered differential problem.

In the present chapter, we instead propose a different approach, i.e., Isogeometric Collocation, for the spatial discretization of the PDEs describing the electrophysiological problem [83, 179]. To the best of our knowledge, this is the first investigation of electrophysiological phenomena based on an Isogeometric Collocation method [315]. The main idea behind Collocation method is to avoid the computationally demanding integration that arises from the weak formulation [31], solving the strong form of the PDEs discretized via highly continuous B-splines. Based on our findings, the proposed method is suitable for both (i) the reduction of the computational effort associated to the integration of the cellular model, and (ii) the simulation of a tissue composed by different types of cardiomyocytes.

This chapter is organized as follows: the governing equations of the electrophysiology are given in Section 3.1.5 as well as the reactive-term Galerkin modeling-strategies. However, in Section 6.1, we present a different splitting operator adopted in this chapter. In Section 6.2 we discuss the proposed Iso-

geometric Collocation approach for spatial discretization, whereas the discretization in time is addressed in Section 6.3. Details on the post-processing procedure are presented in Section 6.4, while numerical examples investigating the features of the proposed Collocation approaches are described in Section 6.5. Conclusion and future research directions are finally outlined in Section 6.6.

## 6.1 Godunov splitting scheme

*Monodomain* formulation involves a reaction-diffusion equation and the Godunov splitting operator represents an alternative method (cf. Section 3.1.5) for solving it. This algorithm consists of the decoupling of the reaction term (i.e., the ionic current term) and the diffusion term (i.e., the term that involves the divergence operator) in two sub-steps to be solved within a single time step. We note that the Godunov operator is not strictly necessary for the implementation of the proposed technology, as it relies on a spatial and not on a time discretization.

The first step of the Godunov splitting operator is to solve the (local) reactive part of the *Monodomain* problem:

$$\begin{cases} \frac{\partial v}{\partial t} = -\frac{1}{C_m} I^{ion}(\mathbf{x}, v, w^1, \dots, w^k, c^1, \dots, c^q) & (6.1a) \\ \frac{\partial w^r}{\partial t} = m_w^r(\mathbf{x}, v, w^1, \dots, w^k) & \forall r = 1, \dots, k & (6.1b) \\ \frac{\partial c^s}{\partial t} = m_c^s(\mathbf{x}, v, w^1, \dots, w^k, c^1, \dots, c^q) & \forall s = 1, \dots, q & (6.1c) \end{cases}$$

to obtain the gating variables and the ionic concentrations at time  $t_{n+1} = t_n + \Delta t$ , while the transmembrane potential defines the initial conditions of the subsequent diffusion step:

$$\begin{cases} \frac{\partial v}{\partial t} = \frac{\lambda}{\chi C_m (\lambda + 1)} \nabla \cdot (\mathbf{D} \nabla v) + \frac{I^{app}}{\chi C_m} & \text{in } \Omega \setminus \partial\Omega & (6.2a) \\ \mathbf{n} \cdot \mathbf{D} \nabla v = 0 & \text{on } \partial\Omega, & (6.2b) \end{cases}$$

as schematically shown in Figure 6.1. As noted in [199], the Godunov splitting operator is a continuous operator that does not introduce any discretization in time. Therefore, at the moment, we are not introducing any time integration scheme.

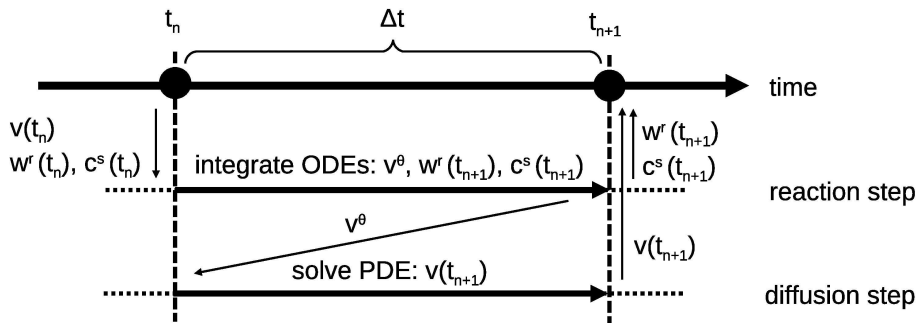


Figure 6.1: Schematic representation of the solution procedure using the Godunov splitting operator:  $v(t_n)$ ,  $w^r(t_n)$ , and  $c^s(t_n)$  represent the transmembrane potential and the state variables at time  $t_n$ , while  $v(t_{n+1})$ ,  $w^r(t_{n+1})$ , and  $c^s(t_{n+1})$  represent the same quantities at time  $t_{n+1}$ . Moreover,  $v^\theta$  represents the initial condition of the diffusion step.

In the remaining part of this work, we adopt the Godunov splitting scheme as it guarantees a convenient implementation of the *Monodomain* model, suitable for large scale simulations. The adoption of a low-order time-splitting scheme offers significant computational advantages and the Godunov method allows to deal with the most sophisticated cell membrane models with limited magnification of the computational burden. Furthermore, it allows a simple implementation for parallel computing [316], which

represents a widespread tool in cardiac electromechanics, and for all these reasons this is the method adopted in this chapter. However, the accuracy of the time scheme can be augmented to second order by switching, e.g., to the Strang splitting scheme [199] or to higher orders using, e.g., implicit-explicit schemes [295], with minimal changes to the presented formulation.

## 6.2 Spatial discretization via Isogeometric Collocation

Isogeometric Galerkin approach has proven to be particularly effective for the solution of the *Monodomain* [82] as well as the bidomain formulation [317, 83] and the cardiac electromechanics [179]. Unfortunately, the implementation of the mixed ICI-SVI[244] (see Section 3.1.5), developed for the finite element method is not efficient in the Isogeometric context because the basis function support is larger. Moreover, spline functions are not interpolatory and, consequently, the projection of the cellular properties (i.e., the coefficients of the ODEs) on the basis functions may be needed, if they vary within the domain.

To overcome these limitations, we propose an Isogeometric Collocation scheme for the electrophysiological problem. In particular, our main aim is to develop a spatial solution scheme that reduces the number of ODE systems solved in the reaction step avoiding the selection of the wave front employed in the mixed ICI-SVI method.

We present the Collocation approach starting from the description of the basis functions employed for the analysis and the fundamental concepts of the methodology. Subsequently, we discretize the reaction and the diffusion steps. We then formulate two different Collocation approaches, considering different hypothesis for the ionic current approximation, as in the standard Galerkin method. The comparison between such Collocation approaches is then left to a subsequent section. The description of the spatial discretization, for the sake of clarity, is carried out with the index notation. When the equations are discretized also in time, the index notation becomes excessively complex and the matrix notation is instead preferred. For this reason we conclude this section recasting the semi-discrete equations in matrix format.

### 6.2.1 Methodological approach for space discretization

Isogeometric analysis employs smooth and highly continuous splines defined on a parametric space both for the description of the geometry, as in Computer Aided Design systems, and for solving the equations in an isoparametric fashion. The high continuity enables the direct discretization of the strong form of partial differential equations through a Collocation method. In the present chapter, we investigate the performance of this kind of solution scheme in the electrophysiological context.

The Collocation approach, described in [315, 318], implies the discretization of the partial differential equations directly in strong form imposing that the solution satisfies the PDE at selected points, namely the collocation points [30]. For the present chapter, we locate these points at the images of the tensor-product Greville abscissae (defined below) of the knot vectors, as described in [319, 188].

**Adopted Isogeometric Collocation scheme** Greville abscissae are points in the parametric space which, in the parametric direction  $\xi$ , are defined as:

$$\tilde{\xi}_\beta = \frac{\xi_{\beta+1} + \dots + \xi_{\beta+p}}{p}, \forall \beta = 1, \dots, m_\xi, \quad (6.3)$$

with similar relations holding for all parametric directions. The tensor product between the univariate Greville abscissae coordinates gives the three-dimensional coordinates in the cubic parametric space  $\tilde{\xi}_\gamma, \forall \gamma = 1, \dots, m$ . We note that, contrarily to control points, Greville abscissae have a counterpart in the physical domain, as the Gauss points in standard isoparametric approaches. The locations in the physical space depend on the control point coordinates and the basis function values at  $\tilde{\xi}_\alpha$ :

$$\tilde{\mathbf{x}}_\alpha = N_s(\tilde{\xi}_\alpha) \mathbf{B}_s. \quad (6.4)$$

Analogously, the transmembrane potential at the collocation points is defined as:

$$\tilde{v}_\alpha(t) = N_s(\tilde{\xi}_\alpha) \hat{v}_s(t) \quad (6.5)$$

or collecting the results at all collocation points in matrix notation:

$$\tilde{\mathbf{v}}_{\dagger}(t) = \mathbf{M}\hat{\mathbf{v}}(t); \quad (6.6)$$

where the components  $M_{\alpha s}$  of the matrix  $\mathbf{M}$  are:

$$M_{\alpha s} = N_s \left( \tilde{\boldsymbol{\xi}}_{\alpha} \right). \quad (6.7)$$

Note that the collocation matrix  $\mathbf{M}$  is square and the existence of its inverse is guaranteed by the location of the Greville abscissae in the parametric space.

The transmembrane potential  $\tilde{\mathbf{v}}$  evaluated at the collocation points located in the internal part of the domain  $\Omega \setminus \partial\Omega$ , involved in Eq. (6.2a), is a subset of  $\tilde{\mathbf{v}}_{\dagger}$  computed using the rectangular sub-matrix  $\bar{\mathbf{M}}$ , that is the selection of the rows of matrix  $\mathbf{M}$  associated with the collocation points  $\tilde{\boldsymbol{\xi}}_{\alpha}, \forall \alpha \in \Omega \setminus \partial\Omega$ :

$$\tilde{\mathbf{v}}_{(g \times 1)} = \bar{\mathbf{M}}_{(g \times m)(m \times 1)} \hat{\mathbf{v}}, \quad (6.8)$$

where  $m$  is the number of control points and  $g = (m_{\xi} - 2) \times (m_{\eta} - 2) \times (m_{\zeta} - 2)$ .

In the following, we identify a generic quantity calculated at the collocation points with a tilde, while we use a hat for control variables computed at the complete set of control points.

The approximated transmembrane potential has to satisfy the strong form of the electrophysiological problem (3.7) at the collocation points, which involves second order differential operators. Consequently, the Collocation scheme requires higher basis function continuity than in standard weak formulations involving only first order differential operators. However,  $C^1$ -continuity can be easily achieved using at least quadratic B-splines.

The key idea of the Collocation method is to avoid the integration arising from the weak formulation, being a computationally-demanding operation [31]. In particular, in the context of electrophysiology, it gives advantages on the treatment of the ionic current term and of the associated system of ODEs. It is worth noting that also the computational effort for matrix formation is significantly reduced. Building the collocation stiffness matrix requires only one evaluation per basis function [31] instead of computations at each quadrature point. This may lead to improved performance even in the context of coupled electro-mechanical simulations, where the stiffness matrix is recomputed at every time step.

## 6.2.2 Semi-discrete Collocation scheme for the reaction step

We propose two different approaches for the discretization of the reaction step: the first is called *State Variables Interpolation - Collocation* (SVI-C) and computes the state variables at collocation points, while the second one is called *Ionic Current Interpolation - Collocation* (ICI-C) and computes the cellular variables at control points.

The differences between the two approaches are limited to the reaction step. Indeed, both approaches share the same solution scheme of the diffusion step, that requires the initial values only at the collocation points inside the domain, because Neumann and Dirichlet boundary conditions do not involve time derivatives.

**State Variable Interpolation - Collocation approach** The Collocation discretization requires that the transmembrane potential satisfies Eq. (6.1a) at collocation points:

$$\begin{aligned} N_b \left( \tilde{\boldsymbol{\xi}}_{\alpha} \right) \dot{\hat{v}}_b &= \dot{\tilde{v}}_{\alpha}(t) = -\frac{1}{C_m} I^{ion}(\tilde{\mathbf{x}}_{\alpha}, t) \\ I^{ion}(\tilde{\mathbf{x}}_{\alpha}, t) &= I^{ion}(\tilde{\mathbf{x}}_{\alpha}, \tilde{v}_{\alpha}(t), \mathbf{w}_{\alpha}^r(t), \mathbf{c}_{\alpha}^s(t)) \\ \forall r &= 1, \dots, k, \quad \forall s = 1, \dots, q, \end{aligned} \quad (6.9)$$

where  $\mathbf{w}_{\alpha}^r(t) = w^r(\mathbf{x}_{\alpha}, t)$  and  $\mathbf{c}_{\alpha}^s(t) = c^s(\mathbf{x}_{\alpha}, t)$  are the state variables computed at collocation points. Consequently, it solves one, point-wise defined, ODE system (6.1) for each collocation point. Since the diffusion step requires the initial conditions only at internal control points, the computational effort of the SVI-C approach is approximatively equal to the one of the most efficient Galerkin method: the ICI approach. Indeed, the number of ODE systems and ionic current computations is equal to the number of

internal collocation points  $g$  (that is smaller than the number of degrees of freedom and Gauss points), i.e.,  $\forall \alpha = 1, \dots, g$ :

$$\begin{cases} \dot{\tilde{\mathbf{v}}}_\alpha(t) = -\frac{1}{C_m} I^{ion}(\tilde{\mathbf{x}}_\alpha, \tilde{\mathbf{v}}_\alpha(t), \tilde{\mathbf{w}}_\alpha^1(t), \dots, \tilde{\mathbf{w}}_\alpha^k(t), \tilde{\mathbf{c}}_\alpha^1(t), \dots, \tilde{\mathbf{c}}_\alpha^q(t)) & (6.10a) \\ \dot{\tilde{\mathbf{w}}}_\alpha^r(t) = m_w^r(\tilde{\mathbf{x}}_\alpha, \tilde{\mathbf{v}}_\alpha(t), \tilde{\mathbf{w}}_\alpha^1(t), \dots, \tilde{\mathbf{w}}_\alpha^k(t)) & \forall r = 1, \dots, k & (6.10b) \\ \dot{\tilde{\mathbf{c}}}_\alpha^s(t) = m_c^s(\tilde{\mathbf{x}}_\alpha, \tilde{\mathbf{v}}_\alpha(t), \tilde{\mathbf{w}}_\alpha^1(t), \dots, \tilde{\mathbf{w}}_\alpha^k(t), \tilde{\mathbf{c}}_\alpha^1(t), \dots, \tilde{\mathbf{c}}_\alpha^q(t)) & \forall s = 1, \dots, q & (6.10c) \end{cases}$$

If the state variables at points on the boundary are needed for the post-processing (see Sec. 6.4), the number of computation of ICI and SVI-C approaches becomes exactly equivalent.

We also note that the SVI-C approach does not underlie any hypothesis on the interpolation of the state variables and that the algorithm solves the ODEs at points in the physical domain.

Nowadays segmentation software, such as [320], render the diagnostic images into a file accessible to simulators through a collection of punctual information, as shown in [1, 4, 242]. If those information are needed as continuous fields (or, equivalently, as control values) for analysis purpose, they have to be projected on B-spline basis functions. This is an additional, and possibly complex, pre-processing step. As the ODEs are solved directly at physical points, the Collocation method avoids the projection of the cellular properties on the parametric space if the control points are chosen such that the images of the collocation points coincide with the rendering points. This simplifies the simulation process, especially in anatomically and biologically detailed models.

One way to avoid the interpolation of the cellular properties and the pre-processing projection in Isogeometric Galerkin method (or any other method that uses non-interpolatory basis functions) is the Gauss Integration approach, but, unfortunately, the computational effort is greater because the number of ODE systems that have to be solved is equal to the number of Gauss points. Instead, the main SVI-C advantage is the reduced computational burden: it solves approximately the same number of equations of the ICI approach with a reduced number of modeling assumptions, avoiding complex pre-processing steps.

Future studies may investigate the computation of the reaction step in parallel using a Graphics Processing Unit (GPU) since the point-wise nature of the SVI-C scheme may be beneficial.

**Ionic Current Interpolation - Collocation approach** We investigate also this approach to verify if the advantages and disadvantages of the ionic current interpolation are recovered also in the context of Isogeometric Collocation method.

As in a standard Galerkin method, the ionic current term is approximated using the additional hypothesis:

$$I^{ion}(\mathbf{x}, t) = \mathbf{N}(\mathbf{x}) \hat{\mathbf{I}}^{ion}(t). \quad (6.11)$$

Introducing this hypothesis in the Collocation scheme, the discretization of Eq. (6.1a) becomes:

$$\begin{aligned} \mathbf{N}_b(\tilde{\boldsymbol{\xi}}_\alpha) \dot{\hat{\mathbf{v}}}_b &= -\frac{1}{C_m} \mathbf{N}_b(\tilde{\boldsymbol{\xi}}_\alpha) \hat{\mathbf{I}}_b^{ion}(t) \\ \hat{\mathbf{I}}_b^{ion}(t) &= I^{ion}(\mathbf{B}_d, \hat{\mathbf{v}}_b(t), \hat{\mathbf{w}}_b^r(t), \hat{\mathbf{c}}_b^s(t)) \\ \forall r &= 1, \dots, k, \forall s = 1, \dots, q, \forall d = 1, \dots, m, \end{aligned} \quad (6.12)$$

where we have highlighted the dependence on the position through the coordinates  $\mathbf{B}_d$  of all the  $m$  control points, since the ionic current is no more computed at physical points in the domain. Eq. (6.12) can be rewritten in vector form as:

$$\dot{\hat{\mathbf{v}}} = -\frac{1}{C_m} \hat{\mathbf{I}}^{ion}, \quad (6.13)$$

as in a standard ICI approach. Since the ODE systems are solved at the control points, the ICI-C approach can be interpreted as the Collocation counterpart to the standard Galerkin *Ionic Current Interpolation* method.

The transmembrane potential initial conditions for the diffusion step are interpolations of the complete set of control variables, as shown in Eq. (6.8). Therefore, we have to solve one ODE system for each

control point, i.e.,  $\forall b = 1, \dots, m$  :

$$\begin{cases} \dot{\hat{v}}_b(t) = \frac{-1}{C_m} I^{ion}(\mathbf{B}_1, \dots, \mathbf{B}_m, \hat{v}_b(t), \hat{w}_b^1(t), \dots, \hat{w}_b^k(t), \hat{c}_b^1(t), \dots, \hat{c}_b^q(t)) & (6.14a) \\ \dot{\hat{w}}_b^r(t) = m_w^r(\mathbf{B}_1, \dots, \mathbf{B}_m, \hat{v}_b(t), \hat{w}_b^1(t), \dots, \hat{w}_b^k(t)) & \forall r = 1, \dots, k \quad (6.14b) \\ \dot{\hat{c}}_b^s(t) = m_c^s(\mathbf{B}_1, \dots, \mathbf{B}_m, \hat{v}_b(t), \hat{w}_b^1(t), \dots, \hat{w}_b^k(t), \hat{c}_b^1(t), \dots, \hat{c}_b^q(t)) & \forall s = 1, \dots, q. \quad (6.14c) \end{cases}$$

For the same discretization, ICI-C requires a number of operations slightly greater than SVI-C in the analysis phase, but the main modeling disadvantage relies on the direct dependence of the system of equation on the spatial position. Indeed, the projection of the material properties at collocation points is trivial only in the case of constant properties. Note that this is a peculiarity inherited by the ICI hypothesis, not from the Collocation scheme.

Although it may seem that the considerations on the SVI-C and ICI-C approaches depend on the splitting operator, we show in C.3 that similar considerations are true also in the case of an Implicit-Explicit time integration scheme that avoids the splitting operator.

### 6.2.3 Semi-discrete Collocation scheme for the diffusion step

The second step of the Godunov splitting solves the diffusion equation and it is common to both SVI-C and ICI-C approaches. The conduction phenomenon is governed by the tensor  $\mathbf{D}$ , that, for the sake of clarity, we assume to be uniform in space. However, the case of non-uniform conductivity tensor (see C.1) is of great interest in organ-level simulations because the effect of the fiber orientation is not negligible. The diffusion step involves second-order differential operators and we introduce the following notation for derivatives:

$$\frac{\partial(\bullet)}{\partial x_i} = \bullet_{,i}. \quad (6.15)$$

to obtain a more compact notation. The Collocation scheme then discretizes the diffusion equation (6.2) as follows:

$$\begin{cases} N_s(\tilde{\xi}_\alpha) \dot{\hat{v}}_s = \frac{\lambda}{\chi C_m (\lambda + 1)} D_{ij} N_{b,ji}(\tilde{\xi}_\alpha) \hat{v}_b + \frac{1}{\chi C_m} I^{app}(\tilde{\xi}_\alpha) & \forall \tilde{\xi}_\alpha \in \Omega \setminus \partial\Omega \quad (6.16a) \\ n_i D_{ij} N_{s,j}(\tilde{\xi}_\alpha) \hat{v}_s = 0, & \forall \tilde{\xi}_\alpha \in \partial\Omega_N \quad (6.16b) \end{cases}$$

where the derivatives with respect to the physical coordinates are computed from the derivatives with respect to the parametric coordinates (see C.2).

In Collocation methods, Dirichlet and Neumann boundary conditions are explicitly enforced. Therefore, the matrix resulting from the discretization is divided in to two parts: one associated to the internal collocation points and one associated to those belonging to the boundary. For the sake of completeness, we present the discretization of Dirichlet boundary conditions. Indeed, they are often used to initiate the propagation of an action potential forcing the solution to assume the imposed values  $\tilde{v}_\alpha^*$  at selected points:

$$N_s(\tilde{\xi}_\alpha) \hat{v}_s = \tilde{v}_\alpha^*(t), \forall \tilde{\xi}_\alpha \in \partial\Omega_D. \quad (6.17)$$

### 6.2.4 Summary of the Collocation schemes in matrix form

In this section, we simply recast the presented equations in matrix format to obtain a more concise notation. We define the elements of the rectangular stiffness matrix  $\mathbf{K}_{\alpha s}$ :

$$\mathbf{K}_{\alpha s} = \frac{\lambda}{\chi C_m (\lambda + 1)} D_{ij} N_{s,ij}(\tilde{\xi}_\alpha), \forall \tilde{\xi}_\alpha \in \Omega \setminus \partial\Omega, \quad (6.18)$$

and we encapsulate the contributions of the Neumann boundary conditions in  $\mathbf{R}_{\alpha s}$ :

$$\mathbf{R}_{\alpha s} = n_i D_{ij} N_{s,j}(\tilde{\xi}_\alpha), \forall \tilde{\xi}_\alpha \in \partial\Omega_N. \quad (6.19)$$

The matrix  $\mathbf{M}^*$ , that imposes the Dirichlet boundary conditions, is the rectangular sub-matrix obtained from the selection of the rows of the matrix  $\mathbf{M}$  related to the collocation points on  $\partial\Omega_D$ . This selection is similar to the extraction of the matrix  $\bar{\mathbf{M}}$  in eq. (6.7).

The resulting equations of the SVI-C reaction step are:

$$\begin{cases} \dot{\tilde{\mathbf{v}}} = -\frac{1}{C_m} \tilde{\mathbf{I}}^{ion} & (6.20a) \\ \dot{\tilde{\mathbf{w}}}^r = \tilde{\mathbf{m}}_w^r & \forall r = 1, \dots, k & (6.20b) \\ \dot{\tilde{\mathbf{c}}}^s = \tilde{\mathbf{m}}_c^s, & \forall s = 1, \dots, q & (6.20c) \end{cases}$$

and the ones for ICI-C approach are:

$$\begin{cases} \dot{\hat{\mathbf{v}}} = -\frac{1}{C_m} \hat{\mathbf{I}}^{ion} & (6.21a) \\ \dot{\hat{\mathbf{w}}}^r = \hat{\mathbf{m}}_w^r & \forall r = 1, \dots, k & (6.21b) \\ \dot{\hat{\mathbf{c}}}^s = \hat{\mathbf{m}}_c^s, & \forall s = 1, \dots, q & (6.21c) \end{cases}$$

while the diffusion step yields:

$$\begin{cases} \bar{\mathbf{M}}\dot{\hat{\mathbf{v}}} = \mathbf{K}\hat{\mathbf{v}} + \frac{1}{\chi C_m} \tilde{\mathbf{I}}^{app} & \text{in } \Omega \setminus \partial\Omega & (6.22a) \\ \mathbf{R}\hat{\mathbf{v}} = \mathbf{0} & \text{on } \partial\Omega_N & (6.22b) \\ \mathbf{M}^*\hat{\mathbf{v}} = \tilde{\mathbf{v}}^* & \text{on } \partial\Omega_D & (6.22c) \end{cases}$$

As in Galerkin-based Isogeometric analysis, the advantages of high-continuity basis functions come at the cost of a denser structure of the collocation stiffness matrix. This is also inherently associated with a condition number that rapidly grows when the mesh is refined and/or the polynomial degree is raised as it happens for standard finite elements [321]. Consequently, a careful choice of the iterative algorithm for the resulting linear system is required not to spoil the cost-to-accuracy gain. In the present formulation, we employ a full orthogonalization method (FOM). Arnoldi-based algorithms were found to be suitable for reaction-diffusion problems both as preconditioner and solver [322]. Efficient preconditioning techniques for Isogeometric Collocation methods represent a current avenue of research [323].

## 6.3 Time discretization

The time is not yet discretized [199] and a time integration schemes is still needed [295] at this point. Usually, an explicit, conditionally-stable, scheme is used to discretize the reaction step, while for the diffusion step an implicit scheme is considered to increase stability of the overall method. In the present chapter, we adopt the Explicit Euler and the Implicit Euler methods for the reaction and the diffusion steps, respectively; as already done in [201].

### 6.3.1 Discrete *Monodomain* approximation employing the SVI-C approach

We discretize the system (6.20) by means of Explicit Euler method:

$$\begin{cases} \tilde{\mathbf{v}}^\theta = \tilde{\mathbf{v}}_n - \frac{\Delta t}{C_m} \tilde{\mathbf{I}}_n^{ion} & (6.23a) \\ \tilde{\mathbf{w}}_{n+1}^r = \tilde{\mathbf{w}}_n^r + \Delta t \tilde{\mathbf{m}}_w^s & \forall r = 1, \dots, k & (6.23b) \\ \tilde{\mathbf{c}}_{n+1}^s = \tilde{\mathbf{c}}_n^s + \Delta t \tilde{\mathbf{m}}_c^s & \forall s = 1, \dots, q & (6.23c) \end{cases}$$

This scheme computes the gate variables and the ionic concentrations at the next time step at collocation points while the transmembrane potential  $\tilde{\mathbf{v}}^\theta$ , according to the Godunov operator, acts as an initial condition for Eq. (6.22a).

In the discretization of the diffusion step we highlight that: (i) as the initial conditions are already computed at the collocation points, the interpolation presented in Eq. (6.5) and applied in Eq. (6.27) is avoided during the integration. (ii) Dirichlet and Neumann boundary conditions do not involve time derivatives. Consequently, the Implicit Euler method applied to Eq. (6.22a) leads to the following linear system:

$$\begin{bmatrix} \bar{\mathbf{M}} - \Delta t \mathbf{K} \\ \mathbf{R} \\ \mathbf{M}^* \end{bmatrix} \hat{\mathbf{v}}_{n+1} = \begin{bmatrix} \tilde{\mathbf{v}}^\theta \\ \mathbf{0} \\ \tilde{\mathbf{v}}_{n+1}^* \end{bmatrix} + \frac{\Delta t}{\chi C_m} \begin{bmatrix} \tilde{\mathbf{I}}_{n+1}^{app} \\ \mathbf{0} \\ \mathbf{0} \end{bmatrix} \quad (6.24)$$

whereas the interpolation

$$\tilde{\mathbf{v}}_{n+1} = \bar{\mathbf{M}}\hat{\mathbf{v}}_{n+1} \quad (6.25)$$

is performed only after Eq. (6.24) to obtain the initial conditions for the next time step.

### 6.3.2 Discrete *Monodomain* approximation employing the ICI-C approach

In the ICI-C method, instead, the Explicit Euler method integrates the gate variables and the ionic concentrations at the control points:

$$\begin{cases} \hat{\mathbf{v}}^\theta = \hat{\mathbf{v}}_n - \frac{\Delta t}{C_m} \hat{\mathbf{I}}_n^{ion} & (6.26a) \\ \hat{\mathbf{w}}_{n+1}^r = \hat{\mathbf{w}}_n^r + \Delta t \hat{\mathbf{m}}_{w_n}^r & \forall r = 1, \dots, k & (6.26b) \\ \hat{\mathbf{c}}_{n+1}^s = \hat{\mathbf{c}}_n^s + \Delta t \hat{\mathbf{m}}_{c_n}^s & \forall s = 1, \dots, q. & (6.26c) \end{cases}$$

In order to solve the diffusion step, the initial conditions  $\hat{\mathbf{v}}^\theta$ , dictated by the Godunov operator, are interpolated at internal collocation points, as:

$$\tilde{\mathbf{v}}^\theta = \bar{\mathbf{M}}\hat{\mathbf{v}}^\theta. \quad (6.27)$$

This equation highlights why the ICI-C approach requires the solution of an higher number of ODE systems with respect to the SVI-C for the solution of the diffusion step (6.24).

## 6.4 State variables recovery in the post-processing phase for the SVI-C approach

The SVI-C approach computes all the transmembrane potential control variables everywhere, while the gate variables and the ionic concentrations are evaluated only at the internal collocation points.

If the SVI-C approach is employed for the analysis, the description of the state variable fields requires a post-processing reconstruction because their values are known at a discrete set of points.

One possibility for the approximation of the gate variables and the ionic concentrations is the projection on the basis functions employed for the analysis. The inversion of the interpolation (6.6) requires the knowledge of the state variables everywhere. Therefore, the set of information is completed via integration of the scalar Eqs. (6.10b) and (6.10c)  $\forall \tilde{\xi}_\alpha \in \partial\Omega$ . Successively, the solution of the linear systems:

$$\mathbf{M}\hat{\mathbf{w}}^r = \tilde{\mathbf{w}}_\dagger^r \quad \mathbf{M}\hat{\mathbf{c}}^s = \tilde{\mathbf{c}}_\dagger^s \quad (6.28)$$

provides the control variables, concluding the description of all the fields in the whole domain<sup>1</sup>.

The previously presented procedure can be avoided if the computation of the gate variables and ionic concentrations is needed at only few specific points. As the transmembrane potential is known in the whole domain, the cellular model can be directly integrated at the selected points.

The development of a unified post-processing procedure is an interesting source for future studies.

## 6.5 Numerical experiments

We verify the efficacy of the proposed Isogeometric Collocation approaches by means of three different types of numerical experiments, that are simulated using our solver based on the library NUTILS [52].

The first test models the action potential propagation in a uni-dimensional cable. With this experiment, we investigate the differences between the algorithms of the SVI-C and the ICI-C approaches, and the convergence in space and time. We also compare the obtained results with others present in the literature.

The second experiment is devoted to simulate a tissue with cellular properties that vary in the domain to prove that the SVI-C method can directly tackle this kind of problems, as shown in Sec. 6.2.2.

The third set of tests is aimed at verifying the ability of the method in reproducing highly curved wave fronts that generate complex tissue activation patterns.

<sup>1</sup>Solution of systems (6.28) can be avoided using a linear interpolation of the values at the collocation points.

For the sake of simplicity, we have employed the same cellular model in all simulations, i.e., the Minimal Ventricular Model [201] being one of the simplest model representing the complex spike-dome action potential shape of the epicardio, as well as the midmyocardial and the endocardial action potential morphology. The reader is referred to the paper by Bueno-Orovio et al. [201] for more details and for the complete set of ordinary differential equations; we simply note that this model is recast in our notation using three gate variables and none ionic concentration.

To directly compare our test results with the literature [201], we have chosen our data such that the rescaled conduction coefficient is equal to  $1.171 \text{ cm}^2/\text{s}$ . In particular we set:  $\lambda = 1.5$ ,  $\chi = 229.7 \text{ mm}^{-1}$ ,  $C_m = 0.01956 \mu\text{F}/\text{mm}^2$ , and an isotropic conductivity tensor characterized by  $D = 0.8769 \mu\text{F}/(\text{mm ms})$ .

### 6.5.1 Cable model

In the first numerical test we solve the *Monodomain* equation on a 2 cm long cable made of epicardial tissue. A stimulus applied at the left end of the cable triggers an action potential whose propagation is analyzed.

In this test we (i) compare the SVI-C and ICI-C approach accuracy, (ii) compare our implementation results with findings from other authors, and (iii) verify the convergence of the method. As the main difference between SVI-C and ICI-C relies on the approximation of the ionic current, we directly check it, while we use the conduction velocity (CV) for comparison with other authors' results. Indeed, this parameter is often used for analysis because it can be experimentally measured and used for summarizing several features of the heart activity [253].

The protocol [201] for conduction velocity determination establishes that the CV refers to an action potential propagating in a tissue paced at 1 Hz up to steady-state conditions. The period of time elapsed between the repolarization and the successive stimulus is called diastolic interval and affects the conduction velocity. In our test, we compute the conduction velocity of the stimulus after a diastolic interval of 400 ms, triggered applying a tension (cf. Eq. (6.17)) of -32 mV, greater than the stimulation threshold, for 2 ms at the left end. Moreover, at the right end (and at the left end when it is not stimulated) we impose no-flux boundary conditions. For the analyzed problem no analytical solution is available. To assess the convergence of the cable model, we compare it with 1D and 3D reference solutions. We simulate the action potential propagation in a 2 cm long cable ( $2 \times 0.0125 \times 0.0125 \text{ cm}^3$  parallelepiped in the 3D model) with stimuli and no-flux boundary conditions set to obtain a planar traveling wave. The reference solutions are obtained using the SVI-C approach: the 3D solution uses a degree  $p=4$ , a knot span size  $h = 2.5 \times 10^{-2} \text{ mm}$ , and a time step size  $dt = 6.25 \times 10^{-4} \text{ ms}$ , whereas the 1D model employs a more refined discretization in space and time as it is used for more detailed convergence studies of a dynamic problem ( $p = 6$ ,  $h = 3.125 \times 10^{-3} \text{ mm}$ ,  $dt = 1.25 \times 10^{-4} \text{ ms}$ ).

In order to reproduce as close by as possible the numerical experiments presented in [201], we compute the conduction velocity analyzing the simulated transmembrane potential in the middle of the cable, as shown in Fig. 6.2(a). Given the time history, we identify the wave arrival instant with the fast upstroke of the action potential related to the fast inward sodium current. In other words, we select the time characterized by the highest value of derivative, as explained in [324].

Our reference solutions predict conduction velocities  $CV_{ref} = 77.6 \text{ cm/s}$  and  $CV_{ref} = 79.9 \text{ cm/s}$  for the 3D and the 1D models, respectively. The difference between the computed results is mainly due to the different time discretization. However, both are in agreement with previous numerical simulations [201, 325] and with the experimental range reported in [201].

**Comparison between SVI-C and ICI-C** Comparison between the SVI and ICI approaches for standard Galerkin methods are usually conducted in terms of the approximated CV. Conversely, a detailed study [244] has highlighted that in the conduction velocity calculation several errors can compensate each other, giving rise to misleading results. To avoid these confusing factors, we compare the time histories of the ionic current and of the diffusive term because they govern the time derivative of the transmembrane potential. In particular, we focus on the wave front arrival because, as shown in [244], the interpolation (6.11) mostly affects this phase.

Fig. 6.2 shows the time histories of ionic current, diffusion term, and potential derivative in the middle of the cable during the wave arrival.

The SVI-C approach (see Fig. 6.2(c)) better approximates the 3D reference solution (reported in Fig. 6.2(b)) than the ICI-C (Fig. 6.2(d)). In particular, in SVI-C the maximum absolute value of the ionic

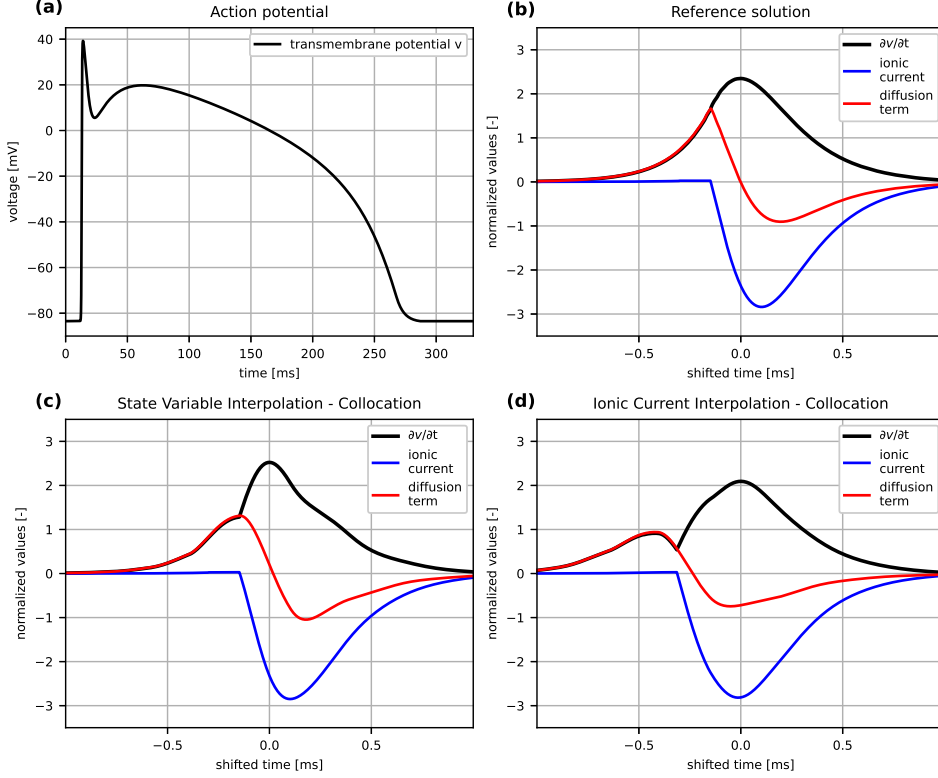


Figure 6.2: Results in the middle of the cable. (a) Action potential predicted by the minimal ventricular model. (b, c, and d) Focus on the differences in the results of the SVI-C and the ICI-C approach. The curves are normalized as presented in [201]. As the conduction velocity depends on the spatial and time discretization, time is shifted so that the wave front arrival occurs at  $t=0$  ms, avoiding inconsistency between the reference 3D solution (b) and the solution given by the coarser 1D mesh  $h = 0.2$  mm and  $dt = 0.00125$  ms for SVI-C (c) and ICI-C (d) approaches.

current occurs after the wave arrival and the transmembrane potential derivative increases monotonically before its maximum.

These results are calculated using a knot span size equal to the element size used in [201]. For finer discretizations both methods converge to the reference solution, as shown in Fig. C.2.

This test highlights the effect of the additional hypothesis (6.11) on the results of the electrophysiological problem. Based on our findings, the ICI-C has no advantages with respect to the SVI-C approach, neither in the accuracy nor in the reduction of computational effort. For this reason, the remaining part of the paper focuses only on the latter method.

**SVI-C convergence** To assess the convergence of the SVI-C method, we compare the conduction velocity of several discretizations with our 1D reference solution. Fig. 6.3 shows the convergence in space and time of the conduction velocity error, defined as:

$$CV_{err} = \frac{|CV - CV_{ref}|}{CV_{ref}}, \quad (6.29)$$

for different basis function degrees.

For a knot span size  $h \leq 0.1$  mm all the curves predict a relative error smaller than 1% and therefore they are suitable for realistic simulations. The convergence under h-refinement, Fig. 6.3(a) shows that all the curves converge toward the same result, characterized by a residual error due to the more refined time step size used in the reference solution. A high basis function degree stabilizes the trend providing a converged solution for a greater knot span size. The anomalous convergence of quadratic and cubic basis functions is due to sign cancellation in the error definition. Indeed,  $p = 4$ ,  $p = 5$ , and  $p = 6$  show

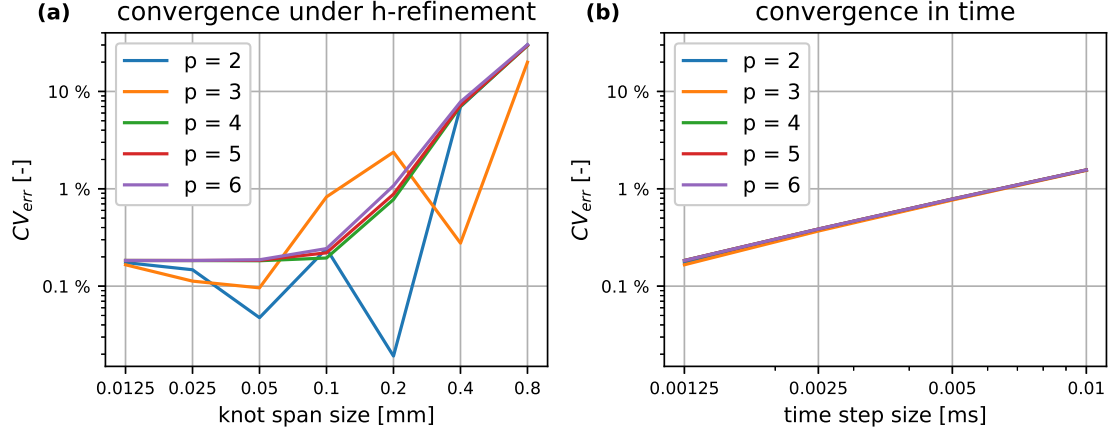


Figure 6.3: Error on the conduction velocity for the cable model compared to the 1D reference solution ( $CV=79.9$  cm/s), as defined in Eq. (6.29). (a) Convergence under h-refinement ( $h = 0.8, 0.4, 0.2, 0.1, 0.05, 0.025, 0.0125$  mm) for a fixed time step size  $dt = 0.00125$  ms. (b) Convergence in time ( $dt = 0.01, 0.005, 0.0025, 0.00125$  ms) for a fixed knot span size  $h = 0.0125$  mm.

a monotonic convergence, while  $p = 2$  and  $p = 3$  oscillate around the solution. Moreover, the decrease in the accuracy of  $p = 3$  with respect to  $p = 2$  reflects the trend already observed for an Isogeometric Collocation approach in convergence analysis on elasticity problems [30]. The logarithmic scale in the error axis provides an easier visualization of the convergence path. For the sake of completeness, we show the convergence path in a semi-logarithmic plot in C.4.

The convergence in time, Fig. 6.3(b), confirms the implementation correctness as all the curves are almost overlapped and their slope is equal to 1, in agreement with the theoretical convergence rate of a first order method.

## 6.5.2 Action potential propagation in layered tissue

The SVI-C approach models directly a non-homogeneous material, without any projection of the material parameters on the basis functions: to prove it, we now simulate a layered cardiac tissue.

The human left ventricle tissue structure is a collection of different cell types organized in stacked layers. In the transmural direction, from the interior to the exterior, they are arranged in three layers: the endocardium, the midmyocardium, and the epicardium. The proposed example studies a simplified hexahedral geometry with constant stratification.

The isolated (i.e., no-flux on the boundary) domain ( $20 \times 10 \times 10 \text{mm}^3$ ) shown in Fig. 6.4(a) is stratified in the Z direction and the layer-thickness is taken from the average values reported in [242]: endocardium consisting of 17% of the thickness, midmyocardium 42% and the epicardium 41%. The action potential is triggered at the left face ( $X=0$ ) constraining the transmembrane potential to 20 mV for 5 ms. On the mid-plane XZ (plane A in Fig. 6.4(a)) we select three points, one per layer, to analyze the different shapes of the simulated action potentials, as reported in Fig. 6.4(b).

**Convergence of the action potential results** We assess the capabilities of the proposed approach evaluating the results at the three selected points highlighted in Fig. 6.4(a, c). We investigate the convergence of the error, defined as:

$$V_{err} = \frac{\int_0^{T_{max}} |v(\mathbf{x}, t) - v_{ref}(\mathbf{x}, t)| dt}{\int_0^{T_{max}} |v_{ref}(\mathbf{x}, t)| dt} \Bigg|_{\mathbf{x}=\mathbf{x}_p}, \quad (6.30)$$

for quadratic and quartic basis functions under  $h$ -refinement. The reference solution  $v_{ref}$  is calculated using knot span size  $h = 0.05$  mm,  $p = 4$ , and  $dt = 0.01$  ms. The effectiveness of this discretization was proven for the 1D model.

We note that, due to the boundary conditions and to the distribution of the material properties, the solution is invariant in the Y direction. To prove that, we have performed two analysis: the first with a discretization with the same knot span size along the three directions ( $p = 2$ ,  $h = 0.1$  mm in X, Y and Z), while the second has knot spans along Y that are 10 times larger ( $p = 2$ ,  $h = 0.1$  mm in X and Z,  $h_Y = 1$  mm). The error is in the order of  $10^{-12}$  and therefore we employ only 10 knot spans in the Y direction to reduce the computational burden in the presented analysis.

Fig. 6.4(d) shows the error convergence for the endocardial, midmyocardial, and epicardial tissue and the comparison with the convergence rates 2 and 4 for quadratic and quartic basis functions, respectively, although we note that no convergence rate is guaranteed for this problem, especially if the cellular properties are discontinuous.

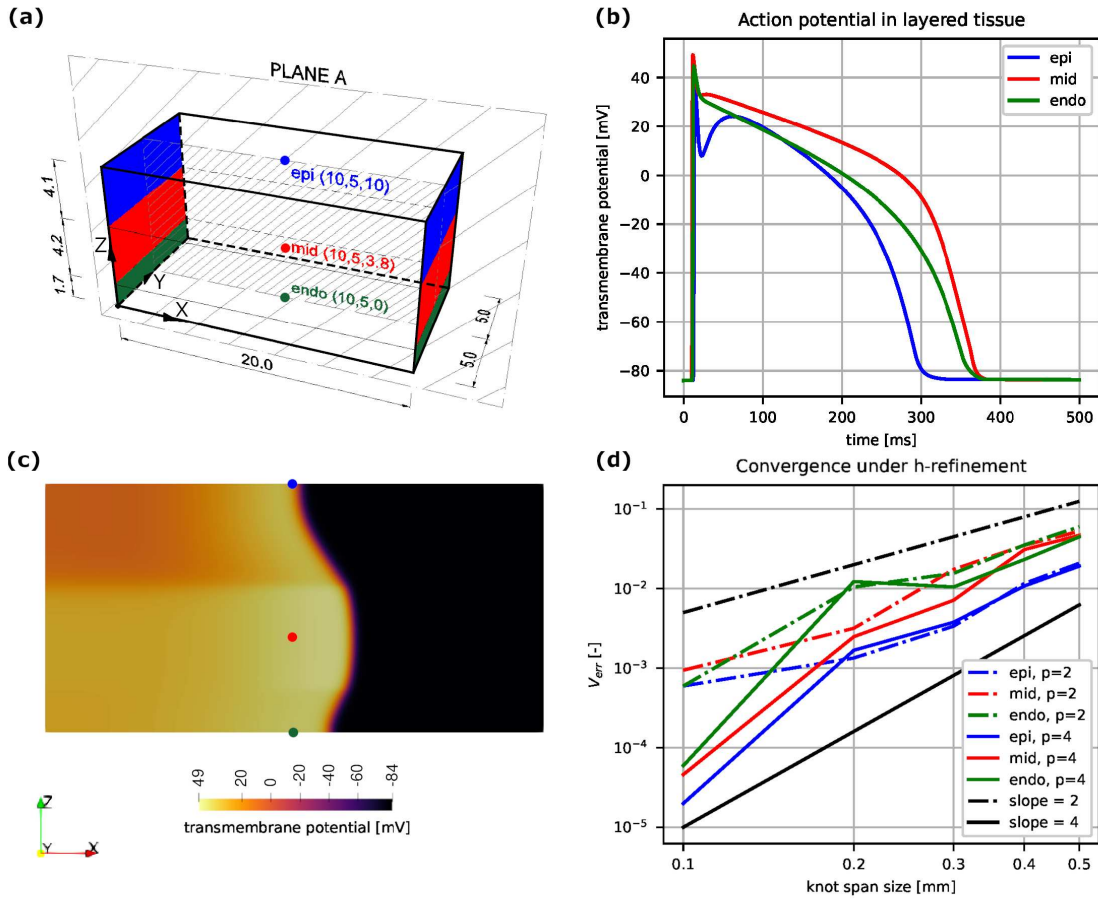


Figure 6.4: Action potential propagation in a layered tissue. (a) Schematic representation of the hexahedral domain composed by three layers. Two opposite faces are colored to show the tissue distribution: in blue we represent the epicardium, in red the midmyocardium, and in green the endocardium. The plane A selects a surface inside the body where the transmembrane potential is depicted in panel (c). Three points on this surface identify the locations where the action potential and its convergence are presented in panels (b) and (d). Measures and point coordinates are expressed in millimeters. (b) Reference solution of the action potentials propagating in the three different tissues. (c) Contour plot of the reference solution representing the transmembrane potential on the selected plane inside the body, at time  $t = 13$  ms. (d) Convergence of the error, defined in Eq. (6.30), under h-refinement ( $h = 0.5, 0.4, 0.3, 0.2, 0.1$  mm) at the three reference points for quadratic ( $p = 2$ ) and quartic ( $p = 4$ ) basis functions.

### 6.5.3 Curved activation patterns

In the previous examples we have simulated planar, or almost planar, wave fronts. In this section, we verify the ability of the approach in simulating curved wave fronts generating complex activation patterns. We propose two tests: (i) simulation of a curved 3D wave front with a qualitative comparison with the finite element software Chaste [326], (ii) simulation of spiral wave dynamics, as presented in [201].

**Simulation of a curved 3D wave front** The finite element software Chaste<sup>2</sup> is a well-established tool for electrophysiological simulations [326]. The proposed test is inspired by that reported in the Chaste documentation: a subset ( $x \in (0, 1)$  mm,  $y \in (0, 1)$  mm,  $z \in (0, 1)$  mm) of an isolated cube (with side of 3 mm) made of endocardial tissue is stimulated with an applied current to trigger an action potential. The wave propagates in all directions originating a fully 3D curved front.

In Fig. 6.5(a) we show the wave front calculated with SVI-C and in Fig. 6.5(b) the action potential at the reference point **P** is represented.

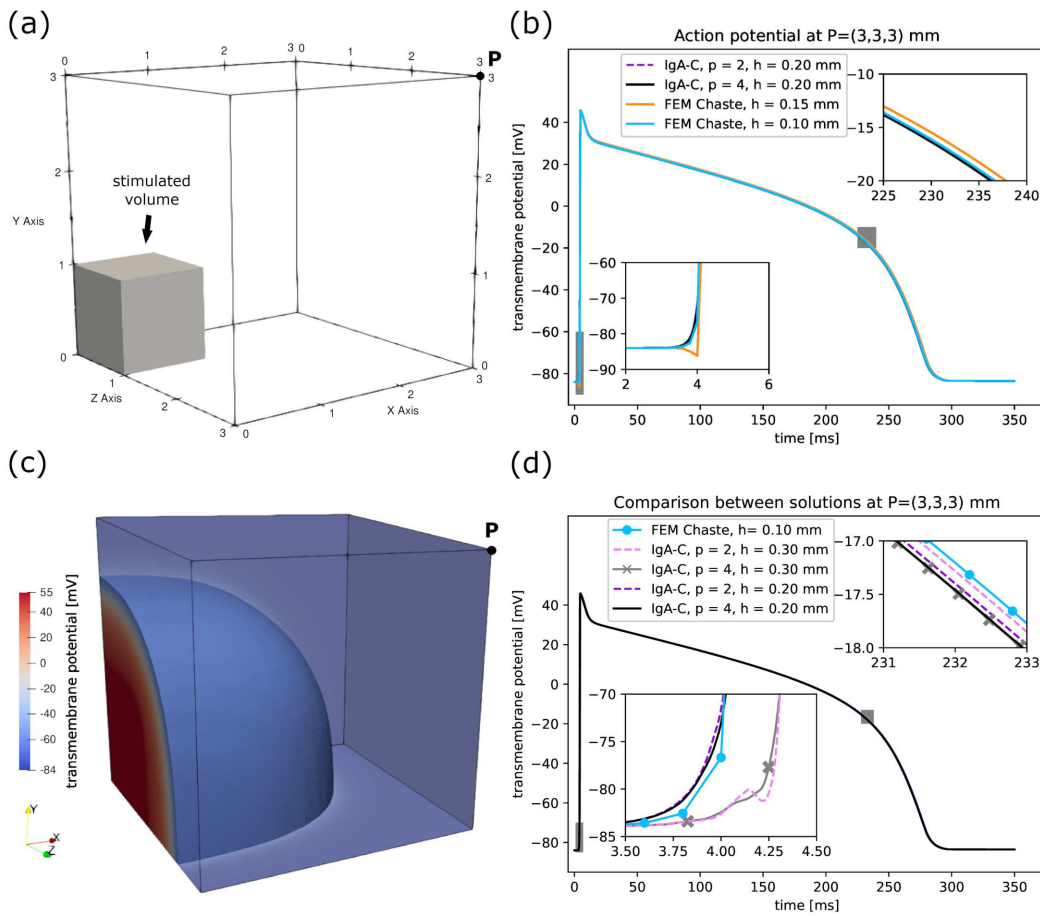


Figure 6.5: Simulation of a curved wave front in a cubic domain. (a) Schematic representation of the geometry. (b) Comparison of the action potentials predicted by our implementation (IgA-C) and by the software Chaste. In the insets we highlight the beginning of the depolarization and the kink before the repolarization. Our solutions are calculated using the SVI-C approach and  $dt = 0.005$  ms, while the Chaste implementation uses linear tetrahedral finite elements and the same time step size. (c) Contour plot of the transmembrane potential where we highlight the curved wave front ( $v \geq -60$  mV) at time  $t = 1.25$  ms. (d) Comparison between SVI-C solutions; note that the scales of insets are different compared to those of panel (b).

<sup>2</sup>We present a qualitative comparison between our implementation and Chaste since a rigorous comparison is out of the scope of this paper.

The action potentials predicted by the different methods are in excellent agreement, and the Iso-geometric Collocation scheme seems more stable at the beginning of the upstroke, even for coarser discretizations. We ascribe this result to the greater stability properties of B-splines.

In Fig. 6.5(d), four simulations, performed using quadratic and quartic B-splines,  $h = 0.2$  mm and  $h = 0.3$  mm (i.e., a knot span size equal to two and three times the reference finite element size, respectively), show the accuracy and the stability of the method. The knot span size affects the solution accuracy mainly at the beginning of the upstroke, whereas the solutions computed with quartic splines are more stable and more accurate at the smooth repolarization kink.

**Simulation of spiral wave dynamics** In this test, we simulate a spiral wave in the epicardial tissue, originated by an applied current. The simulation protocol presented in [326] dictates that an action potential is initiated at the left end of the hexahedral domain ( $70 \times 140 \times 0.2$  mm) as in the layered tissue test. After 340 ms an applied current depolarizes a part of the tissue ( $x \in (0, 35)$  mm,  $y \in (0, 120)$  mm,  $z \in (0, 0.2)$  mm). The tissue cannot be re-stimulated immediately after the first action potential, as explained in [201]. Therefore, the second wave starts propagating as shown in Fig. 6.6 at time  $t = 0.35$  s and  $t = 0.45$  s. After a prescribed period of time, the tissue returns excitable and the wave can propagate in it, originating a self-sustained spiral wave.

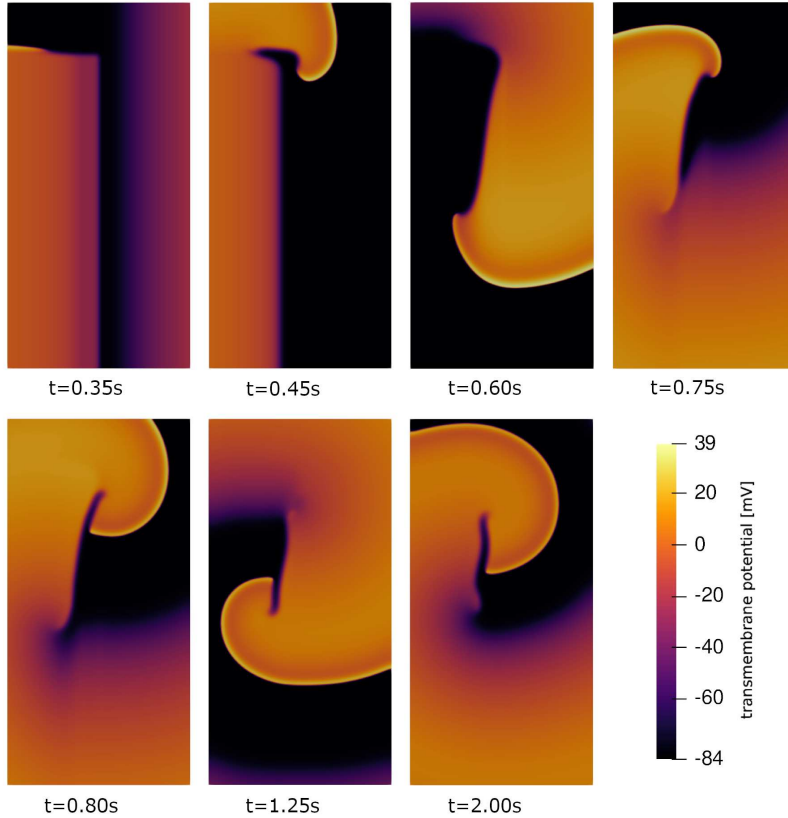


Figure 6.6: Simulation of a spiral wave on a hexahedral domain. The transmembrane potential [mV] on the plane XY at  $Z = 0$  mm is represented.

For this simulation we use quadratic basis functions, knot span size  $h = 0.2$  mm, time step size  $dt = 0.01$  ms, and no-flux boundary conditions, as presented in [201].

Fig. 6.6 shows several snapshots taken from the simulation results. We can clearly recognize the linear notch produced by the spiral wave. Our findings are qualitatively in good agreement with the results presented in [201].

## 6.6 Summary

The present chapter is an introductory investigation on the performance of the Isogeometric Collocation method applied to the *Monodomain* approximation for the simulation of electrophysiology problems.

A standard Galerkin finite element method with direct integration on the reactive term (GI) is often excessively demanding for full scale analysis. For this reason two alternative approaches for ionic current term treatment were developed in the context of finite elements: the SVI and the ICI. The latter is preferred for its reduced computational cost, but it was proven to be less accurate. To overcome this limitation, mixed SVI-ICI method was proposed [244].

Our method moves in a different direction: we employ highly regular B-splines to discretize in space the differential equations directly in the strong form, according to the Isogeometric Collocation concept.

We propose two approaches, namely, SVI-C and ICI-C, differentiated by the hypothesis on the ionic current field. Both require approximately the same computational effort of the Galerkin ICI approach for the solution of the reaction term.

The ICI-C enforces an additional hypothesis on the ionic current approximation, as in standard ICI, but in this case without any benefit, neither in the accuracy nor in the computational effort reduction or modeling strategy simplification. Indeed, the SVI-C approach is more accurate and directly models non homogeneous tissues. Moreover, we have proven the SVI-C ability in reproducing complex activation pattern, as shown in the presented numerical tests.

For these reasons we assert that the SVI-C approach is an appealing method for electrophysiological simulations, but a more detailed comparison with isogeometric Galerkin and standard finite elements would be informative. The computational efficiency of the proposed method can be fully exploited in the context of biophysically detailed membrane models and organ-scale simulations, where the spatial variability of the conductivity tensor plays a relevant role. The myocardial fiber arrangement leads to an anisotropic action potential propagation with principal conductivity directions variable in the domain. The isoparametric mapping used for the geometry should be adopted for the description of the fiber orientation, too, in order to enable the computation of the derivatives of the diffusivity tensor by means of basis function differentiation. In pathological conditions, such as myocardial ischemia, the conductivity tensor exhibits abrupt variations. Further investigations should address the ability of Isogeometric Collocation in modeling such discontinuous material properties using the multi-patch technology, as already done for elasticity problems [30].

In coupled cardiac electro-mechanics, the stiffness matrix of the electrophysiological problem is re-integrated at each time step making our method particularly promising. In fact, a Collocation approach should reduce the computational effort related to the matrix computation, enabling a potentially significant analysis speed-up.

The novel method herein presented, for instance, can be directly applied to the simulation of the engineered ventricle presented in Chapter 3, improving the accuracy of the simulation for the same computational effort since it avoids the ICI approach.



## Chapter 7

# Immersed Isogeometric Analysis based on a Hybrid Collocation/Finite Cell Method for electrophysiology

We propose, in collaboration with the Hamburg University of Technology, an immersed approach for the Isogeometric Collocation method, combined with the Galerkin-based Finite Cell Method, to avoid the subdivision of complex geometries in too many patches.

The presented technology, further develops the Hybrid Collocation concept to accommodate both numerical methods within a single framework, providing a systematic technique for selecting the method to be used.

We perform several numerical tests to demonstrate that the methodology guarantees the same convergence rates obtained using the standard Isogeometric Collocation method. Afterwards, the methodology initially developed for Poisson-like problems is extended to cardiac electrophysiology.

The occlusion of a coronary vessel due to Ischemic Heart Disease may generate a necrosis of part of the myocardial tissue inducing a structural and electrophysiological change of the substrate and increasing the risk of experiencing self-sustaining ventricular tachycardia. Indeed, the formation of the so-called *slow conducting channels*, which are structure composed by survived myocardium within the infarct scar, are often responsible of the initiation and maintenance of reentrant waves, that alters the normal sinus rhythm. The problem complexity is further increased by the change in the properties of the region of transition between the healthy and diseased tissue, named as border zone or gray zone. Indeed, several studies have demonstrated its highly arrhythmogenic properties [327, 328] and therefore border zone has to be considered in accurate simulations [205].

Radiofrequency ablation [242] is a common procedure to prevent such a myocardial infarct-related disease based on surgically modification of the reentry pathway, that generates the ventricular tachycardia. In this context, numerical simulations are a helpful in providing a better understanding of the clinical conditions, and in designing the intervention.

The numerical modeling of this kind of pathologies is a complex task [242, 205] requiring (i) the identification of the scar, (ii) the definition of the ionic channel properties of the cells lying in the border zone, (iii) and the characterization of the tissue conductivity. The results of the last two points can be included directly in the SVI-C approach based on the Isogeometric Collocation method, whereas the modeling of the necrotic tissue deserve a special discussion. Indeed, it is no more active and it can be removed from the computational domain [205] requiring the representation of complex geometries.

As a limitation of IgA-C, meshing complex shapes is critical: in case of holes, for example, the geometry of the body must be subdivided into patches topologically conforming to a hexahedron. We propose to solve this issue extending the IgA-C method to the immersed framework [329, 330]. Indeed, immersed-Galerkin methods were successfully applied to the modeling of complex bodies in several

applications, ranging from the analysis of lattice structures [331] to fluid-structure interaction problems [121, 35].

To the best of our knowledge, no immersed version of IgA-C is currently available and the meshing issue is solved by splitting the geometry and coupling the different patches using ad-hoc algorithms, which significantly increases the complexity of the method. We therefore develop a hybrid method that combines the computational efficiency of IgA-C and the versatility of immersed technologies to perform electrophysiological studies.

This chapter is organized as follows: in Section 7.1 we provide the basis of the used numerical methods and we describe the novel methodology for space discretization with a focus on the Poisson’s problem. In Section 7.2 we extend the approach to the solution of transient problems, whereas Section 7.3 is devoted to numerical tests to assess the method accuracy. Once the immersed formulation is tested, in Section 7.4 we extend it to the electrophysiological context whereas Section 7.5 summarizes the results and delineates possible future studies.

## 7.1 Hybrid formulation for space discretization

The high regularity of the basis functions adopted in Isogeometric Analysis enables the development of the Isogeometric Collocation method for the solution of boundary value problems, where the strong form of the PDEs is solved directly, avoiding the time-consuming computation of integrals. Therefore, IgA-C is more efficient than the standard Galerkin approach [31], especially when high order basis functions are used in 3D simulations, because in such a case the required number of quadrature points can be very high.

Despite this appealing premise, IgA-C imposes a severe restriction in the definition of an analysis-suitable geometrical representation of the body. The geometry is discretized employing highly continuous B-splines defined on a rectangular parametric space. The basis function continuity requires either that the geometry of the body is topologically conforming to a rectangle or a subdivision of the body into several patches to recover conformity [332, 333]. This issue, in practice, limits the use of IgA-C in engineering applications when very complex geometries are involved, requiring either the patch conformity [30], or the imposition of a weak constraint [334], or the implementation of patch coupling schemes [335, 336].

In classical IgA-G and finite element approaches, the meshing issue might be overcome using an immersed technology. The idea behind this method is to embed the geometry in a regular mesh and to reconstruct the actual geometry in the computation of the integrals.

As the basis of immersed technology is the integration, an immersed method for Collocation is not easily obtained due to the absence of integrals to compute. In this chapter, we merge the IgA-C method and the immersed technology adopting a hybrid framework [158] for the solution of boundary value problems. Various immersed methods – such as CutFEM [337], immersogeometric analysis [35], Isogeometric B-Rep analysis [33], and immersed boundary-conformal method [34] – have been developed. We herein select the Finite Cell Method (FCM) as it can handle various types of geometries [338, 339] and it was successfully used in complex engineering applications [340, 341, 342].

In the following, after an introduction to Isogeometric Collocation and to the Finite Cell Method, we describe the novel methodology for the spatial discretization of PDEs that integrates the IgA-C and the FCM.

### 7.1.1 Notation for shell-like manifolds and remarks on the Isogeometric Collocation method

In the Isogeometric context, a bi-dimensional manifold in a three-dimensional space  $\mathbf{x} : \Omega \subset \mathbb{R}^2 \rightarrow \mathbb{R}^3$  is represented as a linear combination of B-splines  $H_{a;p}(\xi)$  and  $L_{b;p}(\eta)$  in the parametric directions  $\xi$  and  $\eta$ , and 3D control point coordinates  $\mathbf{B}_s$  as follows:

$$\mathbf{x}(\xi, \eta) = \sum_{a=1}^{m_\xi} \sum_{b=1}^{m_\eta} H_{a;p}(\xi) L_{b;p}(\eta) \mathbf{B}_{a,b} = \sum_{s=1}^m N_s(\xi, \eta) \mathbf{B}_s. \quad (7.1)$$

Assuming the lexicographical order [31], the tensor product of  $H_{a;p}$  and  $L_{b;p}$  basis functions can be condensed in the symbol  $N_s$  for the sake of brevity. Coherently, the number of control points and basis

functions  $m$  is given by the number of control points in each direction  $m = m_\xi \times m_\eta$ . It is worth noting that the continuity of the mapping function reflects the continuity of the geometry and the topological conformity between the physical geometry and the parametric space.

Clearly, the isoparametric concept still holds:

$$v(\mathbf{x}, t) \simeq N_s(\mathbf{x}) \hat{v}_s(t) = \mathbf{N}(\mathbf{x}) \hat{\mathbf{v}}(t). \quad (7.2)$$

but, in such a notation, the representation of a three-variate solid and a bi-variate manifold are similar, enabling a standardize implementation of the software. However, the PDE defined on a curved manifold are more conveniently computed using a curvilinear reference frame instead of the cartesian one. The IgA-C method, discretizing the strong form at the images  $\tilde{\mathbf{x}}_\gamma$  of the Greville abscissae  $\tilde{\xi}_\gamma$ , produces a system of equations, in which each row  $\gamma$  corresponds to the function evaluation at a given collocation point  $\tilde{\mathbf{x}}_\gamma$ . For instance, the gradient of a generic function  $f = N_s(\mathbf{x}) \hat{f}_s$ , defined in the domain  $\Omega$ ,  $f: \Omega \subset \mathbb{R}^3 \rightarrow \mathbb{R}$ , leads to the following discretization:

$$\nabla f|_{\mathbf{x}=\tilde{\mathbf{x}}_\gamma} = \frac{\partial N_s}{\partial x_i} \Big|_{\mathbf{x}=\tilde{\mathbf{x}}_\gamma} \hat{f}_s \mathbf{e}_i, \quad \forall i = 1, \dots, 3 \quad (7.3)$$

where the vectors  $\mathbf{e}_i$  are the unit vectors defining the Cartesian reference frame. Such a computation is more conveniently expressed in a curvilinear frame, as shown in D.1.

**Remark** The Isogeometric Collocation method is presented and discussed in the previous chapters, Herein, we remark that the simplest way to present the Isogeometric Collocation method is based on the discretization of the strong form of the PDEs. However, a second interpretation can be useful for demonstration purposes. IgA-C can be in fact viewed as a Petrov–Galerkin-based method that uses Dirac delta functions, centered in the collocation points, as test functions. Taking the advantage of the sifting property of the Dirac delta function, the first interpretation can be retrieved.

From the Petrov-Galerkin interpretation, it is clear that the basis function requirements are different with respect to classical Bubnov–Galerkin method, and that, for a second order boundary value problem, at least  $C^1$ -continuity must be guaranteed everywhere. This requirement can be easily fulfilled using quadratic B-splines with no repeated internal knots or sufficiently regular high order B-splines. Previous investigations [30, 188] have demonstrated that the rate of convergence of the error in the  $L^2$ -norm is equal to  $p$  for even degrees and  $p - 1$  for odd degrees. In this introductory work, we adopt the images of the Greville abscissae as collocation points since they are considered as the standard set of points [30, 343], consequently we focus on even degrees only because they are more cost-effective than odd degrees [31, 30]. However, future studies should investigate the improved accuracy for odd degrees provided by different selections of collocation points [343, 344, 345]. Indeed, the cost-effectiveness of the presented method depends on the degree  $p$  not only through the cost of array formation and of highly populated matrices [31], but also because  $p$  governs the number of Gauss points used in the quadrature rule employed in the immersed part of the domain.

### 7.1.2 Basis of the Finite Cell Method

The Finite Cell Method was initially developed within the finite element framework [87, 88] and later on extended to the Isogeometric Galerkin context [35, 339, 32]. FCM is a Bubnov-Galerkin-based method that defines the integrals entailed by the weak form of the PDE over a region extended outside the physical domain to simplify the meshing procedure, as described in [87, 88]. It is worth noting that the computation of the integrals plays a crucial role in the immersed method as it is used to reconstruct the actual geometry.

In the present chapter, we recast the same technology in a Petrov-Galerkin format to adapt it to IgA-C. Indeed, the main concept of addressing the complexity of the geometry in the integration process equally applies in Bubnov- and Petrov-Galerkin approaches.

A complete presentation of the Finite Cell Method is out of the scope of the present Thesis, we focus only on the description of two main features of the FCM: the indicator function and the quadrature rule, since we extensively use them in the proposed method.

**Indicator function  $\alpha$**  In the FCM, the complexity of the geometry description of the body is simplified embedding it in a hexahedral bounding box, that can be easily meshed using a regular grid, as shown in Fig. 7.1. Consequently, part of the mesh represents the actual geometry  $\Omega$  and part represents the surrounding space. We refer to the union of these two disjointed parts as the extended domain  $\Omega^*$ . To keep track of the actual geometry, a discontinuous indicator function  $\alpha$  is introduced as follows:

$$\alpha(\mathbf{x}) = \begin{cases} 1 & \text{if } \mathbf{x} \in \Omega \\ 0 & \text{if } \mathbf{x} \in \Omega^* \setminus \Omega. \end{cases} \quad (7.4)$$

In the solution of the weak form, integrals are computed over the physical domain. Following the immersed approach, the integration domain is extended to the fictitious domain  $\Omega^* \setminus \Omega$  but its contribution is canceled out by the value of  $\alpha$ . Therefore, the integral of the generic function  $f$  can be formally rewritten, elaborating on the integration domain, as:

$$\int_{\Omega} f(\mathbf{x}) dV = \int_{\Omega^*} \alpha(\mathbf{x}) f(\mathbf{x}) dV. \quad (7.5)$$

The simplicity of the method comes at the cost of an accurate integration across the discontinuity in  $\alpha$ . Standard element-wise Gauss quadrature requires the continuity of the integrand, therefore a more refined quadrature rule must be used.

**Quadtree scheme for accurate integration** To improve the accuracy in the computation of the integrals, several optimized schemes, such as the *Smart octree* [346], the *Moment Fitting* [347, 90], and the *Equivalent Legendre polynomials*[348], were developed. In this chapter, we adopt a simpler method. The so called *quadtree* scheme checks the value of the indicator function in the knot span, often referred to as finite cell in this context. If part of the points are inside and part are outside, then the cell is cut by the boundary and the *quadtree* scheme must be used. To accurately integrate across the discontinuity, the cell is split in half in each direction producing 4 sub-cells – 8 sub-cells in 3D – and the inside/outside test is repeated up to a predefined refinement depth, as depicted in Fig. 7.1. Afterwards,  $p + 1$  Gauss points per direction are placed in every sub-cell enabling an accurate integration. Please note that the quadrature rule does not modify the mesh and therefore it does not increase the number of degrees of freedom.

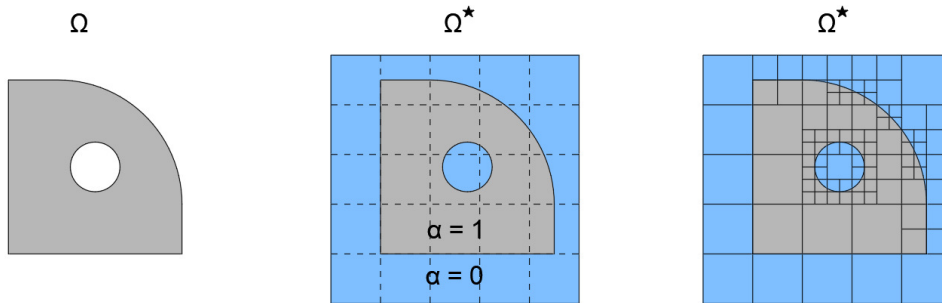


Figure 7.1: Schematic representation of the immersed technology. The physical domain – represented in the leftmost drawing – is embedded into a regular grid representing the body and the surrounding space (in light blue), as shown in the central plot. The actual geometry is then reconstructed in the integration step using the *quadtree* scheme, represented in the schematic on the right.

**Remark** When the FCM is used two parameters must be properly set. The first one is the value of  $\alpha$  outside the physical domain. It must be close to 0 to correctly represent the physical problem but not exactly 0 to avoid ill-conditioning problems in the solution of the resulting linear system. In our simulations we chose values in the range  $10^{-8} \nabla \cdot 10^{-14}$ , depending on the desired level of accuracy. The second parameter is the refinement depth employed in the *quadtree* scheme. Indeed, if the depth is limited, the representation of the geometry is too coarse and a plateau in the error convergence analysis is reached [329]. However, if a sufficiently accurate integration is used, the error in the solution converges as in the case of finite elements.

### 7.1.3 Hybrid Isogeometric Collocation/Finite Cell Method approach for spatial discretization

The proposed hybrid Isogeometric Collocation/Finite Cell Method (Hybrid IgA-C/FCM) approach aims at combining the computational efficiency of Isogeometric Collocation and the ability of the Finite Cell Method to treat complex geometries. To this end, we merge the integral and strong formulations in a single approach elaborating the concept of hybrid Collocation method, introduced in [158]. The main difference relies on the method for the test function selection [158, 334]. We automatically select the region where we apply the Galerkin approach using the value of the indicator function  $\alpha(\mathbf{x})$ , instead of choosing B-spline test functions only on the boundary of the parametric space, as classically done. As in the hybrid Collocation method, the computational efficiency of the approach is partially reduced by the computation of integrals [158, 31] depending on the extension of the immersed part. However, the Hybrid IgA-C/FCM method enables the direct solution of complex problems that would require further manipulations when solved by means of standard IgA-C, as described in Sec. 7.3.2. If compared to a pure standard FCM approach, the proposed strategy requires the same effort in the quadrature entailed by the immersed part of the domain since the number of quadrature point is the same in both methods, while the Hybrid IgA-C/FCM approach is more cost-effective in the collocated part of the domain. Indeed, it benefits of the advantages inherited from the reduced number of points where the functions are evaluated, and of the faster array formation and assembly procedure, as described in [31]. However, an accurate cost comparison between the two methods strongly depends on the geometry of the analyzed problem. To better understand this, let us consider the two extreme situations that may arise: no (or few) cut cells are present or no (or few) internal cells are present. In the former case, the effectiveness of the IgA-C method with respect to a conforming Galerkin method was demonstrated in [31]. On the other hand, if nearly every cell is trimmed – as it may happen in handling complex shapes [32] – the effort linked to the quadrature of the two methods is the same, but the FCM has the advantage of (i) producing symmetric matrices, and (ii) naturally enforcing homogeneous Neumann boundary conditions. The first point results in a memory saving and possibly in a faster solution of the linear system, depending on the adopted solver. Instead, the advantage mentioned in the second point depends on the extension of the area subject to the external load: if the entire boundary is loaded, the computational effort is the same for the FCM and Hybrid IgA-C/FCM approaches. Based on these observations, the presented methodology is suggested for all the kind of simulations where the IgA-C method is appealing, but some (relatively limited) geometrical features increase the complexity of the mesh generation.

The Hybrid IgA-C/FCM method maps the parametric space into the geometry using highly continuous B-splines, as in a standard Collocation approach. The different concept we exploit to derive a residual method is based on a Petrov-Galerkin formulation of the PDE and an appropriate tuning of the test functions to switch between the Collocation approach and the standard Petrov-Galerkin method addressed using the FCM. Indeed, if we choose a Dirac delta function, we retrieve the Collocation method, as explained in Sec. 7.1.1, whereas the standard Petrov-Galerkin formulation is kept if we select a B-spline. In the following, we refer to this latter part of the method as the immersed part.

Using the geometrical mapping, the indicator function can be re-parametrized in terms of parametric coordinates, enabling a direct connection between  $\alpha$  and the test functions through the parametric coordinates of the Collocation points.

The first step of the hybrid method is the definition of the geometrical mapping. Coherently with the immersed technology, it provides a representation of the geometry and the surrounding space, depending on the complexity of the shape. Indeed, the parametric space can be mapped either in a rough hexahedral bounding box or in a simplified shape that partially fits the actual geometry to limit the extension of the immersed region [349].

The automatic selection of the test functions, schematically represented in Fig. 7.3, checks the geometry of the knot span where the collocation point lies in. If the span is completely inside the physical body (i.e., the value of  $\alpha$  is equal to 1 everywhere), then the collocation point is considered active and we associate a Dirac delta function to it. On the contrary, if the span is external or cut, the collocation point is considered inactive and a B-spline is chosen as test function, as in a standard Galerkin method. Moreover, the case of the collocation points that lie exactly on the boundary between two knot spans — for instance, if the basis function degree is odd and the knots are equally spaced — is treated considering the points active only if both spans are internal. This procedure results in a split of the test space as shown in Eq. (7.9): part is composed by Dirac delta functions and part by B-splines.

This separation does not correspond to a split of the physical space. In several spans, we both evaluate the functions at the collocation points and we apply the quadrature rule creating a coupling between the control variables.

Once the test functions are chosen, the PDE can be discretized using both the presented numerical methods: IgA-C is used at the active collocation points whereas the FCM is applied on the support of the B-spline test functions. We highlight that the matrices derived by this discretization process are no more computed using the loop over the elements typical of the Galerkin methods. They are assembled row by row using the numerical scheme entailed by the test function, as shown in the following.

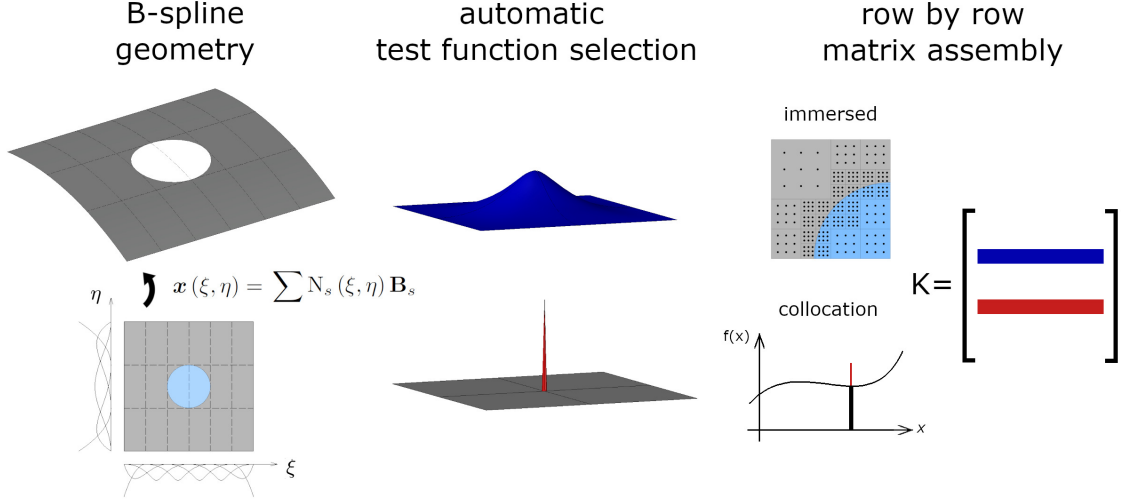


Figure 7.2: Workflow describing the Hybrid IgA-C/FCM approach. Given the parametrization of the extended domain, we select the test functions using the indicator function. Subsequently, the rows of the stiffness matrix are computed employing the numerical method entailed by the test functions.

### Poisson's-like equation as test problem

In this chapter, we test the formulation solving a second order boundary value problem. In particular, we focus on the Poisson's-like problem as it represents various engineering problems – like the thermal process in additive manufacturing [350, 351] – and it is a preliminary step to the solution of cardiac electrophysiology problem [179], for which a Collocation approach has already been proven, in Chapter 6, to be particularly effective [204].

The Poisson's-like problem reads as follows:

$$\begin{cases} \nabla \cdot (\mathbf{D}\nabla v) - I^{app} = 0 & \text{in } \Omega & (7.6a) \\ \mathbf{n} \cdot \mathbf{D}\nabla v - q = 0 & \text{on } \partial\Omega_N & (7.6b) \\ v - v^* = 0 & \text{on } \partial\Omega_D & (7.6c) \end{cases}$$

where  $\mathbf{D}$  is the conductivity tensor,  $I^{app}$  is the source term,  $\mathbf{n}$  is the outward pointing normal to the surface  $\partial\Omega_N$  where Neumann boundary conditions are applied,  $q$  is the imposed flux, and  $v^*$  is the field value on the boundary  $\partial\Omega_D$  where Dirichlet boundary conditions hold. Please, mind the difference between  $(\bullet)^*$  and  $(\bullet)^\star$ . The first symbol is used to identify Dirichlet boundary conditions whereas the second one refers to the extended domain.

According to the procedure described before, we re-write the Poisson's-like problem (7.6) – following [31, 352, 353] – in the Petrov-Galerkin format:

$$\int_{\Omega} (\mathbf{N}^{test})^T [\nabla \cdot (\mathbf{D}\nabla v) - I^{app}] dV + \int_{\partial\Omega_N} (\mathbf{N}^{test})^T [\mathbf{n} \cdot \mathbf{D}\nabla v - q] dA = 0, \quad (7.7)$$

and elaborating further:

$$\int_{\Omega^\star} \alpha (\mathbf{N}^{test})^T [\nabla \cdot (\mathbf{D}\nabla v) - I^{app}] dV + \int_{\partial\Omega_N} (\mathbf{N}^{test})^T [\mathbf{n} \cdot \mathbf{D}\nabla v - q] dA = 0. \quad (7.8)$$

The row vector  $\mathbf{N}^{test}$  has dimensions  $1 \times m$  and collects all the test functions. Using the automatic procedure for test function selection, we fill the vector with Dirac delta and B-splines functions. Consequently, it can be split into two parts, one referring to the Collocation  $\mathbf{N}^\delta$  and one to the FCM  $\mathbf{N}^{Bs}$ . For the sake of clarity in the presentation, we reorder the equations such that the test function vector assumes the following form

$$\mathbf{N}^{test} = [ \mathbf{N}^\delta \mid \mathbf{N}^{Bs} ], \quad (7.9)$$

and the terms related to the two sets of functions can be analyzed separately. In this section, we express the equations in compact notation for the sake of clarity. The reader is referred to D.1 for the actual implementation in curvilinear coordinates.

**Collocation terms** Thanks to the test function selection, Dirac delta functions are associated to internal knot spans where the value of  $\alpha$  is equal to 1. Consequently,  $\alpha$  does not affect Eq. (7.8), that contributes to the composition of the stiffness matrix  $\mathbf{K}$  and the right-hand side  $\mathbf{p}$ , once the control variables  $\hat{\mathbf{v}}$  are collected, using the linear expression of Eq. (7.2). If the collocation point  $\tilde{\mathbf{x}}_\beta$  lies in the internal part of the physical domain  $\Omega \setminus \partial\Omega$ , the contributions given by Eq. (7.8) – taking advantage of the sifting property – read as:

$$\mathbf{K}_{\beta i}^{\delta\Omega} = \nabla \cdot (\mathbf{D} \nabla N_i) |_{\mathbf{x}=\tilde{\mathbf{x}}_\beta} \quad (7.10)$$

and

$$\mathbf{p}_\beta^{\delta\Omega} = I^{app} |_{\mathbf{x}=\tilde{\mathbf{x}}_\beta}. \quad (7.11)$$

In these equations, and in the following, we use a superscript to identify the type of test function (Dirac delta:  $\delta$  or B-spline: Bs) and the part of domain (internal:  $\Omega$  or Neumann boundary:  $N$ ) involved in the computation.

Conversely, if the collocation point  $\tilde{\mathbf{x}}_\gamma$  lies on the boundary  $\partial\Omega_N$ , the contributions are linked to the second integral in Eq. (7.8):

$$\mathbf{K}_{\gamma i}^{\delta N} = \mathbf{n} \cdot \mathbf{D} \nabla N_i |_{\mathbf{x}=\tilde{\mathbf{x}}_\gamma} \quad (7.12)$$

and

$$\mathbf{p}_\gamma^{\delta N} = q |_{\mathbf{x}=\tilde{\mathbf{x}}_\gamma}, \quad (7.13)$$

requiring the direct enforcement of Neumann boundary conditions, even in the homogeneous case.

**Immersed terms** The computation of the immersed terms involves the integration over the support of the B-spline test functions. Differently from the Collocation case, the contribution of the boundary and the internal terms refer to the same set of rows.

The  $j$ -th row of the stiffness matrix is computed applying the *quadtree* integration rule to the following integrals derived from Eq. (7.8):

$$\mathbf{K}_{ji}^{Bs\Omega} = \int_{\Omega^*} \alpha N_j^{Bs} [\nabla \cdot (\mathbf{D} \nabla N_i)] dV, \quad (7.14)$$

$$\mathbf{K}_{ji}^{BsN} = \int_{\partial\Omega_N} N_j^{Bs} [\mathbf{n} \cdot \mathbf{D} \nabla N_i] dA, \quad (7.15)$$

and the corresponding terms at the right-hand side are given by:

$$\mathbf{p}_j^{Bs\Omega} = \int_{\Omega^*} \alpha N_j^{Bs} I^{app} dV, \quad (7.16)$$

$$\mathbf{p}_j^{BsN} = \int_{\partial\Omega_N} N_j^{Bs} q dA, \quad (7.17)$$

requiring again the direct enforcement of Neumann boundary conditions.

**Summary in matrix notation** To simplify the notation, we recast in matrix notation the equations previously presented. Indeed, the discrete form of the Poisson’s-like boundary value problem can be written as a linear system:

$$\mathbf{K}\hat{\mathbf{v}} = \mathbf{p}, \quad (7.18)$$

where the square stiffness matrix is composed by several blocks:

$$\mathbf{K} = \begin{bmatrix} \mathbf{K}^{\delta\Omega} \\ \mathbf{K}^{\delta N} \\ \mathbf{K}^{\text{Bs}\Omega} + \mathbf{K}^{\text{Bs}N} \end{bmatrix}, \quad (7.19)$$

as well as the right-hand side:

$$\mathbf{p} = \begin{bmatrix} \mathbf{p}^{\delta\Omega} \\ \mathbf{p}^{\delta N} \\ \mathbf{p}^{\text{Bs}\Omega} + \mathbf{p}^{\text{Bs}N} \end{bmatrix}. \quad (7.20)$$

The imposition of the essential boundary conditions on the conforming boundary is straightforward. Indeed, the matrix rows corresponding to those collocation points are substituted with the value of the basis functions at that set of points. Conversely, if an essential boundary condition is applied on the immersed boundary, one of the method employed in the FCM [354, 355, 341, 356] can be applied. For instance, the penalty method can be used without any modification [32]. For the computation of the mass matrix-like structures, the reader is referred to the next section of this work.

## 7.2 Extension to dynamics

In this section, we extend the hybrid method, developed for spatial discretization, to the solution of dynamic problems. The simplest strategy is to semi-discretize in space and subsequently to introduce a time marching scheme completing the process. Investigations on space-time discretization methods are left to future studies. Again, we have to distinguish between the contributions of the IgA-C and of the FCM in the composition of the mass matrix.

### 7.2.1 Transient Poisson’s-like problem

The transient version of the Poisson’s-like problem reads:

$$C_m \frac{\partial v}{\partial t} = \nabla \cdot (\mathbf{D}\nabla v) - I^{app}, \quad (7.21)$$

where  $C_m$  represents the system capacitance. Boundary conditions do not introduce any time derivative but a time dependence can hold, as shown in the example in Sec. 7.3.3. According to our methodology and similarly to the stationary case (7.7), the Petrov-Galerkin formulation becomes:

$$\int_{\Omega^*} \alpha (\mathbf{N}^{test})^T C_m \frac{\partial v}{\partial t} dV = \int_{\Omega^*} \alpha (\mathbf{N}^{test})^T [\nabla \cdot (\mathbf{D}\nabla v) - I^{app}] dV + \int_{\partial\Omega_N} (\mathbf{N}^{test})^T [\mathbf{n} \cdot \mathbf{D}\nabla v - q] dA. \quad (7.22)$$

The term we have not yet discretized is the integral at the left-hand side. Please, note that the mass matrix – computed simply setting  $C_m = 1$  in Eqs. (7.23, 7.24) – is also involved in the  $L^2$ -projection needed to compute the initial value of the control variables.

**Collocation mass matrix** The contribution  $\mathbf{M}^{\delta\Omega}$  (cf. left-hand side Eq. (7.22)) to the mass matrix  $\mathbf{M}$ , provided by the Collocation approach, consists in the evaluation of the basis functions at the collocation points:

$$\mathbf{M}_{\beta i}^{\delta\Omega} = C_m N_i|_{\mathbf{x}=\bar{\mathbf{x}}_\beta}. \quad (7.23)$$

**Immersed mass matrix** Similarly to the stiffness matrix, the immersed mass matrix  $\mathbf{M}^{\text{Bs}\Omega}$  is given by the computation of the following integral:

$$\mathbf{M}_{ji}^{\text{Bs}\Omega} = \int_{\Omega^*} \alpha N_j^{\text{Bs}} C_m N_i dV. \quad (7.24)$$

**Discrete formulation of the Poisson’s-like transient problem** In this chapter, we discretize the time by means of the implicit Euler method as it is the simplest unconditionally stable time marching scheme. The application of a single time step to compute the control variables  $\hat{\mathbf{v}}_{n+1}$  at time  $t_{n+1} = t_n + \Delta t$ , given  $\hat{\mathbf{v}}_n$  at time  $t_n$ , leads to the following linear system:

$$\begin{bmatrix} \mathbf{M}^{\delta\Omega} - \Delta t \mathbf{K}^{\delta\Omega} \\ \mathbf{K}^{\delta N} \\ \mathbf{M}^{\text{Bs}\Omega} - \Delta t \mathbf{K}^{\text{Bs}\Omega} + \mathbf{K}^{\text{Bs}N} \\ \mathbf{N}(\tilde{\mathbf{x}}_D \in \partial\Omega_D) \end{bmatrix} \hat{\mathbf{v}}_{n+1} = \begin{bmatrix} \mathbf{M}^{\delta\Omega} \hat{\mathbf{v}}_n - \Delta t \mathbf{p}^{\delta\Omega}(t_{n+1}) \\ \mathbf{p}^{\delta N}(t_{n+1}) \\ \mathbf{M}^{\text{Bs}\Omega} \hat{\mathbf{v}}_n - \Delta t \mathbf{p}^{\text{Bs}\Omega}(t_{n+1}) + \mathbf{p}^{\text{Bs}N}(t_{n+1}) \\ v^*(\tilde{\mathbf{x}}_D \in \partial\Omega_D, t_{n+1}) \end{bmatrix} \quad (7.25)$$

where the last row corresponds to the imposition of Dirichlet boundary conditions (cf. Sec. 7.1.3) as done in one of the following numerical tests (Sec. 7.3.3).

## 7.3 Numerical tests

We perform several tests in 1D and 2D to demonstrate the effectiveness of the proposed method using our in-house software based on the python library Nutils [52]. To this end, we solve the Poisson’s-like problem and we compare the results to analytical solutions and numerical references computed using the commercial software Abaqus [357].

### 7.3.1 Poisson’s-like problem in 1D

As a preliminary benchmark, we study the solution of the stationary Poisson’s-like equation in a 1D domain.

A physical domain of conductivity  $D = 100$ , shown in gray in Fig. 7.3, is embedded into an extended domain of length  $L = 1$ . The body is loaded with a distributed source term  $I^{\text{app}} = -1000 \sin(3\pi x/(2L))$ , a flux  $q = 10000$  at the right end, and a Dirichlet boundary condition  $v^* = 10$  is imposed at the left end.

In Fig. 7.3, we schematically show the selection of the test functions for quadratic B-splines defined on a mesh composed by 4 knot spans. The first and the second knot spans lie completely within the physical domain thus the three collocation points defined in these spans are active. Consequently, we select Dirac delta functions as the first three test functions (I, II, III), whereas the rest of the test functions (IV, V, VI) are equal to the corresponding B-spline basis functions. It is worth noting that we do not split the domain. Indeed, the support of the B-spline test functions – where the active quadrature points are defined – includes the second knot span, demonstrating that the quadrature rule and the Collocation method coexist on intersecting areas. The extension of such an area depends on the size of the support of the basis functions, that for B-splines of maximum continuity is  $p + 1$  knot spans per parametric direction. Consequently, the overlapped area spans  $\text{Round}(p/2)$  cells, where  $\text{Round}(\bullet)$  is the rounding half-up operator. We remark that such an overlap does not imply that both methods are applied at the same time. Indeed, Collocation and the FCM are used in forming different rows of the matrix. For instance, the composition of the stiffness matrix (cf. Sec. 7.1.3 and Fig. 7.2) is the following: rows I, II, and III correspond to the Collocation approach and, therefore the functions are evaluated at the active set of collocation points, while rows IV, V, and VI are computed integrating the immersed formulation over the test function support.

In this problem, we select the length of the physical domain ( $l = 2/3L$ ) such that a conforming mesh is never reached bisecting the knot spans. We want to assess the accuracy of the full Hybrid IgA-C/FCM formulation under  $h$ -refinement and, to this end, we compare the numerical results to the

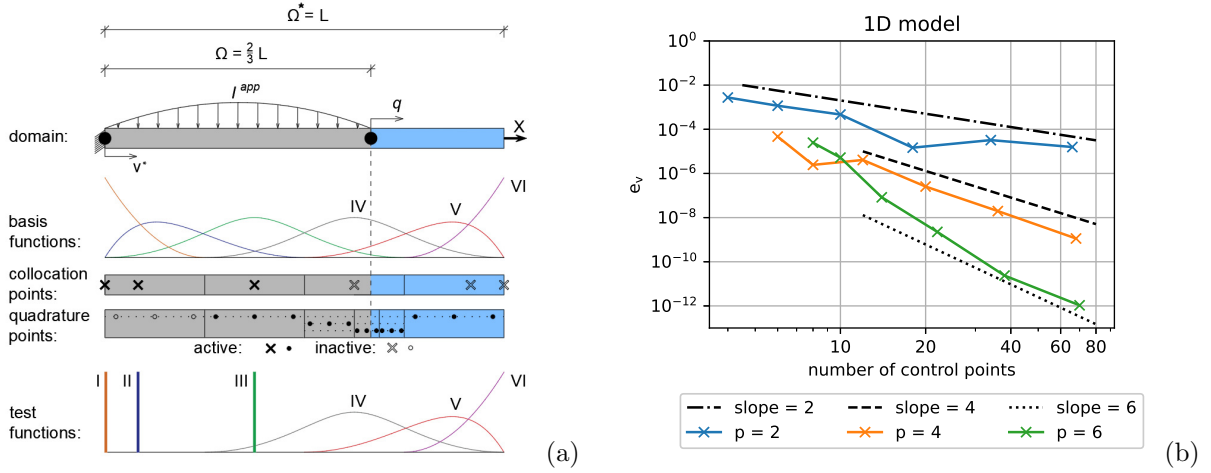


Figure 7.3: Schematic representation of the considered 1D problem. (a) The basis functions are defined over the extended domain, therefore several B-splines span across the fictitious domain, represented in light blue. In the cut cell, we schematize the *quadtrees* rule showing at different levels the Gauss points related to every refinement level. (b) Rates of convergence of the error under  $h$ -refinement. We analyze meshes composed by 2, 4, 8, 16, 32, and 64 uniform knot spans using a maximum of 10 level of refinement in the *quadtrees* scheme. We retrieve the expected rates of convergence, represented by the black lines.

analytic solution  $v^a$  defining the error in the solution as:

$$e_v = \sqrt{\frac{\int_{\Omega^*} \alpha (v - v^a)^2 dV}{\int_{\Omega^*} \alpha (v^a)^2 dV}}. \quad (7.26)$$

The convergence analysis under  $h$ -refinement in Fig. 7.3 shows that the proposed method retrieves the rates of convergence expected for the standard IgA-C method [30].

For the sake of completeness, results for  $p = 3$  and  $p = 5$  are presented in D.2. As expected for a Greville abscissae-based method [315, 30], the rate of convergence of such orders is equal to  $p - 1$ , confirming that the efficiency of the proposed approach for odd degrees is reduced with respect to even degrees of one order lower. This is a well-known limitation IgA-C methods [315, 31] and, consequently, in the following sections, we will focus on even-degree discretizations only.

We perform a second experiment employing the penalty method [32] to enforce essential boundary conditions on the domain, represented in Fig. 7.3, discretized using 15 spans such that several cells are completely in the fictitious part of the domain. In this case, we apply a Dirichlet boundary condition ( $v^* = 10$ ) on the conforming left end, while the condition  $v(2/3L) = 20$  is imposed on the immersed end by means of the penalty method (with the penalty parameter set to  $\epsilon_p = 1000 \times D = 10^5$ ). We do not apply any external source such that the problem should be solved up to machine precision. The results confirm the applicability of the method and the problem is solved exactly up to round-off error for any degree.

### 7.3.2 Diffusion on a square with a hole

This second test is aimed at demonstrating that the proposed methodology overcomes the limitations due to the meshing procedure. Indeed, we simulate the stationary diffusion on a unit square with an internal hole – shown in Fig. 7.4 – using a single rectangular patch, that is not conforming to the physical domain. According to our methodology, we map the parametric space into the square trimming the central hole by means of an immersed method.

In this simulation, we choose the problem setup such as an analytical solution is available. We apply homogeneous Neumann boundary condition on the internal boundary (radius  $R_0 = 0.1$ ) discretizing it with linear segments as in real simulations the geometry is often approximated by planar facets (e.g., stereolithography CAD). On the external boundary, we apply essential boundary conditions to reduce the modeling error. More details on the analytical solution and the simulation setup are provided in D.3.

The convergence analysis in Fig. 7.4 – employing the error definition in Eq. (7.26) – confirms the results obtained for the 1D test in a more complex geometrical setting. To achieve a relative error in the order of  $10^{-8}$ , an accurate representation of the immersed boundary must be used to overcome the saturation phenomenon, described in Sec. 7.1.2, and the modeling error. To this end, we use 10 levels of refinement and  $(p + 1)^2$  Gauss points per cell in the *quadtree* scheme, while 4096 segments discretize the boundary. We greatly overestimate the required accuracy to avoid uncertainties in the convergence path, although precise results can be achieved with fewer refinement levels, as shown in Sec. 7.3.3.

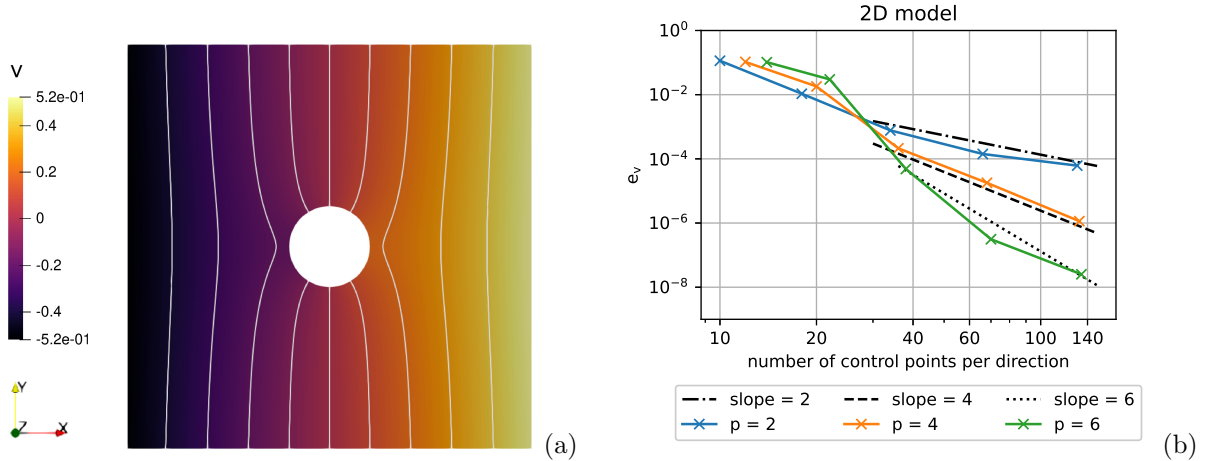


Figure 7.4: Simulation of the Poisson's-like problem on a hollow domain. (a) The boundary conditions impose the skew-symmetry – with respect to the Y-axis (cf. Fig: D.2) – in the solution and the tangential direction of the flux with respect to the immersed boundary, as highlighted by the isolines. (b) Rates of convergence of the method are shown. We analyze meshes composed by 8, 16, 32, 64, and 128 uniform knot spans per direction, retrieving the expected rates of convergence (represented by the black lines).

To the best of our knowledge, this is the first example of a complete square with an internal hole simulated using a single patch in the Isogeometric Collocation context. We consider this result as an important simplification of the geometrical modeling process as we do not deal with multiple patches and we avoid the implementation of complex patch-coupling algorithms to recover the basis function continuity. This example is trivial, but the approach holds in more complex simulation with multiple holes [87]. Moreover, we highlight that the use of an immersed method can reduce the number of needed degrees of freedom [88] because the actual geometry is not directly meshed.

### 7.3.3 Transient diffusion on a curved manifold

This last test demonstrates the ability of the method in solving transient problems. We simulate the propagation of a wave on a 2D curved manifold in a 3D space (see Fig. 7.5 and Fig. D.3) employing the mapping strategy presented in [349]. The parametric space is mapped into the manifold trimming the central hole as in the previous example. In this context, the natural choice is to use a curvilinear reference frame, as typically done for shells [245, 358, 179].

Starting from a rest condition  $v(\mathbf{x}, 0) = 0$ , the field on a part of the boundary suddenly reaches the value  $v^* = 1$  while the opposite edge maintains the initial value  $v^* = 0$  generating a wave, as shown in Fig. 7.5. More details on the simulation are provided in D.4.

The accuracy of the implementation is assessed comparing our results and an overkill simulation performed using the commercial software Abaqus [357] (see Fig. 7.5), since no analytical solution is available. In particular, we use a linear conforming mesh composed of 42776 quadrilateral and 1254 triangular finite elements (42937 degrees of freedom) in the reference computation, whereas the test is performed employing 20 uniform knot spans per parametric direction, sixth order B-splines (676 degrees of freedom) and 4 levels of refinement in the *quadtree* scheme. Both methods integrate in time using the implicit Euler scheme. Therefore, the differences in the results are mostly related to the discretization in space. Fig. 7.5 shows that the results of the proposed hybrid method in 5 different points (P1, P2, P3,

P4, P5) are in very good agreement at all instants with those obtained with the overkill finite element solution, confirming the method reliability.

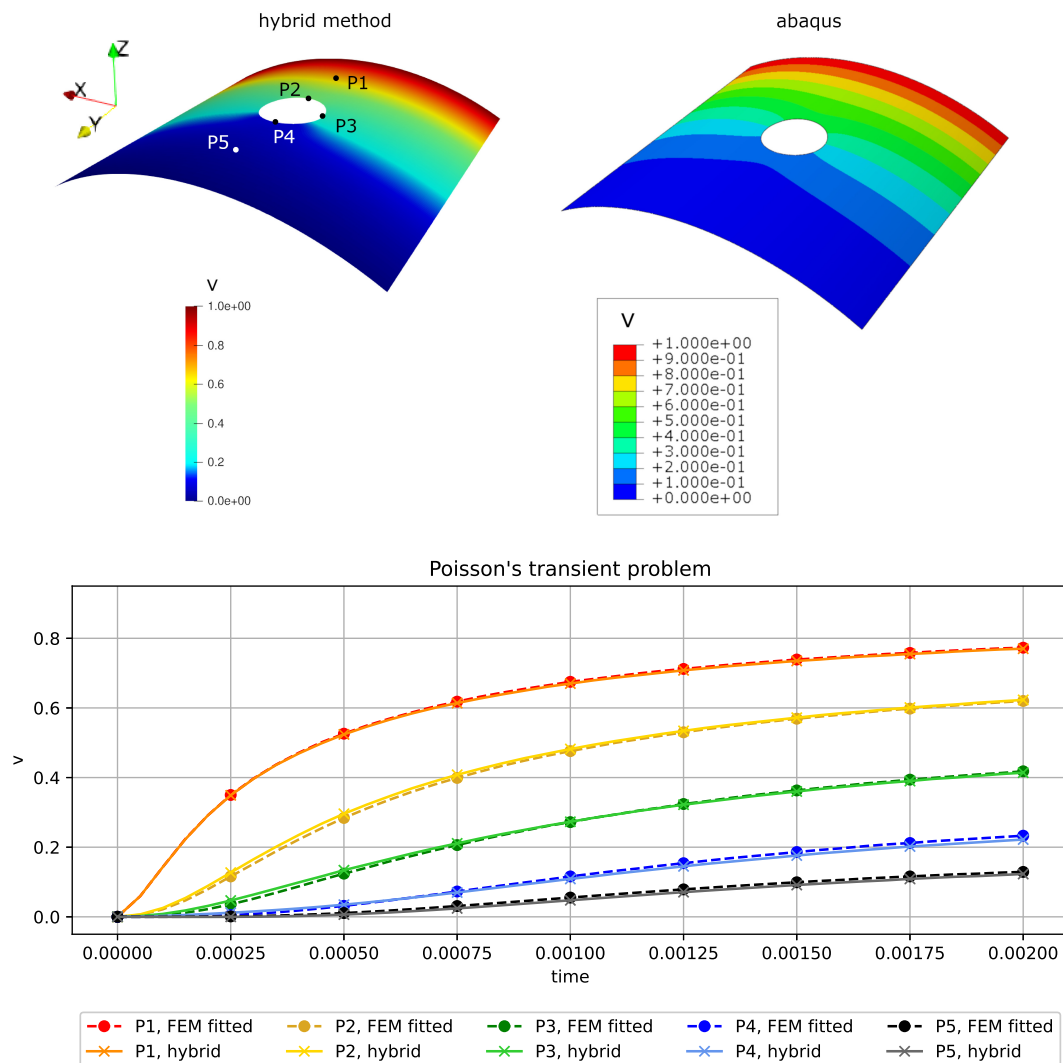


Figure 7.5: Transient Poisson's-like problem: comparison between the Hybrid IgA-C/FCM method and an overkill solution performed in Abaqus using a linear conforming mesh. Contour plots of the field represented on the geometry (see Fig. D.3) at time  $t = 1 \times 10^{-3}$  as well as the time histories in 5 different points are shown. For this test, we select  $C_m = 1$ ,  $D = 100$ , and  $\Delta t = 5 \times 10^{-5}$  in the implicit Euler scheme.

## 7.4 Extension to electrophysiology

The necrotic tissue is often modeled as a perfect insulator applying Neumann boundary conditions on the border of such part of the tissue [242, 205]. Consistently, the inactive region of the tissue can be removed from the computational domain by means of Hybrid IgA-C/FCM method.

Our immersed approach clearly increases the computational effort, in favor of a simplification in defining the geometry as the structured mesh is defined on the entire tissue, without considering the necrotic scar. Indeed, an explicit description of the healthy part of myocardium may be an extremely complex because several situations must be considered in the the meshing of the scar. The meshing tool must handle complex boundary representations and the formation of unconnected regions in the domain, that change the topology of the tissue. This issue is naturally avoided by the immersed technology

assigning the value of the indicator function to the tissue and discretizing, eventually with a triangulation, the border. Moreover, the immersed technology may be beneficial also in case of coupled electromechanics – where part of the tissue is removed from the computational domain of the electrophysiological sub-problem but it is still present in the mechanical step – and in designing the radiofrequency ablation procedure, avoiding a continuous re-meshing during the adaption of the surgery planning.

Herein, we extend the Hybrid IgA-C/FCM method to the electrophysiological simulations presenting the numerical discretization and the simulation of the action potential propagation on a scarred tissue.

#### 7.4.1 Numerical discretization

The discretization of cardiac electrophysiology by means of Hybrid IgA-C/FCM method can be easily derived by the formulation introduced for the transient Poisson's problem. Indeed, a single term, namely the ionic current, must be added to the Eq. (7.22):

$$\int_{\Omega^*} \alpha (\mathbf{N}^{test})^T I^{ion} dV. \quad (7.27)$$

Following the notation introduced for electrophysiology, the semi-discrete ionic current vector  $\tilde{\mathbf{I}}^{ion}(t)$  is given by the contributions of the SVI-C scheme:

$$\tilde{\mathbf{I}}_{\gamma}^{ion \delta\Omega} = I^{ion}|_{\mathbf{x}=\tilde{\mathbf{x}}_{\gamma}} \quad (7.28)$$

and the FCM:

$$\tilde{\mathbf{I}}_j^{ion \text{Bs}\Omega} = \int_{\Omega^*} \alpha \mathbf{N}_j^{\text{Bs}} I^{ion} dV. \quad (7.29)$$

In the computation of the integral (7.29), we calculate the ionic current adopting the Gaussian Integration approach for canonical electrophysiology (see Section 3.1.5), therefore we integrate the cellular model at the Gauss points.

In time, among the various possibilities [295, 359], we adopt an Implicit-Explicit (IMEX) time marching scheme to complete the discretization. In particular, we use the Implicit Euler method to discretize the diffusion terms, as shown previously, whereas the ionic current is integrated by means of Explicit Euler method leading to the additional term

$$\mathbf{p}^{ion} = -\Delta t \tilde{\mathbf{I}}_n^{ion} = -\Delta t \tilde{\mathbf{I}}^{ion}(t_n) \quad (7.30)$$

at the right-hand side of Eq. (7.25) in the computation of the potential at time  $t_{n+1} = t_n + \Delta t$ .

#### 7.4.2 Simplified example of scar modeling

We present a simplified example of infarction modeling simulating the propagation of the action potential on the trimmed surface presented previously. In this test, the central circular area in Fig. 7.6 represents the necrotic tissue removed from the computational domain by means of Hybrid IgA-C/FCM method ( $\alpha = 10^{-14}$ ) but, as a simplification, we do not model any border zone. The tissue parameters listed in [263]. An alternative situation, that involves a similar geometry, is related to the modeling of real *in-vitro* experiments [224]: the cardiac tissue can be perforated on purpose to investigate several pathologies. These two examples motivates the development of the immersed framework.

According to our methodology, we discretize the transmembrane potential using quadratic B-splines defined on a mesh composed by 24 knot spans per parametric direction while, to represent the immersed boundary, we use 128 segments and 2 levels of refinement in the *quadtrees* scheme. Concerning the time, we adopt the IMEX method to discretize 100 [ms] using  $10^4$  steps, proving the efficacy of an alternative time stepping scheme, other than that shown in previous electrophysiological simulations.

The results in Fig. 7.6 show the ability of the method in simulating the propagation of the action potential on a trimmed surface, confirming the viability of the proposed method.

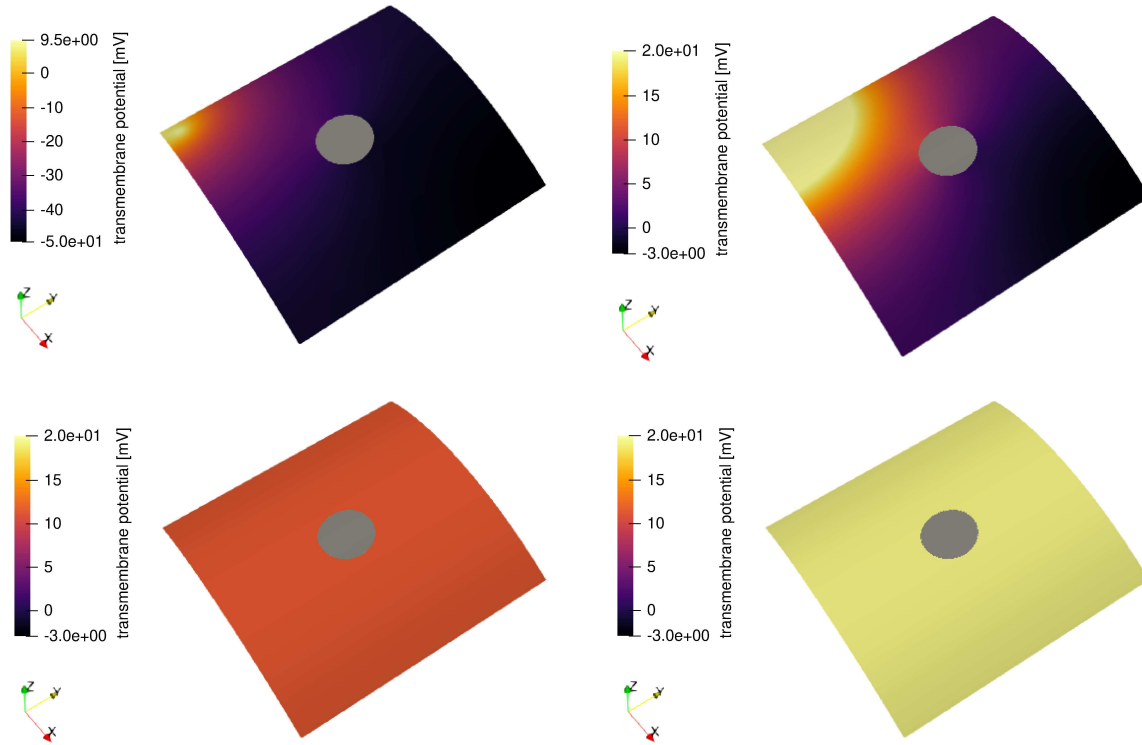


Figure 7.6: Electrophysiological simulation employing Hybrid IgA-C/FCM method to represent the scared tissue (in grey). Propagation of the action potential on the trimmed surface at time (from the left to the right and from the top to the bottom)  $t = 1, 2, 3,$  and  $100$  [ms]

## 7.5 Summary

The present chapter represents the first extension of the Isogeometric Collocation method to the immersed framework. The aim is to overcome the limitations in the meshing linked to the topology of the parametric space, that requires the implementation of patch-coupling schemes to generate meshes conforming to complex geometries.

We elaborate the concept of the hybrid Collocation method to solve the strong and integral form of the PDEs within a single framework. Since the immersed technology is based on the computation of integrals, our methodology uses IgA-C in the internal part of the domain, whereas part of the boundary is discretized by means of the Finite Cell Method. The switch between the strong and the integral form is dictated by the value of the indicator function, enabling the immersed discretization of boundaries internal to the patch.

Numerical experiments demonstrate the capabilities of the method. In particular, we were able to analyze a hollow square using a single patch, retrieving the rates of convergence of standard IgA-C method.

The methodology can be further improved investigating the applicability of more refined quadrature rules, as the *Moment Fitting* [90], for an efficient simulation of solids bodies and the possibility of achieving superconvergence with a different selection of the collocation points [343, 344, 345]. Moreover, interesting studies can also address the implementation of local refinement schemes [61, 330] and the possible mitigation of the cross-talking phenomenon [61] provided by the explicit enforcement of homogeneous Neumann boundary conditions on the immersed boundary. Furthermore, investigations about the imposition of essential boundary conditions on the immersed boundary by means of advanced techniques [32] (e.g., Nitsche's method) should be carried out. Regarding fluid-structure-interaction problems, IgA-C has been successfully employed [165] and it can be combined with the proposed approach to model immersed bodies using immersogeometric analysis [35].

The methodology is proven to be suitable for to dynamic problems increasing the applicability of the method. For instance, it has a direct application to thin active film modeling [179] and cardiac

electrophysiology. For this kind of problems a Collocation implementation has already been developed in Chapter 6, and the Hybrid IgA-C/FCM approach can be used to remove from the computational domain the part associated to the diseased tissue [242, 205], as shown in the previous section. The Hybrid IgA-C/FCM can be further improved. Indeed, during the integration of the ionic current, we use the time-consuming Gauss Integration approach for electrophysiology combined with the *quadtree* scheme, that may be excessively demanding in 3D realistic simulations. An important achievement is the combination of an efficient quadrature rule, such as the *Moment Fitting*, and the State Variable Interpolation or Ionic Current Interpolation approaches to limit the computational effort. Moreover, interesting studies can also address the implementation of local refinement schemes [61, 330] near to the trimmed part of the domain and the possible mitigation of the cross-talking phenomenon [61] provided by the explicit enforcement of homogeneous Neumann boundary conditions on the immersed boundary.

Eventually, the methodology herein presented may also be applied to punch the geometry of the ventricle presented in Chapter 3, recreating the actual holes [224] used to investigate pathologies.



## Chapter 8

# Isogeometric Collocation scheme for coupled electromechanics

We present an extension of Isogeometric Collocation to coupled cardiac electromechanical problems. We develop a staggered solution scheme that takes advantage of Isogeometric Collocation to reduce the computational effort in the simulation of the mechanical step, guaranteeing high accuracy for all field variables.

We mainly focus on the strategy adopted to couple the electrical and mechanical sub-problems; the possibility of handling different meshes to better represent the spatial scales; and the mitigation of *volumetric locking*. To this end, we propose a suitable mixed formulation for finite elasticity.

Several numerical tests demonstrate that the mixed formulation retrieves the expected convergence rates under  $h$ -refinement and the effectiveness of the proposed solution scheme for electromechanics.

The mathematical model to simulate the muscle contraction governed by the electrical activity of the cell is presented in Chapter 4 and employed in Chapter 5. In this chapter, we develop a coupled formulation based Isogeometric-Collocation. To better focus on the numerical aspects, we simplify the biological problem as much as possible using a one-way coupling strategy, that couples electrophysiology to mechanics only. Consequently, we neglect several effects, like the Frank-Starling law [360], that can be successively included in the formulation, when realistic scenarios are simulated.

The numerical simulation of the cardiac EM activity involves the solution of complex coupled partial differential equations, requiring an efficient numerical algorithm to limit the computational burden. In this field, the canonical discretization approach for these equations is the Finite Element Method [361, 326, 3]. However, in Chapter 6, we have proposed a treatment of cardiac electrophysiology (EP) using the Isogeometric Collocation method (IgA-C) [204, 315, 31]. The main motivation in using IgA-C is the cost-effectiveness with respect to Galerkin approaches [31]: It efficiently addresses the computation of the cellular model exploiting the capabilities of the numerical scheme enabled by the B-spline regularity. So far, such a newly-proposed methodology has not been extended to EM simulations, thus limiting possible practical applications. Therefore, we propose an extension of the IgA-C approach explicitly tailored for cardiac electromechanics.

The mechanical and the electrophysiological sub-problems are characterized by different time and space scales [362, 259], typically calling for staggered solution algorithms to adopt different space discretizations. In the development of the numerical scheme for the mechanical sub-problem, we pay particular attention (i) to the capability of handling different meshes, (ii) to the efficiency of the coupling strategy, and (iii) to the mitigation of the volumetric locking issue. Indeed, the cardiac tissue is often modeled as a nearly-incompressible material [182, 363] requiring proper discretization techniques [353, 38] to avoid inaccurate results. We therefore propose a mixed formulation to tackle locking in finite elasticity, extending the approaches developed for the small strain regime [188, 189]. To the best of our knowledge, no formulation for nearly-incompressible elasticity in finite deformations is currently available for IgA-C.

The presentation of the approach to electromechanics by means of IgA-C is organized in two main sections: first, we describe the mixed formulation and, then, we employ it for the discretization of cardiac EM. Therefore, Section 8.1 provides an introductory review of the finite elasticity theory and a thorough

description of the proposed mixed method, that is successively tested, leading to considerations on the applicability to the coupled problem. Using such a basis, we present in Section 8.2 the Collocation scheme for electromechanics starting from a presentation of the problem at the continuous level, that is later discretized coupling the collocated formulations of the electrophysiological and mechanical sub-problems. With a staggered solution scheme, two different discretizations may be employed to reduce the computational effort, therefore we investigate such a possibility using, in cascade, the previous findings. We conclude the section presenting convincing numerical tests as well as some remarks related to the coupled problem. Finally, afterwards, the work is completed by remarks and outlooks, reported in Section 8.3.

## 8.1 Mixed u-p formulation for nearly-incompressible materials in finite deformations

In this section, we derive a formulation suitable for IgA-C to model nearly-incompressible materials undergoing finite deformations. Indeed, biological materials often exhibit high bulk modulus values, possibly leading to the well-known numerical instability phenomena referred to as volumetric locking.

In Galerkin-based discretizations, this issue is usually solved using either high order basis functions [185, 12], or strain-projection based methods (such as the  $\bar{\mathbf{B}}$  and the  $\bar{\mathbf{F}}$  methods [187]), or mixed formulations [186], but in the Isogeometric Collocation context the literature is limited. High order discretization can be easily employed thanks to the reduced computational cost of the method [31]. However, recent investigations have demonstrated the effectiveness of mixed formulations in the small strain regime [189, 188], proving that locking phenomena can be mitigated even when low order B-splines are used.

In EP simulations the sharp front of the action potential must be correctly captured and, to this end, a fine mesh of linear finite elements is widely adopted in the literature [362, 43, 263, 3, 364, 314]. Following this concept, we develop an IgA-C scheme based on B-splines focusing on the cost-effectiveness of their use for electromechanical problems.

We start the description of the proposed mixed formulation with a brief review of the nearly-incompressible hyperelastic boundary value problem, that is then discretized by means of the IgA-C method, while numerical tests and considerations on the proposed approach are presented later.

### 8.1.1 Nearly-incompressible hyperelasticity

By definition of hyperelastic material, the first Piola-Kirchhoff stress tensor  $\mathbf{P}$  is given by the gradient with respect to  $\mathbf{F}$  of the strain energy function  $\psi$  (see Eq. (4.8)), that we assume decomposed in the deviatoric,  $\psi^{dev}$ , and the volumetric,  $\psi^{vol}$ , parts:  $\psi = \psi^{dev} + \psi^{vol}$  using the latter term to enforce the nearly-incompressibility constraint penalizing the variations of volume  $J = \det(\mathbf{F})$ .

In this chapter, we adopt, for the deviatoric component, the Neo-Hookean [256] constitutive model

$$\mathbf{P}^{dev} = GJ^{-2/3} \left( \mathbf{F} - \frac{1}{3} \text{tr}(\mathbf{F}^T \mathbf{F}) \mathbf{F}^{-T} \right) \quad (8.1)$$

for the sake of simplicity and in agreement with [180], although it may not accurately model the response of the cardiac tissue. Indeed, a single shear modulus  $G$  fully characterizes the model. Instead, the volumetric component of the first Piola-Kirchhoff stress tensor  $\mathbf{P}^{vol}$  – according to the formulation used in cardiac EM [257] – depends on the bulk modulus  $K$  as:

$$\mathbf{P}^{vol} = K(J - 1) J \mathbf{F}^{-1}. \quad (8.2)$$

In [256], the quantity:

$$p = K(J - 1) \quad (8.3)$$

is interpreted as the isotropic pressure  $p$ , that is extensively involved in the derivation of the mixed formulation.

To complete the description of the boundary value problem, we recall the static equilibrium equations:

$$\begin{cases} \nabla_{\mathbf{x}} \cdot \mathbf{P} + \mathbf{b}_0 = \mathbf{0} & \text{in } \Omega_0 \setminus \partial\Omega_0 \\ \mathbf{P}\bar{\mathbf{N}} - \mathbf{t}_N = \mathbf{0} & \text{on } \partial\Omega_{0N} \end{cases} \quad (8.4a)$$

$$\quad (8.4b)$$

where  $\mathbf{b}_0$  represents the distributed body load,  $\mathbf{t}_N$  the traction applied to the Neumann boundary  $\partial\Omega_{0N}$ , and  $\bar{\mathbf{N}}$  is the outward-pointing normal. Please, note the difference between the symbols  $\bar{\mathbf{N}}$  and  $\mathbf{N}$ , that is used to represent the matrix collecting the basis functions. We adopt a capital letter to be consistent with the classical notation of the reference configuration.

Appropriate essential boundary conditions  $\mathbf{u}^*$  on the Dirichlet boundary  $\Omega_{0D}$  (with  $\partial\Omega_{0N} \cup \Omega_{0D} = \partial\Omega_0$  and  $\partial\Omega_{0N} \cap \Omega_{0D} = \emptyset$ )

$$\mathbf{u} = \mathbf{u}^* \text{ on } \partial\Omega_{0D} \quad (8.5)$$

complete the description of the boundary value problem, solved using the mixed formulation proposed in the following section.

### 8.1.2 Mixed u-p formulation for Isogeometric Collocation method

The mixed formulation is described herein after a brief introduction to the IgA-C method. For a more comprehensive presentation of the discretization approach, the reader is referred to [315, 30] and to [31] for an accurate cost-comparison with the Galerkin method.

To tackle the volumetric locking issue, we extend the methodology presented in [189] for the small deformation regime to the finite deformation one.

We adopt a two field discretization, based on displacements and pressure, following the isoparametric concept and adopting an equal-order strategy. Consequently, we use the same basis functions for the discretization of the displacements  $\mathbf{u}$  and pressure  $p$  – that possibly depend on time  $t$  – approximated as follows:

$$\mathbf{u}(\mathbf{X}, t) = \sum_{s=1}^{3 \times m} \mathbf{N}_s(\mathbf{X}) \hat{\mathbf{u}}_s(t) = \mathbf{N}^u(\mathbf{X}) \hat{\mathbf{u}}(t), \quad (8.6)$$

$$p(\mathbf{X}, t) = \sum_{s=1}^m N_s(\mathbf{X}) \hat{p}_s(t) = \mathbf{N}^p(\mathbf{X}) \hat{\mathbf{p}}(t). \quad (8.7)$$

In a standard finite element context, the cardiac mechanics is often discretized using mixed non-locking-free elements, for instance the P1-P0 tetrahedron, achieving accurate results [362, 10]. In our formulation, we adopt the equal order approximation to exploit its cost-effectiveness, although strategies even more effective against locking can be employed [188]. Indeed, this approach avoids the definition of an additional mesh for the pressure field, that increases the complexity of the formulation, especially when the mechanics is coupled to the electrophysiological problem (and possibly to the fluid dynamic problem) employing a different mesh refinement.

In the discrete form, the first Piola-Kirchhoff stress tensor is function of both fields

$$\mathbf{P}(\mathbf{u}, p) = \mathbf{P}^{dev}(\mathbf{u}) + p J(\mathbf{u}) \mathbf{F}^{-1}(\mathbf{u}), \quad (8.8)$$

and the following equality

$$p = K [J(\mathbf{u}) - 1] \quad (8.9)$$

must be enforced to recover the original formulation. Consequently, in the equal order strategy we define four degrees of freedom per control point (three displacements and one pressure variable) and, to achieve a solvable system, we discretize four scalar equations per collocation point, leading to the residual form:

$$\begin{cases} \nabla_{\mathbf{X}} \cdot \mathbf{P}(\tilde{\mathbf{X}}_\alpha) + \mathbf{b}_0(\tilde{\mathbf{X}}_\alpha) = \mathbf{0} & \forall \tilde{\mathbf{X}}_\alpha \in \Omega_0 \setminus \partial\Omega_0 & (8.10a) \\ \mathbf{P}(\tilde{\mathbf{X}}_\alpha) \bar{\mathbf{N}}(\tilde{\mathbf{X}}_\alpha) - \mathbf{t}_N(\tilde{\mathbf{X}}_\alpha) = \mathbf{0} & \forall \tilde{\mathbf{X}}_\alpha \in \partial\Omega_{0N} & (8.10b) \\ \mathbf{u}(\tilde{\mathbf{X}}_\alpha) - \mathbf{u}^*(\tilde{\mathbf{X}}_\alpha) = \mathbf{0} & \forall \tilde{\mathbf{X}}_\alpha \in \partial\Omega_{0D} & (8.10c) \\ p(\tilde{\mathbf{X}}_\alpha) - K [J(\tilde{\mathbf{X}}_\alpha) - 1] = 0 & \forall \tilde{\mathbf{X}}_\alpha \in \Omega_0. & (8.10d) \end{cases}$$

At each collocation point, alternatively either Eq. (8.10a), or Eq. (8.10b), or Eq. (8.10c) is evaluated along with the last scalar Eq. (8.10d) defining a nonlinear system of  $4 \times m$  equations in  $4 \times m$  unknowns, that is solved by means of the Newton-Raphson method.

### 8.1.3 Numerical tests and discussion

To assess the performance of the proposed method, we perform several tests using our in-house software based on the Python library Nutils [52].

We first confirm that the equal-order formulation is able to significantly mitigate locking issue [189] in the Collocation context testing the deformation of a cube. We consider the linear-elastic response of the structure to compare the simulation to an analytical solution, reducing the formulation to the one presented in [189].

To stress the numerical solver, we assume a Young modulus  $E = 1000$ , a Poisson ratio  $\nu = 0.49999$  and a geometrical configuration prone to locking. More details on the simulation setup and on the analytical solution  $\mathbf{u}^a$ , that exactly fulfills the incompressibility constraint, are provided in E.1.

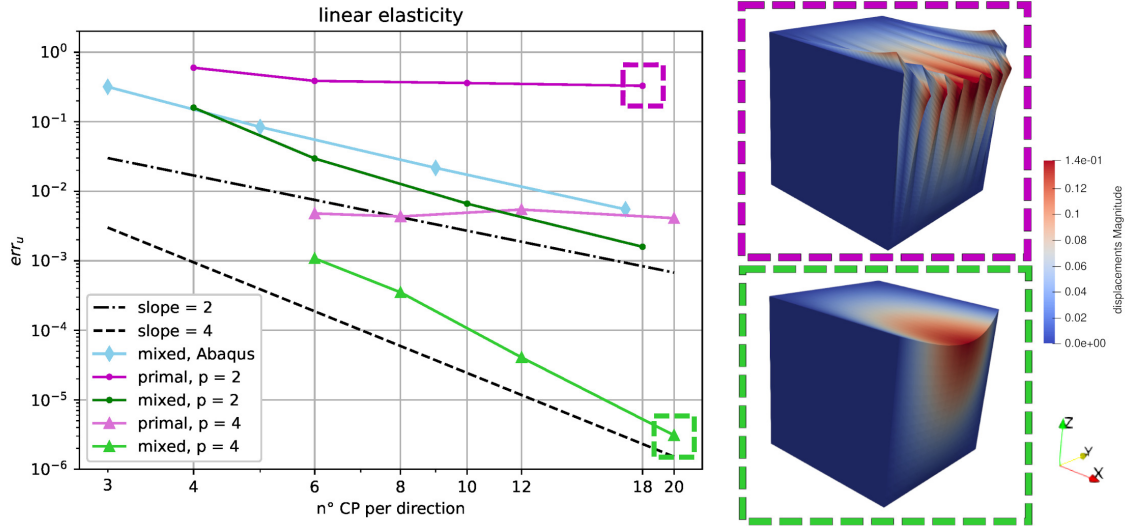


Figure 8.1: Comparison of different discretization methods for nearly-incompressible linear elasticity. On the left, the results of the convergence study are shown, while the deformed configurations related to the finest quadratic primal (top) and quartic  $\mathbf{u}$ - $\mathbf{p}$  (bottom) discretizations are shown on the right.

We compare three different types of discretization: (i) the IgA-C displacement-based formulation, here referred as “primal”, (ii) the IgA-C mixed  $\mathbf{u}$ - $\mathbf{p}$  formulation, (iii) and the mixed  $\mathbf{u}$ - $\mathbf{p}$  finite element formulation implemented in Abaqus [357], which employs the hybrid continuum hexahedral C3D8H element (linear displacements and constant pressure).

In the Collocation approaches, we test quadratic and quartic basis functions as they are the most cost-effective degrees for Collocation-based electrophysiology [204], as shown in Chapter 6. Indeed, higher order discretizations do not increase the accuracy significantly. Moreover, in dealing with complex geometries, an immersed approach may be beneficial thanks to the very simple and standardized meshing procedure. In this regard, the so called “Hybrid IgA-C/FCM” approach, introduced in Chapter 7, is more effective when even degrees are employed.

In the convergence test under  $h$ -refinement (see Fig. 8.1), we adopt the classical L2-norm of the displacements as error definition:

$$err_u = \sqrt{\frac{\int_{\Omega_0} (\mathbf{u} - \mathbf{u}^a) \cdot (\mathbf{u} - \mathbf{u}^a) dV}{\int_{\Omega_0} \mathbf{u}^a \cdot \mathbf{u}^a dV}}, \quad (8.11)$$

since a correct description of the displacement field is fundamental in cardiac electromechanical simulations, especially when they are coupled to fluid dynamic problems.

In Fig. 8.1, we test meshes composed by 2, 4, 8, and 16 uniform knot span – herein referred as elements – per direction. Both the finite element and the equal-order mixed Collocation formulations converge to the analytical solution, retrieving the expected rates of convergence, while the primal formulation exhibits locking. In particular, the solution computed using quadratic basis functions suffers from severe locking whereas the high order mildly mitigates the issue, without however guaranteeing good convergence

rates. We expect that the primal quartic formulation will start to converge for a more refined mesh, as demonstrated in [189], due to the particularly stressful simulation setup.

Previous studies [159] investigated the rate of convergence of the IgA-C method also in the finite deformation regime. No analytical proofs are available, but numerical tests proved that the convergence in problems with singularities in the solution, that are representative of practical applications, is at most quadratic, even for high order basis functions.

In testing the formulation in the finite deformation regime, we simulate the deformation of the curved body shown in Fig. 8.2, adopting the same material parameters of the previous example as data for the Neo-Hookean model and same discretization features. In the computation of error, we replace  $\mathbf{u}^a$  with an overkill reference solution as no analytical solution is available. More details on the simulation setup are provided in E.2.

The convergence tests in Fig. 8.2 and E.2 show the quadratic rate of convergence of the mixed formulation for  $p = 2$  and  $p = 4$ , in agreement with the results obtained in [159]. Furthermore, the convergence rate for the pressure field, presented in E.4, is approximately one, as in the case of standard linear finite elements for compressible linear elasticity. We recall that such a field represents only part of the hydrostatic stress in the coupled electromechanical simulation.

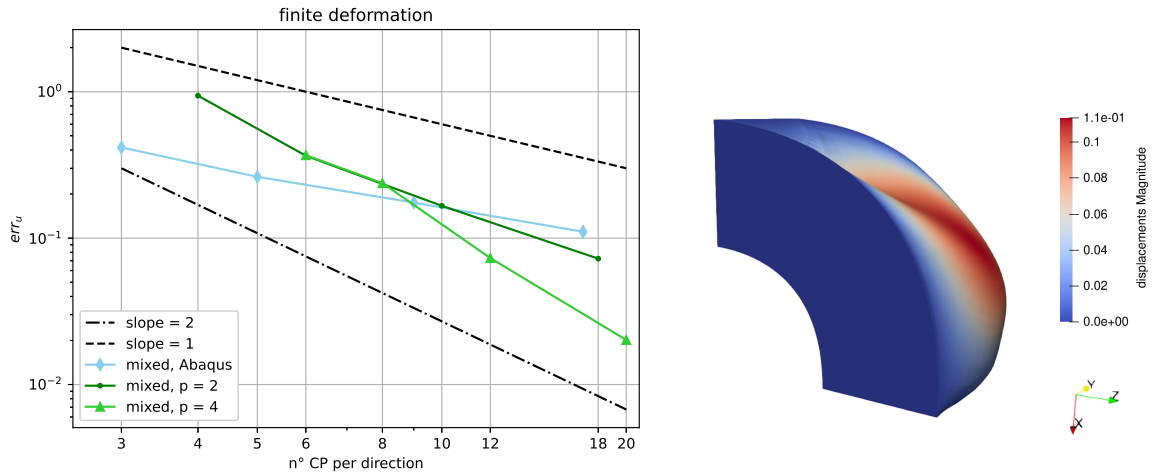


Figure 8.2: Convergence of the mixed  $\mathbf{u}$ - $p$  formulation in the finite deformation regime. On the left, results of the convergence test for quadratic and quartic B-splines are shown along with mixed Finite Element simulations. On the right, representation of the deformed body, displacements are magnified by a factor of 5.

#### 8.1.4 Considerations on the applicability to cardiac electromechanics

In cardiac electromechanics, the electrophysiology drives the process defining the finest time scale, related to the AP upstroke, while the deformation of the tissue occurs at a greater time scale. This observation reflects the selection of different time step sizes in the discretization of the mechanical and electrical sub-problems to reduce the computational expense [362, 259, 197]. Although the computational save is significant, this approach requires a complex problem-dependent calibration of the two time increments. Alternatively, an approach based on an explicit dynamics scheme for the mechanics can be used to reduce the simulation time. Indeed, we may use the same time step size limiting the computational burden thanks to the faster discretization method. In this second case, the pairs of space and time discretization schemes must be chosen properly to guarantee the algorithm efficiency, while keeping the desired accuracy.

In an explicit method for mechanics, the direct solution of the nonlinear system of equations is circumvented avoiding the assembly of the stiffness matrix. This greatly reduces the computational effort. However, a great efficiency of the time marching scheme is fundamental because many steps are simulated to fulfill the conditioned stability requirement. Researches [30, 365] have developed an explicit predictor-corrector scheme for IgA-C based on the the lumped mass matrix, that further reduces the

computational effort: such explicit scheme avoids the direct solution of the nonlinear system of equations at the cost of fast matrix multiplications on a finer time stepping.

Considering that the time step size dictated by the electrophysiological sub-problem is small – up to 100 or 200 times finer [362, 197]–, a minimal number of corrector steps is preferable to limit the computational effort. As demonstrated before, the convergence rate achieved by the  $\mathbf{u}$ -p formulation is quadratic and a single corrector step is sufficient to maintain the accuracy, limiting the computational burden.

Based on these considerations, quadratic B-splines seem to be the preferable choice for coupled EM simulations as the higher degrees result in a greater computational cost – in both space and time discretizations – that may not be compensated by an increase in the accuracy.

We conclude this section noting that explicit dynamics can be used to simulate static processes as well [134], extending the applicability of the approach to time-dependent simulations [263, 10].

In the present chapter, inertia forces have been neglected, and quasi static process are simulated to elucidate the potential of the novel space discretization approach. However, inertial effects cannot be ignored in multiphysics simulations, such as when coupling the mechanical activation of a ventricle with the blood hemodynamics. In this context, our numerical procedure can be effectively extended to dynamic problems with the explicit treatment of the inertia term.

## 8.2 Isogeometric Collocation scheme for cardiac electromechanics

Coupled EM simulations involve the solution of large systems of equations requiring optimized software to limit the computational time, for instance using parallel computing techniques [362, 212]. In this chapter, we investigate a different perspective proposing a methodology based on IgA-C to efficiently discretize the PDEs, that can be also successively parallelized.

The relevance of the shape function regularity in the solution of the cardiac electromechanics was pointed out in the Hermite Finite Element context [9, 131] and then further exploited in the Isogeometric-Galerkin framework [179]. Herein, we introduce a new approach that aims to combine the B-spline regularity and the Isogeometric-Collocation cost-effectiveness.

We structure this section as follows: The coupled electromechanical problem is presented in Chapter 4. Therefore, we start presenting the adopted numerical algorithm extensively using the results shown in Chapter 6 and in Section 8.1. Afterwards, a scheme to simulate the two sub-problems using different meshes to represent the different spatial scales is proposed and discussed.

### 8.2.1 Isogeometric Collocation scheme for cardiac electromechanics

In this Chapter, we adopt the active stress approach (see Chapter 4) to rule the tissue activation. Moreover, to better assess the effect of the spatial discretization on the solution of the ME problem, we neglect (i) the inertia term in the equilibrium equation, and (ii) the effect of the displacement field in the *Monodomain* problem (i.e.,  $\mathbf{F} = \mathbf{I}$  and  $J = 1$ ). The resulting formulation is one-way coupled: the EP simulation drives the mechanics through the ACT model without any feedback (cf. Fig 4.1, essential model) disentangling the errors due to the time integration.

Since this chapter aims at presenting the methodology, we adopt the following simplified models:

- the Aliev-Panfilov cell model [366],
- the stretch-independent Nash-Panfilov activation model [367], modified as shown in [263],
- an isotropic conductivity tensor  $\mathbf{D}$ ,
- the Neo-Hookean hyperelastic model [180] introduced in Eqs. (8.1, 8.2) assuming  $G = 1.5$  [MPa] and  $k = 74.5$  [MPa],

while the remaining parameters are taken from [263].

The mathematical formulation presented in this section is discretized introducing a B-spline approximation of the field variables and collocating the strong formulation, according to the IgA-C methodology, as described in the following.

The Isogeometric Collocation method, differently from standard Galerkin methods, discretizes directly the strong form of the PDEs [315, 30]. Therefore, equations (3.7, 4.15, 4.10) are directly evaluated at the collocation points to derive the semi-discrete form.

In time, we adopt a staggered solution scheme, as done in [259, 257] enforcing the hypotheses previously presented to complete the decoupling of the EP sub-problem from the ACT and ME steps. Consequently, EP is solved stand-alone and the results are successively used in the remaining parts of the simulation.

**SVI-C method for electrophysiology** The discrete form of the EP sub-problem has been derived in Chapter 6 and, for the sake of brevity, the reader is referred to Chapter 6 for a complete description of the algorithm. Indeed, we adopt exactly the same strategy to compute the evolution of transmembrane potential

$$v(\mathbf{X}, t) = N_s(\mathbf{X}) \hat{v}_s(t). \quad (8.12)$$

More specifically, we employ the so called SVI-Collocation method to discretize the monodomain formulation using the Godunov operator to split the reactive and diffusive terms in the integration from instant  $t_n$  to  $t_{n+1} = t_n + \Delta t$ .

At every time step  $t_n$ , the control variables  $\hat{\mathbf{v}}(t_n)$  and the transmembrane potential at the collocation points  $v(\tilde{\mathbf{X}}_\alpha, t_n) \forall \tilde{\mathbf{X}}_\alpha \in \Omega_0$  are computed, whereas the gating variables  $w^r$  and the ionic concentrations  $c^s$  are updated at the collocation points only. These quantities are used in the tissue activation model to compute the active stress and, in turn, the displacements.

**Mixed u-p formulation for cardiac mechanics** In this chapter, we neglect the inertia of the system in Eq. (4.15) enabling a quasi-static ME simulation in which each time step can be simulated independently. Indeed, the active stress varies in time according to the evolution of the transmembrane potential without any feedback.

Nearly-incompressible constitutive models are often employed in the cardiac tissue modeling [182, 363, 257] and, to mitigate volumetric locking, we apply the mixed u-p formulation presented in Section 8.1. To this end, we include the active term in Eqs. (8.10a, 8.10b), that are replaced by:

$$\begin{cases} \nabla_{\mathbf{X}} \cdot \mathbf{P}^{pas}(\tilde{\mathbf{X}}_\alpha) + \nabla_{\mathbf{X}} \cdot \mathbf{P}^{act}(\tilde{\mathbf{X}}_\alpha) + \mathbf{b}_0(\tilde{\mathbf{X}}_\alpha) = \mathbf{0} & \forall \tilde{\mathbf{X}}_\alpha \in \Omega_0 \setminus \partial\Omega_0 \\ \mathbf{P}^{pas}(\tilde{\mathbf{X}}_\alpha) \bar{\mathbf{N}}(\tilde{\mathbf{X}}_\alpha) + \mathbf{P}^{act}(\tilde{\mathbf{X}}_\alpha) \bar{\mathbf{N}}(\tilde{\mathbf{X}}_\alpha) - \mathbf{t}_N(\tilde{\mathbf{X}}_\alpha) = \mathbf{0} & \forall \tilde{\mathbf{X}}_\alpha \in \partial\Omega_{0N}, \end{cases} \quad (8.13a)$$

$$\quad (8.13b)$$

where the active term  $\mathbf{P}^{act}$  is given by the ACT step, described in the next Section.

As in the standard formulation (8.10), we solve the nonlinear problem by means of the canonical Newton-Raphson method.

**Discretization of the activation model** The ACT model connects the EP and ME sub-problems through the active stress tensor  $\mathbf{P}^{act}$ , that depends on the value of  $v$  and/or ionic concentrations. Indeed, they affect the evolution of the scalar active stress  $\sigma^{act}$  in the time integration of the ODE system (4.10) defined at the collocation points.

In this chapter, we adopt the ACT model formulated by Nash and Panfilov [367], that is stretch-independent (i.e., it does not depend on  $\Lambda$ ), as it is compatible with the adopted cellular model. This simplification does not create any lack of generality in the methodology. In fact, in case of stretch-dependent models, the same approach can be applied using an explicit scheme [262], but in this chapter, the Implicit Euler method is sufficient.

In the solution of the ME sub-problem, the active stress tensor is evaluated at the collocation points, as shown in Eq. (8.13), that are the points where the SVI-C approach computes the ion concentrations and the transmembrane potential. Consequently, the ODEs in Eq. (4.10) are directly integrated, enabling the computation of the active stress tensor, once the stress  $\sigma^{act}$  is computed at time step  $t_n$ . Indeed, the fiber orientation  $\mathbf{a}_0$  is known and the displacement field is assigned within each Newton-Raphson iteration.

Eq. (8.13a) involves the computation of the divergence of the active stress tensor requiring a more detailed discussion. The divergence can be written in index notation as:

$$\frac{\partial P_{ij}^{act}}{\partial X_j} = \frac{\partial \sigma^{act}}{\partial X_j} \left[ \mathbf{F} \frac{\mathbf{a}_0 \otimes \mathbf{a}_0}{\mathbf{a}_0^T \mathbf{F}^T \mathbf{F} \mathbf{a}_0} \right]_{ij} + \sigma^{act} \frac{\partial}{\partial X_j} \left[ \mathbf{F} \frac{\mathbf{a}_0 \otimes \mathbf{a}_0}{\mathbf{a}_0^T \mathbf{F}^T \mathbf{F} \mathbf{a}_0} \right]_{ij} \quad (8.14)$$

highlighting the complexity arising from the computation of the derivative of  $\sigma^{act}$ , because this function is known in a point-wise manner.

The active stress  $\sigma^{act}(\tilde{\mathbf{X}}_\alpha, t_n)$  can be easily evaluated at the discrete set of collocation points because the ionic concentration are computed there, but the reconstruction of its spatial distribution  $\sigma^{act}(\mathbf{X}, t_n)$ , needed for differentiation, is unknown at this stage. We propose two methods, denominated Control Variable Projection (CVP) and Collocation Point Differentiation (CPD), to compute the gradient.

Method CVP calculates the control variables of the active stress, as shown in Chapter 6, by means of linear system solution

$$\mathbf{M} \hat{\boldsymbol{\sigma}}^{act} = \tilde{\boldsymbol{\sigma}}^{act}, \quad (8.15)$$

where  $\mathbf{M}$  represents the collocation matrix (i.e., the matrix collecting the values of the basis functions at the collocation points):

$$M_{jk} = N_k(\tilde{\boldsymbol{\xi}}_j) \quad (8.16)$$

and  $\tilde{\boldsymbol{\sigma}}^{act}$  is the vector of the active stress values at the collocation points. Afterwards, the gradient can be computed deriving the basis functions and evaluating them at the collocation points.

The alternative strategy (Method CPD) avoids the solution of system (8.15) splitting the derivative of the stress as follows:

$$\frac{\partial \sigma^{act}}{\partial X_j} = \frac{\partial \sigma^{act}}{\partial \xi_k} \frac{\partial \xi_k}{\partial X_j}. \quad (8.17)$$

The second term at the right hand side is computed using the geometrical mapping, whereas the first one is approximated by means of a finite difference method. Indeed, the stress is known at the vertex of a rectangular grid in the parametric space, enabling a simple implementation of the finite difference method. In EM simulations, a second-order centered difference scheme is sufficient to guarantee quadratic convergence under  $h$ -refinement, coherently with the strategy delineated in Sec. 8.1.4, but higher order schemes are applicable as well.

We note that, if the ACT model depends on the potential  $v$  only, a direct integration of the stress control variable in a Ionic Current Interpolation [244] fashion is possible. However, it is a special case and it is not investigated in the following numerical test, where we compare the two general alternatives CVP and CPD.

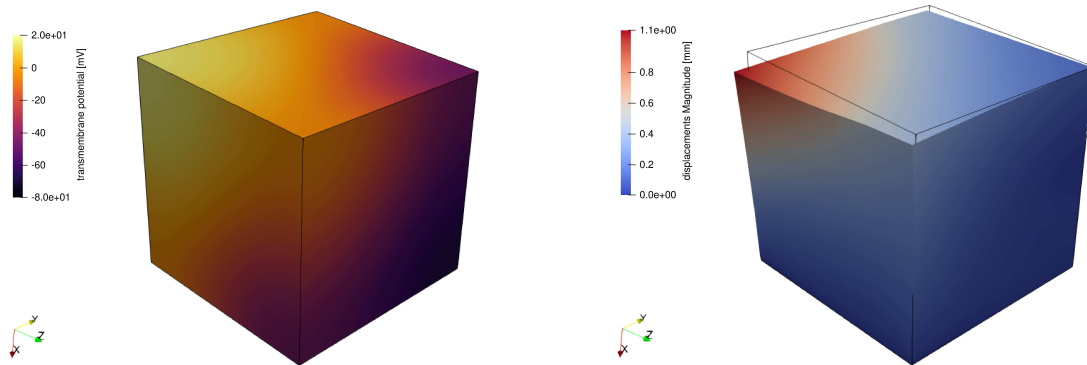


Figure 8.3: Results of the coupled electromechanical simulation at  $t = 30\text{ms}$ . On the left, the contour plot of the transmembrane potential and, on the right, the corresponding tissue deformation.

**Test problem** To verify the accuracy of the schemes CVP and CPD, we simulate the propagation of the action potential, triggered by setting  $v = 20\text{mV}$  for 20ms in the location shown in Fig. 8.4(a), in a

cubic domain (side  $L = 10\text{mm}$ ). The deformation is induced by contractile fibers, oriented along the X axis, fixed at the face at  $X = 10\text{mm}$ , as shown in Fig. 8.3.

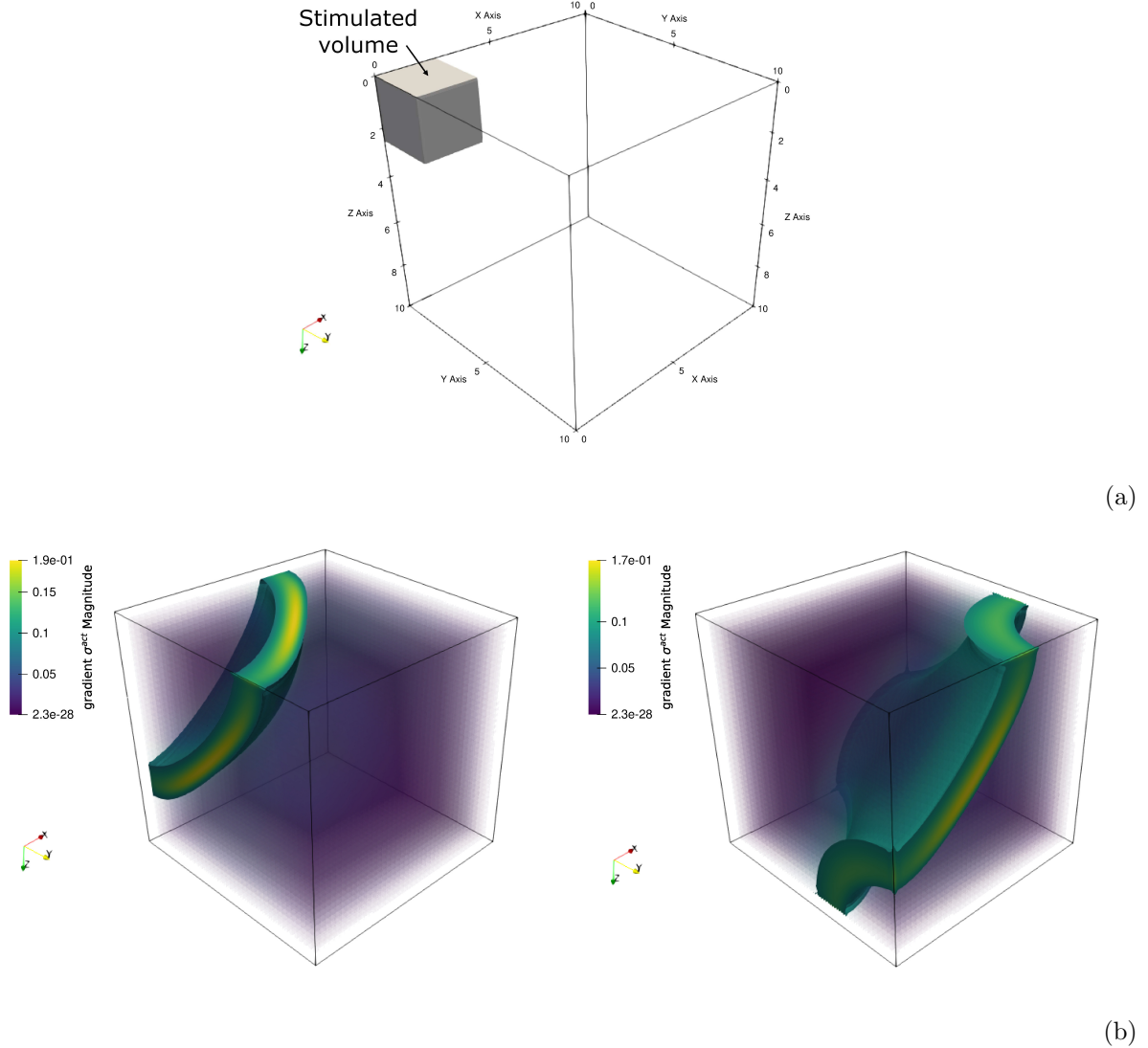


Figure 8.4: Computation of the active stress gradient. (a): representation of the computational domain and of tissue stimulation site. (b): representation of the magnitude of the active stress gradient ( $\|\nabla_{\mathbf{X}}\sigma^{act}\|$ ) at time  $t = 30\text{ms}$  (left) and  $t = 35\text{ms}$  (right). The gradient is represented only in the internal part of the domain  $\Omega_0 \setminus \partial\Omega_0$  where the divergence of  $\mathbf{P}^{act}$  is computed.

In this analysis, we employ three meshes of quadratic B-splines ( $h = 1.0, 0.5, 0.25\text{mm}$ ) and a time step size  $\Delta t = 0.01\text{ms}$  to simulate 50ms.

The coupling hypotheses ensure a fair comparison between the methods CVP and CPD because the same EP simulation is used to compute tissue deformations. We select for the analysis of the deformation two instants such that the simulated action potential concentrates a highly curved active stress gradient inside the domain, recreating the most unfavorable situations, as shown in Fig. 8.4(b).

In Tab. 8.1, we assess the differences between the methods in predicting the gradient of  $\sigma^{act}$  and the displacements  $\mathbf{u}$  according to Eqs. (8.18, 8.19), respectively: the subscripts  $\bullet_{CVP}$  and  $\bullet_{CPD}$  refer to the adopted approach.

$$\epsilon_\sigma = \sqrt{\frac{\sum_\alpha \sum_{i=1}^3 \left[ \nabla_{\mathbf{x}} \sigma_{CPD}^{act}(\tilde{\mathbf{X}}_\alpha) \right]_i^2 - \sum_\alpha \sum_{i=1}^3 \left[ \nabla_{\mathbf{x}} \sigma_{CVP}^{act}(\tilde{\mathbf{X}}_\alpha) \right]_i^2}{\sum_\alpha \sum_{i=1}^3 \left[ \nabla_{\mathbf{x}} \sigma_{CVP}^{act}(\tilde{\mathbf{X}}_\alpha) \right]_i^2}}, \quad (8.18)$$

$$\epsilon_u = \sqrt{\frac{\int_{\Omega_0} (\mathbf{u}_{CPD} - \mathbf{u}_{CVP}) \cdot (\mathbf{u}_{CPD} - \mathbf{u}_{CVP}) dV}{\int_{\Omega_0} \mathbf{u}_{CVP} \cdot \mathbf{u}_{CVP} dV}} \quad (8.19)$$

We test the methods to verify that at least two coupling strategies, featuring different algorithmic implementations, are available. It shows the versatility of the Collocation approach in such a key point [212] while future investigation may address different schemes [259].

We compare the formulations using typical element sizes [242, 43, 9, 201]: the results are in good agreement, highlighting the viability of both approaches; in the successive time steps, the tissue is completely contracted and the contribution to the deformation given by the gradient is approximately null.

$t$ [ms]	$h$ [mm]	$\epsilon_\sigma$ [-]	$\epsilon_u$ [-]	$t$ [ms]	$h$ [mm]	$\epsilon_\sigma$ [-]	$\epsilon_u$ [-]
30	1.0	0.077	0.0069	35	1.0	0.053	0.0021
	0.5	0.045	0.0021		0.5	0.040	0.0015
	0.25	0.019	0.0005		0.25	0.012	0.0003

Table 8.1: Error estimates (8.18 - 8.19) between the CVP and CPD approaches for the calculation of the active stress gradient for several meshes at two different time steps.

## 8.2.2 Coupled simulations employing separate meshes

The different space scales involved in the EM simulation are represented using a coarser mesh for the ME sub-problem reducing the computational effort [259], but the data interpolation between the grids must be efficient [212] to maintain such a gain. In the following, we propose a methodology to efficiently handle different meshes taking advantage of the knot insertion algorithm.

The initial geometrical representation of the domain is typically based on a mesh too coarse to produce accurate results in EM simulations, in particular for the EP sub-problem. Therefore, we define a finer mesh for EP and a coarser one for ME inserting in the initial knot vectors two different sets of new knots [11]. Doing so, the EP and ME simulations are performed exactly on the same geometry, as B-splines exactly preserve the parametrization and the geometry during mesh refinement [12].

In the coupled EM context, the active stress  $\sigma^{act}$  and its gradient, computed on the finest EP mesh, must be interpolated at the collocation points used in the ME sub-problem.

If the method CVP is used to compute the control values of  $\sigma^{act}$ , then the data can be interpolated at the new set of collocation points evaluating the basis functions and their derivatives, thanks to the conservation of the parametrization. This process is standard and it comes at the cost of a matrix-vector multiplication per mechanical time step.

Method CPD, instead, computes the data at a discrete set of points only. In this second case, the idea is to select the mechanical mesh such that its collocation points are a subset of the collocation points used in the EP simulation. This requires the definition of a scheme, as shown in Fig. 8.5, constraining the selection of the two meshes, but has the advantage that a simple and fast data selection replaces the solution of the linear system (8.15) and the matrix-vector multiplications.

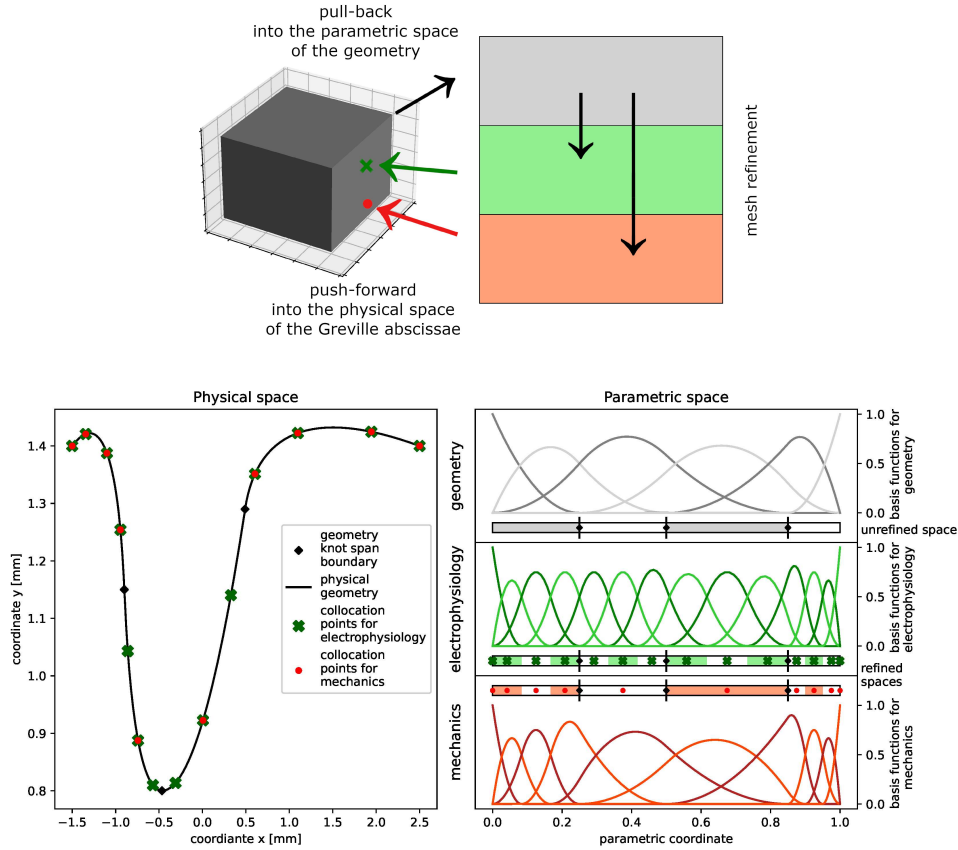


Figure 8.5: Representation of the mesh selection process. Top: schematic of the process. The geometry is analyzed to define two different meshes for the sub-problems such as the collocation points of ME mesh are a subset of the EP set. Bottom-left: representation of a 1D geometry along with the initial knot span subdivision and the two set of collocation points. Bottom-right: in grey, the basis functions and knot span subdivision used to describe the geometry. In green, the discretization used for the EP sub-problem and the initial knot span subdivision in black. In orange, the coarser discretization employed for the ME sub-problem.

Thanks to the tensor product structure of the basis functions, the scheme can be applied one parametric direction at a time, guaranteeing a better control of the mesh refinement. For instance, if the knot vector is uniform and the basis functions are quadratic  $C^1$  B-splines, the collocation points of the internal knot spans are in the middle of the span and the knot vectors of the two meshes can be easily calibrated to overlap the collocation points, as shown in Fig. 8.5. Nevertheless, several alternative schemes can be developed for different types mesh, as shown in E.5.

To demonstrate the applicability of this approach, we simulate the contraction of an arch using a coarser discretization for the ME sub-problem. The cardiac tissue is electrically stimulated at the rectangular left surface imposing  $v = 20\text{mV}$  for 20ms, as shown in Fig. 8.6, and the contractile fibers, oriented along the Z axis and fixed at the ends, induce the structure lowering.

In this test, we simulate 100ms using a time step size  $\Delta t = 0.005\text{ms}$  and quadratic basis functions. We employ two different discretizations for the EP and ME sub-problems: the finer EP mesh is composed by  $30 \times 10 \times 198$  knot spans, while the coarser ME mesh is obtained applying the scheme in Fig. 8.5 in the longitudinal direction only ( $30 \times 10 \times 70$  knot spans). Results of the simulation employing the same mesh for the two sub-problems are also reported in Fig. 8.6 for completeness.

The simulation results demonstrate that the proposed method can be successfully applied, reducing the computational effort needed to solve the problem, while keeping very limited (1.04% at  $t = 40$  ms and 1.28% at  $t = 60$  ms in Fig.8.6) the relative error – with respect to the fine discretization – in terms of maximum displacement.

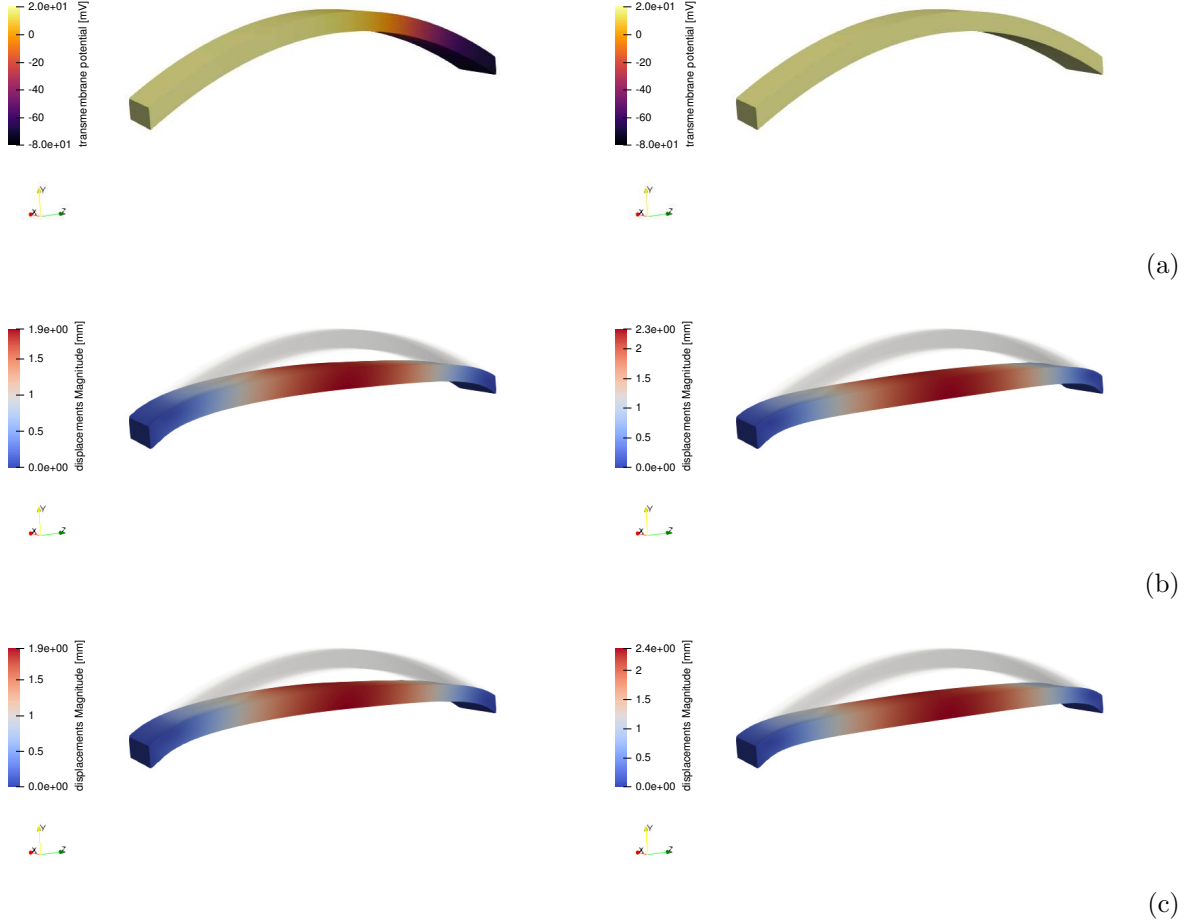


Figure 8.6: Simulation of the deformation of an arch. Two different instants are represented:  $t = 40\text{ms}$  on the left, and  $t = 60\text{ms}$  on the right. (a): transmembrane potential represented on the undeformed structure. (b): the displacement field computed using the coarse mesh is shown along with the undeformed configuration in grey. (c): reference IgA-C solution for displacements computed using the finer EP mesh also for the ME sub-problem.

### 8.2.3 Considerations on the coupled electromechanical simulator towards future developments

In this chapter, we have investigated the possibility of applying the IgA-C method in the spatial discretization of the ME part of coupled EM simulations. To assess the effectiveness of the method, we have adopted a simplified formulation to completely split the sub-problems, noting that the two-way coupled formulation and the effect of stretch-activated channels can be reintroduced using staggered schemes, as presented in several works [262, 257]. Moreover, we neglected the effect of the stretch-activated channels but they could be considered using an explicit scheme as done for the ionic current.

The considerations in Section 8.1.4 and the results of this section highlight that quadratic B-splines are suitable for accurate simulations of this kind of problems, especially if the mechanical sub-problem is solved in the explicit dynamics framework as suggested in [365]. Specifically, the reduced number of corrector steps in the explicit dynamics scheme can be combined with (i) the faster coupling method CPD, (ii) and the efficient mesh selection based on the collocation point sub-sampling. Future studies can address a more general algorithm to couple independent meshes [259] more efficiently than the approach entailing the computation of the control variables.

### 8.3 Summary

Most of the state of the art approaches to EM simulation are based on the finite element method, but several alternative numerical schemes have been recently proposed. Among them, the IgA-C method has been applied in Chapter 6 to discretize the EP problem. To extend the IgA-C method to coupled EM simulations, we have developed a mixed  $\mathbf{u}$ - $p$  formulation for finite elasticity, as shown in Section 8.1, based on the formulation presented in [189]. The numerical results show that the formulation follows the expected convergence trends [159].

Such a mixed formulation has then been successfully employed in Sec. 8.2.1 for the solution of the coupled EM problem and two alternative coupling strategies have been proposed and successfully employed.

Different time and space scales are involved in the coupled problem, as described in [9, 362, 259]. Regarding the space scales, we propose several approaches to embed different meshes for the EP and the ME sub-problems in the same analysis (see Sec. 8.2.2) considering the efficiency of the data transfer between the meshes. Instead, concerning time, future works may address efficient alternative time discretization [365] and address the complexity of the fully coupled model by means of explicit schemes [262].

In the development of the proposed approach, several topics for future investigations have arisen. In particular, given the target biomedical applications of the method, from the geometrical-modeling point of view, the development of a patch coupling algorithm and/or the integration in this framework of an immersed method may be of interest to model complex geometries arising from pathological conditions. Afterwards, further studies should address the interaction of the cardiac tissue with a fluid to simulate the heart pumping activity.

Specifically, the presented coupled formulation may be applied to simulate the motion of the jellyfish bell, presented in Chapter 3. Furthermore, when combined with the immersed approach presented in Chapter 7, it can be used to model the mechanics of the diseased engineered ventricle, drafted in Chapter 3.



## Chapter 9

# Conclusions and outlook

In this Thesis, we have investigated the simulation of active tissues by means of Isogeometric Analysis with a focus on engineered cell culture platforms ranging from 3D miniaturized replicas of the heart ventricle to simplified 2D and 1D geometries. Furthermore, we demonstrated how these techniques can be applied to different fields such as bioactive soft robotics.

In simulating the engineered ventricle made of human induced pluripotent-stem-cell-derived cardiomyocytes, in Chapter 3, we have assessed the effect of basis function continuity and degree on the accuracy of the solution, observing a dependence of the solution on the correct representation of the sharp depolarization wave front. Therefore, to limit the computational burden, we have proposed an Isogeometric Collocation scheme for the *Monodomain* formulation, in Chapter 6. It exploits the cost-effectiveness of the numerical approach avoiding the interpolation of the state variables, which are computed directly at the collocation points. Successively, the Collocation strategy is extended in Chapter 7, developing the Hybrid IgA-C/FCM method, to the immersed framework simplifying the meshing operations.

The electrophysiological problem coupled to the mechanics enables the modeling of the tissue contraction and relaxation according to the biology of the cells. Two alternative strategies, as discussed in Chapter 4, can be adopted to model such a phenomenon: the *active stress* and the *active strain* approaches. Both of them are applicable in the Galerkin framework. As demonstrated in Chapter 8, also the Isogeometric Collocation method offers the possibility of coupling the different meshes adopted for the two sub-problems and in a simple manner using nested meshes. Furthermore, in case of severe locking effects, the proposed  $\mathbf{u}$ - $p$  formulation can be integrated into the solver improving the accuracy of the simulation.

In the case where the mechanics is more efficiently discretized using the Galerkin method, for instance thin shell structures, the Collocation solver for electrophysiology may be coupled to the classical weak formulation to combine the strength of both methods. Indeed, thin films, nicely approximated by shells, are often employed in Organ-On-Chips. Such a tool can be used to investigate the time delay between the electrical stimulation and the mechanical contraction [207].

In the modeling of swimmers, presented in Chapter 5, the electromechanics is further coupled to the fluid dynamics defining a complex multiphysics problem. In this regard, we have combined several biophysical models and discretization techniques to define a high fidelity solver that simulates the swimming of a jellyfish. With this implementation, several parametric investigations on the efficiency of the swimming can be conducted.

The investigated framework offers a great potential, but further studies are needed. In particular, the Hybrid IgA-C/FCM method may be tested in the fluid dynamic context trying to incorporate the benefits of a strong formulation into the framework of Immersogeometric Analysis. Furthermore, the immersed approach may be used to remove part of the computational domain of the electrophysiological problem leaving the mechanical domain untouched. This approach may be used in simulations where pathologies affect the biological behavior of the cell, as in the case of infarction scars, leaving the coupling strategy untouched since both problems share the same mesh. In such a particular task, a conforming mesh of the geometry may reduce the computational effort linked to the quadrature. Therefore, the algorithm proposed for the geometrical reconstruction should be further improved.

Finally, the described methodology may be parallelized to implement an high performance software simulating the activity of the heart with biophysically detailed models.



# Appendix A

## Details on the engineered ventricle simulations

### A.1 Mapping procedure for unstructured surfaces

In this section, we present an alternative algorithm to map a surface, provided through a stereolithography file, using a B-spline manifold. Indeed, if the analytical formulation describing the surface is unknown, the definition of the relation that associates the points on the spline surface to the points in the real surface may be a complex task.

The procedure involves several steps, as shown in Fig. A.1. For illustration purposes, we apply the methodology to remap a portion of the apex of a real human left ventricle although it is not used in the present work. We note that, in this examples, the mapping procedure smooths some artifacts due to the extraction of the selected surface from the four chambers geometry, as shown in Fig. A.2.

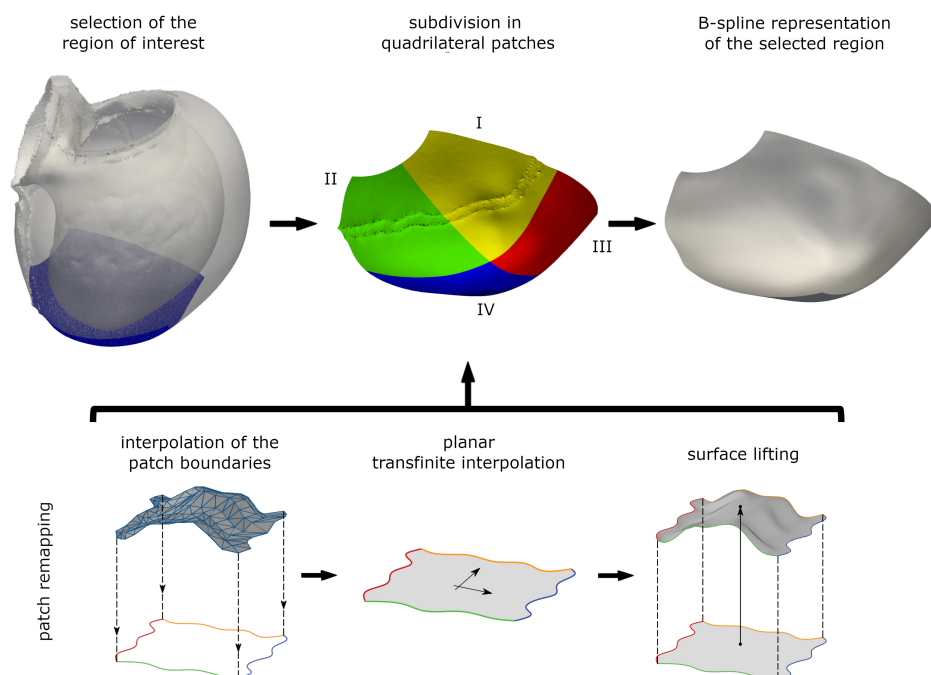


Figure A.1: Mapping procedure for stereolithography surfaces.

- The first step subdivides faceted surface in patches, requiring that every point in the patch can be projected on a predefined plane without intersecting the patch surface, clearly the choice of the plane can vary from patch to patch.

- Once the surface is subdivided in patches, we interpolate the flat projection of the 4 boundaries – subdivided using 4 user-defined points – using 2 sets of B-splines, adopting the same degree and knot vector on opposite edges.
- Given the planar interpolation of the 4 edges, we fill the flat spline surface by means of transfinite interpolation of the control point coordinates, as described in [368].
- The third coordinate, the elevation, of the points representing the manifold is retrieved by means of  $L_2$  projection, avoiding the definition of the ordering of the points. Indeed, the parametric coordinates of a point are mapped into the planar B-spline surface and then elevated interpolating the nodes coordinates of the original facet.
- Given the geometrical mapping of every patches, either we can use a multipatch-geometry or we can remap the surface into a single patch by means of  $L_2$  approximation, if the patch union constitutes a rectangle in the parametric space.

Unfortunately, this procedure suffers of two main limitations: (i) an algorithm for the automatic subdivision in patches is not yet implemented, and (ii) the transfinite interpolation may fails if the shape is highly concave. However, a proper patch subdivision may alleviate this second issue, demonstrating the importance of conducting investigations along this research line.



Figure A.2: Artifacts generated during the extraction of the selected surface from the four-chamber geometry.

Left: the complete geometry. Center: particular of the extracted stereolithography surface highlighted in the frame. Right: the corresponding result of the B-spline mapping procedure.

## A.2 Alternative organization of the convergence plots

In this section, we present the results shown in Section 3.3.1 organized by polynomial degrees instead of by basis function continuity.

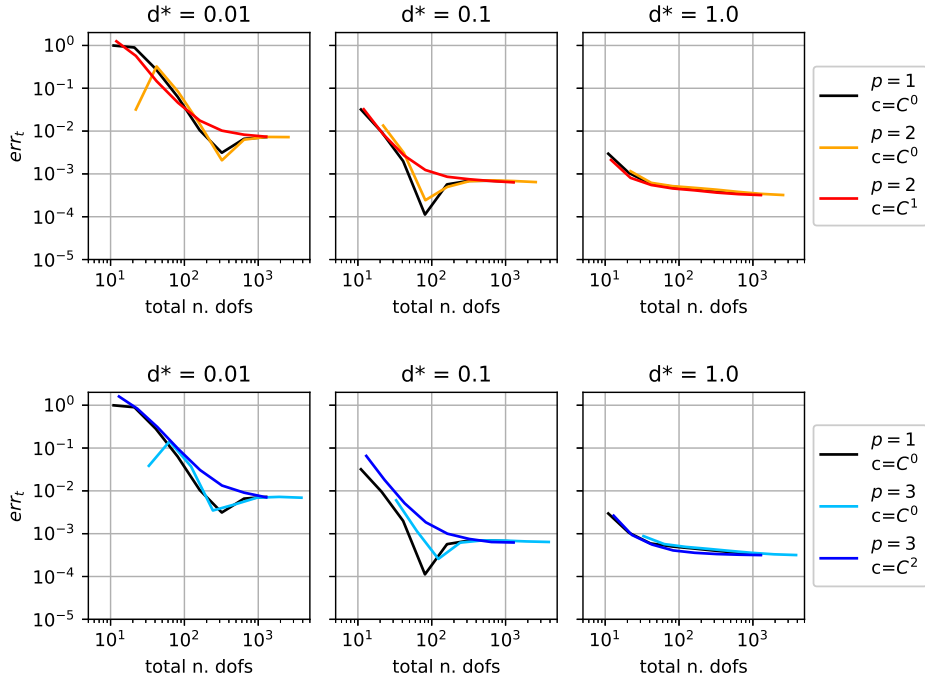


Figure A.3: Relative errors in the time trace for basis quadratic (top) and cubic (bottom) basis functions. The black curve, representing linear functions, is repeated in both plot for better comparison (cf., Figure 3.6).

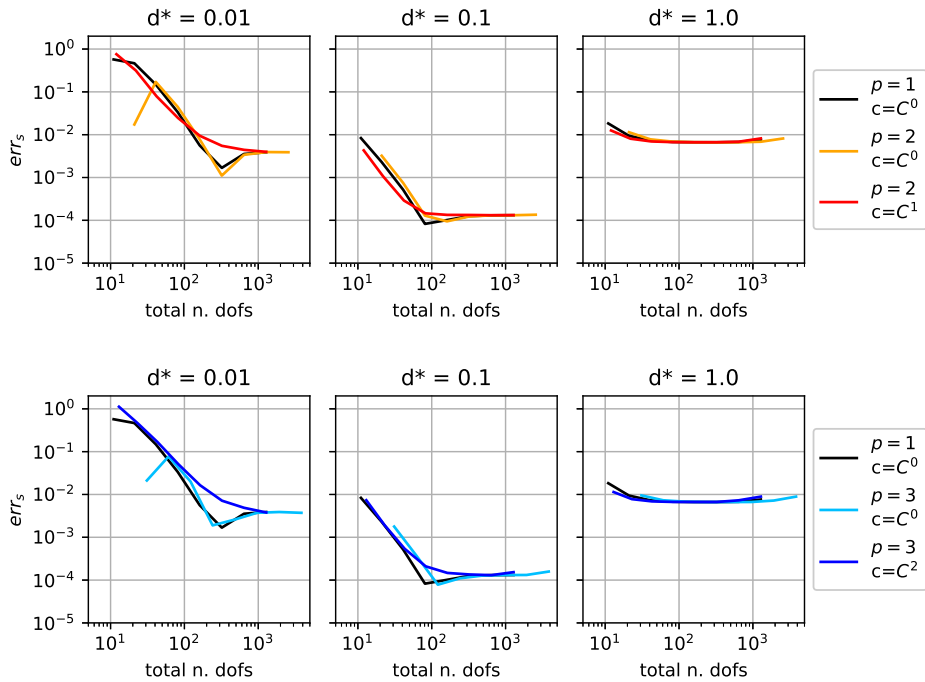


Figure A.4: Relative errors in the time trace for basis quadratic (top) and cubic (bottom) basis functions. The black curve, representing linear functions, is repeated in both plot for better comparison (cf. Figure 3.7).



# Appendix B

## Details on the jellyfish modeling

### B.1 Summary of physical parameter for the jellyfish model

Description	Symbol	value
Bell outer diameter	$2a_{ex}$	30 [mm]
Bell shear modulus	$c_{10}$	400 [Pa]
Bell bulk modulus	$K$	$5.0 \times 10^4$ [Pa]
Pacing frequency of electrophysiological stimulation	$\phi$	0.5 [Hz]
Peak radial muscle stretching	$a_1$	0 [-]
Peak coronal muscle stretching	$a_3$	0.096 [-]
Bell density	$\rho_s$	1200 [kg/m <sup>3</sup> ]
Active tissue capacitance	$C_m$	$1.0 \times 10^{-3}$ [mF/mm <sup>2</sup> ]
Active tissue conductivity	$D$	$1.3745 \times 10^{-5}$ [nA/(mm mV)]
Current magnitude for stimulation	$i_a$	0.1 [nA/mm <sup>3</sup> ]
Duration of applied current for stimulation	-	0.1 [ms]
Fluid density	$\rho_f$	1000 [kg/m <sup>3</sup> ]
Fluid viscosity	$\mu$	$1.0 \times 10^{-3}$ [Pa s]
Reynolds number	Re	1.0 450 [-]

Table B.1: Summary of physical parameters used for the baseline simulation whose results are presented in section 5.3.

### B.2 Validation of the structural solver

The elastic solver is initially verified against two benchmark problems for which the analytical solution is available. In second instance, the solver is tested against two nonlinear cases undergoing finite displacements and finite strains, and the solutions are compared with those obtained with the commercial software Abaqus [357].

#### B.2.1 Linear analysis

At first, a thick cylindrical tube with constant thickness and an inner pressure load has been simulated. The cylinder has inner and outer radii equal to  $R_i = 0.5$  m and  $R_o = 1.0$  m, respectively. Axial displacements are constrained on both cylinder ends. For a slender tube, the radial displacement approaches the analytical solution of a thick cylinder with infinite length under internal pressure [369]:

$$u_r(r) = p \frac{R_i^2(1 + \nu)(R_o^2 + r^2(1 - 2\nu))}{E(R_o^2 - R_i^2)r}. \quad (\text{B.1})$$

In the present case the IGA solution was obtained by using:  $E = 100$  MPa,  $\nu = 0.3$ ,  $p = 0.1$  MPa. Fig. B.1 provides the comparison with the analytical solution. The successful output of this test certifies the effectiveness of the formulation for a configuration with non-unitary, orthogonal local bases.

In second instance, a test-case entailing also non-orthogonal bases is considered. In the field of linear analysis, we simulate a thick hollow sphere subjected to a uniform external pressure. The analytical solution is available from [370] in terms of radial displacement as a function of the radial position:

$$u_r(r) = r \frac{-pR_o^3}{E(R_o^3 - R_i^3)} (1 - 2\nu) + \frac{1}{r^2} \frac{-pR_i^3 R_o^3}{2E(R_o^3 - R_i^3)} (1 + \nu). \quad (\text{B.2})$$

Our simulation was run with the following parameters:  $R_i = 0.5$  m,  $R_o = 1.0$  m,  $E = 100$  MPa,  $\nu = 0.3$ ,  $p = 0.1$  MPa. Unlike the previous test-case, this entails the symmetry axis crossing a solid part of the body. The replication of the analytical solution (see Fig. B.2a) ensures the robustness of the present implementation in presence of quadrature points close to the symmetry axis [38]. One quarter of a circle is simulated, where the tangential displacement is prevented on the equatorial line. The distribution of the radial displacement is checked at different tangential locations. Furthermore, a convergence analyses under h- and p-refinement is performed to check if the integration over the near axis elements degrades the accuracy of the method. The theoretical accuracy is confirmed with quadratic, cubic, and quartic basis functions (see Fig. B.2b).

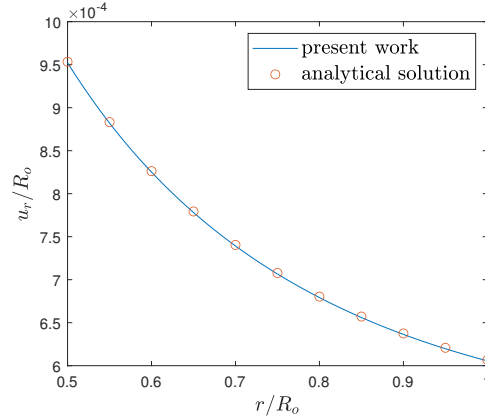


Figure B.1: Radial displacement as a function of the radial coordinate for a thick cylindrical tube subjected to uniform internal pressure.

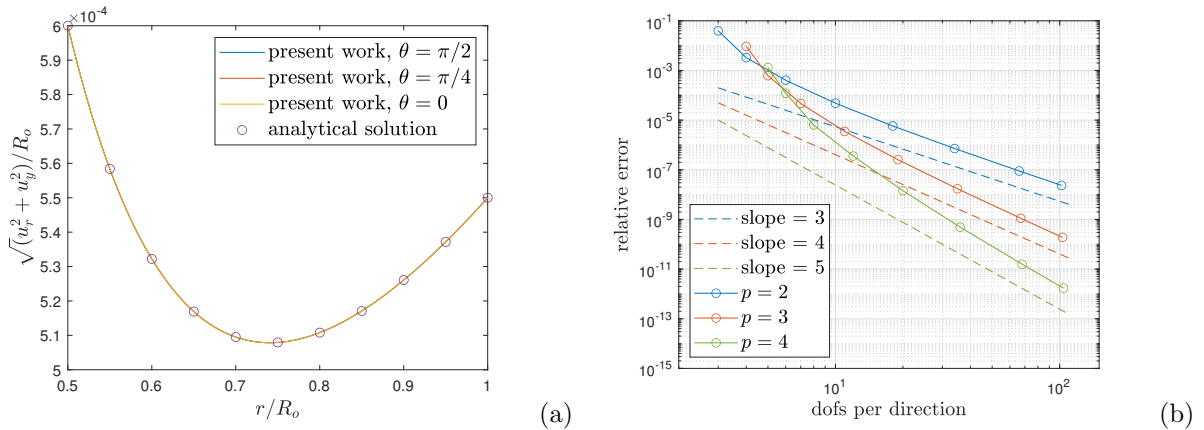


Figure B.2: Radial displacement of a thick hollow sphere subjected to external pressure as a function of the radial coordinate, for different tangential location (a). Convergence of the error in the local displacement under h-refinement for different basis function orders (b).

## B.2.2 Nonlinear analysis

A cantilever thick tube subjected to internal pressure load is simulated. Boundary and loading conditions are illustrated in the sketch in Fig. B.3a, along with the deformed configuration. For the present test, the compressible Neo-Hookean strain energy function (5.13) is employed. The chosen physical parameters are:  $h = 1.5$  m,  $R_i = 0.5$  m,  $R_o = 0.8$  m,  $p = 0.2$  MPa,  $c_{10} = 0.5$  MPa,  $K = 1000$  MPa. An accurate IGA solution is achieved with 200 cubic elements, which are able to replicate the Abaqus solution obtained with 4500 CAX8H elements. The numerical solutions have been compared in Fig. B.3b by superposing the radial and axial displacement on the outer profile of the cylinder.

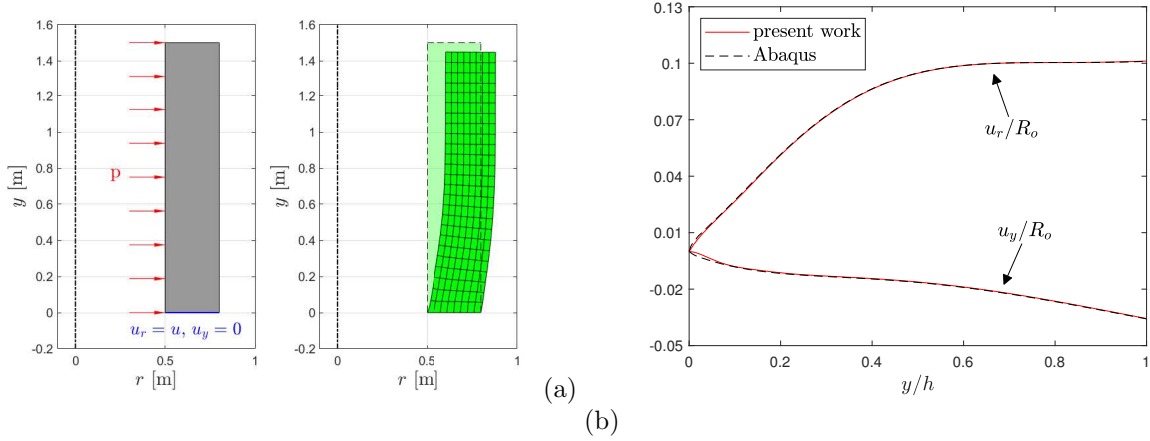


Figure B.3: Boundary and loading conditions for a cantilever nonlinear cylinder subjected to inner pressure, superposition of reference and deformed configurations (a). Radial and axial displacement as a function of the axial coordinate at the outer cylinder profile (b).

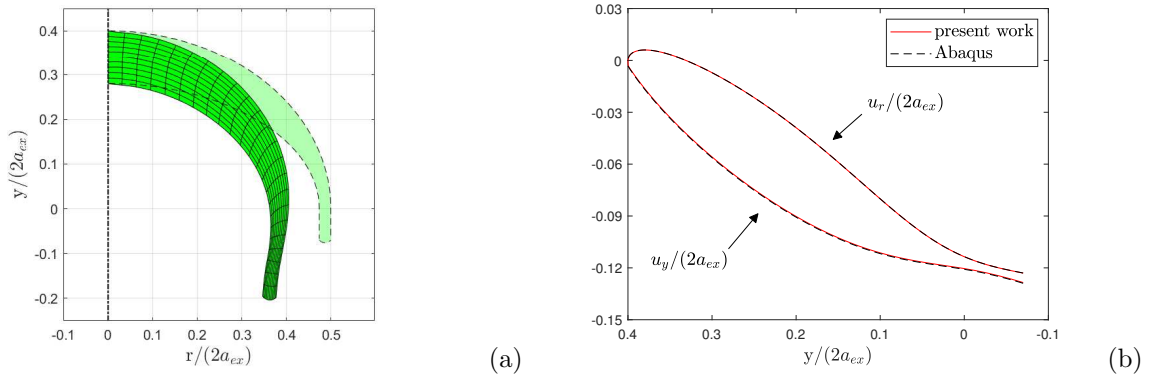


Figure B.4: Superposition of reference and deformed configurations for a jellyfish model subjected to uniformly distributed horizontal force (a). Radial and axial displacement as a function of the axial coordinate at the outer jellyfish profile (b).

Eventually, the previously described jellyfish geometry was tested with a uniformly distributed radial loading (no displacement-dependent loading) applied on the inner elliptical profile. The force magnitude was calibrated such that the target radial displacement corresponds to a 40% reduction of the cross section area at the bell margin. This represents the largest deformation achieved in our simulation, according to the experimental observations of [292]. In the present test the bell is pinned at the symmetry axis and subjected to a uniformly distributed radial load, obtained by projecting the stress value  $p = 2.5$  Pa onto the radial directors over the inner edge. The material law follows Eq. (5.13), and the material parameters are  $c_{10} = 21.67$  Pa,  $K = 4.33 \times 10^4$  Pa. The simulation was carried out with 230 cubic elements, and results are compared with those obtained with Abaqus (see Fig. B.4). The Abaqus simulation was

run with 13800 CAX4H elements by using the mixed pressure-displacement formulation to alleviate locking effects. With the Abaqus displacement formulation a nearly incompressible material subjected to very large displacement exhibits severe locking effects [353]. The agreement of the IGA solution with the Abaqus output proves that the present implementation with cubic basis functions does not suffer from relevant locking effects, therefore no special treatment is needed. In the present simulation the bulk modulus  $K$  yields a volume variations equal to -0.0088%, which nearly fulfills the incompressibility condition. We verified that similar volume variations are obtained when achieving the maximal bell contraction with the active strain approach.

### B.3 Validation of the electrophysiological solver

The consistency of the discrete solution of the monodomain problem (Eq. (5.55)) is verified by separately assessing the diffusion and reaction contributions. The diffusion effect is verified by solving the axisymmetric heat equation for the generic scalar field  $\phi$  over a plane circular domain. We consider a disk of radius  $R = 40$  m, with Dirichelet boundary conditions  $\phi = 1$  prescribed at the domain edge. We assume a thermal diffusivity  $k = 60.0$  m<sup>2</sup>/s. The initial solution consists of  $\phi = 0$  all over the inner nodes. Initial solution and boundary conditions entail an axisymmetric diffusion process, where  $\phi$  gradually settles to  $\phi = 1.0$  in the whole domain. One should bear in mind that the solution substantially differs from that arising from the diffusion over a cable due to tangential diffusion effects.

The problem is solved up to  $t = 2.0$  s over a 1D domain discretized by 600 quadratic elements. A time step size equal to  $\Delta t = 0.01$  s is employed. The analytical solution used as reference is obtained by means of the Bessel functions of the first type  $J_0(r)$  and its derivative  $J_1(r)$ , as shown in [371]:

$$\phi(r, t) = 1 - 2 \sum_{n=1}^{\infty} \frac{J_0(\alpha_n r/R)}{\alpha_n J_1(\alpha_n)} \exp(-\alpha_n^2 k t / R^2), \quad (\text{B.3})$$

where  $\alpha_n$  is the n-th positive zero of  $J_0(r)$ . Numerical and analytical solutions are found to coincide at subsequent time steps, as shown in Fig. B.5. Furthermore, the solution is observed to have null gradient at the symmetry axis, testifying the correctness of the implementation.

The reaction effects are validated by integrating the ordinary differential equation associated with the pure neuronal activity, and comparing the time-traces of the action potential with data reported in [286].

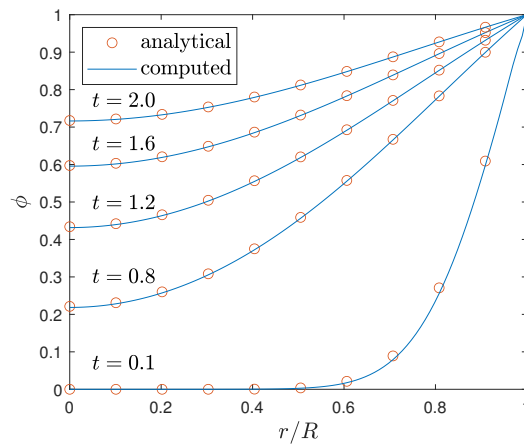


Figure B.5: Axisymmetric solution of the heat equation over a disk with symmetry-Dirichelet boundary conditions, at subsequent time instants and comparison with the analytical solution (B.3).

## B.4 Validation of the flow solver

### B.4.1 Laminar vortex ring formation

Vortex rings are fundamental features for the propulsion of oblate species [277]. The simulation of vortex-dominated flows requires the conservation of circulation and kinetic energy to a relatively tight tolerance to ensure that spurious vorticity is not generated. The present scheme, inspired to the work of [290], does preserve these properties in absence of viscosity and time differencing errors. In this regard, simulations of an impulsively started jet are performed to check the formation and evolution of a laminar vortex ring. The test case consists of a cylindrical domain where a coaxial inflow jet impulsively produces a shear layer which evolves into an axisymmetric vortex ring. This actually mimics the jet produced by a piston moving a fluid column through an orifice of diameter  $D$ . At time  $t = 0$  the flow inside the computational domain is assumed to be at rest. At the inlet the hyperbolic tangent profile is specified:

$$q_2(r, t) = \frac{1}{2}U_p(t) \left[ 1 - \tanh \left( \frac{2}{\delta_w} \left( \frac{r}{D} - \frac{1}{2} \right) \right) \right], \quad (\text{B.4})$$

where  $\delta_w$  is the width of the shear layer at the inlet, and  $U_p(t)$  provides the time program, defined as:

$$\frac{U_p(t)}{U} = \begin{cases} \frac{1}{2} \left[ 1 - \cos \left( \pi \frac{t}{t_1} \right) \right], & t \leq t_1 \\ 1.0, & t_1 < t \leq t_2 \\ \frac{1}{2} \left[ 1 + \cos \left( \pi \frac{t - t_2}{t_1} \right) \right], & t_2 < t \leq t_1 + t_2 \\ 0.0, & t > t_1 + t_2 \end{cases} \quad (\text{B.5})$$

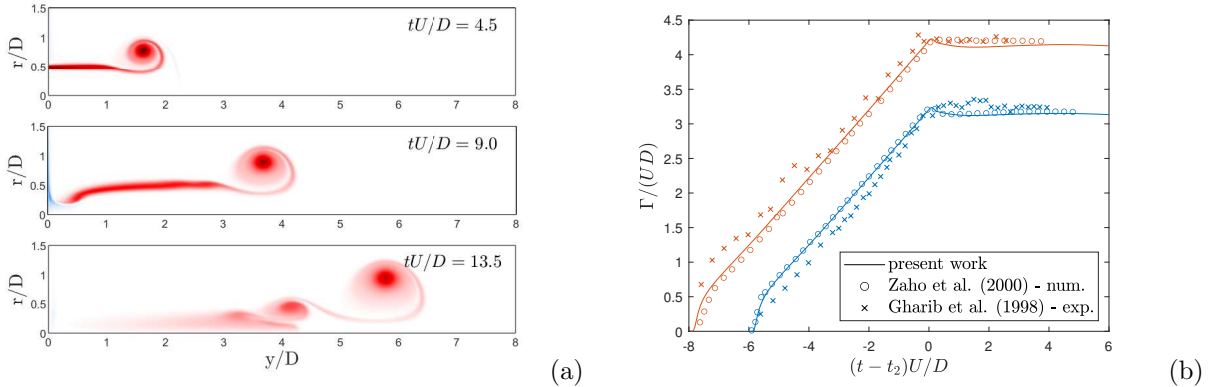


Figure B.6: Instantaneous vorticity contours showing the detachment of the head vortex ring at three successive time instants for the case  $t_2 = 8U/D$  (a). Comparison between present numerical predictions and available measurements for total circulation. Blue refers to the stroke time  $t_2 = 6U/D$ , whereas orange refers to  $t_2 = 8U/D$  (b).

Here,  $t_1$  is the acceleration/deceleration time of the piston, and  $t_2$  represents the stroke ratio. For all cases the piston acceleration was set to  $t_1Um/D = 0.3$  to match the piston motion described in the experiments of [372]. We used a computational domain of extension  $[0, 15D] \times [0, 6D]$  with minimal grid size  $\Delta y = D/60$  and constant time step size  $\Delta t = 0.002U/D$ . A free-slip condition is enforced at the outer radial wall, whereas a radiative outflow conditions is employed for the outlet profile. We present two cases for which both computational [373] and experimental [372] data are available. The first is defined by  $\delta_w = 0.04$ ,  $t_2 = 6U/D$ ,  $\text{Re} = 3100$ , whereas the second by:  $\delta_w = 0.05$ ,  $t_2 = 8U/D$ ,  $\text{Re} = 3100$ . The time traces of the dimensionless circulation  $\Gamma/(UD)$ , plotted in Fig. B.6, reveal full consistency with both experimental and computational data. A qualitative comparison can be carried out by superposing the instantaneous contours of vorticity  $\omega = \partial q_2/\partial r - \partial q_1/\partial y$  in Fig. B.6(a) with those illustrated in the reference [373].

case	$\rho$	$U_\infty$	Re	Fr
C1	1.167	0.128	31.9	0.334
C2	1.164	0.091	11.6	0.237
C3	1.161	0.060	4.1	0.156

Table B.2: Density ratio, settling velocity in infinite medium, Reynolds number and Froude number used in the simulations of a sphere settling under gravity in a closed container.

### B.4.2 Sphere settling under gravity

Eventually, a well-established FSI benchmark test involving axisymmetric flow fields is replicated. The reference work [374] provides an experimental investigation of a sphere settling under gravity in a tank. Measurements carried out by particle image velocimetry, provided the sphere trajectory and velocity, from the moment of its release until rest at the bottom of the tank. The small dimension of the container used in the experiments allows to simulate the flow field under very similar conditions. In the experiments a liquid free surface exists at the top of the domain, whereas we use the no-slip condition at the top of the domain. Several researchers also reproduced the same test with a similar computational setting obtaining a satisfactory agreement with experimental data [375, 376]. Half of the sphere is simulated with a local Eulerian resolution of  $\Delta = D/50$ . The simulation is initialized with the sphere hanging at  $8.5D$  from the domain edge and the fluid in a quiescent state. The domain has extension  $[0, 10.67D] \times [0, -3.33D]$  with no-slip boundary conditions on every boundary, except the symmetry axis. The sphere is allowed to precipitate until it touches the domain boundary. No special treatment is implemented to solve the lubrication layer, but the simulation is stopped when the body approaches the last inner node before the edge. However, the fluid resolution was fine enough to capture the particle deceleration and the formation of an axisymmetric vortex dipole in the wall-approaching phase. The governing parameters of the system are the phase density ratio  $\rho$ , and the particle diameter  $D$ . We keep the latter constant and run three cases with different  $\rho$  values. This inherently leads to different sedimentation velocities and consequently different Reynolds and Froude numbers (parameters listed in table B.2).

The sedimentation trajectory and the sphere velocity are reported in Fig. B.7, where the present results are compared with the experimental data of Ten Cate et al. [374]. A very good agreement is obtained for all the considered configurations.

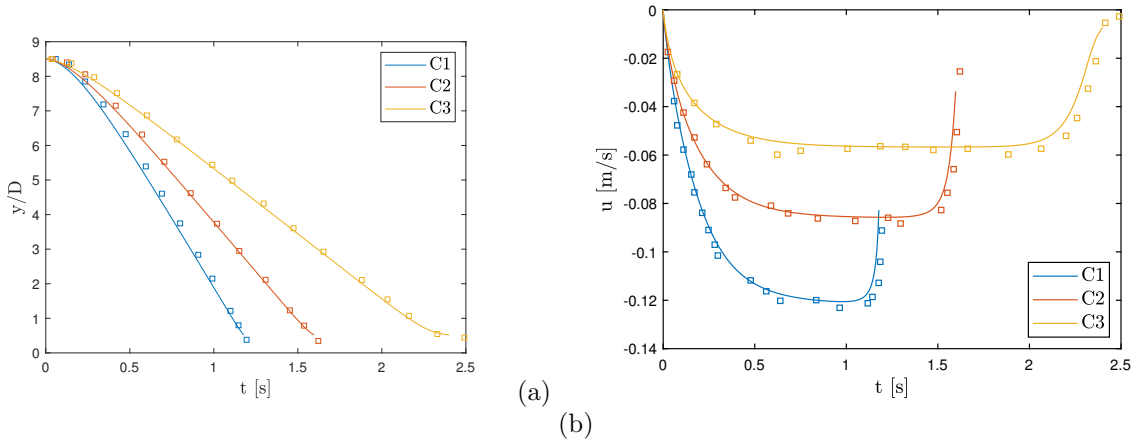


Figure B.7: Time-traces of position (a) and velocity (b) for a sphere settling under gravity for different phase density ratios. Markers denote the data from [374], whereas lines indicates the numerical solution.

## Appendix C

# Details on the Isogeometric collocation method for electrophysiology

### C.1 Stiffness matrix for the case of non-constant conductivity tensor

The stiffness matrix is given by the discretization of the diffusion term

$$\frac{\lambda}{\chi C_m (\lambda + 1)} \nabla \cdot (\mathbf{D} \nabla v). \quad (\text{C.1})$$

If the conductivity tensor  $\mathbf{D}$  is not uniform through the computational domain, also the derivatives of this term have to be computed:

$$\frac{\lambda}{\chi C_m (\lambda + 1)} (\mathbf{D}_{ij} \nabla v_{,ji} + \mathbf{D}_{ij,i} \nabla v_{,j}), \quad (\text{C.2})$$

and an additional term in eq. (3.35) arises:

$$\mathbf{K}_{\alpha s} = \frac{\lambda}{\chi C_m (\lambda + 1)} \left[ \mathbf{D}_{ij} (\tilde{\boldsymbol{\xi}}_\alpha) \mathbf{N}_{s,ji} (\tilde{\boldsymbol{\xi}}_\alpha) + \mathbf{D}_{ij,i} (\tilde{\boldsymbol{\xi}}_\alpha) \mathbf{N}_{s,j} (\tilde{\boldsymbol{\xi}}_\alpha) \right]. \quad (\text{C.3})$$

The general expression of the conductivity tensor is provided by the form [200]:

$$\mathbf{D}_{ij}(\mathbf{x}) = \sigma_f(\mathbf{x}) f_i(\mathbf{x}) f_j(\mathbf{x}) + \sigma_s(\mathbf{x}) s_i(\mathbf{x}) s_j(\mathbf{x}) + \sigma_m(\mathbf{x}) m_i(\mathbf{x}) m_j(\mathbf{x}). \quad (\text{C.4})$$

The three conductivity values  $\sigma_f$ ,  $\sigma_s$ , and  $\sigma_m$  correspond to principal fiber directions  $\mathbf{f}$ ,  $\mathbf{s}$ , and  $\mathbf{m}$ .

### C.2 Computation of the derivatives of the basis functions with respect to the physical coordinates

The physical geometry is defined as a linear combination of basis functions and control point coordinates

$$\mathbf{x} = \mathbf{x}(\xi, \eta, \zeta) = \mathbf{x}(\boldsymbol{\xi}) = \mathbf{N}_c(\boldsymbol{\xi}) \mathbf{B}_c, \quad (\text{C.5})$$

leading to the following relation for a single physical coordinate:

$$x_i = \mathbf{N}_c[\mathbf{B}_c]_{(i)}. \quad (\text{C.6})$$

Moreover, the geometrical mapping from the parametric to the physical space is locally invertible, therefore:

$$\boldsymbol{\xi} = \mathbf{x}^{-1}(\mathbf{x}(\boldsymbol{\xi})). \quad (\text{C.7})$$

The first derivative of a basis function with respect to the physical coordinates in a given point  $\{N_{s,i}|_{\mathbf{x}_\alpha}$ , using the chain rule

$$\frac{\partial N_s}{\partial \xi_j} = \frac{\partial N_s}{\partial x_i} \frac{\partial x_i}{\partial \xi_j}, \quad (\text{C.8})$$

is expressed as:

$$\left\{ \frac{\partial N_s(\boldsymbol{\xi})}{\partial x_i} \right\}_{\mathbf{x}_\alpha} = \left\{ \frac{\partial N_s(\boldsymbol{\xi})}{\partial \xi_j} \right\}_{\boldsymbol{\xi}_\alpha} \left[ \left\{ \frac{\partial x_i}{\partial \xi_j} \right\}_{\boldsymbol{\xi}_\alpha} \right]^{-1} = \left\{ \frac{\partial N_s(\boldsymbol{\xi})}{\partial \xi_j} \right\}_{\boldsymbol{\xi}_\alpha} \left[ \left\{ \frac{\partial N_c(\boldsymbol{\xi})}{\partial \xi_j} [\mathbf{B}_c]^{(i)} \right\}_{\boldsymbol{\xi}_\alpha} \right]^{-1}. \quad (\text{C.9})$$

For the calculation of the second derivative, we apply the chain rule recursively

$$\frac{\partial^2 N_s}{\partial \xi_j \partial \xi_k} = \frac{\partial^2 N_s}{\partial x_q \partial x_i} \frac{\partial x_q}{\partial \xi_j} \frac{\partial x_i}{\partial \xi_k} + \frac{\partial N_s}{\partial x_i} \frac{\partial^2 x_i}{\partial \xi_j \partial \xi_k} \quad (\text{C.10})$$

and the previous results in solving the linear system:

$$\left\{ \frac{\partial^2 N_s}{\partial x_q \partial x_i} \right\}_{\mathbf{x}_\alpha} = \left[ \left\{ \frac{\partial x_q}{\partial \xi_j} \right\}_{\boldsymbol{\xi}_\alpha} \left\{ \frac{\partial x_i}{\partial \xi_k} \right\}_{\boldsymbol{\xi}_\alpha} \right]^{-1} \left[ \left\{ \frac{\partial^2 N_s}{\partial \xi_j \partial \xi_k} \right\}_{\boldsymbol{\xi}_\alpha} - \left\{ \frac{\partial N_s}{\partial x_i} \right\}_{\boldsymbol{\xi}_\alpha} \left\{ \frac{\partial^2 x_i}{\partial \xi_j \partial \xi_k} \right\}_{\boldsymbol{\xi}_\alpha} \right]. \quad (\text{C.11})$$

### C.3 Implicit-Explicit Euler time discretization scheme without splitting operator

The collocation approach can be applied to the monodomain equation independently of the Godunov operator. We prove it using an implicit–explicit time integration scheme for both the approaches. Moreover, all the arguments proved in the main part of the text are not affected by this modification in the time discretization scheme.

SVI-C:

$$\left[ \frac{\bar{\mathbf{M}} - \Delta t \mathbf{K}}{\mathbf{R}} \right] \hat{\mathbf{v}}_{n+1} = \left[ \frac{\tilde{\mathbf{v}}_n}{\mathbf{0}} \right] - \frac{\Delta t}{C_m} \left[ \frac{\tilde{\mathbf{I}}_n^{ion}}{\mathbf{0}} \right] + \frac{\Delta t}{\chi C_m} \left[ \frac{\tilde{\mathbf{I}}_{n+1}^{app}}{\mathbf{0}} \right] \quad (\text{C.12})$$

$$\begin{cases} \tilde{\mathbf{w}}_{n+1}^s = \tilde{\mathbf{w}}_n^s + \Delta t \tilde{\mathbf{m}}_{w_n}^s & \forall s = 1, \dots, k \\ \tilde{\mathbf{c}}_{n+1}^s = \tilde{\mathbf{c}}_n^s + \Delta t \tilde{\mathbf{m}}_{c_n}^s & \forall s = 1, \dots, q \\ \tilde{\mathbf{I}}_{n+1}^{ion} = \tilde{\mathbf{I}}^{ion}(\tilde{\mathbf{x}}, \tilde{\mathbf{v}}_{n+1}, \tilde{\mathbf{w}}_{n+1}^1, \dots, \tilde{\mathbf{w}}_{n+1}^k, \tilde{\mathbf{c}}_{n+1}^1, \dots, \tilde{\mathbf{c}}_{n+1}^q) \end{cases} \quad (\text{C.13a})$$

$$\tilde{\mathbf{c}}_{n+1}^s = \tilde{\mathbf{c}}_n^s + \Delta t \tilde{\mathbf{m}}_{c_n}^s \quad \forall s = 1, \dots, q \quad (\text{C.13b})$$

$$\tilde{\mathbf{I}}_{n+1}^{ion} = \tilde{\mathbf{I}}^{ion}(\tilde{\mathbf{x}}, \tilde{\mathbf{v}}_{n+1}, \tilde{\mathbf{w}}_{n+1}^1, \dots, \tilde{\mathbf{w}}_{n+1}^k, \tilde{\mathbf{c}}_{n+1}^1, \dots, \tilde{\mathbf{c}}_{n+1}^q) \quad (\text{C.13c})$$

ICI-C:

$$\left[ \frac{\bar{\mathbf{M}} - \Delta t \mathbf{K}}{\mathbf{R}} \right] \hat{\mathbf{v}}_{n+1} = \left[ \frac{\tilde{\mathbf{v}}_n}{\mathbf{0}} \right] - \frac{\Delta t}{C_m} \left[ \frac{\bar{\mathbf{M}} \hat{\mathbf{I}}_n^{ion}}{\mathbf{0}} \right] + \frac{\Delta t}{\chi C_m} \left[ \frac{\tilde{\mathbf{I}}_{n+1}^{app}}{\mathbf{0}} \right] \quad (\text{C.14})$$

$$\begin{cases} \hat{\mathbf{w}}_{n+1}^s = \hat{\mathbf{w}}_n^s + \Delta t \hat{\mathbf{m}}_{w_n}^s & \forall s = 1, \dots, k \\ \hat{\mathbf{c}}_{n+1}^s = \hat{\mathbf{c}}_n^s + \Delta t \hat{\mathbf{m}}_{c_n}^s & \forall s = 1, \dots, q \\ \hat{\mathbf{I}}_{n+1}^{ion} = \hat{\mathbf{I}}^{ion}(\hat{\mathbf{v}}_{n+1}, \hat{\mathbf{w}}_{n+1}^1, \dots, \hat{\mathbf{w}}_{n+1}^k, \hat{\mathbf{c}}_{n+1}^1, \dots, \hat{\mathbf{c}}_{n+1}^q) \end{cases} \quad (\text{C.15a})$$

$$\hat{\mathbf{c}}_{n+1}^s = \hat{\mathbf{c}}_n^s + \Delta t \hat{\mathbf{m}}_{c_n}^s \quad \forall s = 1, \dots, q \quad (\text{C.15b})$$

$$\hat{\mathbf{I}}_{n+1}^{ion} = \hat{\mathbf{I}}^{ion}(\hat{\mathbf{v}}_{n+1}, \hat{\mathbf{w}}_{n+1}^1, \dots, \hat{\mathbf{w}}_{n+1}^k, \hat{\mathbf{c}}_{n+1}^1, \dots, \hat{\mathbf{c}}_{n+1}^q) \quad (\text{C.15c})$$

### C.4 Conduction velocity convergence in semi-logarithmic scale

In Fig. C.1, we present the conduction velocity convergence for the 1D cable model in a semi–logarithmic plot. To this end, we modify the error definition (6.29) avoiding the absolute value in the numerator.

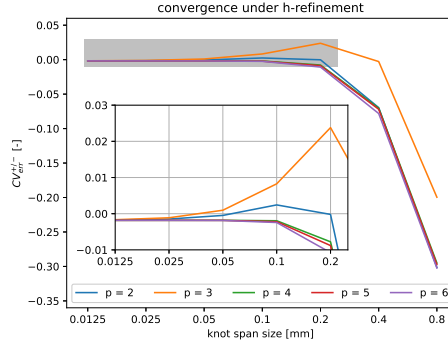


Figure C.1: Convergence under h-refinement of the 1D cable model using the SVI-C approach (cf. Fig 6.3(a)).

## C.5 Ionic current approximations for different knot span sizes

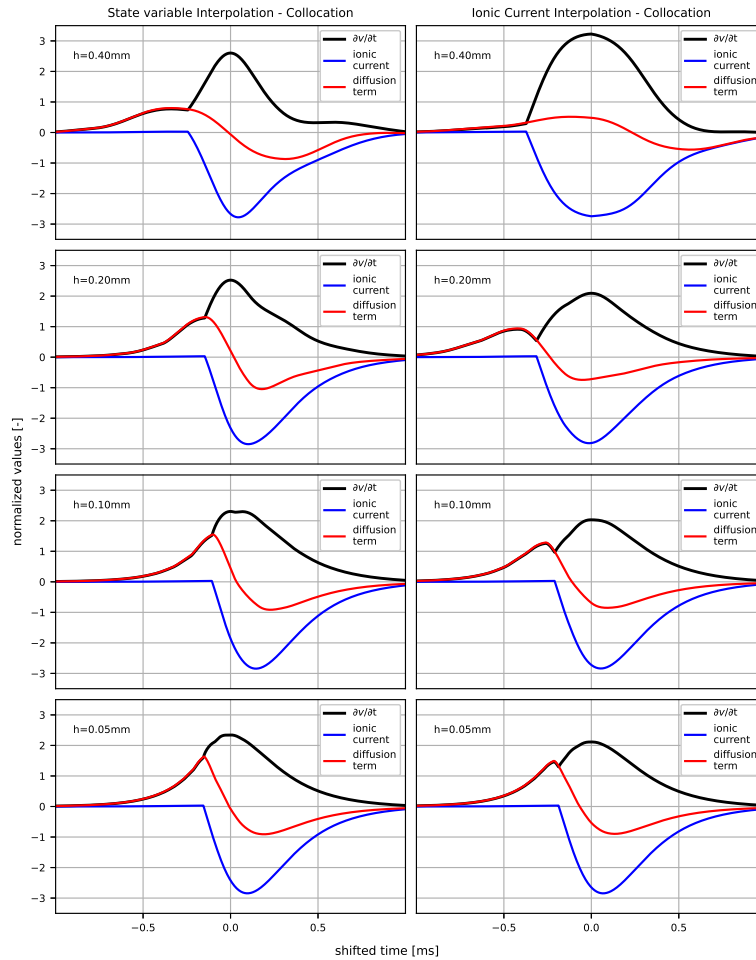


Figure C.2: Comparison between SVI-C and ICI-C approaches for several knot span sizes, fixed time step size  $dt = 0.00125$  ms and basis function degree  $p = 2$ . Reference solution is presented in Fig. 6.2.

In Fig C.2 we compare the SVI-C and the ICI-C approaches using different discretizations. Both methods converge to the reference solution, for a sufficiently fine discretization.



# Appendix D

## Details on the Hybrid Collocation/Finite Cell Method

### D.1 Equations in curvilinear coordinates

In this Section, we present the computation of the stiffness matrix using a curvilinear reference frame. The mass matrix and the right-hand side rely on the direct evaluation of scalar functions, that do not involve the computation of the derivatives. For a more details on the derivation, the reader is referred to [179, 245].

**Base vectors and curvilinear coordinates** The derivation we present is based on the representation of a manifold  $\boldsymbol{x} : \Omega \subset \mathbb{R}^2 \rightarrow \mathbb{R}^3$  through the following identities:

$$\boldsymbol{x} = x_j \mathbf{e}_j = \xi^\alpha \mathbf{g}_\alpha = \xi_\alpha \mathbf{g}^\alpha, \quad j = 1, 2, 3 \text{ and } \alpha = 1, 2 \quad (\text{D.1})$$

where  $\xi_\alpha$ ,  $\xi^\alpha$  are the co-variant and contra-variant coordinates and  $\mathbf{g}_\alpha$ ,  $\mathbf{g}^\alpha$  are the co-variant and contra-variant base vectors, respectively. In this derivation, the Greek indices take on values  $\{1, 2\}$ , while Latin indices take on values  $\{1, 2, 3\}$  excluded  $s$  and  $i$  that take on values  $\{1, \dots, m\}$ .

The co-variant base vectors are computed using the geometrical mapping Eq. (3.23):

$$\mathbf{g}_\alpha = \frac{\partial \boldsymbol{x}}{\partial \xi^\alpha} = \frac{\partial \mathbf{N}_s(\xi^1, \xi^2)}{\partial \xi^\alpha} \mathbf{B}_s \quad (\text{D.2})$$

and the third base vector, normal to the manifold, is given by

$$\mathbf{g}_3 = \frac{\mathbf{g}_1 \times \mathbf{g}_2}{\|\mathbf{g}_1 \times \mathbf{g}_2\|} \quad (\text{D.3})$$

The contra-variant base vectors are computed using the co-variant base:

$$\mathbf{g}^\alpha = g^{\alpha\beta} \mathbf{g}_\beta \quad (\text{D.4})$$

where the contra-variant metric coefficient  $g^{\alpha\beta}$  are obtained by the inverse of the co-variant coefficient matrix:

$$g^{\alpha\beta} = [g_{\alpha\beta}]^{-1} \quad (\text{D.5})$$

and the metric tensor  $g_{\alpha\beta}$  is given by:

$$g_{\alpha\beta} = \mathbf{g}_\alpha \cdot \mathbf{g}_\beta. \quad (\text{D.6})$$

In a 3D solid, the presented framework is generalized extending the range of the Greek indices to 3.

**Differential area** In the computation of the matrices, the 2D differential area  $dS$  arises in the integration. It is computed using the determinant of the metric tensor, as follows:

$$dS = \sqrt{|g_{\alpha\beta}|} d\xi^1 d\xi^2. \quad (\text{D.7})$$

**Gradient of the field** The gradient of the field  $v$ , according to [377] Eq. (2.62) pag. 48, is given by:

$$\nabla v = \frac{\partial v}{\partial \xi^\alpha} \mathbf{g}^\alpha = \frac{\partial v}{\partial \xi^\alpha} [g_{\alpha\beta}]^{-1} \mathbf{g}_\beta. \quad (\text{D.8})$$

Introducing the field approximation Eq. (7.2), the discrete form reads as follows:

$$\nabla v_j = \frac{\partial N_i}{\partial \xi^\alpha} \hat{v}_i [g_{\alpha\beta}]^{-1} \frac{\partial N_s}{\partial \xi^\beta} \mathbf{B}_{sj} \quad (\text{D.9})$$

**Conductivity tensor** The conductivity tensor  $\mathbf{D}$  is usually provided in cartesian coordinates  $\mathbf{D}_{ca}$ . To transform it in curvilinear coordinates  $\mathbf{D}_{cu}$ , we use the following procedure [179]:

$$\mathbf{D} = D_{ca}^{kj} (\mathbf{e}_k \otimes \mathbf{e}_j) = D_{cu}^{\alpha\beta} (\mathbf{g}_\alpha \otimes \mathbf{g}_\beta). \quad (\text{D.10})$$

Pre- and post- multiplying the matrix with the contravariant base vectors, we derive:

$$D_{cu}^{\alpha\beta} = D_{ca}^{kj} g_i^\alpha g_j^\beta. \quad (\text{D.11})$$

**Normal vector** Following the previous strategy, the normal vector  $\mathbf{n}$  in curvilinear coordinates is given by:

$$\mathbf{n} = n_i^{ca} \mathbf{e}_i = n_\alpha^{cu} \mathbf{g}^\alpha, \quad (\text{D.12})$$

$$n_\alpha^{cu} = n_i^{ca} g_{\alpha i} \quad (\text{D.13})$$

**Flux of the field** The flux  $\mathbf{f} = -\mathbf{D}\nabla v$  is computed as follows:

$$f^\alpha \mathbf{g}_\alpha = -D_{cu}^{\alpha\beta} (\mathbf{g}_\alpha \otimes \mathbf{g}_\beta) \frac{\partial v}{\partial \xi^\beta} \mathbf{g}^\beta \quad (\text{D.14})$$

and the discrete form reads as:

$$f^\alpha \mathbf{g}_\alpha = -D_{cu}^{\alpha\beta} \frac{\partial N_i}{\partial \xi^\beta} \hat{v}_i \mathbf{g}_\alpha. \quad (\text{D.15})$$

**Flux in the normal direction** In the imposition of the Neumann boundary conditions, the flux in the normal direction  $q = \mathbf{n} \cdot \mathbf{f}$  is computed as follows:

$$-q = n_\alpha^{cu} D_{cu}^{\alpha\beta} \frac{\partial N_i}{\partial \xi^\beta} \hat{v}_i. \quad (\text{D.16})$$

The product  $n_\alpha^{cu} D_{cu}^{\alpha\beta} \frac{\partial N_i}{\partial \xi^\beta}$  gives the term in Eq. (7.12) and part of the integrand in Eq. (7.15). It can be evaluated directly at the Greville abscissae or at the Gauss points to compute the stiffness matrix.

**Divergence of the flux** The divergence operator involved in the Poisson's-like equation can be written, according to [377] Eq. (2.135) pag. 60, as:

$$\nabla \cdot (\mathbf{D}\nabla v) = \frac{\partial}{\partial \xi^\alpha} \left( D_{cu}^{\beta\gamma} \frac{\partial v}{\partial \xi^\gamma} \mathbf{g}_\beta \right) \cdot \mathbf{g}^\alpha. \quad (\text{D.17})$$

Consequently, the discrete form reads as follows:

$$\nabla \cdot (\mathbf{D}\nabla v) = \left[ \frac{\partial D_{cu}^{\beta\gamma}}{\partial \xi^\beta} \frac{\partial N_i}{\partial \xi^\gamma} + D_{cu}^{\beta\gamma} \frac{\partial^2 N_i}{\partial \xi^\gamma \partial \xi^\beta} + D_{cu}^{\beta\gamma} \frac{\partial N_i}{\partial \xi^\gamma} \frac{\partial^2 N_s}{\partial \xi^\alpha \partial \xi^\beta} \mathbf{B}_{sk} \mathbf{g}_k^\alpha \right] \hat{v}_i. \quad (\text{D.18})$$

In the case of constant isotropic conductivity tensor:

$$\frac{\partial D_{cu}^{\beta\gamma}}{\partial \xi^\beta} = D_{ca}^{kj} \left[ \left( \mathbf{e}_k \cdot \frac{\partial \mathbf{g}^\beta}{\partial \xi^\beta} \right) (\mathbf{e}_j \cdot \mathbf{g}^\gamma) + (\mathbf{e}_k \cdot \mathbf{g}^\beta) \left( \mathbf{e}_j \cdot \frac{\partial \mathbf{g}^\gamma}{\partial \xi^\beta} \right) \right] \quad (\text{D.19})$$

and

$$\begin{aligned} \frac{\partial \mathbf{g}^\gamma}{\partial \xi^\alpha} = & -\frac{1}{2} \left( [g_{\alpha\gamma}]^{-1} [g_{\beta\delta}]^{-1} + [g_{\alpha\delta}]^{-1} [g_{\beta\gamma}]^{-1} \right) \left( \frac{\partial \mathbf{g}_\gamma}{\partial \xi^\alpha} \cdot \mathbf{g}_\delta + \mathbf{g}_\gamma \cdot \frac{\partial \mathbf{g}_\delta}{\partial \xi^\alpha} \right) \mathbf{g}_\beta \\ & + [g_{\gamma\beta}]^{-1} \frac{\partial \mathbf{g}_\beta}{\partial \xi^\alpha} \quad (\text{D.20}) \end{aligned}$$

These equations represent the stiffness matrix contributions in Eqs. (7.10) and (7.14).

## D.2 Convergence test for odd degrees

In this Section, we report the results of the 1D problem (cf., Fig. 7.3) for  $p = 3$  and  $p = 5$ : the convergence rates for odd degrees are equal to  $p - 1$ , as expected for the isogeometric collocation method [315, 30]. Although the hybrid IgA-C/FCM method is applicable to every degree  $p \geq 2$ , its performance is clearly reduced when odd degrees are employed, if the images of the Greville abscissae are used as collocation points. Indeed, (i) the increased burden for the solution of the linear system (due to the denser matrix structure) [31], (ii) the higher effort for array formation [31], and (iii) the greater cost for quadrature in the immersed part of the domain (i.e.,  $p + 1$  Gauss points per parametric direction per cell) [158] may not be compensated by a substantial improvement in the accuracy when compared to even basis functions of one degree lower, as shown in Fig. D.1. This reduction in the cost-effectiveness is even more pronounced in higher dimensional domains (e.g., in a 2D domain), where the advantages of the collocation method are more appealing [31].

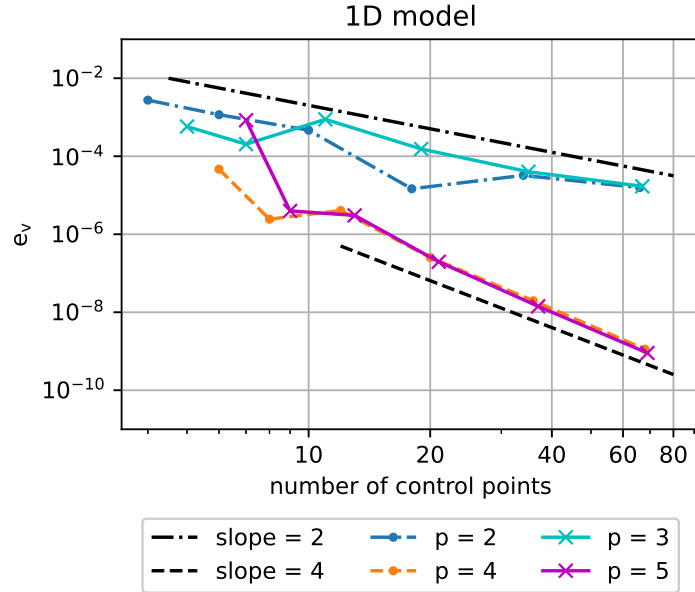


Figure D.1: Results of the convergence test presented in Sec. 7.3.1 for  $p = 3$  and  $p = 5$ . For better comparison, the results for  $p = 2$ ,  $p = 4$ , and the corresponding rates of convergence are reported as well.

## D.3 Solution of the Poisson's-like problem on a hollow 2D space

In the example in Sec. 7.3.2, we compare the numerical simulation and the analytical solution of the Poisson's-like problem. To this end, herein we derive the analytical solution and then we provide the simulation setup.

We investigate the diffusion phenomenon in a homogeneous isotropic 2D plane cut by a circular hole and subject to a flux, and no distributed source, as schematically depicted in Fig. D.2. Specifically, we

assume that at infinite distance from the hole, the field is unperturbed and the flux is oriented in the X-direction. The adiabatic circular boundary introduces a perturbation in the field near to the origin, that is the focus of this study.

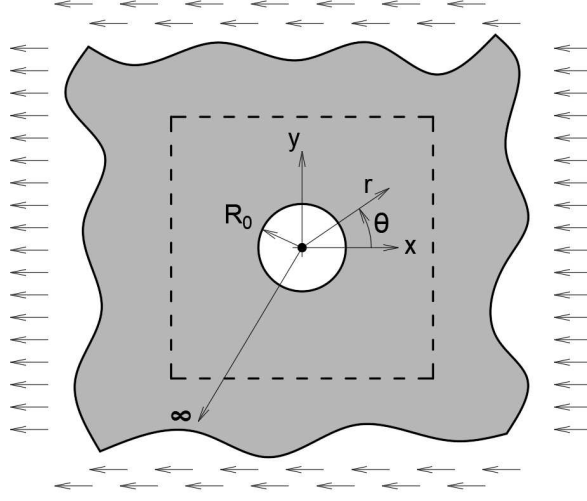


Figure D.2: Schematic representation of the problem in Sec. 7.3.2.

The boundary value problem reads as follows:

$$\begin{cases} \text{D}\nabla^2 v = 0 & \text{in } \Omega & \text{(D.21a)} \\ \text{D}\mathbf{n} \cdot \nabla v = 0 & \text{on } r = R_0 & \text{(D.21b)} \\ \text{D}\nabla v = q\mathbf{e}_x & \text{on } r = \infty, & \text{(D.21c)} \end{cases}$$

or in polar coordinates:

$$\begin{cases} \frac{\partial^2 v}{\partial r^2} + \frac{1}{r} \frac{\partial v}{\partial r} + \frac{1}{r^2} \frac{\partial^2 v}{\partial \theta^2} = 0 & \text{in } \Omega & \text{(D.22a)} \\ \frac{\partial v}{\partial r} = 0 & \text{on } r = R_0 & \text{(D.22b)} \\ \begin{pmatrix} \frac{\partial v}{\partial r} \\ \frac{1}{r} \frac{\partial v}{\partial \theta} \end{pmatrix} = \frac{q}{D} \begin{pmatrix} \cos \theta \\ -\sin \theta \end{pmatrix} & \text{on } r = \infty. & \text{(D.22c)} \end{cases}$$

In the following, we assume  $D = 100$  and  $q = 100$ .

Using the separation of variables technique, we split  $v$  as:  $v = \rho(r)\phi(\theta)$ , Eq. (D.22a) leads to:

$$r^2 \frac{\rho''}{\rho} + r \frac{\rho'}{\rho} = \lambda = -\frac{\phi''}{\phi}, \quad \text{(D.23)}$$

where we use the apostrophe to represent the total derivative operator. Solving the second part of the equation, taking advantage of the periodicity  $\phi(0) = \phi(2\pi)$  and symmetry of the solution  $\phi(\theta) = \phi(-\theta)$ , we compute the the function:

$$\phi(\theta) = \sum_{n=1}^{+\infty} c_n \cos(n\theta), \quad \sqrt{\lambda} = n = 1, 2, \dots, +\infty. \quad \text{(D.24)}$$

The first part of Eq. (D.23) leads to the homogeneous Euler's differential equation, whose general solution is:

$$\rho(r) = \sum_{n=1}^{+\infty} a_n r^n + b_n r^{-n} \quad \text{(D.25)}$$

Combining Eqs. (D.24) and (D.25), we obtain:

$$v = \sum_{n=1}^{+\infty} a_n r^n \cos(n\theta) + b_n r^{-n} \cos(n\theta) \quad (\text{D.26})$$

and imposing the boundary conditions we solve the boundary value problem:

$$v(r, \theta) = \left( r + \frac{R_0^2}{r} \right) \cos(\theta). \quad (\text{D.27})$$

To reduce the computational effort in the numerical simulation, we restrict the computational domain to a unit square centered in the origin, as depicted in Fig. D.2. To be coherent with the analytical solution, we use it as essential boundary condition on the square sides.

## D.4 Transient problem on a curved manifold

In this test, the geometry, shown in Fig. D.3, is defined using a stereolithography file. The manifold spans the space  $X \in (0, 1)$ ,  $Y \in (0, 1)$ , the curvature radius in the  $Z$ -direction is equal to  $R = 1$ , and the internal hole is approximately a circle of radius  $r = 0.1$ . The boundary fitted finite element simulation imports the .stl file to define the geometry, whereas the geometry for Hybrid IgA-C/FCM approach is an approximation of it by means of B-spline surface.

In the simulations, we impose homogeneous Neumann boundary conditions at the internal boundary and at the straight edges oriented in the  $Y$ -direction, whereas essential boundary conditions are applied to the curved edges oriented in  $X$ -direction. In particular, the side  $Y = 0$  generates the wave increasing the value of  $v$  from 0 to 1.

As in previous simulations, the diffusion coefficient is assumed  $D = 100$ , the capacitance is  $C_m = 1$  and the time step size employed in the implicit Euler method is  $\Delta t = 5 \times 10^{-5}$ .

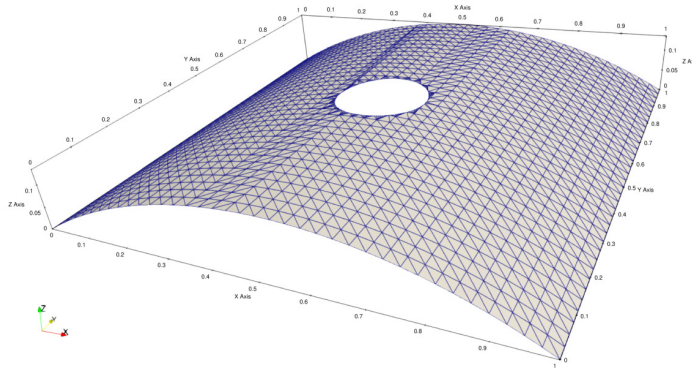


Figure D.3: Stereolithographic geometry of the curved manifold analyzed in Sec. 7.3.3.



# Appendix E

## Details on the Isogeometric Collocation method for coupled electromechanics

### E.1 Simulation setup for the nearly-incompressible cube

In this Section we provide the details on the simulation setup of the analysis shown in Fig. 8.1.

A unit cube  $X, Y, Z \in (0, 1)$  is loaded such that an analytical solution for the displacement field exists. Therefore, we adopt the divergence-free field

$$\mathbf{u}^a = 0.1 \begin{pmatrix} \sin\left(\frac{\pi}{2}XZ\right) X \sin(\pi Y) \\ 0 \\ -\sin\left(\frac{\pi}{2}XZ\right) Z \sin(\pi Y) \end{pmatrix} \quad (\text{E.1})$$

and compute the corresponding tractions and body loads from the equilibrium. Summarizing, we apply, as explained in [315], the following conditions:

- We fix the faces  $X = 0$ ,  $Y = 0$ ,  $Y = 1$ , and  $Z = 0$ .
- We apply body loads according to:

$$\mathbf{b}_0 = -\nabla_{\mathbf{x}} \cdot (\mathbb{C} \boldsymbol{\varepsilon}^a), \quad (\text{E.2})$$

where  $\mathbb{C}$  is the constitutive tensor for isotropic linear elastic materials and  $\boldsymbol{\varepsilon}^a$  is the symmetric gradient of the displacement field  $\mathbf{u}^a$ .

- We apply tractions on the free faces according to:

$$\mathbf{t}_N = (\mathbb{C} \boldsymbol{\varepsilon}^a) \bar{\mathbf{N}}. \quad (\text{E.3})$$

In the constitutive tensor  $\mathbb{C}$ , we adopt  $E = 1000$  and  $\nu = 0.49999$ , that are related to the shear and bulk moduli through:

$$G = \frac{E}{2(1+\nu)} \quad (\text{E.4})$$

and

$$K = \frac{E}{3(1-2\nu)}. \quad (\text{E.5})$$

## E.2 Simulation setup of the curved body in finite deformation regime

In this section we provide the details on the simulation setup of the analysis shown in Fig. 8.2.

The structure represented in Fig. E.1 is constrained and loaded as follows:

- We fix the displacements of all the external surfaces, except the loaded one.
- On the external curved surface we apply a uniform traction  $\mathbf{t}_N = (0, 0, 200)^T$ .
- We assume that no body load is applied.

Moreover, we use the same shear and bulk moduli as in Sec. E.1.

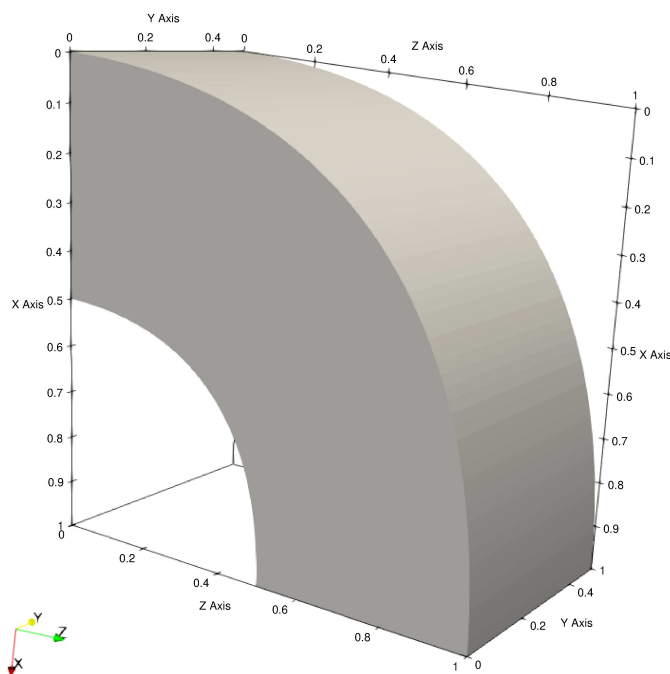


Figure E.1: Geometry of the analyzed structure.

For this second problem no analytical solution is available, therefore we use an overkill solution as a reference. This is computed using quartic basis functions defined on a mesh composed by 32 knot spans per direction, that corresponds to 186624 degrees of freedom.

## E.3 Additional convergence test

In this section we provide an additional convergence analysis for the mixed  $\mathbf{u}$ - $p$  formulation for nearly-incompressible materials in finite deformations.

In the simple test presented in Fig. E.2, we analyze the same structure presented in E.1, subject to the same loads and boundary conditions, but in the finite deformation regime.

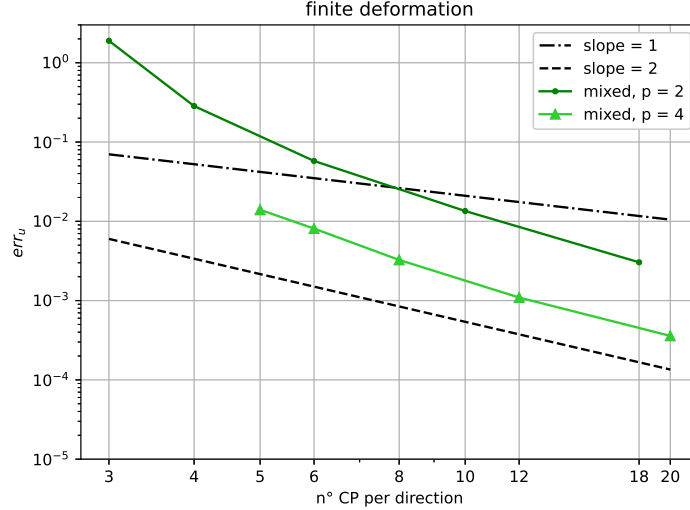


Figure E.2: Convergence test for the cube in finite deformations.

Since no analytical solution is available for the nonlinear problem, we use as a reference an overkill solution computed using quartic basis functions, 32 knot spans per direction, and 186624 degrees of freedom.

The results confirm the quadratic rate of convergence investigated in a more complex and realistic test reported in Section 8.1.3.

## E.4 Convergence analysis of the passive component of the pressure field

In Fig. E.3, we present the convergence analysis for the pressure field of the nonlinear problem in Sec. 8.1.3, defining the relative L2-error as:

$$err_p = \sqrt{\frac{\int_{\Omega_0} (p - p^{ref})^2 dV}{\int_{\Omega_0} (p^{ref})^2 dV}}. \quad (E.6)$$

In this definition,  $p^{ref}$  is the pressure field of the reference solution.

Based on our results, the convergence rate of the error is one, independently of the basis function degree. However, quartic B-splines produce more accurate results than quadratic basis functions. The results of the convergence analysis of the cube, presented in Fig. E.4, confirms this.

We conclude this Section recalling that, in the coupled electromechanical simulation, the contribution of the active component of the stress tensor should be added to the passive contribution to compute the hydrostatic pressure.

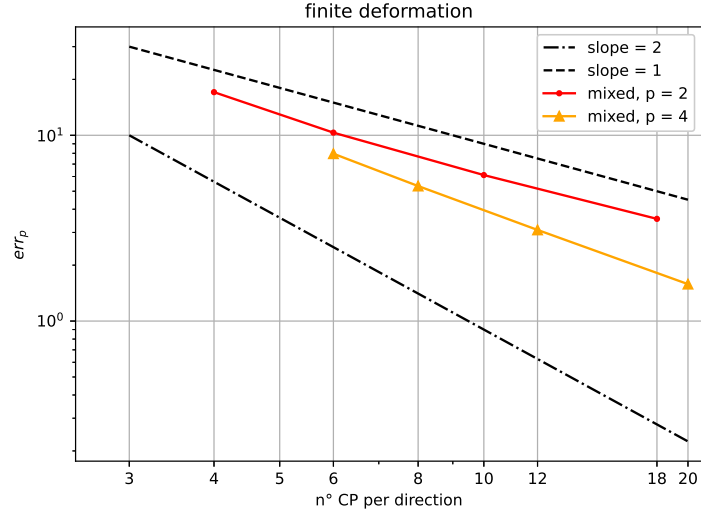


Figure E.3: Convergence analysis of the pressure field for the curved geometry in Sec. 8.1.3.

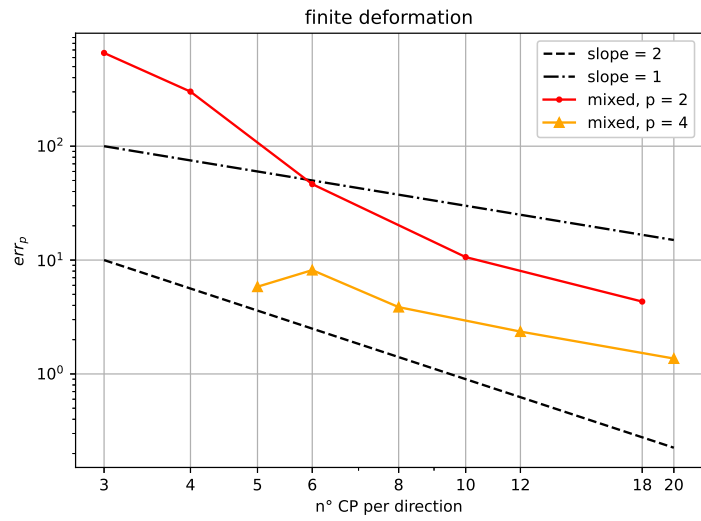


Figure E.4: Convergence analysis of the pressure field for the cubic geometry in E.3.

## E.5 Alternative selections of meshes

In Fig. 8.5 we present a possible scheme for an efficient selection of the meshes for the EP and ME sub-problems. Herein, we report two examples of alternative schemes for quadratic and quartic basis functions in Fig. E.5 and E.6, respectively.

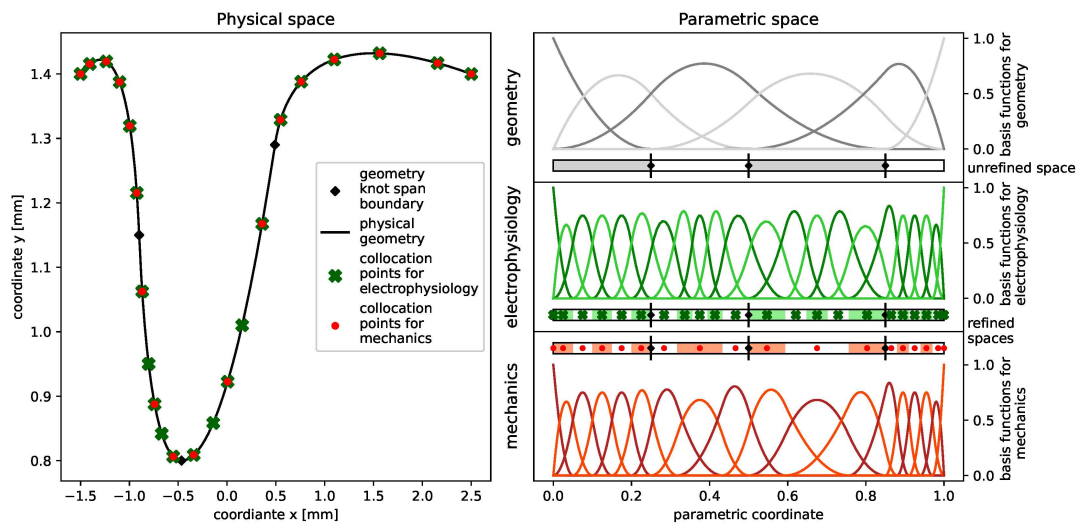


Figure E.5: Example of meshes for quadratic basis functions.

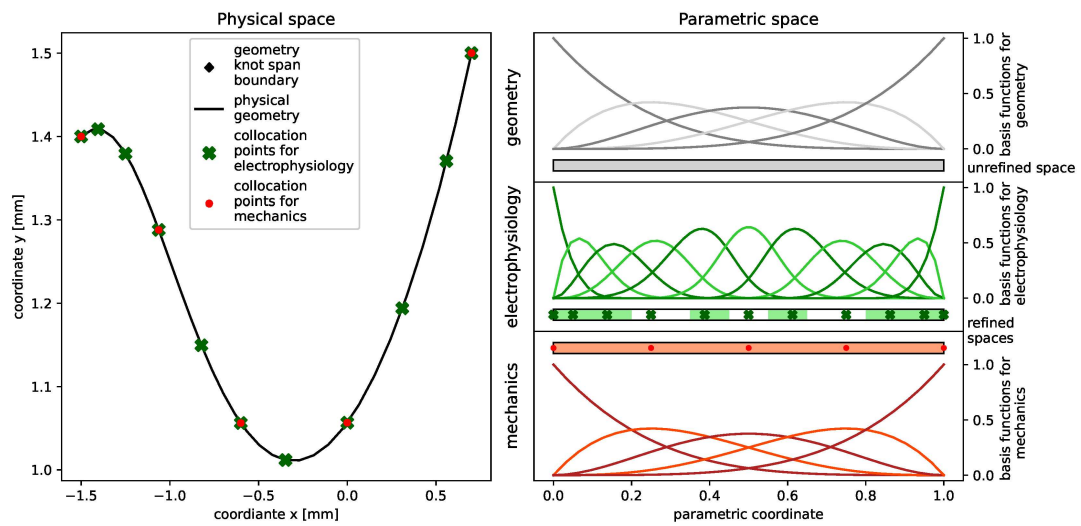


Figure E.6: Example of meshes for quartic basis functions.



# Bibliography

- [1] M. Strocchi, C. M. Augustin, M. A. Gsell, E. Karabelas, A. Neic, K. Gillette, O. Razeghi, A. J. Prassl, E. J. Vigmond, J. M. Behar, et al., *A publicly available virtual cohort of four-chamber heart meshes for cardiac electro-mechanics simulations*, PLoS one **15**, e0235145 (2020).
- [2] Zygote, *3D Human Anatomy Models* (2023).
- [3] M. Peirlinck, F. S. Costabal, J. Yao, J. Guccione, S. Tripathy, Y. Wang, D. Ozturk, P. Segars, T. Morrison, S. Levine, et al., *Precision medicine in human heart modeling: Perspectives, challenges, and opportunities*, Biomechanics and modeling in mechanobiology **20**, 803 (2021).
- [4] C. Rodero, M. Strocchi, M. Marciniak, S. Longobardi, J. Whitaker, M. D. O’Neill, K. Gillette, C. Augustin, G. Plank, E. J. Vigmond, et al., *Linking statistical shape models and simulated function in the healthy adult human heart*, PLoS computational biology **17**, e1008851 (2021).
- [5] S. N. Doost, D. Ghista, B. Su, L. Zhong, and Y. S. Morsi, *Heart blood flow simulation: a perspective review*, Biomedical engineering online **15**, 1 (2016).
- [6] C. Yamamoto and N. A. Trayanova, *Atrial fibrillation: Insights from animal models, computational modeling, and clinical studies*, EBioMedicine **85**, 104310 (2022).
- [7] E. Sung, S. Etoz, Y. Zhang, and N. A. Trayanova, *Whole-heart ventricular arrhythmia modeling moving forward: Mechanistic insights and translational applications*, Biophysics reviews **2**, 031304 (2021).
- [8] S. A. Niederer, J. Lumens, and N. A. Trayanova, *Computational models in cardiology*, Nature Reviews Cardiology **16**, 100 (2019).
- [9] N. A. Trayanova, *Whole-heart modeling: applications to cardiac electrophysiology and electromechanics*, Circulation research **108**, 113 (2011).
- [10] B. Baillargeon, N. Rebelo, D. D. Fox, R. L. Taylor, and E. Kuhl, *The living heart project: a robust and integrative simulator for human heart function*, European Journal of Mechanics-A/Solids **48**, 38 (2014).
- [11] L. Piegl and W. Tiller, *The NURBS book*, Springer Science & Business Media (1996).
- [12] J. A. Cottrell, T. J. Hughes, and Y. Bazilevs, *Isogeometric analysis: toward integration of CAD and FEA*, John Wiley & Sons (2009).
- [13] T. J. Hughes, J. A. Cottrell, and Y. Bazilevs, *Isogeometric analysis: CAD, finite elements, NURBS, exact geometry and mesh refinement*, Computer methods in applied mechanics and engineering **194**, 4135 (2005).
- [14] T. W. Sederberg, J. Zheng, A. Bakenov, and A. Nasri, *T-splines and T-NURCCs*, ACM transactions on graphics (TOG) **22**, 477 (2003).
- [15] T. W. Sederberg, D. L. Cardon, G. T. Finnigan, N. S. North, J. Zheng, and T. Lyche, *T-spline simplification and local refinement*, ACM transactions on graphics (TOG) **23**, 276 (2004).

- [16] A. Buffa, D. Cho, and G. Sangalli, *Linear independence of the T-spline blending functions associated with some particular T-meshes*, Computer Methods in Applied Mechanics and Engineering **199**, 1437 (2010).
- [17] C. Giannelli, B. Jüttler, and H. Speleers, *THB-splines: The truncated basis for hierarchical splines*, Computer Aided Geometric Design **29**, 485 (2012).
- [18] Y. Otaguro, K. Takizawa, and T. E. Tezduyar, *Space-time VMS computational flow analysis with isogeometric discretization and a general-purpose NURBS mesh generation method*, Computers & Fluids **158**, 189 (2017).
- [19] M. Ruess, D. Schillinger, A. I. Oezcan, and E. Rank, *Weak coupling for isogeometric analysis of non-matching and trimmed multi-patch geometries*, Computer Methods in Applied Mechanics and Engineering **269**, 46 (2014).
- [20] M. Kapl, G. Sangalli, and T. Takacs, *Isogeometric analysis with  $C^1$  functions on planar, unstructured quadrilateral meshes*, The SMAI journal of computational mathematics **5**, 67 (2019).
- [21] J. Kiendl, M.-C. Hsu, M. C. Wu, and A. Reali, *Isogeometric Kirchhoff–Love shell formulations for general hyperelastic materials*, Computer Methods in Applied Mechanics and Engineering **291**, 280 (2015).
- [22] A. Reali and H. Gomez, *An isogeometric collocation approach for Bernoulli–Euler beams and Kirchhoff plates*, Computer Methods in Applied Mechanics and Engineering **284**, 623 (2015).
- [23] J. A. Cottrell, A. Reali, Y. Bazilevs, and T. J. Hughes, *Isogeometric analysis of structural vibrations*, Computer methods in applied mechanics and engineering **195**, 5257 (2006).
- [24] T. J. Hughes, J. A. Evans, and A. Reali, *Finite element and NURBS approximations of eigenvalue, boundary-value, and initial-value problems*, Computer Methods in Applied Mechanics and Engineering **272**, 290 (2014).
- [25] F. Auricchio, F. Calabro, T. J. Hughes, A. Reali, and G. Sangalli, *A simple algorithm for obtaining nearly optimal quadrature rules for NURBS-based isogeometric analysis*, Computer Methods in Applied Mechanics and Engineering **249**, 15 (2012).
- [26] T. J. Hughes, A. Reali, and G. Sangalli, *Efficient quadrature for NURBS-based isogeometric analysis*, Computer methods in applied mechanics and engineering **199**, 301 (2010).
- [27] C. Adam, T. J. Hughes, S. Bouabdallah, M. Zarroug, and H. Maitournam, *Selective and reduced numerical integrations for NURBS-based isogeometric analysis*, Computer Methods in Applied Mechanics and Engineering **284**, 732 (2015).
- [28] F. Calabro, G. Sangalli, and M. Tani, *Fast formation of isogeometric Galerkin matrices by weighted quadrature*, Computer Methods in Applied Mechanics and Engineering **316**, 606 (2017).
- [29] A. Mantzaflaris and B. Jüttler, *Integration by interpolation and look-up for Galerkin-based isogeometric analysis*, Computer Methods in Applied Mechanics and Engineering **284**, 373 (2015).
- [30] F. Auricchio, L. B. Da Veiga, T. J. Hughes, A. Reali, and G. Sangalli, *Isogeometric collocation for elastostatics and explicit dynamics*, Computer methods in applied mechanics and engineering **249**, 2 (2012).
- [31] D. Schillinger, J. A. Evans, A. Reali, M. A. Scott, and T. J. Hughes, *Isogeometric collocation: Cost comparison with Galerkin methods and extension to adaptive hierarchical NURBS discretizations*, Computer Methods in Applied Mechanics and Engineering **267**, 170 (2013).
- [32] D. Schillinger, M. Ruess, N. Zander, Y. Bazilevs, A. Düster, and E. Rank, *Small and large deformation analysis with the p- and B-spline versions of the Finite Cell Method*, Computational Mechanics **50**, 445 (2012).

- [33] M. Breitenberger, A. Apostolatos, B. Philipp, R. Wüchner, and K.-U. Bletzinger, *Analysis in computer aided design: Nonlinear isogeometric B-Rep analysis of shell structures*, Computer Methods in Applied Mechanics and Engineering **284**, 401 (2015).
- [34] X. Wei, B. Marussig, P. Antolin, and A. Buffa, *Immersed boundary-conformal isogeometric method for linear elliptic problems*, Computational Mechanics **68**, 1385 (2021).
- [35] D. Kamensky, M.-C. Hsu, D. Schillinger, J. A. Evans, A. Aggarwal, Y. Bazilevs, M. S. Sacks, and T. J. Hughes, *An immersogeometric variational framework for fluid–structure interaction: Application to bioprosthetic heart valves*, Computer methods in applied mechanics and engineering **284**, 1005 (2015).
- [36] M. Torre, S. Morganti, F. S. Pasqualini, A. Düster, and A. Reali, *Immersed isogeometric analysis based on a hybrid collocation/finite cell method*, Computer Methods in Applied Mechanics and Engineering **405**, 115856 (2023).
- [37] T. Terahara, K. Takizawa, T. E. Tezduyar, A. Tsushima, and K. Shiozaki, *Ventricle-valve-aorta flow analysis with the space-time isogeometric discretization and topology change*, Computational Mechanics **65**, 1343 (2020).
- [38] O. C. Zienkiewicz, R. L. Taylor, and J. Z. Zhu, *The finite element method: its basis and fundamentals*, Elsevier (2005).
- [39] I. Babuska, B. A. Szabo, and I. N. Katz, *The p-version of the finite element method*, SIAM journal on numerical analysis **18**, 515 (1981).
- [40] G. Lorenzo, M. Scott, K. Tew, T. Hughes, and H. Gomez, *Hierarchically refined and coarsened splines for moving interface problems, with particular application to phase-field models of prostate tumor growth*, Computer Methods in Applied Mechanics and Engineering **319**, 515 (2017).
- [41] V. P. Nguyen, C. Anitescu, S. P. Bordas, and T. Rabczuk, *Isogeometric analysis: an overview and computer implementation aspects*, Mathematics and Computers in Simulation **117**, 89 (2015).
- [42] G. R. Mirams, C. J. Arthurs, M. O. Bernabeu, R. Bordas, J. Cooper, A. Corrias, Y. Davit, S.-J. Dunn, A. G. Fletcher, D. G. Harvey, et al., *Chaste: an open source C++ library for computational physiology and biology*, PLoS computational biology **9**, e1002970 (2013).
- [43] A. Quarteroni, T. Lassila, S. Rossi, and R. Ruiz-Baier, *Integrated Heart—Coupling multiscale and multiphysics models for the simulation of the cardiac function*, Computer Methods in Applied Mechanics and Engineering **314**, 345 (2017).
- [44] M. Bucelli, A. Zingaro, P. C. Africa, I. Fumagalli, L. Dede, and A. Quarteroni, *A mathematical model that integrates cardiac electrophysiology, mechanics and fluid dynamics: application to the human left heart*, International Journal for Numerical Methods in Biomedical Engineering page e3678 (2022).
- [45] M. Fedele, R. Piersanti, F. Regazzoni, M. Salvador, P. C. Africa, M. Bucelli, A. Zingaro, A. Quarteroni, et al., *A comprehensive and biophysically detailed computational model of the whole human heart electromechanics*, Computer Methods in Applied Mechanics and Engineering **410**, 115983 (2023).
- [46] Y. Lai, Y. J. Zhang, L. Liu, X. Wei, E. Fang, and J. Lua, *Integrating CAD with Abaqus: a practical isogeometric analysis software platform for industrial applications*, Computers & Mathematics with Applications **74**, 1648 (2017).
- [47] M. J. Borden, M. A. Scott, J. A. Evans, and T. J. Hughes, *Isogeometric finite element data structures based on Bézier extraction of NURBS*, International Journal for Numerical Methods in Engineering **87**, 15 (2011).
- [48] D. D’Angella, S. Kollmannsberger, E. Rank, and A. Reali, *Multi-level Bézier extraction for hierarchical local refinement of Isogeometric Analysis*, Computer Methods in Applied Mechanics and Engineering **328**, 147 (2018).

- [49] D. D’Angella and A. Reali, *Efficient extraction of hierarchical b-splines for local refinement and coarsening of isogeometric analysis*, Computer Methods in Applied Mechanics and Engineering **367**, 113131 (2020).
- [50] R. Vázquez, *A new design for the implementation of isogeometric analysis in Octave and Matlab: GeoPDEs 3.0*, Computers & Mathematics with Applications **72**, 523 (2016).
- [51] E. M. Garau and R. Vázquez, *Algorithms for the implementation of adaptive isogeometric methods using hierarchical B-splines*, Applied Numerical Mathematics **123**, 58 (2018).
- [52] G. van Zwieten, J. van Zwieten, and W. Hoitinga, *Nutils* (2022).
- [53] D. Kamensky and Y. Bazilevs, *tIGAr: Automating isogeometric analysis with FEniCS*, Computer Methods in Applied Mechanics and Engineering **344**, 477 (2019).
- [54] M. S. Alnaes, J. Blechta, J. Hake, A. Johansson, B. Kehlet, A. Logg, C. Richardson, J. Ring, M. E. Rognes, and G. N. Wells, *The FEniCS Project Version 1.5*, Archive of Numerical Software **3** (2015).
- [55] D. Kamensky, *Open-source immersogeometric analysis of fluid–structure interaction using FEniCS and tIGAr*, Computers & Mathematics with Applications **81**, 634 (2021).
- [56] Y. Güçlüa, S. Hadjouta, and A. Ratnanić, *PSYDAC: a parallel finite element solver with automatic code generation*, in *Numerical Methods for the Kinetic Equations of Plasma Physics (NumKin2019)* (2019).
- [57] A.-V. Vuong, C. Heinrich, and B. Simeon, *ISOGAT: A 2D tutorial MATLAB code for Isogeometric Analysis*, Computer Aided Geometric Design **27**, 644 (2010).
- [58] L. Dalcin, N. Collier, P. Vignal, A. Côrtes, and V. M. Calo, *PetIGA: A framework for high-performance isogeometric analysis*, Computer Methods in Applied Mechanics and Engineering **308**, 151 (2016).
- [59] M. S. Pauletti, M. Martinelli, N. Cavallini, and P. Antolin, *Igatools: An isogeometric analysis library*, SIAM Journal on Scientific Computing **37**, C465 (2015).
- [60] Technical Univesity of Munich, Technical Univesity of Hamburg, and Leibniz Supercomputing Center, *AdhoC++* (2023).
- [61] L. Coradello, D. D’Angella, M. Carraturo, J. Kiendl, S. Kollmannsberger, E. Rank, and A. Reali, *Hierarchically refined isogeometric analysis of trimmed shells*, Computational Mechanics **66**, 431 (2020).
- [62] B. Jüttler, U. Langer, A. Mantzaflaris, S. E. Moore, and W. Zulehner, *Geometry+ simulation modules: Implementing isogeometric analysis*, PAMM **14**, 961 (2014).
- [63] R. Taylor, *Isogeometric analysis of nearly incompressible solids*, International Journal for Numerical Methods in Engineering **87**, 273 (2011).
- [64] P. Karakitsios, I. Prentzas, A. Leontaris, and A. Papakonstantinou, *A Comparison Study between Isogeometric Analysis and Finite Element Analysis for Nonlinear Inelastic Dynamic Problems with Geomiso DNL Software*, WCCM-APCOM 2022 **1200** (2022).
- [65] Ansys, *LS-DYNA* (2023).
- [66] M. Scott, M. Sederberg, D. Thomas, K. Tew, M. Borden, and T. J. R. Hughes, *Coreform* (2023).
- [67] A. Bauer, P. Längst, K.-U. Bletzinger, J. Lienhard, and A. Michalski, *Kiwi!3D* (2023).
- [68] R. A. Malinauskas, P. Hariharan, S. W. Day, L. H. Herbertson, M. Buesen, U. Steinseifer, K. I. Aycock, B. C. Good, S. Deutsch, K. B. Manning, et al., *FDA benchmark medical device flow models for CFD validation*, Asaio Journal **63**, 150 (2017).

- [69] C. A. Taylor, T. A. Fonte, and J. K. Min, *Computational fluid dynamics applied to cardiac computed tomography for noninvasive quantification of fractional flow reserve: scientific basis*, Journal of the American College of Cardiology **61**, 2233 (2013).
- [70] A. L. Marsden, *Optimization in cardiovascular modeling*, Annual review of fluid mechanics **46**, 519 (2014).
- [71] J. P. Heners, L. Radtke, M. Hinze, and A. Düster, *Adjoint shape optimization for fluid–structure interaction of ducted flows*, Computational Mechanics **61**, 259 (2018).
- [72] Y. Bazilevs, J. Gohean, T. Hughes, R. Moser, and Y. Zhang, *Patient-specific isogeometric fluid–structure interaction analysis of thoracic aortic blood flow due to implantation of the Jarvik 2000 left ventricular assist device*, Computer Methods in Applied Mechanics and Engineering **198**, 3534 (2009).
- [73] D. Tang, C. Yang, T. Geva, and J. Pedro, *Image-based patient-specific ventricle models with fluid–structure interaction for cardiac function assessment and surgical design optimization*, Progress in pediatric cardiology **30**, 51 (2010).
- [74] S. S. Hossain, S. F. Hossainy, Y. Bazilevs, V. M. Calo, and T. J. Hughes, *Mathematical modeling of coupled drug and drug-encapsulated nanoparticle transport in patient-specific coronary artery walls*, Computational Mechanics **49**, 213 (2012).
- [75] L. Zhong, J.-M. Zhang, B. Su, R. S. Tan, J. C. Allen, and G. S. Kassab, *Application of patient-specific computational fluid dynamics in coronary and intra-cardiac flow simulations: Challenges and opportunities*, Frontiers in physiology **9**, 742 (2018).
- [76] L. Radtke, M. König, and A. Düster, *The influence of geometric imperfections in cardiovascular FSI simulations*, Computers & Mathematics with Applications **74**, 1675 (2017).
- [77] A. D. Caballero and S. Lain, *A review on computational fluid dynamics modelling in human thoracic aorta*, Cardiovascular Engineering and Technology **4**, 103 (2013).
- [78] A. Nitti, G. De Cillis, and M. de Tullio, *Numerical investigation of turbulent features past different mechanical aortic valves*, Journal of Fluid Mechanics **940** (2022).
- [79] B. Urick, T. M. Sanders, S. S. Hossain, Y. J. Zhang, and T. J. Hughes, *Review of patient-specific vascular modeling: template-based isogeometric framework and the case for CAD*, Archives of Computational Methods in Engineering **26**, 381 (2019).
- [80] Y. Zhang, Y. Bazilevs, S. Goswami, C. L. Bajaj, and T. J. Hughes, *Patient-specific vascular NURBS modeling for isogeometric analysis of blood flow*, Computer methods in applied mechanics and engineering **196**, 2943 (2007).
- [81] M. Bucelli, M. Salvador, A. Quarteroni, et al., *Multipatch isogeometric analysis for electrophysiology: simulation in a human heart*, Computer Methods in Applied Mechanics and Engineering **376**, 113666 (2021).
- [82] A. S. Patelli, L. Dedè, T. Lassila, A. Bartzaghi, and A. Quarteroni, *Isogeometric approximation of cardiac electrophysiology models on surfaces: An accuracy study with application to the human left atrium*, Computer Methods in Applied Mechanics and Engineering **317**, 248 (2017).
- [83] L. Pegolotti, L. Dedè, and A. Quarteroni, *Isogeometric analysis of the electrophysiology in the human heart: numerical simulation of the bidomain equations on the atria*, Computer Methods in Applied Mechanics and Engineering **343**, 52 (2019).
- [84] G. Lorenzo, M. A. Scott, K. Tew, T. J. Hughes, Y. J. Zhang, L. Liu, G. Vilanova, and H. Gomez, *Tissue-scale, personalized modeling and simulation of prostate cancer growth*, Proceedings of the National Academy of Sciences **113**, E7663 (2016).
- [85] T. Kuraishi, S. Yamasaki, K. Takizawa, T. E. Tezduyar, Z. Xu, and R. Kaneko, *Space–time isogeometric analysis of car and tire aerodynamics with road contact and tire deformation and rotation*, Computational Mechanics pages 1–24 (2022).

- [86] Y. J. Zhang, *Geometric modeling and mesh generation from scanned images*, Chapman and Hall/CRC (2018).
- [87] J. Parvizian, A. Düster, and E. Rank, *Finite cell method*, Computational Mechanics **41**, 121 (2007).
- [88] A. Düster, J. Parvizian, Z. Yang, and E. Rank, *The finite cell method for three-dimensional problems of solid mechanics*, Computer methods in applied mechanics and engineering **197**, 3768 (2008).
- [89] E. Rank, M. Ruess, S. Kollmannsberger, D. Schillinger, and A. Düster, *Geometric modeling, isogeometric analysis and the finite cell method*, Computer Methods in Applied Mechanics and Engineering **249**, 104 (2012).
- [90] W. Garhuom and A. Düster, *Non-negative moment fitting quadrature for cut finite elements and cells undergoing large deformations*, Computational Mechanics **70**, 1059 (2022).
- [91] S. C. Divi, C. V. Verhoosel, F. Auricchio, A. Reali, and E. H. van Brummelen, *Topology-preserving scan-based immersed isogeometric analysis*, Computer Methods in Applied Mechanics and Engineering **392**, 114648 (2022).
- [92] S. C. Divi, P. H. van Zuijlen, T. Hoang, F. de Prenter, F. Auricchio, A. Reali, E. H. van Brummelen, and C. V. Verhoosel, *Residual-based error estimation and adaptivity for stabilized immersed isogeometric analysis using truncated hierarchical B-splines*, Journal of Mechanics **38**, 204 (2022).
- [93] C. Taylor and P. Hood, *A numerical solution of the Navier-Stokes equations using the finite element technique*, Computers & Fluids **1**, 73 (1973).
- [94] P.-A. Raviart and J.-M. Thomas, *Primal hybrid finite element methods for 2nd order elliptic equations*, Mathematics of computation **31**, 391 (1977).
- [95] A. Buffa, C. De Falco, and G. Sangalli, *Isogeometric analysis: stable elements for the 2D Stokes equation*, International Journal for Numerical Methods in Fluids **65**, 1407 (2011).
- [96] A. Bressan and G. Sangalli, *Isogeometric discretizations of the Stokes problem: stability analysis by the macroelement technique*, IMA Journal of Numerical Analysis **33**, 629 (2013).
- [97] J. A. Evans and T. J. Hughes, *Isogeometric divergence-conforming B-splines for the Darcy–Stokes–Brinkman equations*, Mathematical Models and Methods in Applied Sciences **23**, 671 (2013).
- [98] T. J. Hughes, L. P. Franca, and G. M. Hulbert, *A new finite element formulation for computational fluid dynamics: VIII. The Galerkin/least-squares method for advective-diffusive equations*, Computer methods in applied mechanics and engineering **73**, 173 (1989).
- [99] J. Douglas and J. P. Wang, *An absolutely stabilized finite element method for the Stokes problem*, Mathematics of computation **52**, 495 (1989).
- [100] T. E. Tezduyar, *Stabilized finite element formulations for incompressible flow computations*, Advances in applied mechanics **28**, 1 (1991).
- [101] T. J. Hughes, G. R. Feijóo, L. Mazzei, and J.-B. Quincy, *The variational multiscale method—a paradigm for computational mechanics*, Computer methods in applied mechanics and engineering **166**, 3 (1998).
- [102] T. J. Hughes, L. Mazzei, A. A. Oberai, and A. A. Wray, *The multiscale formulation of large eddy simulation: Decay of homogeneous isotropic turbulence*, Physics of fluids **13**, 505 (2001).
- [103] Y. Bazilevs, V. Calo, J. Cottrell, T. Hughes, A. Reali, and G. Scovazzi, *Variational multiscale residual-based turbulence modeling for large eddy simulation of incompressible flows*, Computer methods in applied mechanics and engineering **197**, 173 (2007).
- [104] R. Becker and M. Braack, *A finite element pressure gradient stabilization for the Stokes equations based on local projections*, Calcolo **38**, 173 (2001).

- [105] M. Braack and E. Burman, *Local projection stabilization for the Oseen problem and its interpretation as a variational multiscale method*, SIAM Journal on Numerical Analysis **43**, 2544 (2006).
- [106] Y. Bazilevs, K. Takizawa, and T. E. Tezduyar, *Computational fluid-structure interaction: methods and applications*, John Wiley & Sons (2013).
- [107] F. Viola, V. Meschini, and R. Verzicco, *Fluid–Structure–Electrophysiology interaction (FSEI) in the left-heart: a multi-way coupled computational model*, European Journal of Mechanics-B/Fluids **79**, 212 (2020).
- [108] A. Tagliabue, L. Dedè, and A. Quarteroni, *Complex blood flow patterns in an idealized left ventricle: a numerical study*, Chaos: An Interdisciplinary Journal of Nonlinear Science **27**, 093939 (2017).
- [109] A. Tagliabue, L. Dede, and A. Quarteroni, *Fluid dynamics of an idealized left ventricle: the extended Nitsche’s method for the treatment of heart valves as mixed time varying boundary conditions*, International Journal for Numerical Methods in Fluids **85**, 135 (2017).
- [110] K. Takizawa and T. E. Tezduyar, *Multiscale space–time fluid–structure interaction techniques*, Computational Mechanics **48**, 247 (2011).
- [111] K. Takizawa, T. E. Tezduyar, H. Uchikawa, T. Terahara, T. Sasaki, and A. Yoshida, *Mesh refinement influence and cardiac-cycle flow periodicity in aorta flow analysis with isogeometric discretization*, Computers & Fluids **179**, 790 (2019).
- [112] T. J. Hughes, L. Mazzei, and K. E. Jansen, *Large eddy simulation and the variational multiscale method*, Computing and visualization in science **3**, 47 (2000).
- [113] Y. Bazilevs and I. Akkerman, *Large eddy simulation of turbulent Taylor–Couette flow using isogeometric analysis and the residual-based variational multiscale method*, Journal of Computational Physics **229**, 3402 (2010).
- [114] Y. Bazilevs, M.-C. Hsu, I. Akkerman, S. Wright, K. Takizawa, B. Henicke, T. Spielman, and T. Tezduyar, *3D simulation of wind turbine rotors at full scale. Part I: Geometry modeling and aerodynamics*, International journal for numerical methods in fluids **65**, 207 (2011).
- [115] R. Torii, M. Oshima, T. Kobayashi, K. Takagi, and T. E. Tezduyar, *Computer modeling of cardiovascular fluid–structure interactions with the deforming-spatial-domain/stabilized space–time formulation*, Computer Methods in Applied Mechanics and Engineering **195**, 1885 (2006).
- [116] R. Torii, M. Oshima, T. Kobayashi, K. Takagi, and T. E. Tezduyar, *Influence of wall elasticity in patient-specific hemodynamic simulations*, Computers & Fluids **36**, 160 (2007).
- [117] R. Torii, M. Oshima, T. Kobayashi, K. Takagi, and T. E. Tezduyar, *Fluid–structure interaction modeling of a patient-specific cerebral aneurysm: influence of structural modeling*, Computational Mechanics **43**, 151 (2008).
- [118] Y. Bazilevs, M.-C. Hsu, D. J. Benson, S. Sankaran, and A. L. Marsden, *Computational fluid–structure interaction: methods and application to a total cavopulmonary connection*, Computational Mechanics **45**, 77 (2009).
- [119] Y. Bazilevs, M.-C. Hsu, Y. Zhang, W. Wang, T. Kvamsdal, S. Hentschel, and J. Isaksen, *Computational vascular fluid–structure interaction: methodology and application to cerebral aneurysms*, Biomechanics and modeling in mechanobiology **9**, 481 (2010).
- [120] Y. Bazilevs, V. M. Calo, Y. Zhang, and T. Hughes, *Isogeometric fluid–structure interaction analysis with applications to arterial blood flow*, Computational Mechanics **38**, 310 (2006).
- [121] M.-C. Hsu, D. Kamensky, Y. Bazilevs, M. S. Sacks, and T. J. Hughes, *Fluid–structure interaction analysis of bioprosthetic heart valves: significance of arterial wall deformation*, Computational mechanics **54**, 1055 (2014).

- [122] M.-C. Hsu, D. Kamensky, F. Xu, J. Kiendl, C. Wang, M. C. Wu, J. Mineroff, A. Reali, Y. Bazilevs, and M. S. Sacks, *Dynamic and fluid–structure interaction simulations of bioprosthetic heart valves using parametric design with T-splines and Fung-type material models*, *Computational mechanics* **55**, 1211 (2015).
- [123] K. Takizawa, Y. Bazilevs, T. E. Tezduyar, M.-C. Hsu, and T. Terahara, *Computational cardiovascular medicine with isogeometric analysis*, *Journal of Advanced Engineering and Computation* **6**, 167 (2022).
- [124] I. E. Vignon-Clementel, C. A. Figueroa, K. E. Jansen, and C. A. Taylor, *Outflow boundary conditions for three-dimensional finite element modeling of blood flow and pressure in arteries*, *Computer methods in applied mechanics and engineering* **195**, 3776 (2006).
- [125] Y. Bazilevs and T. J. Hughes, *Weak imposition of Dirichlet boundary conditions in fluid mechanics*, *Computers & fluids* **36**, 12 (2007).
- [126] Y. Bazilevs, C. Michler, V. Calo, and T. Hughes, *Weak Dirichlet boundary conditions for wall-bounded turbulent flows*, *Computer Methods in Applied Mechanics and Engineering* **196**, 4853 (2007).
- [127] Y. Bazilevs, C. Michler, V. Calo, and T. Hughes, *Isogeometric variational multiscale modeling of wall-bounded turbulent flows with weakly enforced boundary conditions on unstretched meshes*, *Computer Methods in Applied Mechanics and Engineering* **199**, 780 (2010).
- [128] M. Esmaily Moghadam, Y. Bazilevs, T.-Y. Hsia, I. E. Vignon-Clementel, A. L. Marsden, and M. of Congenital Hearts Alliance (MOCHA), *A comparison of outlet boundary treatments for prevention of backflow divergence with relevance to blood flow simulations*, *Computational Mechanics* **48**, 277 (2011).
- [129] F. Xu, E. L. Johnson, C. Wang, A. Jafari, C.-H. Yang, M. S. Sacks, A. Krishnamurthy, and M.-C. Hsu, *Computational investigation of left ventricular hemodynamics following bioprosthetic aortic and mitral valve replacement*, *Mechanics Research Communications* **112**, 103604 (2021).
- [130] A. Krishnamurthy, C. T. Villongco, J. Chuang, L. R. Frank, V. Nigam, E. Belezouli, P. Stark, D. E. Krummen, S. Narayan, J. H. Omens, et al., *Patient-specific models of cardiac biomechanics*, *Journal of computational physics* **244**, 4 (2013).
- [131] A. Krishnamurthy, M. J. Gonzales, G. Sturgeon, W. P. Segars, and A. D. McCulloch, *Biomechanics simulations using cubic Hermite meshes with extraordinary nodes for isogeometric cardiac modeling*, *Computer aided geometric design* **43**, 27 (2016).
- [132] F. Robicsek, M. J. Thubrikar, and A. A. Fokin, *Cause of degenerative disease of the trileaflet aortic valve: review of subject and presentation of a new theory*, *The Annals of thoracic surgery* **73**, 1346 (2002).
- [133] F. Saremi, *Revisiting cardiac anatomy: a computed-tomography-based atlas and reference*, John Wiley & Sons (2011).
- [134] S. Morganti, F. Auricchio, D. Benson, F. Gambarin, S. Hartmann, T. Hughes, and A. Reali, *Patient-specific isogeometric structural analysis of aortic valve closure*, *Computer methods in applied mechanics and engineering* **284**, 508 (2015).
- [135] F. Xu, S. Morganti, R. Zakerzadeh, D. Kamensky, F. Auricchio, A. Reali, T. J. Hughes, M. S. Sacks, and M.-C. Hsu, *A framework for designing patient-specific bioprosthetic heart valves using immersogeometric fluid–structure interaction analysis*, *International journal for numerical methods in biomedical engineering* **34**, e2938 (2018).
- [136] E. L. Johnson, D. W. Laurence, F. Xu, C. E. Crisp, A. Mir, H. M. Burkhart, C.-H. Lee, and M.-C. Hsu, *Parameterization, geometric modeling, and isogeometric analysis of tricuspid valves*, *Computer Methods in Applied Mechanics and Engineering* **384**, 113960 (2021).

- [137] M. C. Wu, R. Zakerzadeh, D. Kamensky, J. Kiendl, M. S. Sacks, and M.-C. Hsu, *An anisotropic constitutive model for immersogeometric fluid–structure interaction analysis of bioprosthetic heart valves*, *Journal of biomechanics* **74**, 23 (2018).
- [138] W. Zhang, G. Rossini, D. Kamensky, T. Bui-Thanh, and M. S. Sacks, *Isogeometric finite element-based simulation of the aortic heart valve: Integration of neural network structural material model and structural tensor fiber architecture representations*, *International journal for numerical methods in biomedical engineering* **37**, e3438 (2021).
- [139] C.-H. Lee, D. W. Laurence, C. J. Ross, K. E. Kramer, A. R. Babu, E. L. Johnson, M.-C. Hsu, A. Aggarwal, A. Mir, H. M. Burkhart, et al., *Mechanics of the tricuspid valve—From clinical diagnosis/treatment, in-vivo and in-vitro investigations, to patient-specific biomechanical modeling*, *Bioengineering* **6**, 47 (2019).
- [140] J. Kiendl, K.-U. Bletzinger, J. Linhard, and R. Wüchner, *Isogeometric shell analysis with Kirchhoff–Love elements*, *Computer methods in applied mechanics and engineering* **198**, 3902 (2009).
- [141] D. N. Arnold, F. Brezzi, R. S. Falk, and L. D. Marini, *Locking-free Reissner–Mindlin elements without reduced integration*, *Computer methods in applied mechanics and engineering* **196**, 3660 (2007).
- [142] T. Belytschko, J. I. Lin, and T. Chen-Shyh, *Explicit algorithms for the nonlinear dynamics of shells*, *Computer methods in applied mechanics and engineering* **42**, 225 (1984).
- [143] D. Benson, Y. Bazilevs, M.-C. Hsu, and T. Hughes, *Isogeometric shell analysis: the Reissner–Mindlin shell*, *Computer Methods in Applied Mechanics and Engineering* **199**, 276 (2010).
- [144] D. Kamensky, F. Xu, C.-H. Lee, J. Yan, Y. Bazilevs, and M.-C. Hsu, *A contact formulation based on a volumetric potential: Application to isogeometric simulations of atrioventricular valves*, *Computer methods in applied mechanics and engineering* **330**, 522 (2018).
- [145] K. Takizawa, T. E. Tezduyar, A. Buscher, and S. Asada, *Space–time interface-tracking with topology change (ST-TC)*, *Computational Mechanics* **54**, 955 (2014).
- [146] T. Terahara, K. Takizawa, T. E. Tezduyar, Y. Bazilevs, and M.-C. Hsu, *Heart valve isogeometric sequentially-coupled FSI analysis with the space–time topology change method*, *Computational Mechanics* **65**, 1167 (2020).
- [147] L. Radtke, A. Larena-Avellaneda, E. S. Debus, and A. Düster, *Convergence acceleration for partitioned simulations of the fluid–structure interaction in arteries*, *Computational Mechanics* **57**, 901 (2016).
- [148] W. Dornisch, R. Müller, and S. Klinkel, *An efficient and robust rotational formulation for isogeometric Reissner–Mindlin shell elements*, *Computer Methods in Applied Mechanics and Engineering* **303**, 1 (2016).
- [149] Z. Zou, M. A. Scott, D. Miao, M. Bischoff, B. Oesterle, and W. Dornisch, *An isogeometric Reissner–Mindlin shell element based on Bézier dual basis functions: Overcoming locking and improved coarse mesh accuracy*, *Computer Methods in Applied Mechanics and Engineering* **370**, 113283 (2020).
- [150] J. Kiendl, E. Marino, and L. De Lorenzis, *Isogeometric collocation for the Reissner–Mindlin shell problem*, *Computer Methods in Applied Mechanics and Engineering* **325**, 645 (2017).
- [151] J. Kiendl, Y. Bazilevs, M.-C. Hsu, R. Wüchner, and K.-U. Bletzinger, *The bending strip method for isogeometric analysis of Kirchhoff–Love shell structures comprised of multiple patches*, *Computer Methods in Applied Mechanics and Engineering* **199**, 2403 (2010).
- [152] D. Benson, S. Hartmann, Y. Bazilevs, M.-C. Hsu, and T. Hughes, *Blended isogeometric shells*, *Computer Methods in Applied Mechanics and Engineering* **255**, 133 (2013).

- [153] I. Temizer, P. Wriggers, and T. Hughes, *Contact treatment in isogeometric analysis with NURBS*, Computer Methods in Applied Mechanics and Engineering **200**, 1100 (2011).
- [154] L. Krstulović-Opara, P. Wriggers, and J. Korelc, *A  $C1$ -continuous formulation for 3D finite deformation frictional contact*, Computational Mechanics **29**, 27 (2002).
- [155] M. Stadler, G. A. Holzapfel, and J. Korelc,  *$C_n$  continuous modelling of smooth contact surfaces using NURBS and application to 2D problems*, International Journal for Numerical Methods in Engineering **57**, 2177 (2003).
- [156] I. Temizer, P. Wriggers, and T. Hughes, *Three-dimensional mortar-based frictional contact treatment in isogeometric analysis with NURBS*, Computer Methods in Applied Mechanics and Engineering **209**, 115 (2012).
- [157] L. De Lorenzis, P. Wriggers, and T. J. Hughes, *Isogeometric contact: a review*, GAMM-Mitteilungen **37**, 85 (2014).
- [158] L. De Lorenzis, J. A. Evans, T. J. Hughes, and A. Reali, *Isogeometric collocation: Neumann boundary conditions and contact*, Computer Methods in Applied Mechanics and Engineering **284**, 21 (2015).
- [159] R. Kruse, N. Nguyen-Thanh, L. De Lorenzis, and T. J. Hughes, *Isogeometric collocation for large deformation elasticity and frictional contact problems*, Computer Methods in Applied Mechanics and Engineering **296**, 73 (2015).
- [160] M. De Tullio, L. Afferrante, G. Demelio, G. Pascazio, and R. Verzicco, *Fluid–structure interaction of deformable aortic prostheses with a bileaflet mechanical valve*, Journal of biomechanics **44**, 1684 (2011).
- [161] M. Fedele, E. Faggiano, L. Dedè, and A. Quarteroni, *A patient-specific aortic valve model based on moving resistive immersed implicit surfaces*, Biomechanics and modeling in mechanobiology **16**, 1779 (2017).
- [162] M. A. Fernández, J.-F. Gerbeau, and V. Martin, *Numerical simulation of blood flows through a porous interface*, ESAIM: Mathematical Modelling and Numerical Analysis **42**, 961 (2008).
- [163] F. Viola, V. Spandan, V. Meschini, J. Romero, M. Fatica, M. D. de Tullio, and R. Verzicco, *FSEI-GPU: GPU accelerated simulations of the fluid–structure–electrophysiology interaction in the left heart*, Computer physics communications **273**, 108248 (2022).
- [164] A. Nitti, J. Kiendl, A. Reali, and M. D. de Tullio, *An immersed-boundary/isogeometric method for fluid–structure interaction involving thin shells*, Computer Methods in Applied Mechanics and Engineering **364**, 112977 (2020).
- [165] H. Casquero, C. Bona-Casas, and H. Gomez, *A NURBS-based immersed methodology for fluid–structure interaction*, Computer Methods in Applied Mechanics and Engineering **284**, 943 (2015).
- [166] R. M. Aronson and J. A. Evans, *Divergence-conforming isogeometric collocation methods for the incompressible Navier–Stokes equations*, Computer Methods in Applied Mechanics and Engineering **410**, 115990 (2023).
- [167] H. Casquero, Y. J. Zhang, C. Bona-Casas, L. Dalcin, and H. Gomez, *Non-body-fitted fluid–structure interaction: Divergence-conforming B-splines, fully-implicit dynamics, and variational formulation*, Journal of Computational Physics **374**, 625 (2018).
- [168] H. Casquero, C. Bona-Casas, D. Toshniwal, T. J. Hughes, H. Gomez, and Y. J. Zhang, *The divergence-conforming immersed boundary method: Application to vesicle and capsule dynamics*, Journal of Computational Physics **425**, 109872 (2021).
- [169] D. Kamensky, J. A. Evans, and M.-C. Hsu, *Stability and conservation properties of collocated constraints in immersogeometric fluid–thin structure interaction analysis*, Communications in Computational Physics **18**, 1147 (2015).

- [170] M.-C. Hsu and D. Kamensky, *Immersogeometric analysis of bioprosthetic heart valves, using the dynamic augmented Lagrangian method*, *Frontiers in Computational Fluid-Structure Interaction and Flow Simulation* pages 167–212 (2018).
- [171] D. Kamensky, J. A. Evans, M.-C. Hsu, and Y. Bazilevs, *Projection-based stabilization of interface Lagrange multipliers in immersogeometric fluid–thin structure interaction analysis, with application to heart valve modeling*, *Computers & Mathematics with Applications* **74**, 2068 (2017).
- [172] Y. Yu, D. Kamensky, M.-C. Hsu, X. Y. Lu, Y. Bazilevs, and T. J. Hughes, *Error estimates for projection-based dynamic augmented Lagrangian boundary condition enforcement, with application to fluid–structure interaction*, *Mathematical Models and Methods in Applied Sciences* **28**, 2457 (2018).
- [173] D. Kamensky, M.-C. Hsu, Y. Yu, J. A. Evans, M. S. Sacks, and T. J. Hughes, *Immersogeometric cardiovascular fluid–structure interaction analysis with divergence-conforming B-splines*, *Computer methods in applied mechanics and engineering* **314**, 408 (2017).
- [174] T. Terahara, T. Kuraishi, K. Takizawa, and T. E. Tezduyar, *Computational flow analysis with boundary layer and contact representation: II. Heart valve flow with leaflet contact*, *Journal of Mechanics* **38**, 185 (2022).
- [175] D. Schillinger, L. Dede, M. A. Scott, J. A. Evans, M. J. Borden, E. Rank, and T. J. Hughes, *An isogeometric design-through-analysis methodology based on adaptive hierarchical refinement of NURBS, immersed boundary methods, and T-spline CAD surfaces*, *Computer Methods in Applied Mechanics and Engineering* **249**, 116 (2012).
- [176] M. J. Borden, T. J. Hughes, C. M. Landis, and C. V. Verhoosel, *A higher-order phase-field model for brittle fracture: Formulation and analysis within the isogeometric analysis framework*, *Computer Methods in Applied Mechanics and Engineering* **273**, 100 (2014).
- [177] J. Kiendl, M. Ambati, L. De Lorenzis, H. Gomez, and A. Reali, *Phase-field description of brittle fracture in plates and shells*, *Computer Methods in Applied Mechanics and Engineering* **312**, 374 (2016).
- [178] M. Carraturo, P. Hennig, G. Alaimo, L. Heindel, F. Auricchio, M. Kästner, and A. Reali, *Additive manufacturing applications of phase-field-based topology optimization using adaptive isogeometric analysis*, *GAMM-Mitteilungen* **44**, e202100013 (2021).
- [179] A. Nitti, J. Kiendl, A. Gizzi, A. Reali, and M. D. de Tullio, *A curvilinear isogeometric framework for the electromechanical activation of thin muscular tissues*, *Computer Methods in Applied Mechanics and Engineering* **382**, 113877 (2021).
- [180] F. Nobile, A. Quarteroni, and R. Ruiz-Baier, *An active strain electromechanical model for cardiac tissue*, *International journal for numerical methods in biomedical engineering* **28**, 52 (2012).
- [181] J. M. Guccione and A. D. McCulloch, *Finite element modeling of ventricular mechanics*, *Theory of Heart: biomechanics, biophysics, and nonlinear dynamics of cardiac function* pages 121–144 (1991).
- [182] G. A. Holzapfel and R. W. Ogden, *Constitutive modelling of passive myocardium: a structurally based framework for material characterization*, *Philosophical Transactions of the Royal Society A: Mathematical, Physical and Engineering Sciences* **367**, 3445 (2009).
- [183] Z. Zou, T. Hughes, M. Scott, R. Sauer, and E. Savitha, *Galerkin formulations of isogeometric shell analysis: Alleviating locking with Greville quadratures and higher-order elements*, *Computer Methods in Applied Mechanics and Engineering* **380**, 113757 (2021).
- [184] A. Düster, S. Hartmann, and E. Rank, *p-FEM applied to finite isotropic hyperelastic bodies*, *Computer Methods in Applied Mechanics and Engineering* **192**, 5147 (2003).
- [185] U. Heisserer, S. Hartmann, A. Düster, and Z. Yosibash, *On volumetric locking-free behaviour of p-version finite elements under finite deformations*, *Communications in numerical methods in engineering* **24**, 1019 (2008).

- [186] T. Netz, A. Düster, and S. Hartmann, *High-order finite elements compared to low-order mixed element formulations*, ZAMM-Journal of Applied Mathematics and Mechanics/Zeitschrift für Angewandte Mathematik und Mechanik **93**, 163 (2013).
- [187] T. Elguedj, Y. Bazilevs, V. M. Calo, and T. J. Hughes, *B and F projection methods for nearly incompressible linear and non-linear elasticity and plasticity using higher-order NURBS elements*, Computer methods in applied mechanics and engineering **197**, 2732 (2008).
- [188] F. Fahrenndorf, S. Morganti, A. Reali, T. J. Hughes, and L. De Lorenzis, *Mixed stress-displacement isogeometric collocation for nearly incompressible elasticity and elastoplasticity*, Computer Methods in Applied Mechanics and Engineering **369**, 113112 (2020).
- [189] S. Morganti, F. Fahrenndorf, L. De Lorenzis, J. Evans, T. Hughes, and A. Reali, *Isogeometric collocation: A mixed displacement-pressure method for nearly incompressible elasticity*, Computer Modeling in Engineering and Sciences (2021).
- [190] A. B. Tepole, H. Kabaria, K.-U. Bletzinger, and E. Kuhl, *Isogeometric Kirchhoff–Love shell formulations for biological membranes*, Computer methods in applied mechanics and engineering **293**, 328 (2015).
- [191] B. Dortdivanlioglu, A. Javili, and C. Linder, *Computational aspects of morphological instabilities using isogeometric analysis*, Computer Methods in Applied Mechanics and Engineering **316**, 261 (2017).
- [192] A. B. Tepole, M. Gart, A. K. Gosain, and E. Kuhl, *Characterization of living skin using multi-view stereo and isogeometric analysis*, Acta biomaterialia **10**, 4822 (2014).
- [193] B. Borzeszkowski, T. X. Duong, R. A. Sauer, and I. Lubowiecka, *Isogeometric shell analysis of the human abdominal wall*, in *Innovations in Biomedical Engineering*, pages 11–18, Springer (2021).
- [194] F. Roohbakhshan and R. A. Sauer, *Efficient isogeometric thin shell formulations for soft biological materials*, Biomechanics and modeling in mechanobiology **16**, 1569 (2017).
- [195] A. Moure and H. Gomez, *Influence of myosin activity and mechanical impact on keratocyte polarization*, Soft Matter **16**, 5177 (2020).
- [196] G. Lorenzo, T. J. Hughes, P. Dominguez-Frojan, A. Reali, and H. Gomez, *Computer simulations suggest that prostate enlargement due to benign prostatic hyperplasia mechanically impedes prostate cancer growth*, Proceedings of the National Academy of Sciences **116**, 1152 (2019).
- [197] R. C. Kerckhoffs, S. N. Healy, T. P. Usyk, and A. D. McCULLOCH, *Computational methods for cardiac electromechanics*, Proceedings of the IEEE **94**, 769 (2006).
- [198] J. Keener and J. Sneyd, *Mathematical physiology: II: Systems physiology*, Springer (2009).
- [199] J. Sundnes, G. T. Lines, X. Cai, B. F. Nielsen, K.-A. Mardal, and A. Tveito, *Computing the electrical activity in the heart*, volume 1, Springer Science & Business Media (2007).
- [200] P. C. Franzone, L. F. Pavarino, and S. Scacchi, *Mathematical cardiac electrophysiology*, volume 13, Springer (2014).
- [201] A. Bueno-Orovio, E. M. Cherry, and F. H. Fenton, *Minimal model for human ventricular action potentials in tissue*, Journal of theoretical biology **253**, 544 (2008).
- [202] J. M. Rogers and A. D. McCulloch, *A collocation-Galerkin finite element model of cardiac action potential propagation*, IEEE Transactions on Biomedical Engineering **41**, 743 (1994).
- [203] M. Paci, J. Hyttinen, K. Aalto-Setälä, and S. Severi, *Computational models of ventricular-and atrial-like human induced pluripotent stem cell derived cardiomyocytes*, Annals of biomedical engineering **41**, 2334 (2013).

- [204] M. Torre, S. Morganti, A. Nitti, M. D. de Tullio, F. S. Pasqualini, and A. Reali, *An efficient isogeometric collocation approach to cardiac electrophysiology*, Computer Methods in Applied Mechanics and Engineering **393**, 114782 (2022).
- [205] A. J. Connolly and M. J. Bishop, *Computational representations of myocardial infarct scars and implications for arrhythmogenesis*, Clinical Medicine Insights: Cardiology **10**, CMC (2016).
- [206] R. Kerckhoffs, P. Bovendeerd, J. Kotte, F. Prinzen, K. Smits, and T. Arts, *Homogeneity of cardiac contraction despite physiological asynchrony of depolarization: a model study*, Annals of biomedical engineering **31**, 536 (2003).
- [207] J. Shim, A. Grosberg, J. C. Nawroth, K. K. Parker, and K. Bertoldi, *Modeling of cardiac muscle thin films: pre-stretch, passive and active behavior*, Journal of biomechanics **45**, 832 (2012).
- [208] D. Ambrosi and S. Pezzuto, *Active stress vs. active strain in mechanobiology: constitutive issues*, Journal of Elasticity **107**, 199 (2012).
- [209] S. Göktepe, A. Menzel, and E. Kuhl, *The generalized Hill model: A kinematic approach towards active muscle contraction*, Journal of the Mechanics and Physics of Solids **72**, 20 (2014).
- [210] K. Gillette, M. A. Gsell, J. Bouyssier, A. J. Prassl, A. Neic, E. J. Vigmond, and G. Plank, *Automated framework for the inclusion of a his-purkinje system in cardiac digital twins of ventricular electrophysiology*, Annals of Biomedical Engineering **49**, 3143 (2021).
- [211] L. Molinari, L. Gerardo-Giorda, and A. Gizzi, *A transversely isotropic thermo-hyperelastic constitutive model of myocardial tissue with a three-state cell death dynamics for cardiac radiofrequency ablation*, Journal of the Mechanics and Physics of Solids **161**, 104810 (2022).
- [212] A. Santiago, J. Aguado-Sierra, M. Zavala-Aké, R. Doste-Beltran, S. Gómez, R. Arís, J. C. Cajas, E. Casoni, and M. Vázquez, *Fully coupled fluid-electro-mechanical model of the human heart for supercomputers*, International journal for numerical methods in biomedical engineering **34**, e3140 (2018).
- [213] M. Torre, S. Morganti, A. Nitti, M. D. de Tullio, F. S. Pasqualini, and A. Reali, *Isogeometric mixed collocation of nearly-incompressible electromechanics in finite deformations for cardiac muscle simulations*, Computer Methods in Applied Mechanics and Engineering **411**, 116055 (2023).
- [214] A. Nitti, M. Torre, A. Reali, J. Kiendl, and M. D. de Tullio, *A multiphysics model for fluid-structure-electrophysiology interaction in rowing propulsion*, Submitted (2023).
- [215] M. Elhaddad, N. Zander, T. Bog, L. Kudela, S. Kollmannsberger, J. Kirschke, T. Baum, M. Ruess, and E. Rank, *Multi-level hp-finite cell method for embedded interface problems with application in biomechanics*, International journal for numerical methods in biomedical engineering **34**, e2951 (2018).
- [216] M. de Lucio, M. Bures, A. M. Ardekani, P. P. Vlachos, and H. Gomez, *Isogeometric analysis of subcutaneous injection of monoclonal antibodies*, Computer Methods in Applied Mechanics and Engineering **373**, 113550 (2021).
- [217] M. de Lucio, Y. Leng, A. Hans, I. Bilonis, M. Brindise, A. M. Ardekani, P. P. Vlachos, and H. Gomez, *Modeling large-volume subcutaneous injection of monoclonal antibodies with anisotropic porohyperelastic models and data-driven tissue layer geometries*, Journal of the Mechanical Behavior of Biomedical Materials **138**, 105602 (2023).
- [218] M. C. Wu, H. M. Muchowski, E. L. Johnson, M. R. Rajanna, and M.-C. Hsu, *Immersogeometric fluid-structure interaction modeling and simulation of transcatheter aortic valve replacement*, Computer Methods in Applied Mechanics and Engineering **357**, 112556 (2019).
- [219] E. L. Johnson, M. R. Rajanna, C.-H. Yang, and M.-C. Hsu, *Effects of membrane and flexural stiffnesses on aortic valve dynamics: identifying the mechanics of leaflet flutter in thinner biological tissues*, Forces in mechanics **6**, 100053 (2022).

- [220] W. Zhang, S. Motiwale, M.-C. Hsu, and M. S. Sacks, *Simulating the time evolving geometry, mechanical properties, and fibrous structure of bioprosthetic heart valve leaflets under cyclic loading*, Journal of the mechanical behavior of biomedical materials **123**, 104745 (2021).
- [221] E. Marino, *Locking-free isogeometric collocation formulation for three-dimensional geometrically exact shear-deformable beams with arbitrary initial curvature*, Computer Methods in Applied Mechanics and Engineering **324**, 546 (2017).
- [222] J. Kiendl, F. Auricchio, and A. Reali, *A displacement-free formulation for the Timoshenko beam problem and a corresponding isogeometric collocation approach*, Meccanica **53**, 1403 (2018).
- [223] F. Auricchio, M. Conti, M. Ferraro, S. Morganti, A. Reali, and R. Taylor, *Innovative and efficient stent flexibility simulations based on isogeometric analysis*, Computer Methods in Applied Mechanics and Engineering **295**, 347 (2015).
- [224] L. A. MacQueen, S. P. Sheehy, C. O. Chantre, J. F. Zimmerman, F. S. Pasqualini, X. Liu, J. A. Goss, P. H. Campbell, G. M. Gonzalez, S.-J. Park, et al., *A tissue-engineered scale model of the heart ventricle*, Nature biomedical engineering **2**, 930 (2018).
- [225] S. Botti and M. Torre, *Isogeometric simulation of a derived stem cell engineered ventricle*, Submitted (2023).
- [226] M. Torre, S. Morganti, F. S. Pasqualini, and A. Reali, *A numerical guide to the Isogeometric modeling of the heart biophysics*, Submitted (2023).
- [227] J. C. Nawroth, H. Lee, A. W. Feinberg, C. M. Ripplinger, M. L. McCain, A. Grosberg, J. O. Dabiri, and K. K. Parker, *A tissue-engineered jellyfish with biomimetic propulsion*, Nature biotechnology **30**, 792 (2012).
- [228] K. Takahashi and S. Yamanaka, *Induction of Pluripotent Stem Cells from Mouse Embryonic and Adult Fibroblast Cultures by Defined Factors*, Cell **126**, 663 (2006).
- [229] K. Takahashi, K. Tanabe, M. Ohnuki, M. Narita, T. Ichisaka, K. Tomoda, and S. Yamanaka, *Induction of Pluripotent Stem Cells from Adult Human Fibroblasts by Defined Factors*, Cell **131**, 861 (2007).
- [230] S. D. Lundy, W. Zhu, M. Regnier, and M. A. Laflamme, *Structural and Functional Maturation of Cardiomyocytes Derived from Human Pluripotent Stem Cells*, Stem Cells and Development **22**, 1991 (2013).
- [231] L. MacQueen, S. Sheehy, C. Chantre, J. Zimmerman, F. Pasqualini, L. Xujie, et al., *Addendum: A tissue-engineered scale model of the heart ventricle*, Nature Biomed. Eng. pages 1–1 (2022).
- [232] A. Eder, I. Vollert, A. Hansen, and T. Eschenhagen, *Human engineered heart tissue as a model system for drug testing*, Advanced Drug Delivery Reviews **96**, 214 (2016).
- [233] E. Tzatzalos, O. J. Abilez, P. Shukla, and J. C. Wu, *Engineered heart tissues and induced pluripotent stem cells: Macro- and microstructures for disease modeling, drug screening, and translational studies*, Advanced Drug Delivery Reviews **96**, 234 (2016).
- [234] I. Goldfracht, Y. Efraim, R. Shinnawi, E. Kovalev, I. Huber, A. Gepstein, G. Arbel, N. Shaheen, M. Tiburcy, W. H. Zimmermann, M. Machluf, and L. Gepstein, *Engineered heart tissue models from hiPSC-derived cardiomyocytes and cardiac ECM for disease modeling and drug testing applications*, Acta Biomaterialia **92**, 145 (2019).
- [235] A. M. Lodrini, L. Barile, M. Rocchetti, and C. Altomare, *Human induced pluripotent stem cells derived from a cardiac somatic source: insights for an in-vitro cardiomyocyte platform*, International journal of molecular sciences **21**, 507 (2020).
- [236] M. Paci, J. Hyttinen, K. Aalto-Setälä, and S. Severi, *Computational Models of Ventricular- and Atrial-Like Human Induced Pluripotent Stem Cell Derived Cardiomyocytes*, Annals of Biomedical Engineering **41**, 2334 (2013).

- [237] M. Paci, R.-P. Pölönen, D. Cori, K. Penttinen, K. Aalto-Setälä, S. Severi, and J. Hyttinen, *Automatic optimization of an in silico model of human iPSC derived cardiomyocytes recapitulating calcium handling abnormalities*, *Frontiers in physiology* **9**, 709 (2018).
- [238] S. Botti, *Mathematical modeling of Human Induced Pluripotent Stem Cell-Derived Cardiomyocytes (hiPSC-CMs): from ionic currents to 3D ventricle models*, Ph.D. thesis, University of Pavia (2022).
- [239] J. T. Koivumäki, T. Korhonen, and P. Tavi, *Impact of Sarcoplasmic Reticulum Calcium Release on Calcium Dynamics and Action Potential Morphology in Human Atrial Myocytes: A Computational Study*, *PLoS Computational Biology* **7**, e1001067 (2011).
- [240] J. P. Keener and J. Sneyd, *Mathematical physiology*, volume 1, Springer (1998).
- [241] J. U. Lind, T. A. Busbee, A. D. Valentine, F. S. Pasqualini, H. Yuan, M. Yadid, S.-J. Park, A. Kotikian, A. P. Nesmith, P. H. Campbell, et al., *Instrumented cardiac microphysiological devices via multimaterial three-dimensional printing*, *Nature materials* **16**, 303 (2017).
- [242] A. Lopez-Perez, R. Sebastian, M. Izquierdo, R. Ruiz, M. Bishop, and J. M. Ferrero, *Personalized cardiac computational models: from clinical data to simulation of infarct-related ventricular tachycardia*, *Frontiers in physiology* **10**, 580 (2019).
- [243] V. Iyer, R. Mazhari, and R. L. Winslow, *A computational model of the human left-ventricular epicardial myocyte*, *Biophysical journal* **87**, 1507 (2004).
- [244] P. Pathmanathan, G. R. Mirams, J. Southern, and J. P. Whiteley, *The significant effect of the choice of ionic current integration method in cardiac electro-physiological simulations*, *International Journal for Numerical Methods in Biomedical Engineering* **27**, 1751 (2011).
- [245] J. Kiendl, *Isogeometric analysis and shape optimal design of shell structures*, Ph.D. thesis, Technische Universität München (2011).
- [246] K. P. Vincent, M. J. Gonzales, A. K. Gillette, C. T. Villongco, S. Pezzuto, J. H. Omens, M. J. Holst, and A. D. McCulloch, *High-order finite element methods for cardiac monodomain simulations*, *Frontiers in physiology* **6**, 217 (2015).
- [247] H. Yang and A. Veneziani, *Efficient estimation of cardiac conductivities via POD-DEIM model order reduction*, *Applied Numerical Mathematics* **115**, 180 (2017).
- [248] A. Barone, F. Fenton, and A. Veneziani, *Numerical sensitivity analysis of a variational data assimilation procedure for cardiac conductivities*, *Chaos: An Interdisciplinary Journal of Nonlinear Science* **27**, 093930 (2017).
- [249] A. Barone, M. G. Carlino, A. Gizzi, S. Perotto, and A. Veneziani, *Efficient estimation of cardiac conductivities: A proper generalized decomposition approach*, *Journal of Computational Physics* **423**, 109810 (2020).
- [250] A. Barone, A. Gizzi, F. Fenton, S. Filippi, and A. Veneziani, *Experimental validation of a variational data assimilation procedure for estimating space-dependent cardiac conductivities*, *Computer Methods in Applied Mechanics and Engineering* **358**, 112615 (2020).
- [251] Z. F. Issa, J. M. Miller, and D. P. Zipes, *Clinical arrhythmology and electrophysiology: a companion to Braunwald's heart disease*, Elsevier Health Sciences (2009).
- [252] J. E. Hall and M. E. Hall, *Guyton and Hall textbook of medical physiology e-Book*, Elsevier Health Sciences (2020).
- [253] A. M. Katz, *Physiology of the Heart*, Lippincott Williams & Wilkins (2010).
- [254] R. A. Gray and P. Pathmanathan, *Patient-specific cardiovascular computational modeling: diversity of personalization and challenges*, *Journal of cardiovascular translational research* **11**, 80 (2018).

- [255] A. K. Schroer, M. S. Shotwell, V. Y. Sidorov, J. P. Wikswo, and W. D. Merryman, *I-Wire Heart-on-a-Chip II: Biomechanical analysis of contractile, three-dimensional cardiomyocyte tissue constructs*, *Acta biomaterialia* **48**, 79 (2017).
- [256] J. Bonet and R. D. Wood, *Nonlinear continuum mechanics for finite element analysis*, Cambridge university press (1997).
- [257] P. Colli Franzone, L. F. Pavarino, and S. Scacchi, *Bioelectrical effects of mechanical feedbacks in a strongly coupled cardiac electro-mechanical model*, *Mathematical Models and Methods in Applied Sciences* **26**, 27 (2016).
- [258] A. Loppini, A. Gizzi, R. Ruiz-Baier, C. Cherubini, F. H. Fenton, and S. Filippi, *Competing mechanisms of stress-assisted diffusivity and stretch-activated currents in cardiac electromechanics*, *Frontiers in physiology* **9**, 1714 (2018).
- [259] M. Salvador, L. Dede, and A. Quarteroni, *An intergrid transfer operator using radial basis functions with application to cardiac electromechanics*, *Computational Mechanics* **66**, 491 (2020).
- [260] M. Böl, S. Reese, K. K. Parker, and E. Kuhl, *Computational modeling of muscular thin films for cardiac repair*, *Computational Mechanics* **43**, 535 (2009).
- [261] P. Nardinocchi and L. Teresi, *On the active response of soft living tissues*, *Journal of Elasticity* **88**, 27 (2007).
- [262] P. Pathmanathan, S. Chapman, D. Gavaghan, and J. Whiteley, *Cardiac electromechanics: the effect of contraction model on the mathematical problem and accuracy of the numerical scheme*, *The Quarterly Journal of Mechanics & Applied Mathematics* **63**, 375 (2010).
- [263] S. Göktepe and E. Kuhl, *Electromechanics of the heart: a unified approach to the strongly coupled excitation–contraction problem*, *Computational Mechanics* **45**, 227 (2010).
- [264] Z. Lin, A. Hess, Z. Yu, S. Cai, and T. Gao, *A fluid–structure interaction study of soft robotic swimmer using a fictitious domain/active-strain method*, *Journal of Computational Physics* **376**, 1138 (2019).
- [265] G. Herschlag and L. Miller, *Reynolds number limits for jet propulsion: a numerical study of simplified jellyfish*, *Journal of theoretical biology* **285**, 84 (2011).
- [266] A. P. Hoover, B. E. Griffith, and L. A. Miller, *Quantifying performance in the medusan mechanospace with an actively swimming three-dimensional jellyfish model*, *Journal of Fluid Mechanics* **813**, 1112 (2017).
- [267] A. P. Hoover, A. J. Porras, and L. A. Miller, *Pump or coast: the role of resonance and passive energy recapture in medusan swimming performance*, *J. Fluid Mech* **863**, 1031 (2019).
- [268] E. E. Ruppert, R. D. Barnes, and R. S. Fox, *Invertebrate zoology: a functional evolutionary approach*, 592 RUPi (2004).
- [269] X. Wang, H. Wang, and H. R. Brown, *Jellyfish gel and its hybrid hydrogels with high mechanical strength*, *Soft Matter* **7**, 211 (2011).
- [270] M. N. Arai, *A functional biology of Scyphozoa*, Springer Science & Business Media (1997).
- [271] W. M. Megill, J. M. Gosline, and R. W. Blake, *The modulus of elasticity of fibrillin-containing elastic fibres in the mesoglea of the hydromedusa *Polyorchis penicillatus**, *Journal of Experimental Biology* **208**, 3819 (2005).
- [272] K. Joshi, A. Villanueva, C. Smith, D. Maurya, J. Blottman, and S. Priya, *Aurelia aurita inspired artificial mesoglea*, *Integrated Ferroelectrics* **148**, 53 (2013).
- [273] M. E. Demont and J. M. Gosline, *Mechanics of jet propulsion in the hydromedusan jellyfish, *polyorchis pericillatus*: III. A natural resonating bell; the presence and importance of a resonant phenomenon in the locomotor structure*, *Journal of Experimental Biology* **134**, 347 (1988).

- [274] A. Lowndes, *Percentage of water in jelly-fish*, Nature **150**, 234 (1942).
- [275] S. Hartmann and P. Neff, *Polyconvexity of generalized polynomial-type hyperelastic strain energy functions for near-incompressibility*, International journal of solids and structures **40**, 2767 (2003).
- [276] C. Gambini, B. Abou, A. Ponton, and A. J. Cornelissen, *Micro-and macrorheology of jellyfish extracellular matrix*, Biophysical journal **102**, 1 (2012).
- [277] J. H. Costello, S. P. Colin, J. O. Dabiri, B. J. Gemmell, K. N. Lucas, and K. R. Sutherland, *The hydrodynamics of jellyfish swimming*, Annual Review of Marine Science **13** (2020).
- [278] R. A. Satterlie, *Control of swimming in the hydrozoan jellyfish *Aequorea victoria*: subumbrellar organization and local inhibition*, Journal of experimental Biology **211**, 3467 (2008).
- [279] A. P. Hoover, N. W. Xu, B. J. Gemmell, S. P. Colin, J. H. Costello, J. O. Dabiri, and L. A. Miller, *Neuromechanical wave resonance in jellyfish swimming*, Proceedings of the National Academy of Sciences **118** (2021).
- [280] C. Cherubini, S. Filippi, P. Nardinocchi, and L. Teresi, *An electromechanical model of cardiac tissue: Constitutive issues and electrophysiological effects*, Progress in biophysics and molecular biology **97**, 562 (2008).
- [281] D. Ambrosi, G. Arioli, F. Nobile, and A. Quarteroni, *Electromechanical coupling in cardiac dynamics: the active strain approach*, SIAM Journal on Applied Mathematics **71**, 605 (2011).
- [282] J. H. Costello, S. P. Colin, and J. O. Dabiri, *Medusan morphospace: phylogenetic constraints, biomechanical solutions, and ecological consequences*, Invertebrate Biology **127**, 265 (2008).
- [283] R. A. Satterlie, *Neuronal control of swimming in jellyfish: a comparative story*, Canadian Journal of Zoology **80**, 1654 (2002).
- [284] N. Nakanishi, V. Hartenstein, and D. K. Jacobs, *Development of the rhopalial nervous system in *Aurelia* sp. 1 (Cnidaria, Scyphozoa)*, Development genes and evolution **219**, 301 (2009).
- [285] P. A. Anderson, *Physiology of a bidirectional, excitatory, chemical synapse*, Journal of neurophysiology **53**, 821 (1985).
- [286] F. Pallasdies, S. Goedeke, W. Braun, and R.-M. Memmesheimer, *From single neurons to behavior in the jellyfish *Aurelia aurita**, Elife **8**, e50084 (2019).
- [287] G. A. Horridge et al., *The nerves and muscles of medusae. I. Conduction in the nervous system of *Aurelia aurita* Lamarck* (1954).
- [288] T. L. Daniel, *Mechanics and energetics of medusan jet propulsion*, Canadian Journal of Zoology **61**, 1406 (1983).
- [289] R. A. Satterlie, *Cnidarian nerve nets and neuromuscular efficiency*, Integrative and Comparative Biology **55**, 1050 (2015).
- [290] R. Verzicco and P. Orlandi, *A finite-difference scheme for three-dimensional incompressible flows in cylindrical coordinates*, Journal of Computational Physics **123**, 402 (1996).
- [291] S. P. Colin and J. H. Costello, *Morphology, swimming performance and propulsive mode of six co-occurring hydromedusae*, Journal of experimental biology **205**, 427 (2002).
- [292] M. Ford and J. Costello, *Kinematic comparison of bell contraction by four species of hydromedusae*, Scientia Marina **64**, 47 (2000).
- [293] J. O. Dabiri, S. P. Colin, J. H. Costello, and M. Gharib, *Flow patterns generated by oblate medusan jellyfish: field measurements and laboratory analyses*, Journal of Experimental Biology **208**, 1257 (2005).

- [294] M. Sahin and K. Mohseni, *An arbitrary Lagrangian–Eulerian formulation for the numerical simulation of flow patterns generated by the hydromedusa *Aequorea victoria**, *Journal of Computational Physics* **228**, 4588 (2009).
- [295] M. Ethier and Y. Bourgault, *Semi-implicit time-discretization schemes for the bidomain model*, *SIAM Journal on Numerical Analysis* **46**, 2443 (2008).
- [296] P. Orlandi, *Fluid flow phenomena: a numerical toolkit*, volume 55, Springer Science & Business Media (2000).
- [297] P. Moin and J. Kim, *Numerical investigation of turbulent channel flow*, *Journal of fluid mechanics* **118**, 341 (1982).
- [298] J. Kim, D. Kim, and H. Choi, *An immersed-boundary finite-volume method for simulations of flow in complex geometries*, *Journal of computational physics* **171**, 132 (2001).
- [299] J. H. Ferziger, M. Perić, and R. L. Street, *Computational methods for fluid dynamics*, volume 3, Springer (2002).
- [300] D. B. Haidvogel and T. Zang, *The accurate solution of Poisson’s equation by expansion in Chebyshev polynomials*, *Journal of Computational Physics* **30**, 167 (1979).
- [301] M. Uhlmann, *An immersed boundary method with direct forcing for the simulation of particulate flows*, *Journal of computational physics* **209**, 448 (2005).
- [302] W.-P. Breugem, *A second-order accurate immersed boundary method for fully resolved simulations of particle-laden flows*, *Journal of Computational Physics* **231**, 4469 (2012).
- [303] M. Vanella and E. Balaras, *A moving-least-squares reconstruction for embedded-boundary formulations*, *Journal of computational physics (Print)* **228**, 6617 (2009).
- [304] M. D. de Tullio and G. Pascazio, *A moving-least-squares immersed boundary method for simulating the fluid–structure interaction of elastic bodies with arbitrary thickness*, *Journal of Computational Physics* **325**, 201 (2016).
- [305] G.-R. Liu and Y.-T. Gu, *An introduction to meshfree methods and their programming*, Springer Science & Business Media (2005).
- [306] C. Förster, W. A. Wall, and E. Ramm, *Artificial added mass instabilities in sequential staggered coupling of nonlinear structures and incompressible viscous flows*, *Computer methods in applied mechanics and engineering* **196**, 1278 (2007).
- [307] W.-X. Huang and H. J. Sung, *An immersed boundary method for fluid–flexible structure interaction*, *Computer methods in applied mechanics and engineering* **198**, 2650 (2009).
- [308] B. J. Gemmell, J. H. Costello, S. P. Colin, C. J. Stewart, J. O. Dabiri, D. Tafti, and S. Priya, *Passive energy recapture in jellyfish contributes to propulsive advantage over other metazoans*, *Proceedings of the National Academy of Sciences* **110**, 17904 (2013).
- [309] G. A. Horridge, *The nerves and muscles of medusae: V. double innervation in scyphozoa*, *Journal of experimental Biology* **33**, 366 (1956).
- [310] L. Passano, *Pacemakers and activity patterns in medusae: homage to Romanes*, *American zoologist* **5**, 465 (1965).
- [311] R. A. Satterlie and A. N. Spencer, *Neuronal control of locomotion in hydrozoan medusae*, *Journal of comparative physiology* **150**, 195 (1983).
- [312] B. J. Gemmell, S. P. Colin, J. H. Costello, and J. O. Dabiri, *Suction-based propulsion as a basis for efficient animal swimming*, *Nature communications* **6**, 1 (2015).
- [313] S. Krishnamoorthi, M. Sarkar, and W. S. Klug, *Numerical quadrature and operator splitting in finite element methods for cardiac electrophysiology*, *International journal for numerical methods in biomedical engineering* **29**, 1243 (2013).

- [314] P. Pathmanathan, M. O. Bernabeu, R. Bordas, J. Cooper, A. Garny, J. M. Pitt-Francis, J. P. Whiteley, and D. J. Gavaghan, *A numerical guide to the solution of the bidomain equations of cardiac electrophysiology*, Progress in biophysics and molecular biology **102**, 136 (2010).
- [315] F. Auricchio, L. B. Da Veiga, T. Hughes, A. Reali, and G. Sangalli, *Isogeometric collocation methods*, Mathematical Models and Methods in Applied Sciences **20**, 2075 (2010).
- [316] Z. Qu and A. Garfinkel, *An advanced algorithm for solving partial differential equation in cardiac conduction*, IEEE Transactions on Biomedical Engineering **46**, 1166 (1999).
- [317] L. A. Charawi, *Isogeometric overlapping Schwarz preconditioners for the bidomain reaction–diffusion system*, Computer Methods in Applied Mechanics and Engineering **319**, 472 (2017).
- [318] A. Reali and T. J. Hughes, *An introduction to isogeometric collocation methods*, in *Isogeometric methods for numerical simulation*, pages 173–204, Springer (2015).
- [319] S. Morganti, C. Callari, F. Auricchio, and A. Reali, *Mixed isogeometric collocation methods for the simulation of poromechanics problems in 1D*, Meccanica **53**, 1441 (2018).
- [320] CIBC (2016), seg3D: Volumetric Image Segmentation and Visualization. Scientific Computing and Imaging Institute (SCI), Download from: <http://www.seg3d.org>.
- [321] L. B. Da Veiga, D. Cho, L. Pavarino, and S. Scacchi, *Overlapping Schwarz preconditioners for isogeometric collocation methods*, Computer Methods in Applied Mechanics and Engineering **278**, 239 (2014).
- [322] M. Deo, S. Bauer, G. Plank, and E. Vigmond, *Accelerating large cardiac bidomain simulations by Arnoldi preconditioning*, in *2006 International Conference of the IEEE Engineering in Medicine and Biology Society*, pages 3923–3926, IEEE (2006).
- [323] D. Cho, *Optimal multilevel preconditioners for isogeometric collocation methods*, Mathematics and Computers in Simulation **168**, 76 (2020).
- [324] Y. Rudy, *From Genes and Molecules to Organs and Organisms: Heart*, in E. H. Egelman, editor, *Comprehensive Biophysics*, pages 268–327, Elsevier, Amsterdam (2012).
- [325] M. M. Elshrif and E. M. Cherry, *A quantitative comparison of the behavior of human ventricular cardiac electrophysiology models in tissue*, PloS one **9**, e84401 (2014).
- [326] J. Pitt-Francis, P. Pathmanathan, M. O. Bernabeu, R. Bordas, J. Cooper, A. G. Fletcher, G. R. Mirams, P. Murray, J. M. Osborne, A. Walter, et al., *Chaste: a test-driven approach to software development for biological modelling*, Computer Physics Communications **180**, 2452 (2009).
- [327] T. P. Nguyen, Z. Qu, and J. N. Weiss, *Cardiac fibrosis and arrhythmogenesis: the road to repair is paved with perils*, Journal of molecular and cellular cardiology **70**, 83 (2014).
- [328] S. L. Rutherford, M. L. Trew, G. B. Sands, I. J. LeGrice, and B. H. Smaill, *High-resolution 3-dimensional reconstruction of the infarct border zone: impact of structural remodeling on electrical activation*, Circulation research **111**, 301 (2012).
- [329] A. Düster, E. Rank, and B. Szabó, *The p-Version of the Finite Element and Finite Cell Methods*, Encyclopedia of computational mechanics second edition pages 1–35 (2017).
- [330] D. Schillinger, A. Düster, and E. Rank, *The hp-d-adaptive finite cell method for geometrically nonlinear problems of solid mechanics*, International Journal for Numerical Methods in Engineering **89**, 1171 (2012).
- [331] N. Korshunova, G. Alaimo, S. Hosseini, M. Carraturo, A. Reali, J. Niiranen, F. Auricchio, E. Rank, and S. Kollmannsberger, *Image-based numerical characterization and experimental validation of tensile behavior of octet-truss lattice structures*, Additive Manufacturing **41**, 101949 (2021).

- [332] M. Ruess, D. Schillinger, A. I. Özcan, and E. Rank, *Weak coupling for isogeometric analysis of non-matching and trimmed multi-patch geometries*, Computer Methods in Applied Mechanics and Engineering **269**, 46 (2014).
- [333] L. Coradello, G. Loli, and A. Buffa, *A projected super-penalty method for the  $C^1$ -coupling of multi-patch isogeometric Kirchhoff plates*, Computational Mechanics **67**, 1133 (2021).
- [334] D. Schillinger, M. J. Borden, and H. K. Stolarski, *Isogeometric collocation for phase-field fracture models*, Computer Methods in Applied Mechanics and Engineering **284**, 583 (2015).
- [335] M. Kapl and V. Vitrih, *Isogeometric collocation on planar multi-patch domains*, Computer Methods in Applied Mechanics and Engineering **360**, 112684 (2020).
- [336] Y. Jia, C. Anitescu, Y. J. Zhang, and T. Rabczuk, *An adaptive isogeometric analysis collocation method with a recovery-based error estimator*, Computer Methods in Applied Mechanics and Engineering **345**, 52 (2019).
- [337] E. Burman, S. Claus, P. Hansbo, M. G. Larson, and A. Massing, *CutFEM: discretizing geometry and partial differential equations*, International Journal for Numerical Methods in Engineering **104**, 472 (2015).
- [338] B. Wassermann, S. Kollmannsberger, S. Yin, L. Kudela, and E. Rank, *Integrating CAD and numerical analysis: ‘Dirty geometry’ handling using the Finite Cell Method*, Computer Methods in Applied Mechanics and Engineering **351**, 808 (2019).
- [339] E. Rank, M. Ruess, S. Kollmannsberger, D. Schillinger, and A. Düster, *Geometric modeling, isogeometric analysis and the finite cell method*, Computer Methods in Applied Mechanics and Engineering **249-252**, 104 (2012).
- [340] N. Korshunova, G. Alaimo, S. Hosseini, M. Carraturo, A. Reali, J. Niiranen, F. Auricchio, E. Rank, and S. Kollmannsberger, *Bending behavior of octet-truss lattice structures: Modelling options, numerical characterization and experimental validation*, Materials & Design **205**, 109693 (2021).
- [341] M. Ruess, D. Tal, N. Trabelsi, Z. Yosibash, and E. Rank, *The finite cell method for bone simulations: verification and validation*, Biomechanics and modeling in mechanobiology **11**, 425 (2012).
- [342] S. Heinze, M. Joulaian, and A. Düster, *Numerical homogenization of hybrid metal foams using the finite cell method*, Computers & Mathematics with Applications **70**, 1501 (2015).
- [343] C. Anitescu, Y. Jia, Y. J. Zhang, and T. Rabczuk, *An isogeometric collocation method using superconvergent points*, Computer Methods in Applied Mechanics and Engineering **284**, 1073 (2015).
- [344] H. Gomez and L. De Lorenzis, *The variational collocation method*, Computer Methods in Applied Mechanics and Engineering **309**, 152 (2016).
- [345] M. Montardini, G. Sangalli, and L. Tamellini, *Optimal-order isogeometric collocation at Galerkin superconvergent points*, Computer Methods in Applied Mechanics and Engineering **316**, 741 (2017).
- [346] L. Kudela, N. Zander, S. Kollmannsberger, and E. Rank, *Smart octrees: Accurately integrating discontinuous functions in 3D*, Computer Methods in Applied Mechanics and Engineering **306**, 406 (2016).
- [347] S. Hubrich, P. Di Stolfo, L. Kudela, S. Kollmannsberger, E. Rank, A. Schröder, and A. Düster, *Numerical integration of discontinuous functions: moment fitting and smart octree*, Computational Mechanics **60**, 863 (2017).
- [348] A. Abedian and A. Düster, *Equivalent Legendre polynomials: Numerical integration of discontinuous functions in the finite element methods*, Computer Methods in Applied Mechanics and Engineering **343**, 690 (2019).
- [349] E. Rank, S. Kollmannsberger, C. Sorger, and A. Düster, *Shell finite cell method: a high order fictitious domain approach for thin-walled structures*, Computer Methods in Applied Mechanics and Engineering **200**, 3200 (2011).

- [350] M. Carraturo, S. Kollmannsberger, A. Reali, F. Auricchio, and E. Rank, *An immersed boundary approach for residual stress evaluation in selective laser melting processes*, Additive Manufacturing **46**, 102077 (2021).
- [351] M. Carraturo, J. Jomo, S. Kollmannsberger, A. Reali, F. Auricchio, and E. Rank, *Modeling and experimental validation of an immersed thermo-mechanical part-scale analysis for laser powder bed fusion processes*, Additive Manufacturing **36**, 101498 (2020).
- [352] J. Fish and T. Belytschko, *A first course in finite elements*, volume 1, John Wiley & Sons New York (2007).
- [353] T. J. Hughes, *The finite element method: linear static and dynamic finite element analysis*, Courier Corporation (2012).
- [354] I. Babuška, *The finite element method with penalty*, Mathematics of computation **27**, 221 (1973).
- [355] S. Fernández-Méndez and A. Huerta, *Imposing essential boundary conditions in mesh-free methods*, Computer Methods in Applied Mechanics and Engineering **193**, 1257 (2004).
- [356] A. Hansbo and P. Hansbo, *An unfitted finite element method, based on Nitsche’s method, for elliptic interface problems*, Computer Methods in Applied Mechanics and Engineering **191**, 5537 (2002).
- [357] Dassault Systemes Simulia Corp., *ABAQUS Standard User’s Manual* (2017).
- [358] A. Patton, P. Antolín, J. Kiendl, and A. Reali, *Efficient equilibrium-based stress recovery for isogeometric laminated curved structures*, Composite Structures **272**, 113975 (2021).
- [359] T. Roy, Y. Bourgault, and C. Pierre, *Analysis of time-stepping methods for the monodomain model*, Computational and Applied Mathematics **39**, 1 (2020).
- [360] S. A. Niederer and N. P. Smith, *The role of the Frank–Starling law in the transduction of cellular work to whole organ pump function: a computational modeling analysis*, PLoS computational biology **5**, e1000371 (2009).
- [361] E. J. Vigmond, M. Hughes, G. Plank, and L. J. Leon, *Computational tools for modeling electrical activity in cardiac tissue*, Journal of electrocardiology **36**, 69 (2003).
- [362] C. M. Augustin, A. Neic, M. Liebmann, A. J. Prassl, S. A. Niederer, G. Haase, and G. Plank, *Anatomically accurate high resolution modeling of human whole heart electromechanics: a strongly scalable algebraic multigrid solver method for nonlinear deformation*, Journal of computational physics **305**, 622 (2016).
- [363] T. P. Usyk, I. J. LeGrice, and A. D. McCulloch, *Computational model of three-dimensional cardiac electromechanics*, Computing and visualization in science **4**, 249 (2002).
- [364] J. P. Whiteley, *An efficient numerical technique for the solution of the monodomain and bidomain equations*, IEEE Transactions on Biomedical Engineering **53**, 2139 (2006).
- [365] J. A. Evans, R. R. Hiemstra, T. J. Hughes, and A. Reali, *Explicit higher-order accurate isogeometric collocation methods for structural dynamics*, Computer Methods in Applied Mechanics and Engineering **338**, 208 (2018).
- [366] R. R. Aliev and A. V. Panfilov, *A simple two-variable model of cardiac excitation*, Chaos, Solitons & Fractals **7**, 293 (1996).
- [367] M. P. Nash and A. V. Panfilov, *Electromechanical model of excitable tissue to study reentrant cardiac arrhythmias*, Progress in biophysics and molecular biology **85**, 501 (2004).
- [368] W. J. Gordon and L. C. Thiel, *Transfinite mappings and their application to grid generation*, Appl. Math. Comput. **10**, 171 (1982).
- [369] S. P. Timoshenko and J. N. Goodier, *Theory of elasticity*, McGraw-hill (1951).

- [370] M. Kholdi, A. Loghman, H. Ashrafi, and M. Arefi, *Analysis of thick-walled spherical shells subjected to external pressure: Elastoplastic and residual stress analysis*, Proceedings of the Institution of Mechanical Engineers, Part L: Journal of Materials: Design and Applications **234**, 186 (2020).
- [371] E. W. Weisstein, *Heat Conduction Equation–Disk*, <https://mathworld.wolfram.com/HeatConductionEquationDisk.html> (2022).
- [372] M. Gharib, E. Rambod, and K. Shariff, *A universal time scale for vortex ring formation*, Journal of Fluid Mechanics **360**, 121 (1998).
- [373] W. Zhao, S. H. Frankel, and L. G. Mongeau, *Effects of trailing jet instability on vortex ring formation*, Physics of Fluids **12**, 589 (2000).
- [374] A. Ten Cate, C. Nieuwstad, J. Derksen, and H. Van den Akker, *Particle imaging velocimetry experiments and lattice-Boltzmann simulations on a single sphere settling under gravity*, Physics of Fluids **14**, 4012 (2002).
- [375] T. Kempe and J. Fröhlich, *An improved immersed boundary method with direct forcing for the simulation of particle laden flows*, Journal of Computational Physics **231**, 3663 (2012).
- [376] C.-C. Liao, Y.-W. Chang, C.-A. Lin, and J. McDonough, *Simulating flows with moving rigid boundary using immersed-boundary method*, Computers & Fluids **39**, 152 (2010).
- [377] M. Itskov et al., *Tensor algebra and tensor analysis for engineers*, Springer (2007).